

UNSW



>014954702

THE UNIVERSITY OF NEW SOUTH WALES  
Thesis/Dissertation Sheet

Surname or Family name: **Vogt**

First name: **Jonathan**

Other name/s: **William**

Abbreviation for degree as given in the University calendar: **Ph.D.**

School: **Mechanical and Manufacturing Engineering**

Faculty: **Engineering**

Title: **An Examination of Ground Effect Phenomena and the Development of Ground Effect Induced Flow Separation on a Downforce Generating Wing**

**Abstract 350 words maximum:**

The 'ground effect' phenomenon can be characterised as a change in the aerodynamic behaviour of a body when in close ground proximity. It has been heavily exploited in the motor racing industry where inverted wings are used to produce more downforce. However, several aspects of how ground effect manifests about wings is still not well understood. Chief among them is how flow separation develops about inverted wings in ground effect.

Ground effect's influence on several aerofoil and wing arrangements was studied through various Computational Fluid Dynamics (CFD) analyses. The CFD modelling was validated by moving-ground wind tunnel experimentation.

A two-dimensional CFD investigation identified two ground effect mechanisms apparent for both upright and inverted aerofoils: a reduction in the effective angle of attack and a diversion of flow over the wing. Top surface camber was found to be important in generating underwing suction on inverted aerofoils as was a rapid upward curve on the bottom surface.

A CFD model was developed which was able to model the unsteady turbulent behaviour about a quasi-two-dimensional inverted Tyrrell wing in extreme ground effect. The model utilised span-normal periodic boundary walls which offered a significant computational efficiency. Various CFD methodologies were also assessed resulting in an LES model employing the Dynamic Smagorinsky-Lilly sub-grid turbulence model.

LES simulations modelled the flow separation on an inverted Tyrrell wing in extreme ground effect. Featuring a separation bubble, both a progressive and sudden form of separation were identified. The progressive form (worsening with reduced clearance) initiates at the trailing edge and is caused by the strengthening diffuser effect whose growing outlet-to-inlet ratio eventually creates a jet flow near the ground which cannot supply kinetic energy to the boundary layer. This separation was not caused by an excessive adverse pressure gradient, as often thought. The sudden form of separation is associated with the eventual inability of the shear layer to reattach. This is caused by the diversion of flow over the wing, starving the boundary layer of energy, and due to movement of the transition point further away from the boundary layer which prevents the separated shear layer from reattaching.

**Declaration relating to disposition of project thesis/dissertation**

I hereby grant to the University of New South Wales or its agents the right to archive and to make available my thesis or dissertation in whole or in part in the University libraries in all forms of media, now or here after known, subject to the provisions of the Copyright Act 1968. I retain all property rights, such as patent rights. I also retain the right to use in future works (such as articles or books) all or part of this thesis or dissertation.

I also authorise University Microfilms to use the 350 word abstract of my thesis in Dissertation Abstracts International (this is applicable to doctoral theses only).

Date

The University recognises that there may be exceptional circumstances requiring restrictions on copying or conditions on use. Requests for restriction for a period of up to 2 years must be made in writing. Requests for a longer period of restriction may be considered in exceptional circumstances and require the approval of the Dean of Graduate Research.

**FOR OFFICE USE ONLY**

Date of completion of requirements for Award:

10/06/10



**UNSW**  
THE UNIVERSITY OF NEW SOUTH WALES  
SYDNEY • AUSTRALIA

**An Examination of Ground Effect  
Phenomena and the Development of  
Ground Effect Induced Flow Separation on  
a Downforce Generating Wing**

by

**Jonathan William Vogt**

A thesis submitted for the degree of Doctor of Philosophy

The University of New South Wales  
School of Mechanical and Manufacturing Engineering

March, 2010

# Author Declaration

## COPYRIGHT STATEMENT

'I hereby grant the University of New South Wales or its agents the right to archive and to make available my thesis or dissertation in whole or part in the University libraries in all forms of media, now or here after known, subject to the provisions of the Copyright Act 1968. I retain all proprietary rights, such as patent rights. I also retain the right to use in future works (such as articles or books) all or part of this thesis or dissertation.

I also authorise University Microfilms to use the 350 word abstract of my thesis in Dissertation Abstract International (this is applicable to doctoral theses only).

I have either used no substantial portions of copyright material in my thesis or I have obtained permission to use copyright material; where permission has not been granted I have applied/will apply for a partial restriction of the digital copy of my thesis or dissertation.'

Signed .....

Date ..... 19/7/2010 .....

## AUTHENTICITY STATEMENT

'I certify that the Library deposit digital copy is a direct equivalent of the final officially approved version of my thesis. No emendation of content has occurred and if there are any minor variations in formatting, they are the result of the conversion to digital format.'

Signed .....

Date ..... 19/7/2010 .....

## ORIGINALITY STATEMENT

'I hereby declare that this submission is my own work and to the best of my knowledge it contains no materials previously published or written by another person, or substantial proportions of material which have been accepted for the award of any other degree or diploma at UNSW or any other educational institution, except where due acknowledgement is made in the thesis. Any contribution made to the research by others, with whom I have worked at UNSW or elsewhere, is explicitly acknowledged in the thesis. I also declare that the intellectual content of this thesis is the product of my own work, except to the extent that assistance from others in the project's design and conception or in style, presentation and linguistic expression is acknowledged.'

Signed .....

Date ..... 19/7/2010 .....

# Thesis Abstract

‘Ground effect’ is a phenomenon that can be characterised as a change in the aerodynamic behaviour of a body when it operates in close proximity to the ground. For many years, it has been exploited in the motor racing industry where inverted wings that produce beneficial downforce (negative lift) are used. Doing so allows these inverted wings to produce yet more downforce.

Despite this application being utilised extensively, several aspects of how ground effect manifests about wings is still not well understood. Chief among them is how flow separation develops about inverted wings in ground effect. It has been shown previously that flow separation develops much more rapidly near the ground, however, a full explanation for how this transpires has been lacking. Additionally, an understanding of how ground effect works about differently shaped wings, and the underlying causes which generate these different behaviours, has not been elucidated.

The influence of ground effect on several aerofoil and wing arrangements has been studied through various Computational Fluid Dynamics (CFD) analyses. The CFD modelling work throughout has been validated by way of moving-ground wind tunnel experimentation, using non-intrusive smoke flow visualisation and Laser Doppler Anemometry (LDA) measurement.

A two-dimensional CFD investigation was undertaken to observe the ground effect behaviour about both an upright and inverted Tyrrell aerofoil, in order to clarify and differentiate the workings of ground effect for both cases. Two general mechanisms were identified in both cases: a reduction in effective angle of attack near the ground and a significant diversion of flow over the wing, when near the ground. Additional analyses on various inverted aerofoil geometries revealed that top surface camber is important in the generation of underwing suction and that a rapid upward curve on the bottom side of the aerofoil increases the effectiveness of the diffuser effect at the rear of the aerofoil.

A project was undertaken to develop a CFD model which would be able to effectively model the unsteady turbulent behaviour about a quasi-two-dimensional inverted Tyrrell wing in extreme ground effect. A model which utilises span-normal periodic boundary walls was developed which offered a significant computational efficiency. Various CFD methodologies

were also assessed resulting in an LES model which uses the Dynamic Smagorinsky-Lilly sub-grid turbulence model.

Extensive LES simulations were conducted to model the ground effect induced flow separation that occurs on an inverted Tyrrell wing in extreme ground effect. Featuring a separation bubble near the leading edge, both a progressive and a sudden form of separation were identified. The progressive form (worsening as the ground is approached) initiated at the trailing edge and was found to be caused by the strengthening diffuser effect whose growing outlet-to-inlet ratio eventually creates a jet flow near the ground which cannot supply kinetic energy to the boundary layer. This form of separation was found not to be due to an excessive adverse pressure gradient, as often thought. The sudden form of separation is associated with the eventual inability of the separated shear layer to reattach. This was caused by both the diversion of flow over the wing, starving the boundary layer of kinetic energy, and also due to movement of the turbulent transition point further away from the boundary layer which ultimately prevents the separated shear layer from reattaching.

# Acknowledgements

I would like to express my gratitude to the following people, without whom this thesis would not have happened.

First and foremost, I extend my most sincere thanks to my supervisor Dr. Tracie Barber who has been a constant source of sage advice, guidance and optimism. Unlike me, no problem was ever large enough to stump her, nor get her down, which was always an enormous encouragement. Additionally, I have greatly appreciated her friendship which has made the last four years a far more pleasant experience than it might have otherwise been.

To my late co-supervisor Prof. Eddie Leonardi, who tragically passed away in late 2008. Eddie was a very busy man but his commitment to supporting and helping his Ph.D. students in any way he could – despite the million things on his plate – was pretty remarkable. He was also a very knowledgeable authority on all things CFD, which was extremely helpful (and challenging).

My thanks go to my current co-supervisor Dr. John Young from the Australian Defence Force Academy who was very gracious in coming on-board this project at a late stage. He has provided excellent advice on how to improve this document and has done so in a pretty tight timeframe.

My sincere thanks go to Joe Tscherry who, over the last couple of years, has helped me conduct the experimental component of this project. Together, we have faced continual infuriating breakages, delays, poor equipment performance and, what we concluded must be, industrial espionage (no, not really, but maybe – we still haven't come up with a better explanation...). The number of times Joe has laboriously realigned the LDA lasers once they've mysteriously decided to misalign themselves again, I really don't want to know. However, with Joe's help, all of these problems were eventually overcome and the experiments were completed. So, for his assistance and patience, he has my thanks.

I also want to thank my brother, Robbie Vogt, who does speaker recognition research (and all manner of complicated related stuff) at the Queensland University of Technology. Robbie was of great help in the frequency analysis part of this work, giving very generously of his

time to ensure my data were analysed correctly and effectively. He even interrupted one of his ever-so-infrequent holidays to help me refine and proof read that section.

To my best friend and fellow sucker-for-punishment, Merrill Lee, I owe an enormous debt of gratitude. Merrill has been my partner in crime throughout this journey, having started his Ph.D. at the same time. He has always been a source of wise counsel, great friendship and, a sympathetic ear when I need to vent. For the many coffees we've shared, for the many afternoons we decided not working was a better idea than working, and for the many other ways he kept me sane, I am extremely grateful.

To another great friend and colleague, Osama Alshroof, who has also given me much to be thankful for. Having also done a CFD Ph.D. alongside me, I have often discussed my work with him at great length, and his advice has always been extremely helpful. More importantly, however, his friendship in times of woe has always been a great comfort.

To my fantastically loving and supportive family – and in particular, my parents – I am so grateful. Having moved from Brisbane to Sydney to undertake all this, I have always found the separation difficult. However, despite the distance between us most of the time, they have still managed to impart enormous encouragement and love. They have always been so keenly interested in precisely how things have been going and have been extremely diligent in keeping me in their prayers. Every time I visit Brisbane, I find everyone has been kept well informed of how I'm going which is very touching. Knowing that I've got a support network such as this is a great blessing indeed.

Finally, I thank God for his provision and seeing fit that I should achieve this goal.

# Table of Contents

<b>Author Declaration</b> .....	<b>i</b>
<b>Thesis Abstract</b> .....	<b>ii</b>
<b>Acknowledgements</b> .....	<b>iv</b>
<b>Table of Contents</b> .....	<b>vi</b>
<b>List of Figures</b> .....	<b>ix</b>
<b>List of Tables</b> .....	<b>xiii</b>
<b>Nomenclature</b> .....	<b>xiv</b>
<b>Chapter 1: Introduction, Review of Literature and Overview of Research Programme</b>	<b>1</b>
1.1 Introduction.....	1
1.2 Review of Literature and Relevance of Topic .....	2
1.2.1 Race Car Aerodynamics .....	2
1.2.2 Inverted Aerofoils and Wings in Ground Effect .....	3
1.2.2.1 Experimental Approach .....	3
1.2.2.2 Numerical Approach.....	7
1.2.3 Upright Aerofoils and Wings in Ground Effect.....	10
1.2.3.1 Experimental Approach .....	11
1.2.3.2 Numerical and/or Analytical Approach .....	11
1.2.4 Relevance of Topic .....	12
1.3 Introduction to Research Programme .....	12
<b>Chapter 2: Computational Fluid Dynamics Theory and Methodology</b> .....	<b>14</b>
2.1 Introduction.....	14
2.2 Introduction to CFD simulation .....	14
2.2.1 Governing Fluid Flow Equations.....	14
2.2.1.1 Conservation of Mass .....	14
2.2.1.2 Conservation of Momentum .....	15
2.2.1.3 Conservation of Energy .....	15
2.2.2 General CFD Solution Process .....	16
2.2.2.1 Pre-processing .....	16
2.2.2.2 Solving.....	16
2.2.2.3 Post-processing.....	16
2.3 Numerical Methods of Finite-Volume CFD Solvers .....	17
2.3.1 The Navier-Stokes and Transport Equations for the Finite-Volume Method .....	17
2.3.2 Solver Solution Process .....	18
2.4 Verification and Validation Process .....	20
2.5 The Reynolds-Averaged Navier-Stokes Solver .....	22
2.5.1 Reynolds-Averaged Navier-Stokes Equations.....	22
2.5.2 Turbulence Modelling.....	23
2.6 Large Eddy Simulation .....	24
2.6.1 Flow Filtering .....	25
2.6.2 Sub-Grid Scale Turbulence Modelling .....	27
2.6.2.1 The Smagorinsky-Lilly Model.....	27
2.6.2.2 The Dynamic Smagorinsky-Lilly model.....	27
2.6.2.3 The Dynamic Sub-grid Kinetic Energy Model .....	28
2.7 Pseudo-Direct Numerical Simulation .....	28
2.8 Current State-of-the-Art of CFD Methodology .....	29
2.8.1 Preliminary Modelling Considerations .....	30
2.8.2 Large Eddy Simulation .....	31
2.8.3 Direct Numerical Simulation .....	32
2.8.4 Periodic Boundary Conditions .....	32
2.8.5 Pseudo-Direct Numerical Simulation .....	35

2.8.6	Grid Structure .....	35
<b>Chapter 3: Experimental Programme.....</b>		<b>37</b>
3.1	Introduction .....	37
3.2	Wind Tunnel Models and Facilities.....	37
3.3	Laser Doppler Anemometry Technique .....	40
3.3.1	Doppler Effect .....	40
3.3.2	System Setup .....	44
3.3.3	Sources of Error.....	47
3.4	CFD Validation Experiment.....	49
3.4.1	Velocity and Boundary Layer Profiles .....	49
3.4.2	Frequency Analysis .....	53
<b>Chapter 4: Development and Description of Computational Fluid Dynamics Models ..</b>		<b>56</b>
4.1	Introduction .....	56
4.2	Development of Two-Dimensional ‘Free-Air’ Condition Model.....	56
4.2.1	Description and Verification of Model.....	56
4.2.2	Validation of Model.....	59
4.3	Development of Quasi-Two-Dimensional Wind Tunnel Condition Models.....	61
4.3.1	Large Eddy Simulation Model.....	64
4.3.2	Pseudo-Direct Numerical Simulation Model.....	78
<b>Chapter 5: Results and Discussion 1: Two-Dimensional Steady Simulations of Inverted Aerofoils in Ground Effect.....</b>		<b>81</b>
5.1	Introduction .....	81
5.2	Ground Effect Phenomena about Lift and Downforce Generating Cambered Aerofoils .....	81
5.2.1	Force Behaviour .....	83
5.2.2	Pressure Coefficient Distributions.....	87
5.2.3	Flow Field.....	89
5.2.3.1	Velocity Contours .....	89
5.2.3.2	Turbulence Intensity.....	91
5.2.4	Dividing Streamline Movement as Part of General Ground Effect Mechanism.....	91
5.2.4.1	Dividing Streamline movement.....	91
5.2.4.2	Dividing Streamline Relationship to General Ground Effect Mechanism.....	93
5.2.5	Stagnation Point Movement as Part of General Ground Effect Mechanism.....	94
5.2.5.1	Stagnation Point Movement .....	94
5.2.5.2	Stagnation Point Relationship to General Ground Effect Mechanism.....	95
5.3	Variation of Ground Effect Phenomena about Downforce Generating Aerofoils Caused by Changes in Aerofoil Shape .....	97
5.3.1	Modified Tyrrell Aerofoils .....	99
5.3.1.1	Leading Edge Modification.....	99
5.3.1.2	Top Surface Modification .....	101
5.3.1.3	Bottom Surface Modification.....	101
5.3.2	Results and Discussion .....	102
5.3.2.1	Tyrrell and NACA4412 Aerofoil Comparison.....	102
5.3.2.1.1	Force Behaviour.....	102
5.3.2.1.2	Pressure Coefficient Distributions .....	106
5.3.2.1.3	Dividing Streamlines .....	108
5.3.2.1.4	Stagnation Point.....	109
5.3.2.2	Modified Tyrrell Aerofoils Comparison.....	111
5.3.2.2.1	Pressure Coefficient Distributions .....	111
5.3.2.2.2	Velocity Contours and Turbulence Intensity.....	115
5.3.2.2.3	Development of New ‘Vogt’ Aerofoil .....	116
5.4	Conclusions .....	117
<b>Chapter 6: Results and Discussion 2: Comparison of Techniques for Modelling Unsteady Flow over an Inverted Aerofoil in Ground Effect .....</b>		<b>121</b>
6.1	Introduction .....	121
6.2	Techniques Assessed .....	121
6.3	Model Selection.....	122
6.3.1	Remarks on Experimental Data .....	122
6.3.2	Model Selection.....	128
6.3.3	Frequency Analysis .....	132
6.4	Conclusions .....	137

<b>Chapter 7: Results and Discussion 3: Flow Separation about a Highly Cambered Inverted Wing in Ground Effect.....</b>	<b>138</b>
7.1 Introduction.....	138
7.2 Results and Discussion .....	139
7.2.1 Force Behaviour.....	139
7.2.2 Pressure Coefficient Plots .....	141
7.2.3 Velocity Contours .....	144
7.2.4 Separation, Transition and Reattachment .....	148
7.2.5 Velocity Profiles and Reynolds Stresses.....	151
7.2.6 Vorticity and Turbulent Wake .....	157
7.2.7 Development of Flow Separation .....	157
7.3 Conclusions.....	163
<b>Chapter 8: Conclusions .....</b>	<b>165</b>
8.1 Conclusions of Research.....	165
8.1.1 Ground Effect Phenomena about 2D Aerofoils .....	165
8.1.2 Performing Numerical Simulations of Unsteady Quasi-2D Flow about Inverted Wings in Ground Effect .....	168
8.1.3 Unsteady Quasi-2D Flow Separation about an Inverted Aerofoil in Ground Effect.....	169
8.2 Recommendations for Future Work.....	171
<b>Chapter 9: References .....</b>	<b>173</b>
<b>Appendix A: Computational Fluid Dynamics Theory.....</b>	<b>176</b>
A.1 Conservation of Momentum Equations.....	176
A.2 Conservation of Energy Equation .....	177
A.3 The Navier-Stokes and Transport Equations for the Finite-Volume Method .....	178
A.4 Discretisation of Flow Properties.....	180
A.5 The SIMPLE Algorithm.....	184
A.6 Verification and Validation Process.....	189
A.7 Error Sources in CFD.....	191
A.8 Reynolds-Averaged Navier-Stokes Equations .....	193
<b>Appendix B: Dividing Streamline Movement .....</b>	<b>196</b>
<b>Appendix C: Derivation of LDA Transformation Matrix.....</b>	<b>199</b>
<b>Appendix D: Experimental and Numerical Velocity Profile Comparisons .....</b>	<b>201</b>
<b>Appendix E: Publications Resulting from Ph.D. Research Programme .....</b>	<b>213</b>
E.1 Peer-Reviewed Journal Papers .....	213
E.2 Peer-Reviewed Conference Papers .....	213

# List of Figures

Figure 1.1: Wall normal Reynolds stress normalised by $U_{\tau,ref}^2$ (Song, DeGraaff, and Eaton, 2000) .....	4
Figure 1.2: $C_L$ in ground effect (Zerihan and Zhang, 2000).....	5
Figure 1.3: Tyrrell wing with 2.9 % Gurney flap (Zerihan and Zhang, 2001).....	6
Figure 1.4: Double-element configuration (Zhang and Zerihan, 2003a) .....	6
Figure 1.5: Lift comparison; road (moving) and wind tunnel (stationary) conditions (Ranzenbach, 1995). Negative $C_l$ indicates positive downforce .....	8
Figure 1.6: Lift curves in ground effect, varying AOA of main element (Soso and Wilson, 2004) .....	9
Figure 1.7: Lift curves in ground effect; varying main element proportion of total chord (Soso and Wilson, 2004) .....	9
Figure 2.1: The SIMPLE algorithm .....	19
Figure 2.2: Unsteady SIMPLE algorithm.....	20
Figure 2.3: Schematic of CFD approach (adapted from Barber, 2005) .....	21
Figure 2.4: Filtering of reference signal (solid) with filter length of $l/16$ (dashed) and $l/4$ (dash-dotted) (Geurts, 2004).....	25
Figure 3.1: Elevation of wind tunnel test section.....	38
Figure 3.2: Elevation of wind tunnel (Diasinos, 2009).....	38
Figure 3.3: Wind tunnel and LDA system .....	39
Figure 3.4: Doppler frequency measurement.....	40
Figure 3.5: LDA Doppler frequency measurement.....	41
Figure 3.6: Laser interference pattern (BSA Flow Software, 2006) .....	42
Figure 3.7: Determination of fringe spacing .....	42
Figure 3.8: LDA velocity measurement with a Bragg cell.....	44
Figure 3.9: Schematic of LDA system.....	44
Figure 3.10: Setup for LDA probes (modified from BSA Flow Software, 2006).....	45
Figure 3.11: LDA velocity profile sweeps, $h/c = 0.05$ , $\alpha = 2^\circ$ .....	49
Figure 3.12: Wind tunnel input velocity profile.....	52
Figure 3.13: Experimental x-velocity profiles at $x/c$ locations labelled; $0.1 x/c = 10$ m/s .....	53
Figure 3.14: LDA frequency analysis points, $h/c = 0.05$ , $\alpha = 2^\circ$ .....	54
Figure 3.15: Example of raw signal for frequency analysis.....	55
Figure 3.16: Example PSD from frequency analysis .....	55
Figure 4.1: Mesh structure about inverted Tyrrell aerofoil, $h/c = 0.15$ , $\alpha = 6^\circ$ (inset) entire domain mesh.....	59
Figure 4.2: Validation case; (a) $C_p$ plot for $h/c = 0.224$ , (b) velocity deficit in wake flow at $x/c = 1.2$ .....	61
Figure 4.3: Geometry of wind tunnel test-section to be simulated by numerical models .....	62
Figure 4.4: Flow visualisation images about Tyrrell wing; arrow indicates trailing edge .....	63
Figure 4.5: First-generation Harpoon mesh (3.4 million cells).....	65
Figure 4.6: Second-generation Harpoon mesh (14.9 million cells).....	66
Figure 4.7: Third-generation Harpoon mesh (13.7 million cells) .....	67
Figure 4.8: Lift coefficient plots of intermediate Harpoon grid at various time-step sizes.....	68
Figure 4.9: Drag coefficient plots of intermediate Harpoon grid at various time-step sizes.....	68
Figure 4.10: Spanwise vorticity contours comparison between intermediate Harpoon mesh and sliver mesh on spanwise midplanes.....	68
Figure 4.11: Sliver model geometry.....	69
Figure 4.12: Temporal $C_l$ and $C_d$ plot of baseline sliver model, test 1 .....	71
Figure 4.13: Qualitative results from sliver model test 1; a-c) iso-surface of vorticity magnitude = 3000 /s coloured by vertical position, d) contours of spanwise vorticity at midplane, e) contours of instantaneous velocity magnitude at midplane .....	72

Figure 4.14: Time step size comparison for sliver model (tests 1 and 2).....	73
Figure 4.15: Sample residual plot for a single time step of an LES sliver model simulation.....	73
Figure 4.16: Sliver model mesh schematic (not to scale).....	74
Figure 4.17: Sliver mesh explosion.....	75
Figure 4.18: Sliver mesh.....	77
Figure 4.19: Grid comparisons; column 1) test 4 coarse mesh, column 2) test 1 baseline mesh, column 3) test 5 fine spanwise mesh, row 1) RMS velocity magnitude, row 2) velocity magnitude and row 3) spanwise vorticity.....	78
Figure 4.20: Comparisons of iso-surface of vorticity magnitude: a) test 4 coarse mesh, b) test 1 baseline mesh and c) test 5 fine-spanwise mesh.....	79
Figure 4.21: Sample residual plot for a single time step of an P-DNS sliver model simulation.....	80
Figure 5.1: Coefficient of normal force vs. ground clearance.....	83
Figure 5.2: Aerofoil surface name convention.....	84
Figure 5.3: Normal force components vs. ground clearance; (a) inverted aerofoil, (b) upright aerofoil.....	85
Figure 5.4: Coefficient of drag vs. ground clearance.....	85
Figure 5.5: Drag force components vs. ground clearance; (a) inverted aerofoil, (b) upright aerofoil.....	86
Figure 5.6: Plot of pressure coefficient $C_p$ about inverted aerofoil at $h/c = 1.00$ .....	86
Figure 5.7: Pressure coefficient distributions for inverted aerofoil at various ground clearances.....	87
Figure 5.8: Leading edge region from Figure 5.7 about inverted aerofoil.....	88
Figure 5.9: Pressure coefficient distributions for upright aerofoil at various ground clearances.....	88
Figure 5.10: Leading edge region from Figure 5.9 about upright aerofoil.....	89
Figure 5.11: Velocity contours ( $V/V_\infty$ ) about inverted aerofoil at; (a) $h/c = 1.00$ , (b) $h/c = 0.30$ and (c) $h/c = 0.15$ , and upright aerofoil at; (d) $h/c = 1.00$ , (e) $h/c = 0.30$ and (f) $h/c = 0.03$ .....	90
Figure 5.12: Contours of turbulence intensity percentage; (a) inverted aerofoil at $h/c = 0.15$ , (b) upright aerofoil at $h/c = 0.03$ .....	91
Figure 5.13: Dividing streamlines on inverted aerofoil at $h/c = 1.00$ , $\alpha = 6^\circ$ .....	92
Figure 5.14: Position of dividing streamline at 3.0 chords distance from aerofoils vs. ground clearance.....	92
Figure 5.15: Stagnation point position vs. ground clearance.....	94
Figure 5.16: Volume flow rate under aerofoil vs. clearance between ground and trailing edge.....	95
Figure 5.17: Volume flow rate under aerofoil normalised by ‘ideal’ flow rate at given ground clearance.....	96
Figure 5.18: NACA4412 and Tyrrell aerofoils at incidence of $6^\circ$ .....	99
Figure 5.19: LE Mod cutting location assessment and final curvature.....	100
Figure 5.20: Superposition of original and modified aerofoils.....	101
Figure 5.21: Normal force coefficients vs. ground clearance.....	102
Figure 5.22: Drag coefficient vs. ground clearance.....	103
Figure 5.23: Normal force components vs. ground clearance; (a) Tyrrell aerofoil, (b) NACA4412 aerofoil.....	104
Figure 5.24: Drag force components vs. ground clearance; (a) Tyrrell aerofoil, (b) NACA4412 aerofoil.....	104
Figure 5.25: Pressure coefficient distributions plotted perpendicular to aerofoil surface.....	106
Figure 5.26: Pressure coefficient distributions at various ground clearances; (a) Tyrrell aerofoil, (b) NACA4412 aerofoil.....	107
Figure 5.27: Position of dividing streamlines at 3 chords distance from aerofoils vs. ground clearance.....	108
Figure 5.28: Stagnation point position vs. ground clearance.....	109
Figure 5.29: Volume flow rate under aerofoils, normalised by ‘ideal’ flow rate at given ground clearance vs. ground clearance.....	110
Figure 5.30: Pressure coefficient distributions for various aerofoils; $h/c = 0.30$ , $\alpha = 6^\circ$ .....	111
Figure 5.31: Tyrrell and New Mod geometry comparison.....	113
Figure 5.32: Pressure coefficient distributions for New Mod and comparison aerofoils; $h/c = 0.30$ , $\alpha = 6^\circ$ .....	114
Figure 5.33: Velocity contour plots (m/s), $h/c = 0.30$ , $\alpha = 6^\circ$ ; (a) NACA4412, (b) Tyrrell, (c) Bot Surf Mod, (d) Top Surf Mod, (e) LE Mod.....	115

Figure 5.34: Turbulence intensity contour plots (%), $h/c = 0.30$ , $\alpha = 6^\circ$ ; (a) NACA4412, (b) Tyrrell, (c) Bot Surf Mod, (d) Top Surf Mod, (e) LE Mod.....	116
Figure 5.35: Tyrrell and Vogt geometry comparison.....	116
Figure 5.36: Pressure coefficient distribution comparison for Tyrrell and Vogt aerofoils; $h/c = 0.30$ , $\alpha = 6^\circ$ .....	117
Figure 6.1: Profiles of x-velocity (a) and y-velocity (b) about Tyrrell wing at various $x/c$ locations; $0.1 x/c = 10$ m/s for x-velocity and 3 m/s for y-velocity .....	124
Figure 6.2: Profiles of z-velocity (a) and RMS-x-velocity fluctuations (b) about Tyrrell wing at various $x/c$ locations; $0.1 x/c = 2$ m/s for z-velocity and 4 m/s for RMS-x-velocity fluctuations	125
Figure 6.3: Profiles of RMS-y-velocity fluctuations (a) and RMS-z-velocity fluctuations (b) about Tyrrell wing at various $x/c$ locations; $0.1 x/c = 4$ m/s.....	126
Figure 6.4: Profiles of velocity components (a-c) and RMS of velocity component fluctuations (d-f) at various $x/c$ locations, comparing the experiment to the Dynamic Smagorinsky LES models with differing inlet turbulence intensities.....	127
Figure 6.5: X-velocity profiles about Tyrrell wing at various $x/c$ locations; $0.1 x/c = 10$ m/s.....	128
Figure 6.6: Number of times models score in each performance category .....	131
Figure 6.7: LDA Experiment and CFD frequency analysis points, $h/c = 0.05$ , $\alpha = 2^\circ$ .....	132
Figure 6.8: Power spectral density of velocity measurements at $x/c = 1.1$ , $y/c = 0.10$ .....	134
Figure 6.9: Power spectral density of velocity measurements at $x/c = 1.1$ , $y/c = 0.05$ .....	135
Figure 6.10: Power spectral density of velocity measurements at $x/c = 1.1$ , $y/c = 0$ .....	135
Figure 6.11: Power spectral density of velocity measurements at $x/c = 1.1$ , $y/c = -0.05$ .....	136
Figure 6.12: Power spectral density of velocity measurements at $x/c = 1.1$ , $y/c = -0.10$ .....	136
Figure 7.1: Instantaneous $C_N$ plots of LES simulations during data-taking period.....	139
Figure 7.2: Time-averaged $C_N$ and $C_D$ plots for LES simulations vs. ground clearance.....	140
Figure 7.3: Root-mean-squared values for LES $C_N$ and $C_D$ quantities vs. ground clearance.....	141
Figure 7.4: Instantaneous velocity contours (m/s) about wing midplane, $h/c = 0.30$ .....	141
Figure 7.5: Comparison of time-averaged and instantaneous $C_p$ at wing midplane for ground clearances $h/c = 0.30$ and $0.22$ , $\alpha = 5^\circ$ .....	142
Figure 7.6: Time-averaged $C_p$ plots at wing midplane for various ground clearances .....	142
Figure 7.7: Contours of mean velocity magnitude (m/s, left column) and instantaneous velocity magnitude (m/s, right column) at midplane for all clearances, freestream velocity = 10 m/s .....	145
Figure 7.8: Instantaneous velocity magnitude (m/s) at midplane near upper leading edge region .....	146
Figure 7.9: Normalised volume flow rate under wing at the lowest point (throat) and the trailing edge; normalised by 'ideal' freestream flow rate through given channel size .....	146
Figure 7.10: Instantaneous streamlines emanating from a vertical line at the midplane near the leading edge for $h/c = 0.30$ and $0.14$ (superimposed over $h/c = 0.30$ ), coloured by instantaneous velocity magnitude (m/s).....	147
Figure 7.11: Time-averaged separation, transition, wall shear stress escalation, and reattachment points at midplane .....	149
Figure 7.12: Time-averaged wall shear stress across wing span at $h/c = 0.30$ , wing chord = $0.075$ m	149
Figure 7.13: Time-averaged separation zones captured by iso-surface of zero x-velocity component, coloured by contours of average velocity magnitude .....	150
Figure 7.14: Profiles of average x-velocity and $UV$ Reynolds stress at various streamwise locations at the midplane for $h/c = 0.30$ and $0.26$ ; $0.1 x/c = 10$ m/s and 10 Pa.....	152
Figure 7.15: Profiles of average x-velocity and $UV$ Reynolds stress at various streamwise locations at the midplane for $h/c = 0.22$ , $0.18$ and $0.14$ ; $0.1 x/c = 10$ m/s and 10 Pa.....	153
Figure 7.16: Profiles of average x-velocity and $UV$ Reynolds stress at various streamwise locations at the midplane for $h/c = 0.11$ , $0.08$ and $0.05$ ; $0.1 x/c = 10$ m/s and 10 Pa.....	154
Figure 7.17: Contour plots of $UV$ Reynolds stress at midplane for all clearances (Pa) .....	156
Figure 7.18: Contours of x-, y- and z-vorticity at selected ground clearances.....	157
Figure 7.19: Contour plots of time-averaged y-velocity at the midplane, only plotting the positive values .....	159
Figure 7.20: Contour plots at midplane of $UV$ Reynolds stress, normalised by $U_x^2$ .....	160
Figure 7.21: Evolution of transition point with ground clearance changes.....	160
Figure 7.22: Location of transition point with changing ground clearance .....	161
Figure A.1: A discretised domain with node and face naming convention.....	181

Figure A.2: Various discretisation scheme approximations for $\phi_w$ .....	182
Figure A.3: The SIMPLE algorithm.....	187
Figure A.4: Unsteady SIMPLE algorithm.....	188
Figure A.5: Schematic of CFD approach (adapted from Barber, 2005).....	189
Figure B.6: Schematic of flow constriction on flow under inverted aerofoil in ground effect.....	197
Figure B.7: Volume proportions under inverted Tyrrell aerofoil vs. ground clearance; (dark) aerofoil-blocked volume proportion, (white) unblocked volume proportion under aerofoil.....	197
Figure C.8: Derivation of transformation matrix.....	199
Figure D.9: Experimental and numerical x-velocity profiles at $x/c = 0, 0.10$ and $0.30$ ; $0.1 x/c = 10$ m/s.....	201
Figure D.10: Experimental and numerical x-velocity profiles at $x/c = 0.5$ and $0.70$ ; $0.1 x/c = 10$ m/s.....	201
Figure D.11: Experimental and numerical x-velocity profiles at $x/c = 0.9, 1.01$ and $1.10$ ; $0.1 x/c = 10$ m/s.....	202
Figure D.12: Experimental and numerical x-velocity profiles at $x/c = 1.30, 1.50$ and $1.70$ ; $0.1 x/c = 10$ m/s.....	202
Figure D.13: Experimental and numerical y-velocity profiles at $x/c = 0, 0.10$ and $0.30$ ; $0.1 x/c = 3$ m/s.....	203
Figure D.14: Experimental and numerical y-velocity profiles at $x/c = 0.5$ and $0.70$ ; $0.1 x/c = 3$ m/s.....	203
Figure D.15: Experimental and numerical y-velocity profiles at $x/c = 0.9, 1.01$ and $1.10$ ; $0.1 x/c = 3$ m/s.....	204
Figure D.16: Experimental and numerical y-velocity profiles at $x/c = 1.30, 1.50$ and $1.70$ ; $0.1 x/c = 3$ m/s.....	204
Figure D.17: Experimental and numerical z-velocity profiles at $x/c = 0, 0.10$ and $0.30$ ; $0.1 x/c = 2$ m/s.....	205
Figure D.18: Experimental and numerical z-velocity profiles at $x/c = 0.5, 0.70$ and $0.9$ ; $0.1 x/c = 2$ m/s.....	205
Figure D.19: Experimental and numerical z-velocity profiles at $x/c = 1.01, 1.10$ and $1.30$ ; $0.1 x/c = 2$ m/s.....	206
Figure D.20: Experimental and numerical z-velocity profiles at $x/c = 1.50$ and $1.70$ ; $0.1 x/c = 2$ m/s.....	206
Figure D.21: Experimental and numerical RMS-x-velocity profiles at $x/c = 0, 0.10$ and $0.30$ ; $0.1 x/c = 4$ m/s.....	207
Figure D.22: Experimental and numerical RMS-x-velocity profiles at $x/c = 0.5, 0.70$ and $0.9$ ; $0.1 x/c = 4$ m/s.....	207
Figure D.23: Experimental and numerical RMS-x-velocity profiles at $x/c = 1.01, 1.10$ and $1.30$ ; $0.1 x/c = 4$ m/s.....	208
Figure D.24: Experimental and numerical RMS-x-velocity profiles at $x/c = 1.50$ and $1.70$ ; $0.1 x/c = 4$ m/s.....	208
Figure D.25: Experimental and numerical RMS-y-velocity profiles at $x/c = 0, 0.10$ and $0.30$ ; $0.1 x/c = 4$ m/s.....	209
Figure D.26: Experimental and numerical RMS-y-velocity profiles at $x/c = 0.5, 0.70$ and $0.9$ ; $0.1 x/c = 4$ m/s.....	209
Figure D.27: Experimental and numerical RMS-y-velocity profiles at $x/c = 1.01, 1.10$ and $1.30$ ; $0.1 x/c = 4$ m/s.....	210
Figure D.28: Experimental and numerical RMS-y-velocity profiles at $x/c = 1.50$ and $1.70$ ; $0.1 x/c = 4$ m/s.....	210
Figure D.29: Experimental and numerical RMS-z-velocity profiles at $x/c = 0, 0.10$ and $0.30$ ; $0.1 x/c = 4$ m/s.....	211
Figure D.30: Experimental and numerical RMS-z-velocity profiles at $x/c = 0.5, 0.70$ and $0.9$ ; $0.1 x/c = 4$ m/s.....	211
Figure D.31: Experimental and numerical RMS-z-velocity profiles at $x/c = 1.01, 1.10$ and $1.30$ ; $0.1 x/c = 4$ m/s.....	212
Figure D.32: Experimental and numerical RMS-z-velocity profiles at $x/c = 1.50$ and $1.70$ ; $0.1 x/c = 4$ m/s.....	212

# List of Tables

Table 4.1: Grid convergence comparison of $C_l$ and $C_d$ values for coarse, baseline and fine grids .....	58
Table 4.2: Boundary locations for three-dimensional numerical model .....	62
Table 4.3: Summary of Harpoon meshes .....	66
Table 4.4: Summary of verification of sliver model .....	70
Table 4.5: Sliver model mesh zone details.....	74
Table 4.6: Summary of sliver model boundary layer meshes for test cases 1, 4 and 5.....	75
Table 5.1: Downforce and drag coefficients; $h/c = 0.30$ , $\alpha = 6^\circ$ , T = Tyrrell, N = NACA4412 .....	112
Table 5.2: Tyrrell New Mod results and comparison; $h/c = 0.30$ , $\alpha = 6^\circ$ , T = Tyrrell .....	114
Table 5.3: Tyrrell and Vogt results and comparison; $h/c = 0.30$ , $\alpha = 6^\circ$ , T = Tyrrell.....	117
Table 6.1: Model rankings for x-velocity profile at $x/c = 0.1$ .....	129
Table 6.2: CFD model scoring system .....	130
Table 6.3: Summary of Model Performance.....	130
Table A.1: Sources of Error (Slater, 2008) .....	191

# Nomenclature

$b$	= Span of wing, m
$c$	= Aerofoil or wing chord length, m – distance between leading and trailing edges
$C_d$	= Coefficient of drag force (2D) = $d / (\frac{1}{2}\rho U_\infty^2 c)$
$C_D$	= Coefficient of drag force (3D) = $D / (\frac{1}{2}\rho U_\infty^2 S)$
$C_{d,max}$	= Maximum drag coefficient (2D)
$C_l$	= Coefficient of lift force (2D) = $l / (\frac{1}{2}\rho U_\infty^2 c)$
$C_L$	= Coefficient of lift force (3D) = $L / (\frac{1}{2}\rho U_\infty^2 S)$
$C_{l,max}$	= Maximum lift coefficient (2D)
$C_n$	= Coefficient of normal force (2D) = $n / (\frac{1}{2}\rho U_\infty^2 c)$
$C_N$	= Coefficient of normal force (3D) = $N / (\frac{1}{2}\rho U_\infty^2 S)$
$C_p$	= Coefficient of pressure = $(p-p_\infty) / (\frac{1}{2}\rho U_\infty^2)$
$d$	= Drag force (2D), N/m (i.e., Newtons / unit depth)
$D$	= Drag force (3D), N
$h$	= height above the ground, m – measured vertically from the lowest point on the aerofoil to the ground
$h/c$	= Non-dimensionalised height above the ground
$k-\varepsilon$	= CFD turbulence model
$k-\omega$	= CFD turbulence model
$l$	= Lift force (2D), N/m
$L$	= Lift force (3D), N
$n$	= Normal force (2D), N/m – force generated on aerofoil perpendicular to direction of travel
$N$	= Normal force (3D), N – force generated on wing in the span-normal plane and perpendicular to direction of travel
$n/d$	= Normal force to drag force ratio (2D)
$N/D$	= Normal force to drag force ratio (3D)
$p$	= Static pressure, Pa
$p_\infty$	= Freestream static pressure, Pa
$Re$	= Reynolds number, based on wing chord = $\rho U_\infty c / \mu$
$s/c$	= Distance normalised by the aerofoil/wing chord
$S$	= Plan area of wing, $m^2 = c \times b$
$U$	= Velocity, m/s
$u_f$	= Friction velocity = $\sqrt{(\tau_w / \rho)}$
$U_{RMS}$	= Root-mean-square of velocity, m/s
$U_\infty$	= Freestream velocity, m/s
$U/U_\infty$	= Velocity normalised by freestream velocity
$u, v, w$	= Velocity components in x-, y- and z-directions, m/s
$u', v', w'$	= Velocity fluctuations in x-, y- and z-directions, m/s
$u_{RMS}, v_{RMS}, w_{RMS}$	= Root-mean-squared value of velocity fluctuations in x-, y- and z-directions, m/s
$v2-f$	= Low Reynolds number turbulence model
$x, y, z$	= Cartesian coordinates, m – x is positive downstream, y is positive vertically upward and (for 3D) z is positive to portside (in accordance with right-hand-rule)
$x/c$	= Position on the x-axis normalised by the aerofoil/wing chord
$y^+$	= Dimensionless wall distance = $u_f y_w / \nu$
$y_w$	= Distance to nearest wall, m
$y/c$	= Position on the y-axis normalised by the aerofoil/wing chord
$z/c$	= Position on the z-axis normalised by the aerofoil/wing chord

## Greek Symbols:

$\alpha$	= Angle of attack of aerofoil, degrees – measured from the horizontal to the chord line; positive for pitch-up of upright aerofoil, positive for pitch-down of inverted aerofoil
$\alpha_{eff}$	= Effective angle of attack, degrees = $\alpha + \Delta\alpha$
$\alpha_{main}$	= Angle of attack of main element in a two-or-more element aerofoil/wing configuration
$\Delta\alpha$	= Change in angle of attack due to non-horizontal inclination of incident flow, degrees
$\mu$	= Dynamic viscosity, kg/m-s
$\rho$	= Air density, kg/m <sup>3</sup>
$\tau_w$	= Wall shear stress, Pa
$\tau_{xy}, \tau_{xz}, \tau_{yz}$	= Reynolds shear stresses, Pa
$\nu$	= Kinematic viscosity, m <sup>2</sup> /s

## Acronyms:

BS	= Bottom surface
CFD	= Computational Fluid Dynamics
DNS	= Direct Numerical Simulation
Dynamic SKE	= Dynamic Sub-grid Kinetic Energy model – LES sub-grid turbulence model
FFT	= Fast Fourier Transform
LDA	= Laser Doppler Anemometry
LE	= Leading edge
LES	= Large Eddy Simulation
LHS	= Left-hand side (of the equality sign of an equation)
NACA	= National Advisory Committee for Aeronautics – precursor to the National Aeronautics and Space Administration (NASA)
N-S	= Navier-Stokes equations
P-DNS	= Pseudo-Direct Numerical Simulation
PIV	= Particle Image Velocimetry
PSD	= Power Spectral Density function
QUICK	= Quadratic Upstream Interpolation for Convective Kinetics scheme – discretisation scheme for CFD
RANS	= Reynolds-Averaged Navier-Stokes equations – modified N-S equations to take account of turbulence
RHS	= Right-hand side (of the equality sign of an equation)
RNG	= Renormalised Group Theory model – $k-\epsilon$ based CFD turbulence model
RMS	= Root-mean-square
RSM	= Reynolds Stress Model – CFD turbulence model
SGS	= Sub-Grid Scale – refers to scale of turbulence not directly resolved by LES grids
SIMPLE	= Semi-Implicit Method for Pressure-Linked Equations algorithm – pressure-velocity coupling scheme for CFD
SIMPLEC	= Modified SIMPLE algorithm
SST	= Shear Stress Transport model – $k-\omega$ based CFD turbulence model
TE	= Trailing edge
TI	= Turbulence Intensity, %
TS	= Top surface
URANS	= Unsteady RANS solver
UNSW	= University of New South Wales

# Chapter 1: Introduction, Review of Literature and Overview of Research Programme

## 1.1 Introduction

The area of ground effect aerodynamics has received much attention over the past two decades as opportunities to understand and exploit this phenomenon have been sought. Apart from the ground effect induced ‘air cushion’ that aircraft pilots experience at landing – which itself has been the subject of much research – the most obvious application of ground effect aerodynamics is on racing cars, which exploit it in various different ways. Other applications include the ekranoplan concept (a large transport aircraft that continually operates just above the surface of the ocean) (Kuhmstedt and Milbradt, 1995), and proposed future high speed trains.

Of the application areas stated above, the exploitation of ground effect is most prevalent within the automotive industry and, more specifically, within the racing car industry. Common to most open-wheel racing cars is the use of an inverted wing located at the front of the vehicle, very close to the ground. When inverted wings are placed near the ground, they have been shown to produce more downforce, which is a great benefit to the performance potential of a racing car (despite the accompanying increase in drag). Consequently, front wings typically produce a large proportion of the car’s downforce (about 30 % in the case of Formula 1 cars) and are therefore a critical performance component.

However, as will be discussed in the next section, these devices are very sensitive to ground proximity and, are far more likely to suffer from flow separation while operating in this ground effect regime. Flow separation – the process where the airflow no longer follows the contours of the wing but rather separates from the wing’s surface – results in a significant loss in downforce (and a further increase in drag) and can occur quite quickly with changes in ground proximity.

Flow separation has been observed experimentally, however, the precise explanation for why and how it occurs – in particular, in the ground effect regime – has not been determined. This

information would be beneficial in terms of achieving better outright performance from racing car wing configurations by allowing them to utilise the benefit of ground effect further through delaying the onset of separation and, thus, increasing the operating range of the device.

The work undertaken throughout this research programme has been published in journals and conferences as listed in Appendix E.

## **1.2 Review of Literature and Relevance of Topic**

### **1.2.1 Race Car Aerodynamics**

In order to establish the context within which this research program exists, it is important to examine the topic of racing car aerodynamics as this is the primary application area in which inverted aerofoils operate.

Race cars have been the subject of generic design analyses on several occasions – Formula 1 cars are a popular subject with the earliest academic investigation concerning early 1990s designs (Dominy, 1992). The various components of the car were examined and the many conflicting design interests that must be traded off during the design process were discussed. One of the primary observations was that there is a significant knock-on effect from one component to another downstream and, indeed, vice-versa. One example is that some downforce is typically sacrificed on the front wing in order to lessen the negative effect of the front wing wake on downstream systems or parts on the car, like engine cooling.

More specific work has looked at the various considerations that must be made in the design of a racing car wing (Katz, 1994). It was noted that the interference between the wing and other components of the car are generally destructive but, sometimes, constructive. These wings typically sacrifice efficiency (high lift-to-drag ratio) for outright downforce by using highly cambered profiles which feature early turbulent transitions in order to delay separation in the highly adverse pressure gradient region induced by the large camber.

Ground effect, as employed in race car aerodynamics, has also been a subject of interest (Zhang, Toet and Zerihan, 2006). It has been established that the front wing, the undertray/diffuser combination and the rear wing of a Formula 1 car each typically produce around a third of the overall downforce generated and that the cars can generate approximately three times its own weight in downforce. Additionally, the overall aerodynamic behaviour of Formula 1 cars is generally very sensitive to pitch angle, ride height and also the centre of aerodynamic pressure. Consequently, it is imperative that a holistic approach is taken to modern aerodynamic design as stability of the car, under all

conditions, is as important to overall on-track performance as is the ultimate downforce levels obtained.

Another important consideration for racing cars is performance when operating in the wake of another racing car. Experimental work has been undertaken to ascertain the influence of an upstream racing car on the performance of a downforce generating wing operating in the upstream car's wake (Soso and Wilson, 2006). The upstream racing car was modelled as a bluff body equipped with a rear diffuser section and an elevated wing at the body's trailing edge. The performance of the wing was significantly affected by the upstream car. Its downforce levels, for a given clearance and incidence, were lower than those seen in an undisturbed flow. Additionally, the drag values recorded were higher. The percentage reduction in downforce was seen to be larger for higher wing clearances and downforce was also noted to be lost more significantly from the central section of the wing, close to the mid-plane, rather than out near the wing tips.

## ***1.2.2 Inverted Aerofoils and Wings in Ground Effect***

Research in the field of ground effect, particularly involving inverted aerofoils, is quite limited as most ground effect research is usually conducted on upright aircraft wings which exhibit completely different aerodynamic behaviour to inverted wings. In this section is summarised the progress to date of research about inverted aerofoils and wings operating in ground effect. Both experimental and numerical work is addressed here, however, a detailed discussion of the theory and literature that underpins the numerical work may be found in Chapter 2.

### ***1.2.2.1 Experimental Approach***

Of particular interest in this research programme is flow separation behaviour in ground effect which may be characterised as separation occurring in high adverse pressure gradient regions. High resolution laser doppler anemometry (LDA) experiments have been conducted to observe the adverse pressure boundary layer, separated flow and then reattaching flow about a smoothly contoured ramp immediately downstream from a flat plate (Song, DeGraaff and Eaton, 2000). Although the reattaching flow behaviour is of lesser interest in this case (as reattachment generally does not occur on a racing car wing), several interesting observations were made regarding the flow near the wall before and after separation. The three components of Reynolds Stress of interest in this investigation, streamwise normal stress ( $\overline{\rho u' u'}$ ), wall normal stress ( $\overline{\rho v' v'}$ ) and the Reynolds shear stress ( $\overline{\rho u' v'}$ ), all exhibited a peak value whose vertical location (at any point along the ramp) was coincident with the inflection point location in the mean velocity profile. The maximum value obtained by each stress

component was compared with that measured on the flat plate upstream of the adverse pressure region. While the peak streamwise normal stress only increased by about 25 % by separation, the peak wall normal and shear stress values were between 3 and 5 times larger than their upstream equivalents. The wall normal stress peak was seen to grow steadily along the ramp up to its maximum, however, the shear stress and streamwise normal stress values both reached a peak value fairly quickly and thereafter remained more-or-less constant to separation. Beyond separation, a separation bubble was formed in which all Reynolds Stress components were noted to reduce in magnitude, particularly the wall shear stress value. The peak values on the stress component profiles progressively shifted from their location near the wall (at the velocity inflection point) to the shear layer in the outer region of the boundary layer. This is demonstrated for the wall normal Reynolds stress in Figure 1.1. The production of turbulent kinetic energy followed a similar pattern with the peak production for all stress components located near the wall before separation. Post separation, the production at the wall fell to zero and was relocated to the separated shear layer location.

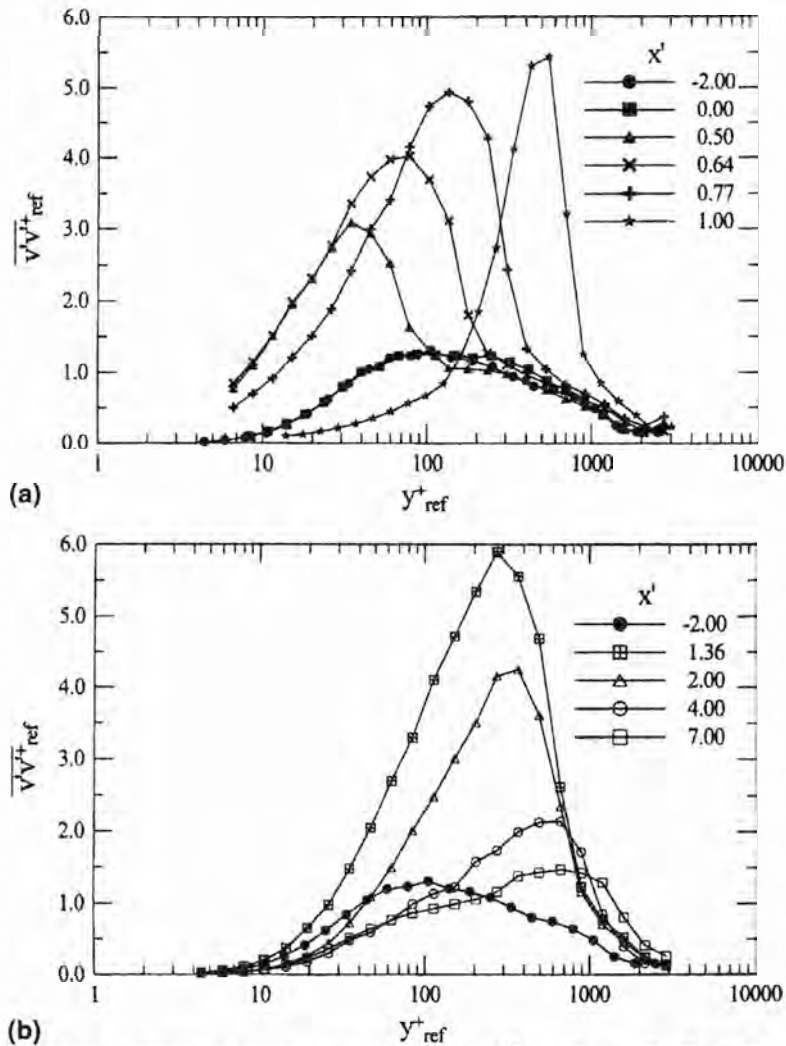


Figure 1.1: Wall normal Reynolds stress normalised by  $U_{\tau,ref}^2$  (Song, DeGraaff, and Eaton, 2000)

The effect of ground proximity on the aerodynamic performance of the Tyrrell wing has been investigated by Zerihan and Zhang (2000). The wing was equipped with vertical endplates

and tested using a large moving ground belt to accurately simulate the ground condition. It was noted that the wing experienced a significant and progressive increase in downforce when ground clearance was reduced. After maximum downforce was achieved, the force dropped off quickly with continued decreasing clearance, see Figure 1.2.

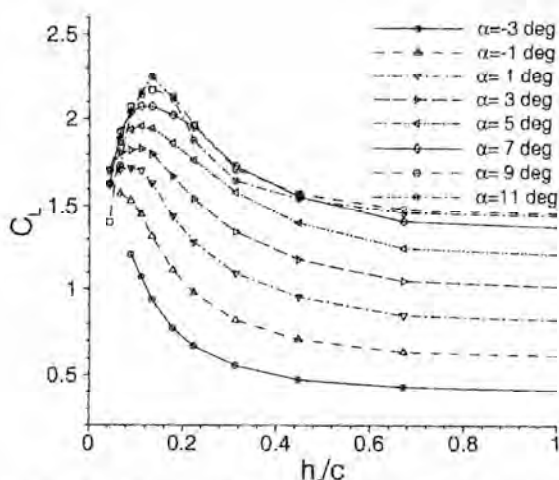


Figure 1.2:  $C_L$  in ground effect (Zerihan and Zhang, 2000)

It was also noted that separation at the trailing edge of the suction surface (the side facing the ground) began to occur as the height was reduced. The separation point steadily moved forward toward the leading edge as the wing height was reduced. This trend continued past the height of maximum downforce. It was concluded that this progressively worsening separation was attributable to the growing adverse pressure gradients (due to the greater suction under the wing) which dissipated the energy in the flow quicker and induced separation earlier as ground clearance was reduced.

The affect on aerodynamic performance of adding a Gurney flap to the trailing edge of the Tyrrell wing was examined experimentally by Zerihan and Zhang (2001). The conditions used by Zerihan and Zhang (2000) were again used, except for the addition of a 1.45 % $c$  and 2.90 % $c$  Gurney flap attached perpendicular to the upper trailing edge of the wing, see Figure 1.3. The effect of adding a Gurney flap to the wing in ground effect was seen to be similar to adding a Gurney flap to a wing in freestream conditions. That is, it increases the downforce on the wing by increasing the pressure on the pressure surface – particularly in the final 30 % of the chord – and by reducing the pressure on the suction side of the wing. The additional downforce produced by the Gurney flap as ground clearance is reduced, relative to a clean wing at each height, is again analogous to the additional force achieved when increasing incidence for a wing with a Gurney flap in freestream. The Gurney induces progressively more downforce for the wing (over what is achieved for a clean wing) as clearance is reduced. It was also noted that the additional downforce produced by a small Gurney is ‘disproportionately’ large compared to what is achieved with a larger Gurney flap.

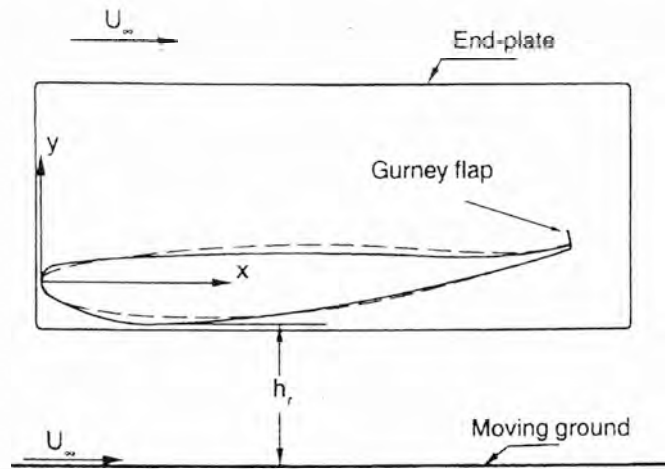


Figure 1.3: Tyrrell wing with 2.9 % Gurney flap (Zerihan and Zhang, 2001)

Wind tunnel tests were conducted on a double-element wing configuration to establish an understanding of the forces and flow field (Zhang and Zerihan, 2003a). The Tyrrell wing was used as the main plane and a small flap was used in addition to this. The flap used for testing was the outboard portion of the flap used on the 1998 Tyrrell 026 Formula 1 car front wing assembly, see Figure 1.4. It was found that most of the downforce was created by the main element and that this element made, by far, the larger contribution to the overall turbulent wake behind the wing. The reason the main plane produces most of the downforce is claimed to be because the flap induces additional circulation about the main wing, in a similar manner to a Gurney flap, by increasing pressure on the top surface and increasing suction on the bottom surface.

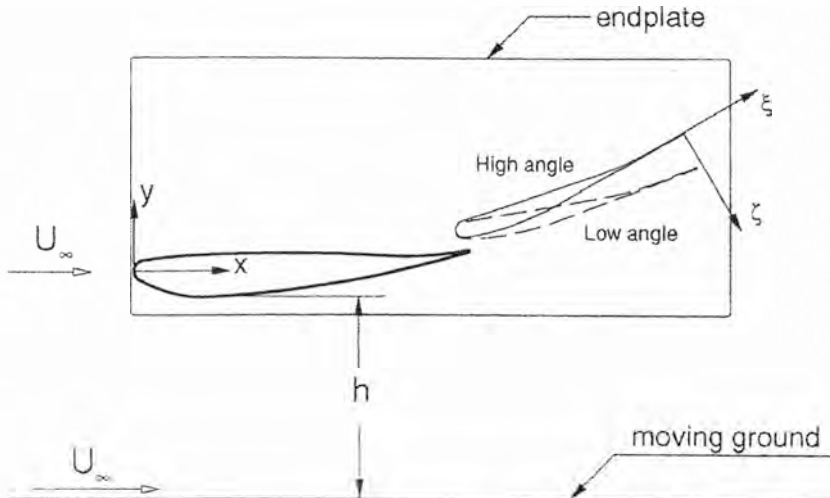


Figure 1.4: Double-element configuration (Zhang and Zerihan, 2003a)

Non-intrusive Particle Image Velocimetry (PIV) and LDA measurements of the Tyrrell wing wake were made to obtain a better understanding of the wake and vortex behaviour of the wing in ground effect (Zhang and Zerihan, 2003b). The mean flow showed that the wake increased in size and was turned further upward as the wing height was reduced. However, as separation started to occur on the suction surface, the wake in this lower region grew stronger and the overall wake was then directed more downward, which maintained the wake closer to

the ground at low clearances. As the flow separated on the suction surface, alternately shedding vortices were replaced by a separated shear layer, departing the suction surface, which was said to flap about in the transverse direction and to undertake vortex convection in the streamwise direction.

As mentioned earlier in Sec. 1.2.2.2, a CFD and experimental study of the near-wake properties of the Tyrrell wing in ground effect was undertaken by Beves, Barber and Leonardi (2005). The experimental component of this study utilised both smoke flow visualisation, and LDA in a low speed moving-ground wind tunnel. The various CFD models' performances were compared to experimental wake velocity-deficit results from LDA, at two stations downstream of the trailing edge. Flow visualisation showed that as the wing moves closer to the ground the recirculation region, formed underneath the rear of the wing, due to flow separation, becomes progressively larger and interacts with the shear layer emanating from the pressure surface. This starts to direct the wake flow down toward the ground at the more extreme ground clearances.

### ***1.2.2.2 Numerical Approach***

Some early ground effect numerical work, utilising Computational Fluid Dynamics (CFD), sought to understand the effect on inverted aerofoils of using different methods of modelling the ground plane. One such CFD analysis compared the stationary and moving ground cases for a two-dimensional inverted NACA4412 aerofoil in ground effect (Ranzenbach, 1995). Both cases saw an increasing level of downforce achieved for a decreasing ground clearance, whereas the moving ground case saw higher downforce levels over the whole range of heights, see Figure 1.5. The downforce in both cases was seen to diminish below the non-dimensionalised ground clearance of about  $h/c = 0.06$ . This force drop-off was postulated to be due to the merging of the ground and aerofoil boundary layers. The drag increased as the ground was approached, for both cases, except the drag for the stationary ground case dropped off slightly at the lowest ground clearance ( $h/c = 0.028$ ). The drag for the moving ground configuration followed a similar trend, although with lower drag values, but did not feature the drag drop-off at the lowest clearance.

A similar analysis was conducted on a generic single slotted, flap equipped, inverted NACA 63<sub>2</sub>-215 Mod B aerofoil (Ranzenbach, Barlow and Diaz, 1997). Both the stationary case (a wind tunnel experiment) and moving ground case (a CFD simulation) were analysed. The maximum downforce ground clearance for this configuration (with the moving ground) was found to be much higher at approximately  $h/c = 0.25$ . The authors postulated that Formula 1 and Indy cars may routinely operate in the force reduction region at certain times on track.

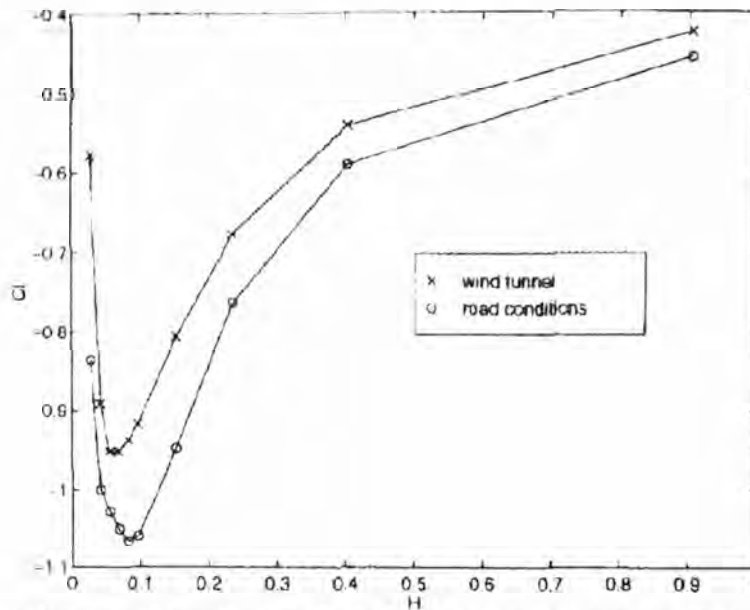


Figure 1.5: Lift comparison; road (moving) and wind tunnel (stationary) conditions (Ranzenbach, 1995). Negative  $C_L$  indicates positive downforce

A thorough investigation into the behaviour of a generic (inverted) double-element aerofoil configuration was achieved by conducting various simulations; varying the ground clearance, angle of attack of both the main element and the flap independently and also the proportion of the overall chord of the elements (increasing the chord of one while reducing the other – thus maintaining the overall chord) (Soso and Wilson, 2004). One of the more interesting observations from this study was a contrast in behaviour between single-element and double-element configurations. For a single element aerofoil, it had previously been observed that an increase in incidence angle leads to an increase in maximum lift coefficient  $C_{l,max}$  as the aerofoil's ground clearance is varied (Ranzenbach, 1995; and Zerihan and Zhang, 2000). However, a reversal in this behaviour was observed when the incidence angle of the main element was increased and the flap incidence was held constant; that is, the maximum lift coefficient decreased with increasing main element incidence angle  $\alpha_{main}$ , see Figure 1.6. In agreement with the single element case, they noted that the clearance at which  $C_{l,max}$  occurred increased with the incidence of the primary element  $\alpha_{main}$ , as did the maximum drag coefficient  $C_{d,max}$ .

Additionally, it was noted that if the percentage of the (constant) overall chord of the assembly constituted by the main element decreased (main element gets shorter, flap gets longer), then, the clearance at which  $C_{l,max}$  occurred decreased and, partly as a consequence,  $C_{l,max}$  increased, see Figure 1.7.

Although Soso and Wilson did not infer the implications of these observations, the results appear to show that:

- reducing  $\alpha_{main}$  to small positive or slightly negative values will yield a higher  $C_{l,max}$  (at a lower ground clearance) and a lower corresponding  $C_d$  and;
- reducing the length main element, in relation to the flap, will yield a higher  $C_{l,max}$ .

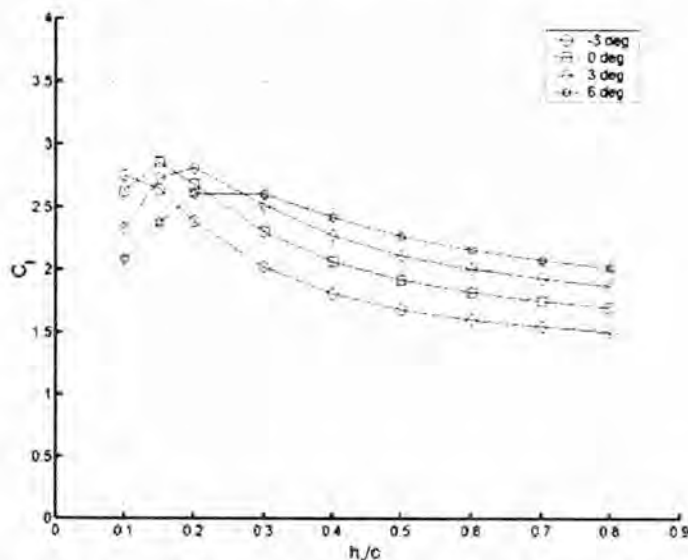


Figure 1.6: Lift curves in ground effect, varying AOA of main element (Soso and Wilson, 2004)

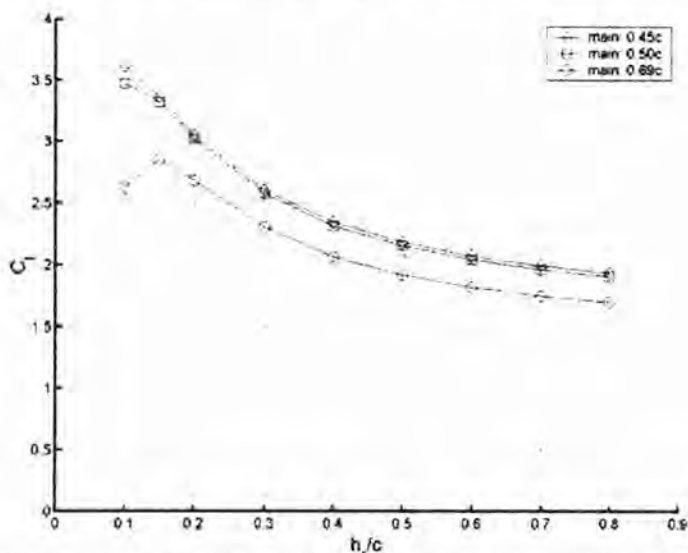


Figure 1.7: Lift curves in ground effect; varying main element proportion of total chord (Soso and Wilson, 2004)

Other work has numerically studied several types of inverted single-element aerofoils primarily to observe their dependence on Reynolds number ( $Re$ ) at low ground clearances (Mokhtar, 2005). Configurations were tested at different ground clearances (down to  $h/c = 0.2$ ), incidence angles and Reynolds Numbers. The results are in agreement with similar studies, however, Mokhtar did observe a lack of sensitivity to  $Re$  in the range  $0.6 \times 10^6 - 3.6 \times 10^6$  (intended to mimic the range of racing car conditions), at a ground clearance of  $h/c = 0.5$  and incidence angle of  $12^\circ$ . There was only a very slight reduction in  $C_l$  and  $C_d$ , with increasing  $Re$ , over this range. It is interesting to note, also, that this trend is reversed, albeit slightly, in freestream conditions where the  $C_l$  and  $C_d$  values were seen to increase very slightly with increasing  $Re$ .

An experimental investigation, to both observe ground effect flow behaviour and to accurately model it in CFD, was undertaken (Beves, Barber and Leonardi, 2005). This study was used to examine the near-wake properties of a highly cambered inverted wing that was used as the main element on the front wing assembly of the Tyrrell 026 Formula 1 racing car of 1998 (the ‘Tyrrell’ wing). The experimental component of this study utilised both smoke flow visualisation and LDA in a low speed moving-ground wind tunnel (the same wind tunnel used in this research programme). The CFD analysis compared the use of the  $k-\omega$ , Renormalised Group  $k-\varepsilon$  and Realisable  $k-\varepsilon$  turbulence models. The models’ performance was compared to experimental wake velocity deficit results, from the LDA system, at two stations downstream of the trailing edge and the Realisable  $k-\varepsilon$  model was found to be superior. Further details of this investigation may be found in Sec. 1.2.2.1.

A numerical study modelled the experimental work of Zerihan and Zhang (2000) (which is discussed in Sec. 1.2.2.1) observed the flow field about an inverted Tyrrell aerofoil operating in ground effect (Mahon and Zhang, 2005). The main purpose of this work was to establish an accurate steady-state Reynolds-Averaged Navier-Stokes solver (RANS) solution to the problem and to evaluate various turbulence models in achieving this goal. They found that the  $k-\omega$  SST turbulence model performed best at predicting surface pressures and that the Realizable  $k-\varepsilon$  model was superior for predicting the wake flow field.

A similar numerical study was performed, this time modelling a double-element inverted aerofoil assembly with the Tyrrell aerofoil as the main element and a small flap situated at its rear (Mahon and Zhang, 2006). This study complements the experimental work of Zhang and Zerihan (2003a). Generally good accuracy is noted in the various turbulence model predictions. Discrepancies were observed in the vertical position of the wake thickness (the numerical models under predicted the height of the wake) and this was postulated to be due to the lack of three-dimensionality in the model as the tip vortex-induced up-wash (present in the experiment) was not modelled in the two-dimensional CFD simulations. They also noted that the majority of the downforce was generated by the main element and the majority of the drag was generated by the flap.

### ***1.2.3 Upright Aerofoils and Wings in Ground Effect***

Although the main topic of interest of this research programme regards the flow about inverted aerofoils and wings in ground effect, it is nevertheless important to understand how this type of flow phenomena differs from the flow phenomena seen about upright aerofoils and wings in ground effect. The main motivation for establishing these differences in flow

behaviour is simply because they are, typically, not well understood and often considered a universal effect termed ‘ground effect’.

### ***1.2.3.1 Experimental Approach***

Wind tunnel experiments were conducted by Ahmed and Goonarate (2002) to ascertain the merits of treating a sea-going vessel as an upright low aspect ratio wing, with flaps and endplates. The potential performance benefit of such a configuration would allow the vessel to create lift and sit up further out of the water and so suffer less hydrodynamic drag. The researchers treated the main fuselage and upper tiers of the vessel as a fairly rough wing shape and utilised catamaran double hulls as endplates. The wind tunnel experiments sought to examine the aerodynamic characteristics of this arrangement at different ground clearances and (presumably, rear) flap angles. The ground plane was simulated by the use of a stationary elevated board in order to minimise the boundary layer thickness under the wing. Additionally, the thickness of the boundary layer was measured and this displacement thickness was deducted from the measured ground clearance to obtain an effective ground clearance. It was concluded that at lower clearances, lift increases, drag decreases and the lift to drag ratio increases for all four flap angles tested. Additionally, for higher flap angles (6 or 10 degrees), the variation in centre of pressure position, as ground clearance is changed, is smaller than for lower angles – which is an advantage in terms of vessel stability.

### ***1.2.3.2 Numerical and/or Analytical Approach***

The effect of angle of attack, camber and thickness on the performance of an upright wing operating in ground effect has been studied by Coulliette and Plotkin (1996). A discrete vortex method was used to study the flow about a parabolic arc of varying camber ratios and angles of attack and a panel method was used to study the flow about a symmetric Joukowski aerofoil of varying thickness-to-chord ratios and angles of attack. It was found that at zero angle of attack the cambered arc generated positive lift while the aerofoil, also at zero angle of attack, generated negative lift. They also found that, for a given ground clearance, increasing the camber of the parabolic arc decreased the normalised lift value – outright lift normalised by its freestream, out of ground equivalent. To put it in clearer terms, the percentage gain in lift reduced with increasing camber. The same reduction in percentage gain was observed for increases in the angle of attack of the aerofoil and parabolic arc. An increase in the thickness-to-chord ratio, at an angle of attack of zero, resulted in an increase in lift percentage gain. Finally, and most curiously, at greater ground clearances – but still in ground effect – the parabolic arc and the thin aerofoil both produce less lift than freestream values, provided they have fairly small angles of attack and low camber.

A more sophisticated numerical investigation into the flow about a NACA4412 aerofoil, operating in ground effect, was undertaken (Hsiun and Chen, 1996). The effect of changes in Reynolds number, ground clearance and angle of attack were sought using a RANS finite volume code with the standard  $k-\varepsilon$  turbulence model. However, the ground plane was modelled as a stationary ground with no non-zero components of velocity specified at this boundary and, thus, the validity of the near-ground results must be called into question. It was concluded that the lift coefficient increased with increases in  $Re$ , particularly for the near-ground ( $h/c = 0.05$ ) case tested. A significant loss of lift was seen for the near-ground case and this was deemed due to ground boundary layer – and this may well be the case, given the stationary ground plane. Additionally, for high angle of attack and low clearance cases, a recirculation region was generated below the leading edge of the aerofoil, again due to the stationary ground. Finally, the drag coefficient was seen to reduce with decreasing ground clearance and this was said to be due to the reduction in pressure drag as a result of the reduced suction over the top of the wing.

#### **1.2.4 Relevance of Topic**

Flow separation is a phenomenon critical to the performance of a wing in ground effect. The onset of flow separation lowers the useful lift that can be generated using aerofoils and, in certain circumstances, can do so very abruptly and dangerously. It is therefore critical to have a good understanding of the flow circumstances in which flow separation is induced and also to gain an understanding of the mechanical process through which the boundary layer separates from the suction surface.

It has been noted by other researchers that flow separation tends to be induced earlier (at a lower angle of incidence) the closer a wing is to the ground (Zerihan and Zhang, 2000). The progression of flow separation, for an increasing incidence, has been seen to initiate at the trailing edge earlier for lower ground clearances and then to progress toward the leading edge quicker for low ground clearances, but a thorough understanding for why this is so and how it comes about is still unknown. This research aims to answer these questions by means of a detailed numerical study of an inverted aerofoil using CFD and will support and validate this programme with wind tunnel experiments using smoke flow visualisation and LDA. The mechanism by which flow separation occurs, the circumstances leading to separation and the overall effect on the resulting aerodynamic behaviour will be investigated.

### **1.3 Introduction to Research Programme**

The various aspects of this research programme will be explained in detail in the following chapters. These chapters and their content will be summarised briefly here.

Chapter 2 covers the underlying theory and state-of-the-art methodology of computational fluid dynamics. This chapter deals with the various CFD techniques either assessed or employed throughout the research programme and also includes a detailed review of literature with regards to the appropriate methodology of applying CFD techniques. This chapter establishes the techniques and methodologies used and discussed throughout the rest of this thesis.

Chapter 3 deals with the experimental validation program, which was undertaken to support the CFD simulation work. This chapter primarily details the setup, techniques and execution of the experimental programme. The discussion of the experimental results may be found in Chapter 6.

Chapter 4 covers the verification and validation of the CFD models used throughout the research programme. It draws on the techniques and methodologies of Chapter 2 and the experimental validation work of Chapter 3. Two models are verified and validated: a) a steady two-dimensional flow over a Tyrrell aerofoil in ground effect and; b) an unsteady quasi-two-dimensional flow over a three-dimensional Tyrrell wing in a low speed moving-ground wind tunnel.

Chapter 5 is the first of three results-and-discussion chapters that examine the results of research work using the models verified and validated in Chapter 4. This chapter looks at the results of the steady two-dimensional flow simulations over the Tyrrell aerofoil and examines how ground effect manifests about inverted and upright aerofoils. It also provides a details examination of the effect on ground effect of changing the geometric features of an inverted aerofoil.

Chapter 6, the second results-and-discussion chapter, examines using the three-dimensional models developed in Chapter 4, the ability of several numerical techniques to simulate the quasi-two-dimensional unsteady flow over a highly cambered inverted aerofoil in ground effect. The best performing technique is selected for use in Chapter 7.

Chapter 7 is the third results-and-discussion chapter and presents the results of definitive simulations of the onset of flow separation on an inverted wing in ground effect, performed using the verified and validated model from Chapter 6.

Chapter 8 presents the conclusions drawn from the entire research programme and outlines potential directions for future work.

# Chapter 2: Computational Fluid Dynamics Theory and Methodology

## 2.1 Introduction

Computational Fluid Dynamics is a powerful tool for simulating a range of fluid dynamics problems by numerically solving the governing conservation equations, lifted directly from physics theory, across the whole physical domain of the problem. This is achieved by breaking the volume of the domain of interest into many small discrete volumes (called ‘discretising’ the domain) and solving the governing equations across each volume.

CFD is a routine part of the design process in many different industries and plays a vital complementary role to experimentation in fluid dynamics research. Firstly, in Sec. 2.2, 2.3 and 2.4, this chapter will initially provide a brief overview of how CFD solvers work and the important considerations in achieving adequate results. Secondly, this chapter will present the three CFD methodologies employed in this research programme; a brief overview of Reynolds-Averaged Navier-Stokes code (Sec. 2.5), a thorough discussion of the Large Eddy Simulation approach (Sec. 2.6) and a discussion of the Pseudo-Direct Numerical Simulation approach (Sec. 2.7). Finally, in Sec. 2.8, this chapter presents a literature survey of the current state-of-the-art of methodology for simulating similar flow regimes to those considered in this programme.

## 2.2 Introduction to CFD simulation

### 2.2.1 Governing Fluid Flow Equations

The governing equations for fluid flow problems are composed of three conservation considerations; conservation of mass (1 equation), conservation of momentum (1 equation for each dimension of the flow) and conservation of energy (1 equation). These equations are presented briefly below.

#### 2.2.1.1 Conservation of Mass

The conservation of mass about a fluid element (which, like all the governing equations, is applied at each discretised fluid volume) can be stated as *‘the rate of increase of mass of a*

*fluid element equals the net rate of flow of mass into the fluid element.* Calculating the fluxes across the surfaces of the fluid element and simplifying yields

$$\boxed{\frac{\partial \rho}{\partial t} + \text{div}(\rho \bar{u}) = \frac{\partial \rho}{\partial t} + \frac{\partial(\rho u)}{\partial x} + \frac{\partial(\rho v)}{\partial y} + \frac{\partial(\rho w)}{\partial z} = 0} \quad (1)$$

where  $\rho$  is the density of the fluid and  $u$ ,  $v$  and  $w$  are the velocity components in the x-, y- and z-directions, respectively. For cases where the fluid can be considered incompressible, such as water or low mach number flows (and all flow problems considered in this research programme), Eqn. 1 can be simplified to

$$\text{div } \bar{u} = \frac{\partial u}{\partial x} + \frac{\partial v}{\partial y} + \frac{\partial w}{\partial z} = 0 \quad (2)$$

### 2.2.1.2 Conservation of Momentum

The conservation of momentum follows a rearrangement of Newton's Second Law ( $F = ma$ ) which can be stated as *'the rate of change of momentum of the fluid element equals the sum of all forces acting on the fluid element.'* The conservation of momentum equations for all three directions are displayed below. A full derivation may be found in Appendix A.1.

$$\boxed{\begin{aligned} \rho \frac{Du}{Dt} &= -\frac{\partial p}{\partial t} + \frac{\partial \tau_{xx}}{\partial x} + \frac{\partial \tau_{yx}}{\partial y} + \frac{\partial \tau_{zx}}{\partial z} + S_{Mx} \\ \rho \frac{Dv}{Dt} &= -\frac{\partial p}{\partial t} + \frac{\partial \tau_{xy}}{\partial x} + \frac{\partial \tau_{yy}}{\partial y} + \frac{\partial \tau_{zy}}{\partial z} + S_{My} \\ \rho \frac{Dw}{Dt} &= -\frac{\partial p}{\partial t} + \frac{\partial \tau_{xz}}{\partial x} + \frac{\partial \tau_{yz}}{\partial y} + \frac{\partial \tau_{zz}}{\partial z} + S_{Mz} \end{aligned}} \quad (3)$$

### 2.2.1.3 Conservation of Energy

The conservation of energy equation is based on the First Law of Thermodynamics. Stated in words; *'the rate of change of energy in a fluid element equals the net rate of heat added to the element plus the net rate of work done on the element.'* The final equation is stated below with a full derivation in Appendix A.2.

$$\boxed{\begin{aligned} \rho \frac{DE}{Dt} &= \text{div}(k \text{ grad } T) - \text{div}(p \bar{u}) + \frac{\partial(u\tau_{xx})}{\partial x} + \frac{\partial(u\tau_{yx})}{\partial y} + \frac{\partial(u\tau_{zx})}{\partial z} \\ &+ \frac{\partial(v\tau_{xy})}{\partial x} + \frac{\partial(v\tau_{yy})}{\partial y} + \frac{\partial(v\tau_{zy})}{\partial z} + \frac{\partial(w\tau_{xz})}{\partial x} + \frac{\partial(w\tau_{yz})}{\partial y} + \frac{\partial(w\tau_{zz})}{\partial z} + S_E \end{aligned}} \quad (4)$$

where  $S_E$  is any body forces or other source terms such as gravity and energy itself  $E$  is defined as

$$\boxed{E = i + \frac{1}{2}(u^2 + v^2 + w^2)} \quad (5)$$

where  $i$  is the internal energy and the second term is the kinetic energy – the potential energy has been accounted for in the body force term.

The energy equation will not feature further in this research programme as flow regime under investigation is considered incompressible, with constant density, thus negating the need to include the energy equation in the CFD solver algorithm.

## **2.2.2 General CFD Solution Process**

In all cases, CFD is applied in three primary steps: pre-processing, solving and post-processing. These are discussed briefly below to present a context within which the rest of this chapter may be understood.

### **2.2.2.1 Pre-processing**

This step includes all the tasks that must be performed before the computational work of solving the flow equations can be carried out. This includes generating a discretised flow domain – that is generating a mesh of discrete volumes to represent the physical domain. This mesh generation process is often very time consuming as much care must be taken to faithfully reproduce the geometry of the problem and to build a mesh of sufficient ‘quality’ that will not induce avoidable numerical errors in the computation process. Also determined during this process are the appropriate boundary conditions for the problem that accurately represent the ‘real world’ problem that is to be simulated. Issues involved with mesh generation, such as numerical error and boundary conditions, will be discussed further in Sec. 2.3.

### **2.2.2.2 Solving**

This step involves the actual simulation of the flow problem of interest using the numerical CFD solver that will be discussed in Sec. 2.2. It is during this step that the numerical settings and initial conditions of the simulation are selected, the simulation performed and resulting data gathered and saved.

### **2.2.2.3 Post-processing**

This final step in the process is to examine the obtained data. This can be done in a variety of ways depending on the type of flow problem simulated and the type of information sought from the simulation. It usually includes both qualitative presentation of data (e.g. iso-surface plots, contour maps on a plane through a 3D domain, stream traces through the domain) and quantitative presentation of data (e.g. force and pressure results, turbulence or temperature measurements).

## 2.3 Numerical Methods of Finite-Volume CFD Solvers

This section will discuss the numerical methods involved in the most common CFD formulation and the formulation used throughout this research programme – the finite-volume method.

### 2.3.1 The Navier-Stokes and Transport Equations for the Finite-Volume Method

This section presents both the Navier-Stokes (N-S) equations and the general transport equation. The N-S equations are a slight development upon the fundamental governing equations discussed in Sec. 2.2.1. The transport equation for the finite-volume method is a very convenient general equation into which all five of the N-S equations may be rearranged. A full derivation is presented in Appendix A.3.

The N-S equations may be expressed in the following form for a compressible fluid.

$$\begin{array}{l}
 \text{Mass} \quad \frac{\partial \rho}{\partial t} + \text{div}(\rho \bar{u}) = 0 \\
 \text{x-momentum} \quad \frac{\partial(\rho u)}{\partial t} + \text{div}(\rho u \bar{u}) = -\frac{\partial p}{\partial x} + \text{div}(\mu \text{ grad } u) + S_{M_x} \\
 \text{y-momentum} \quad \frac{\partial(\rho v)}{\partial t} + \text{div}(\rho v \bar{u}) = -\frac{\partial p}{\partial y} + \text{div}(\mu \text{ grad } v) + S_{M_y} \\
 \text{z-momentum} \quad \frac{\partial(\rho w)}{\partial t} + \text{div}(\rho w \bar{u}) = -\frac{\partial p}{\partial z} + \text{div}(\mu \text{ grad } w) + S_{M_z} \\
 \text{Internal energy} \quad \frac{\partial(\rho i)}{\partial t} + \text{div}(\rho i \bar{u}) = -p \text{ div } \bar{u} + \text{div}(k \text{ grad } T) + \Phi + S_I
 \end{array} \tag{6}$$

It can be shown that, for the internal energy equation

$$\Phi = \mu \left\{ \begin{array}{l} 2 \left[ \left( \frac{\partial u}{\partial x} \right)^2 + \left( \frac{\partial v}{\partial y} \right)^2 + \left( \frac{\partial w}{\partial z} \right)^2 \right] + \left( \frac{\partial u}{\partial y} + \frac{\partial v}{\partial x} \right)^2 \\ \left( \frac{\partial u}{\partial z} + \frac{\partial w}{\partial x} \right)^2 + \left( \frac{\partial v}{\partial z} + \frac{\partial w}{\partial y} \right)^2 \end{array} \right\} + \lambda (\text{div } \bar{u})^2 \tag{7}$$

And finally, the equations of state for a perfect gas:

$$\begin{array}{l}
 p = \rho R T \\
 i = C_v T
 \end{array} \tag{8}$$

The general transport equation may be determined by observing the similarity between the N-S equations (Eqns. 6). The following general form, for an arbitrary quantity  $\phi$ , includes all the important elements of the N-S equations with any non-conforming terms recast as part of the source term  $S_\phi$

$$\boxed{\frac{\partial(\rho\phi)}{\partial t} + \text{div}(\rho\phi\bar{u}) = \text{div}(\Gamma \text{grad } \phi) + S_\phi} \quad (9)$$

### 2.3.2 Solver Solution Process

This section will briefly summarise the iterative solution process employed in the finite-volume method. The last section looked at solving the discretised convection-diffusion equation for an arbitrary flow quantity  $\phi$  but it was assumed that the velocity field was known. This section will introduce the process for obtaining the correct velocity and pressure fields in order to obtain a correct overall flow field solution.

All flow quantities are expressed by the general transport equation (Eqn. 9) and the momentum equations can be similarly discretised in order that the flow velocities and pressure be determined throughout the flow field.

There is a complication to this process, however, in that for a two-dimensional flow (for example) there will be two discretised momentum equations and one discretised continuity equation that must be solved but these equations are all heavily coupled. It is for this reason that CFD solutions are iterative as obtaining values for flow quantities  $u$ ,  $v$  and  $p$ , that manage to satisfy all three equations, is a challenging task and is most easily achieved through an iterative process.

The following equations are the discretised equations for  $u$  and  $v$ -momentum, presented in standard form.

$$\begin{aligned} a_{i,j}u_{i,j} &= \sum a_{nb}u_{nb} + (p_{I-1,J} - p_{I,J})A_{i,j} + b_{i,j} \\ a_{I,j}v_{I,j} &= \sum a_{nb}v_{nb} + (p_{I,J-1} - p_{I,J})A_{I,j} + b_{I,j} \end{aligned} \quad (10)$$

Note there is a different subscript notation employed (instead of  $WW$ ,  $W$ ,  $P$ ,  $E$ , etc) because the velocity components are calculated on a staggered grid which is shifted half a cell from those considered previously – which in practise means the velocity values are stored at the faces of the original cells, whereas scalar quantities ( $p$ ,  $\phi$ , temperature, etc) are stored at the nodes. This is done to avoid numerical errors in estimating rapid (spatial) changes in the pressure field – this change in notation is of little other interest in this discussion and will not be mentioned further.

In Eqns. 10,  $b_{i,j}$  is the momentum source term,  $A_{i,j}$  is the east or west face of the cell (same), the pressure gradient at this point is expressed as a central difference between the two bounding scalar node values of  $p$  and the value of coefficients  $a_{i,j}$  and  $a_{nb}$  are dependant on the discretisation scheme employed (eg. second-order upwind or QUICK).

The SIMPLE (Semi-Implicit Method for Pressure-Linked Equations) algorithm, or one of its variants, is the most common process used to obtain a solution for the velocity and pressure fields (and all other flow quantities) in a CFD solution.

A full explanation of this numerical process may be found in Appendix A.5, however, a brief flowchart summary of the algorithm is presented here in Figure 2.1.

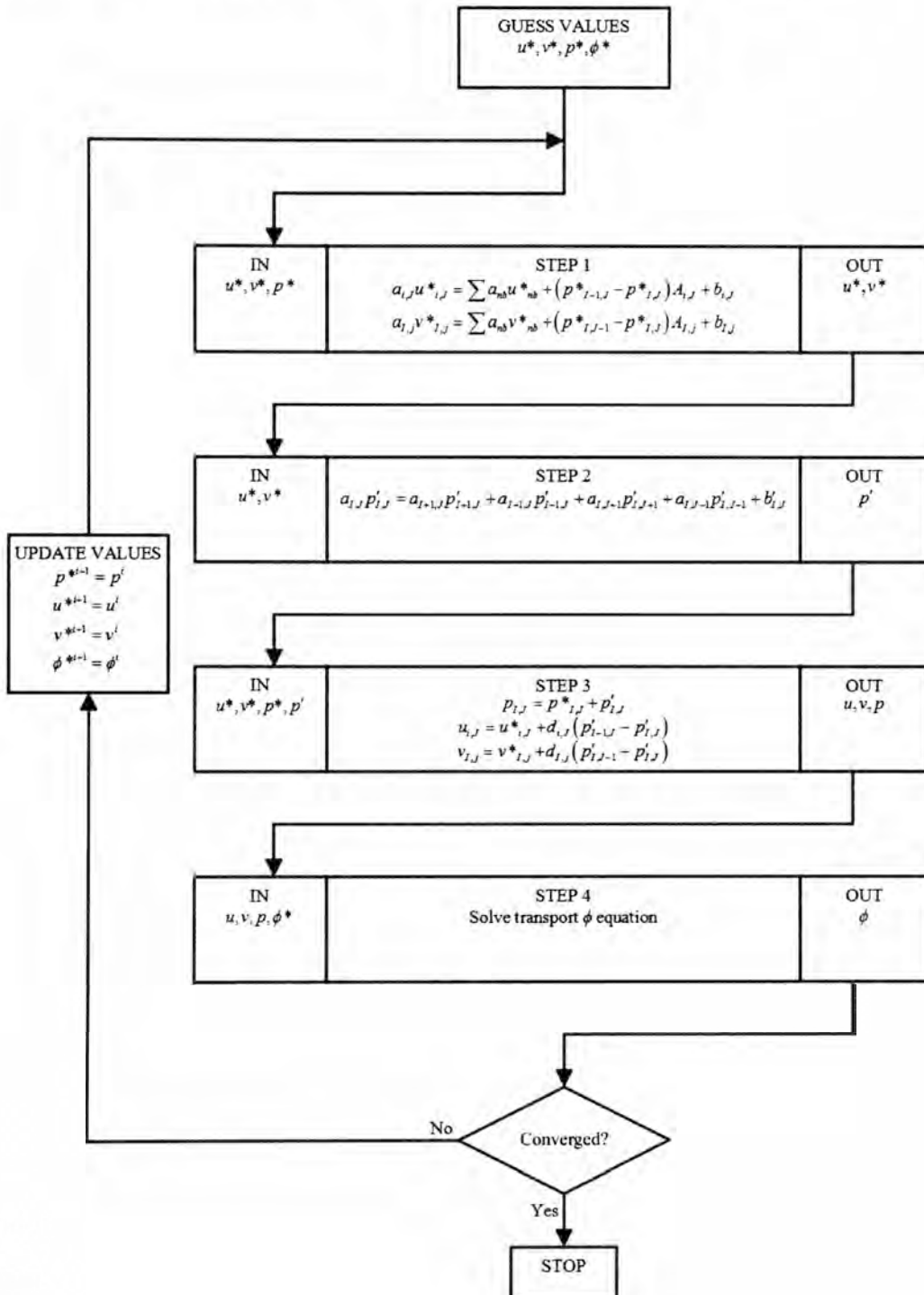


Figure 2.1: The SIMPLE algorithm

With an unsteady solution process, the iterative SIMPLE algorithm is run till acceptable convergence within each timestep and then the time-step is updated and the SIMPLE iterative

process is repeated. This is shown in the flowchart of Figure 2.2. The process is also explained in Appendix A.5.

This research programme employs the SIMPLEC algorithm for all cases.

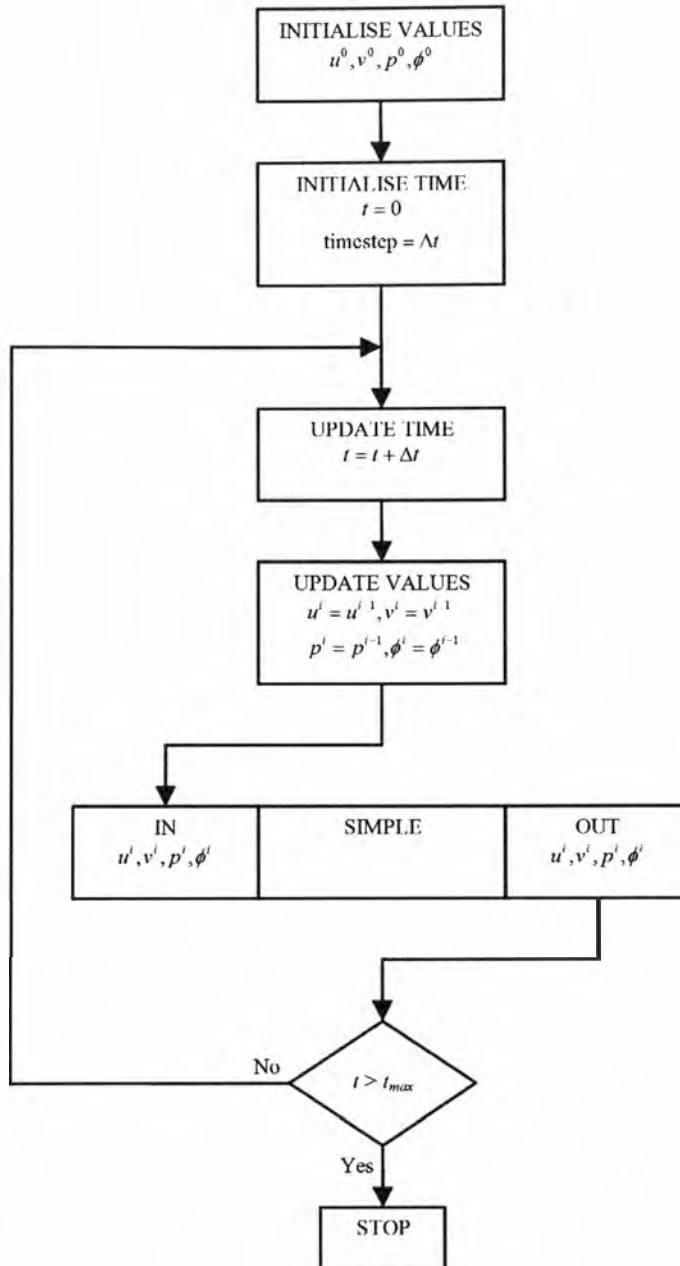


Figure 2.2: Unsteady SIMPLE algorithm

## 2.4 Verification and Validation Process

Verification and validation are processes that, when performed thoroughly, ensure a solution is sufficiently accurate for the user's requirements. Verification and Validation is essential to obtaining a credible numerical solution and the way it is conducted has been the subject of much work (Roache, 1998; AIAA, 1999).

Implicit in this process is the control and minimisation of several kinds of error that may be generated in a CFD code. A detailed discussion of the CFD verification and validation

process is provided in Appendix A.6. A thorough discussion of error in CFD codes is presented in Appendix A.7.

Both verification and validation processes are well summarised in Figure 2.3, which is adapted from a similar figure in an undergraduate course on CFD by Barber (2005). CFD attempts to simulate the reality (the top box in Figure 2.3) and achieves this by first creating a conceptual model of reality. This conceptual model is then implemented in a computer model and the resulting computer simulation is finally checked against reality to ensure its validity.

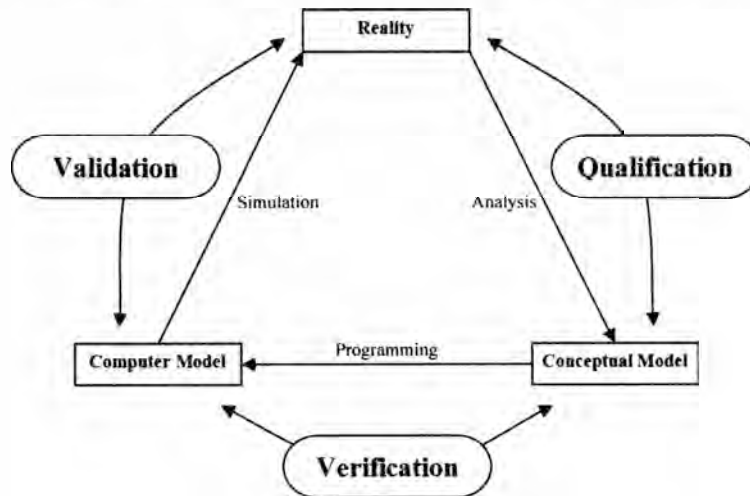


Figure 2.3: Schematic of CFD approach (adapted from Barber, 2005)

The first step in the process (analysis to achieve the conceptual model) is the stage where the applicable governing equations are determined, the simplifying assumptions are made (e.g. no buoyancy effects or simplifying complex geometry) and the boundary conditions specified. All these choices must be justified through a qualification process.

Whereas verification is described as ‘solving the equations right’, validation is often described as ‘solving the right equations’ – this is, it aims to ensure the computer simulation that has been developed is capable of predicting reality. Are we solving the right equations in order to simulate reality? This process is achieved by comparing the simulation against a benchmark study of some kind or a reliable set of experimental values which one can confidently describe, in this context, as ‘reality’. The final step, therefore, before one can claim that a CFD model is fit for use as a flow prediction tool is to ‘prove’ it works by comparing it against reality.

Once the verification and validation process has been completed – and, thus, the model has proved itself capable of faithfully replicating a real world flow problem, it may then confidently be used to predict other flow situations for which experimental data does not exist (for if it did, why would one use CFD?). The user must be careful not to apply the model to

application areas too far beyond those in which it was verified and validated, but, as long as this is not abused, the model can be used with confidence.

## **2.5 The Reynolds-Averaged Navier-Stokes Solver**

The Reynolds-Averaged Navier-Stokes solver is one of three solvers that are used throughout this research programme – the others are Large Eddy Simulation and Pseudo-Direct Numerical Simulation, both of which will be discussed shortly in Secs. 2.6 and 2.7, respectively. Although the three solvers work in different ways, they all follow the same basic numerical processes described in Sec. 2.3 and are subject to the same verification and validation requirements addressed in Sec. 2.4.

The RANS solver is essentially a result of the limitations imposed on CFD through a lack of computing power. It is still by far the most common solver used in industrial applications and, indeed, is still prevalent in applied research. The basic problem in attempting to simulate a turbulent flow field is that, not only does the flow domain need to be adequately resolved spatially (using an adequately fine grid), it also must be adequately resolved temporally – that is, with a timestep small enough to resolve the temporal behaviour of the turbulent eddies in the flow.

Until recently, this was simply not possible to achieve given the computing power available as it would have taken an extraordinarily long time to calculate. Even today, and with access to some impressive supercomputing power, this approach is still only applicable for relatively simple flow problems.

The RANS solver thus represents a compromise where time-averaging is introduced into the governing flow equations (Eqns. 6) in order to eliminate the need to temporally resolve the flow solution. This approach saves enormous amounts of computation time, however, it is only really applicable to steady flow problems and a simulation's resulting flow field is a time-averaged solution rather than an instantaneous snapshot of the flow field at any particular point in time.

### ***2.5.1 Reynolds-Averaged Navier-Stokes Equations***

A full derivation of these equations and the time-averaging process is provided in Appendix A.8. The time-averaged N-S equations are as follows:

$$\text{Mass } \text{div } \mathbf{U} = 0$$

$$\begin{aligned} x\text{-momentum } \frac{\partial U}{\partial t} + \text{div}(UU) + \text{div}(\overline{u'u'}) &= -\frac{1}{\rho} \frac{\partial P}{\partial x} + \nu \text{div grad } U \\ y\text{-momentum } \frac{\partial V}{\partial t} + \text{div}(VU) + \text{div}(\overline{v'u'}) &= -\frac{1}{\rho} \frac{\partial P}{\partial y} + \nu \text{div grad } V \\ z\text{-momentum } \frac{\partial W}{\partial t} + \text{div}(WU) + \text{div}(\overline{w'u'}) &= -\frac{1}{\rho} \frac{\partial P}{\partial z} + \nu \text{div grad } W \end{aligned} \quad (11)$$

The time-averaging process yields additional terms in the governing equations. The momentum equations from Eqns. 11 are repeated below with the third term, in each, moved to the RHS and written in longhand to identify the resulting extra quantities obtained through the time-averaging process.

$$\begin{aligned} \frac{\partial U}{\partial t} + \text{div}(UU) &= -\frac{1}{\rho} \frac{\partial P}{\partial x} + \nu \text{div grad } U + \left[ -\frac{\partial \overline{u'^2}}{\partial x} - \frac{\partial \overline{u'v'}}{\partial y} - \frac{\partial \overline{u'w'}}{\partial z} \right] \\ \frac{\partial V}{\partial t} + \text{div}(VU) &= -\frac{1}{\rho} \frac{\partial P}{\partial y} + \nu \text{div grad } V + \left[ -\frac{\partial \overline{u'v'}}{\partial x} - \frac{\partial \overline{v'^2}}{\partial y} - \frac{\partial \overline{v'w'}}{\partial z} \right] \\ \frac{\partial W}{\partial t} + \text{div}(WU) &= -\frac{1}{\rho} \frac{\partial P}{\partial z} + \nu \text{div grad } W + \left[ -\frac{\partial \overline{u'w'}}{\partial x} - \frac{\partial \overline{v'w'}}{\partial y} - \frac{\partial \overline{w'^2}}{\partial z} \right] \end{aligned} \quad (12)$$

As can be seen from Eqns. 12, there are six additional quantities as a result of time-averaging – three normal stresses and three shear stresses. These are termed the Reynolds stresses:

$$\begin{aligned} \tau_{xx} &= -\rho \overline{u'^2}, & \tau_{yy} &= -\rho \overline{v'^2}, & \tau_{zz} &= -\rho \overline{w'^2} \\ \tau_{xy} &= -\rho \overline{u'v'}, & \tau_{xz} &= -\rho \overline{u'w'}, & \tau_{yz} &= -\rho \overline{v'w'} \end{aligned} \quad (13)$$

## 2.5.2 Turbulence Modelling

These additional quantities presents what is termed the ‘turbulent closure problem’ – for the set of RANS equations to be solved, additional expressions must be found to describe the Reynolds stresses. Closing this system of equations is the role played by turbulence models.

Turbulence models are designed to take account of the relevant physics related to the fluctuating turbulent flow, as best as is possible, and to then present the mean flow that results from the turbulence. The physical laws behind the behaviour of turbulence are generally not well understood and so creating a model that accurately predicts the behaviour of the Reynolds stresses for just one flow situation, let alone universally, is no simple task. Consequently, there are many different turbulence models in use, of greatly varying complexity. Each has its strengths and weaknesses and certain flow types for which its mathematical model best predicts the behaviour.

This research program makes use of the Reynolds Stress Model (RSM). It is one of the more computationally expensive turbulence models – as it solves a different partial differential equation for each value of Reynolds stress. The RSM model is known to be quite robust across a wide range of flows and offers “markedly improved predictions” in comparison to the simpler eddy-viscosity turbulence models that are widely used (Launder, 1989). A good summary of the model may be found in Versteeg and Malalasekera (1995).

## 2.6 Large Eddy Simulation

CFD modelling using LES, in place of the more common RANS-based solvers, represents quite a departure in numerical methodology. LES solvers essentially divide the flow turbulence into two categories via a filter; the large scale swirling turbulent flow, known as eddies, forms one category and the medium and small scale eddies forms the other. LES solves for the physical flow behaviour of the large eddies directly by resolving their structure with a sufficiently fine mesh and solving the (time-dependant) Navier-Stokes equations. The smaller turbulent eddies that fall into the other category are modelled with a form of turbulence model, in a similar manner to RANS-based turbulence modelling. This will be discussed shortly.

LES solvers are considered to be broadly more accurate than RANS solvers as they solve for the actual physical behaviour of the larger turbulent eddies, rather than merely modelling the *effect* of the turbulent eddies, as do all RANS turbulence models. The medium and small eddies are still modelled in LES rather than directly resolved, however, because the turbulence is on a smaller scale and has less energy in this category, it is more isotropic in character (Wilcox, 2006). This means that its behaviour is more universal, less dependant on the problem geometry and flow conditions and, as such, is generally easier to model. The difficulty in designing a turbulence model that would work adequately (let alone well) in all flow and geometry conditions is one of the biggest problems faced in RANS-based modelling.

The other advantage that LES models have over RANS-based models is that, by definition, RANS solvers solve for the time-average of the flow field variables rather than the instantaneous values. This is the case because, as discussed above, the RANS equations differ from the N-S equations by substituting the instantaneous flow variables with a mean value plus a fluctuating component and, in so doing, renders the use of RANS-based solvers, in an unsteady flow environment, inaccurate.

### 2.6.1 Flow Filtering

Flow filtering is the means by which the complexity of the flow solution is controlled in an LES simulation. As already mentioned, filtering determines how much of the range of eddy scales are explicitly resolved in the flow solution and how much are modelled instead. LES represents a complexity reduction in comparison to the real world reality of the flow but the extent of the complexity reduction is a matter for the user to determine and is a trade-off between solution detail and computation time (and resources). This complexity reduction is regulated by means of the filter length  $\Delta$  (which in most cases is equal to the cell size of the mesh). If the filter length is reduced to zero, the solution will retain all the flow complexity, there will be no modelling required and a Direct Numerical Simulation (DNS) will be the result.

The filtering process is similar to the time-averaging that occurs in the RANS equations except that, instead of averaging over a time-period, the filter averages the flow property over a volume of size  $\Delta$  and thus damps out fluctuations in the flow of scales smaller than  $\Delta$ . This is demonstrated below (for one dimension) – and note that the over-bar in this case refers to filtered properties rather than a time-average, as in the RANS section above.

$$\bar{u}(x,t) = \int_{x-\Delta/2}^{x+\Delta/2} \frac{u(\xi,t)}{\Delta} d\xi \quad (14)$$

As shown in Eqn. 14, the filtered quantity is essentially an average over the sub-grid of the ‘real’ quantity in this area. This process can be demonstrated by filtering a known signal to demonstrate its effect as shown by Geurts (2004) which has been adapted in Figure 2.4.

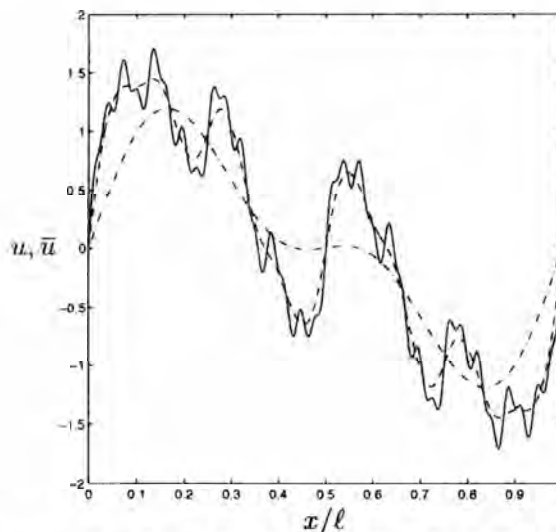


**Figure 2.4: Filtering of reference signal (solid) with filter length of  $l/16$  (dashed) and  $l/4$  (dash-dotted) (Geurts, 2004)**

It can be seen from this figure that the larger scales are retained in the filtered solution, more or less unchanged, and the filtered smaller scales are heavily damped out. This is the basic

objective of applying a filtering process – to eliminate the unnecessary finer features of the flow (and gaining solution speed as a result) while maintaining the larger scale features of the flow. Determining the size of the length scale at which to apply the filter is a trade-off that must be made on a case-by-case basis. In the Fluent commercial package, used throughout this research programme, the filter length is set equal to the grid cell length and thus, the retention of flow field detail is directly controlled by manipulation of the grid resolution.

Large eddy simulation is accomplished by replacing the quantities in the N-S equations with their filtered equivalents, in a similar manner to that of time-averaging in the RANS equations. This will now be demonstrated. Let us take a convenient form of the incompressible N-S equations as shown below:

$$\begin{aligned} \frac{\partial u_j}{\partial x_j} &= \text{div}(u) = 0 \\ \frac{\partial u_i}{\partial t} + \frac{\partial(u_i u_j)}{\partial x_j} + \frac{\partial p}{\partial x_i} - \frac{1}{\text{Re}} \frac{\partial^2 u_i}{\partial x_j^2} &= 0 \quad \text{for } i=1,2,3 \end{aligned} \quad (15)$$

And using the following operating rules for the filtering process,

$$\begin{aligned} \overline{\frac{\partial f}{\partial t}} &= \frac{\partial \overline{f}}{\partial t} \\ \overline{\frac{\partial f}{\partial x_i}} &= \frac{\partial \overline{f}}{\partial x_i} \quad \text{for } i=1,2,3 \end{aligned} \quad (16)$$

It can be shown that the following filtered equations result:

$$\begin{aligned} \overline{\frac{\partial u_j}{\partial x_j}} &= 0 \\ \frac{\partial \overline{u_i}}{\partial t} + \frac{\partial(\overline{u_i u_j})}{\partial x_j} + \frac{\partial \overline{p}}{\partial x_i} - \frac{1}{\text{Re}} \frac{\partial^2 \overline{u_i}}{\partial x_j^2} &= \\ \frac{\partial \overline{u_i}}{\partial t} + \frac{\partial(\overline{u_i u_j})}{\partial x_j} + \frac{\partial \overline{p}}{\partial x_i} - \frac{1}{\text{Re}} \frac{\partial^2 \overline{u_i}}{\partial x_j^2} + \frac{\partial \tau_{ij}}{\partial x_j} &= 0 \end{aligned} \quad (17)$$

where the turbulent stress tensor  $\tau_{ij}$  is defined as:

$$\tau_{ij} = \overline{u_i u_j} - \overline{u_i} \overline{u_j} \quad (18)$$

These equations seek to solve for the value of  $\overline{u_i}$ , however the turbulent stress tensor introduces the filtered quantity  $\overline{u_i u_j}$  for which there is no solution. To solve the momentum equation in Eqns. 17 we must therefore introduce an expression to substitute for the stress tensor. This is the purpose of sub-grid scale turbulence modelling.

## 2.6.2 Sub-Grid Scale Turbulence Modelling

Three sub-grid models are used in this research programme as part of the LES verification programme; the fairly simple Smagorinsky-Lilly model, the Dynamic Smagorinsky-Lilly model and the more advanced Dynamic Sub-grid Kinetic Energy (Dynamic SKE) model. All of these models, like the more-simple RANS turbulence models, are based on the Boussinesq hypothesis which relates the turbulent stresses to velocity gradients. In this case, the sub-grid scale turbulent stress tensor is defined as follows:

$$\tau_{ij} = -2\mu_t \bar{S}_{ij} \quad (19)$$

where  $\mu_t$  is the sub-grid turbulent viscosity and

$$\bar{S}_{ij} = \frac{1}{2} \left( \frac{\partial \bar{u}_i}{\partial x_j} + \frac{\partial \bar{u}_j}{\partial x_i} \right) \quad (20)$$

All sub-grid turbulence models seek to solve for  $\mu_t$ .

### 2.6.2.1 The Smagorinsky-Lilly Model

In the Smagorinsky-Lilly model the sub-grid scale stresses are determined through consideration of the filtered velocities and equilibrium is assumed between the transfer of kinetic energy from the large (unfiltered) scales to the sub-grid scales and the kinetic energy that is dissipated at the sub-grid scale. The sub-grid turbulent viscosity  $\mu_t$  is expressed as follows:

$$\mu_t = \rho L_s^2 (2\bar{S}_{ij}\bar{S}_{ij})^{1/2} \quad (21)$$

where

$$L_s = \min(\kappa d, C_s V^{1/3}) \quad (22)$$

In Eqn. 22,  $\kappa$  is the von Kármán constant,  $d$  is the distance to the nearest wall in the computational domain,  $V$  is the cell volume and  $C_s$  the Smagorinsky constant which, in Fluent, defaults to the value of 0.1, but can be changed by the user. For the standard Smagorinsky-Lilly model employed in this research programme,  $C_s = 0.1$ .

### 2.6.2.2 The Dynamic Smagorinsky-Lilly model

The Dynamic Smagorinsky-Lilly model seeks to enhance the basic Smagorinsky-Lilly model by dynamically determining the model coefficient  $C_s$  in order to better account for the local flow behaviour. This coefficient is determined dynamically in space and time and is realised by introducing the concept of ‘similarity’ to the Smagorinsky-Lilly model. This model is explained in detail in Kim (2004).

The Dynamic procedure introduces a ‘test-filter’, whose filter width is typically twice that used by the real filter (Geurts, 2004). The similarity concept states that the test-sub-grid scale turbulent stress tensor,  $T_{ij}$ , though, in large part, featuring resolved scales, is similar to the real sub-grid scale turbulent stress tensor,  $\tau_{ij}$ . As they are similar, the same model coefficient  $C_s$  is applicable to both. Thus, if  $L_{ij}$  is defined as  $L_{ij} \equiv T_{ij} - \tau_{ij}$ , then  $L_{ij}$  can be thought of as the fully resolved turbulent stress that falls between the test and real filter width.

As  $L_{ij}$  is fully defined by the explicitly resolved scales, the Smagorinsky-Lilly formulations can be applied on this region to determine the applicable value for  $C_s$ . This value for  $C_s$  is then used for the real sub-grid scale turbulence modelling.  $C_s$  can fluctuate heavily in space and time and can lead to numerical instability if it is too negative (even though some transport of turbulent energy to the larger scales, called ‘back-scatter’, can occur). To avoid this problem, the value of  $C_s$  is limited in Fluent between the bounds of zero and 0.23.

### 2.6.2.3 The Dynamic Sub-grid Kinetic Energy Model

The Dynamic SKE model, rather than assuming the sub-grid kinetic energy is in equilibrium with the kinetic energy transferred at the filter, accounts for the transport of the sub-grid kinetic energy directly. The sub-grid turbulent viscosity  $\mu_t$  is expressed as follows:

$$\mu_t = C_k k_{sgs}^{1/2} \Delta_f \quad (23)$$

where  $k_{sgs}$  is the sub-grid scale kinetic energy,  $C_k$  is a dynamically determined coefficient (in the same manner as described for the Dynamic version of the Smagorinsky-Lilly model) and  $\Delta_f$  is the filter length which, in the case of Fluent, was set to  $\Delta_f = V^{1/3}$ . The sub-grid scale kinetic energy  $k_{sgs}$  can be obtained by solving its transport equation

$$\frac{\partial \bar{k}_{sgs}}{\partial t} + \frac{\partial \bar{u}_j \bar{k}_{sgs}}{\partial x_j} = -\tau_{ij} \frac{\partial \bar{u}_i}{\partial x_j} - C_\epsilon \frac{k_{sgs}^{3/2}}{\Delta_f} + \frac{\partial}{\partial x_j} \left( \frac{\mu_t}{\sigma_k} \frac{\partial k_{sgs}}{\partial x_j} \right) \quad (24)$$

where, if Eqn. 23 is substituted into Eqn. 19, the resulting expression for the stress tensor may then be substituted into Eqn. 24. Solution of Eqn. 24 then yields  $k_{sgs}$ . Then, with  $k_{sgs}$  known, Eqn. 25 below may be used to find the value of the stress tensor.

$$\tau_{ij} = -2C_k k_{sgs}^{1/2} \Delta_f \bar{S}_{ij} \quad (25)$$

## 2.7 Pseudo-Direct Numerical Simulation

Pseudo-Direct Numerical Simulation (P-DNS) is a fairly new concept for a CFD solver algorithm. Firstly, Direct Numerical Simulation, as mentioned above, is the limiting case of LES where the filter length tends to zero and therefore all the turbulent eddy scales are

directly solved without the need to implement any sub-grid turbulence modelling. To achieve this, of course, an extremely fine grid – much finer than any LES grid – must be employed.

P-DNS attempts to gain some of the advantages of the DNS approach but at a much more economical numerical cost, more in line with that on LES. P-DNS does away with the sub-grid turbulence modelling and instead deliberately uses an error-prone discretisation scheme (second-order upwind scheme) whose errors throughout the iteration process manifest in the form of ‘numerical diffusion’ – that is, these particular errors, due to the discretisation error, create additional diffusion in the solution process which has been termed by the CFD community as ‘numerical diffusion’. This additional diffusion, it is argued, is a suitable substitute for the diffusion modelled via sub-grid turbulence models. P-DNS is executed on LES size grids (rather than DNS size grids) and, as such, is much more economical than DNS solutions. A thorough discussion of the flow discretisation process in CFD is presented in Appendix A.4.

This concept of harnessing numerical diffusion instead of using a model to generate it was originally proposed by Reizes (Brady, Gaston and Reizes, 2007) – a technique he termed the ‘‘Poor-Person’s Direct Numerical Simulation’ or PPDNS. Reizes argues (Reizes, 2008) that PPDNS not only takes less time to compute (as no turbulence model must be solved at each iteration) but that it may indeed produce superior results compared to a more standard LES procedure. He asserts that the numerical diffusion seems to model sub-grid turbulence better than the current models available for LES. This process has been successfully implemented and validated by Brady, Gaston and Reizes (2007) and this work is discussed in more detail in Sec. 2.8.4.

P-DNS can be implemented in a commercial package by employing a fully laminar flow solver (a standard unsteady RANS-solution without the use of a turbulence model) on a grid of sufficient fineness for an LES simulation. This process that Reizes calls PPDNS is investigated as part of this research programme in Sec. 4.3.2. However, hereafter, it shall be referred to as ‘Pseudo-Direct Numerical Simulation.’

## **2.8 Current State-of-the-Art of CFD Methodology**

This section discusses the most recent literature of relevance to the subject matter of this research programme in terms of the methodology of undertaking the CFD simulation process. The content of each of the following sections had bearing on how the research was conducted and this influence is summarised in each section.

### 2.8.1 Preliminary Modelling Considerations

Ground effect research in general – not just that involving inverted wings – can be performed in several different ways. When experiments are conducted, the way in which the ground plane is modelled can vary significantly. In a wind tunnel, the air is compelled to move at the freestream velocity and the test piece is held stationary. This arrangement recreates the relative velocity seen in reality, but in a controlled environment. In reality, when the ground is considered (and with no wind), it is clear that the ground and the air are both motionless – and are not moving relative to each other – and the vehicle has a velocity relative to the air and ground. In the wind tunnel, the correct method for modelling the ground would then be to create a moving ground plane that moves with the same velocity as the freestream air in the tunnel that passes over the test piece. This has not always been the method used in wind tunnel testing, however.

The importance of using correct boundary condition during a CFD study has been investigated by Barber, Leonardi and Archer (1999) through various tests of a generic two-dimensional aerofoil in ground effect, using different boundary conditions to simulate the ground plane. It was concluded that modelling the ground plane as moving with the same velocity as the freestream is the only appropriate method to use as all other methods introduce unacceptable levels of error.

It is noted in further work on the subject that experimental ground effect research typically uses, in addition to moving grounds, a stationary ground surface and sometimes a slotted surface to progressively suck away the boundary layer that grows as a result of a stationary ground (Barber, Leonardi and Archer, 2002). In experiments involving an upright NACA4412 aerofoil, it is shown that a stationary ground noticeably compromises the results of the experiment in comparison to the more correct results from a moving ground. PIV was also used to analyse the turbulent kinetic energy in the tunnel test section for both moving and stationary ground situations. In the stationary ground case, a significant and erroneous turbulence build-up on the ground plane was observed, due to the presence of a boundary layer. This was noted to be non-physical.

A variety of numerical computations, employing a variety of methods to simulate the ground under an upright NACA4412 aerofoil, were also conducted. Simulated were; a moving ground plane, a stationary plane, a frictionless plane and a reflection plane which theoretically models a mirror image of the test piece using the ground plane as a plane of symmetry. The results show significant flow reversal near the ground for the stationary ground plane and for the image plane (that is, flow actually heading back in the direction from whence it came). A

tending toward reversed flow was seen for the frictionless plane case (velocity profile slows significantly near the ground boundary) and the moving ground cases showed velocity profiles that remained fairly constant throughout the gap between the aerofoil and the ground, except when very close to the ground where the air actually speeds up to meet the speed of the ground plane. It was concluded that a moving ground is the only acceptable method for obtaining reasonable accuracy. Viscous and inviscid (no friction forces) numerical solutions were also compared and it was concluded that, due to the complex nature of the flow near the ground, the error associated with neglecting viscosity is too great to achieve a reasonably accurate solution using inviscid methods and therefore any ground effect numerical computation should be conducted using a moving ground plane and a viscous numerical model.

In a project to verify the performance of the UNSW Moving ground wind tunnel – the tunnel used in this research programme – CFD simulations and LDA data were used to examine the flow field about the moving ground (Diasinos *et al.*, 2005). Measurements were taken at four locations in the test section. At all locations, the velocity profile was very consistent except very close to the ground where a minor dip in velocity was noted. This velocity profile behaviour, including the dip near the ground, was well reproduced in the CFD simulations. This dip, as noted by Diasinos *et al.* (2005), is a common phenomenon that has been found in both moving ground experiments and CFD simulations (Zerihan and Zhang, 2001; Zhang and Zerihan, 2003a and 2003b; Soso and Wilson, 2004; Beves *et al.*, 2005; Mahon and Zhang, 2005 and 2006), without explanation. However, the predominately consistent velocity profiles in Diasinos *et al.* (2005) indicate that their specification of a consistent inlet profile in the CFD simulations is entirely appropriate in this current investigation.

This velocity profile dip behaviour is examined in Sec. 7.2.5.

## **2.8.2 Large Eddy Simulation**

Comparison work was undertaken by Meneveau and Katz (2000) in order to examine the performance of several commonly used sub-grid scale (SGS) turbulence models for LES. Also discussed is the means by which one can verify the performance of such models, typically by employing either ‘a posteriori’ testing or ‘a priori’ testing. The former method compares the numerical results after a completed simulation with those of a reliable benchmark, be it direct numerical simulation or an experiment. The latter method involves comparing the sub-grid scale regions only. This requires a very high resolution of this region, for both the numerical simulation and the comparing medium, so that the SGS Reynolds stresses can be adequately determined. This method is performed without actually doing any

LES calculations – hence the ‘prior’ instead of ‘post’ prefix. It was concluded that, although it was deemed too early to categorically state which SGS model is most effective, dynamic models, with an automatically changing flow filtering threshold, definitely improved the simulation outcome.

As a consequence of this work, the two sub-grid scale models considered in this research programme (Dynamic Smagorinsky-Lilly and Dynamic Sub-grid Kinetic Energy) both make use of a dynamically determined filtering coefficient as it has proven very effective in improving simulation results.

### **2.8.3 Direct Numerical Simulation**

Direct Numerical Simulation attempts to simulate all the turbulent behaviour in the flow down to the smallest scales and thus eliminates the need for sub-grid scale turbulence modelling (at the very great expense of much finer grid resolution and therefore much greater memory and computation-time demands). DNS was adopted to simulate the separating and reattaching flow on a NACA0012 aerofoil at Re of  $1 \times 10^5$ , which is quite similar to that used in this research programme (Shan, Jiang and Liu, 2005). The simulation was carried out in both two and three dimensions, for which the results differ appreciably. In the three-dimensional solution, a separated shear layer was noted at the point of separation and this shear layer progressed to vortex shedding via the Kelvin-Helmholtz mechanism. These shed vortices then fairly quickly deteriorated into finer turbulent scales. This turbulent mechanism was found to be self-sustaining in the absence of any external flow perturbations. It was asserted that the perturbations feeding the Kelvin-Helmholtz mechanism emanated from the inherent unsteadiness in the near wake region behind the wing. This work established the inadequacy of employing the DNS solution technique on a two-dimensional flow domain.

DNS was not employed at any stage during this research programme.

### **2.8.4 Periodic Boundary Conditions**

Periodic boundaries are ideally employed in situations where there is a repetition of a domain feature – like the many coolant pipes through a heat-exchanger – such that the flow can be considered periodic in space. It achieves this by using two identical domain boundaries as a ‘portal’ of sorts, where any fluid exiting through one boundary will re-enter, in the same location, but through the other boundary.

There is no periodicity in the flow field around an aerofoil operating in ground effect (or out of ground, for that matter), however, the following literature gives cause to consider using periodic boundary conditions in the direction ‘ $a$ ’ when seeking to simulate a domain that is

continuous in the direction ‘ $a$ ’. The theory follows for continuous domains in two of the three spatial dimensions and also for domains that are continuous in all spatial dimensions.

The relevance of reviewing the use of periodic boundary conditions may be found later in Sec. 4.3 where periodic boundaries are considered as a means to simplify the LES simulation of an aerofoil operating in ground effect. This is done by reducing the spanwise extent of the domain and employing periodic boundary conditions instead, thus saving millions of cells from the computational grid.

The DNS simulation of a NACA0012 aerofoil, which was just discussed in Sec. 2.8.3, used periodic boundaries on the spanwise sides of the domain in order to simulate an infinite wing (Shan, Jiang and Liu, 2005). The periodic boundary walls were placed  $0.1c$  apart.

A review by Robinson (1991) of the, then, state of the art of coherent (and repeating) motions that occur in turbulent boundary layers notes that the use of spectral methods was popular with DNS solutions but that they necessitated the use of periodic boundary conditions. This was noted in the negative, as periodic boundaries restricted the types of geometric problems that could be modelled using spectral methods, but the accuracy or appropriateness of using periodic boundary conditions was not questioned.

A workshop on large eddy simulation was conducted in 1997 to assess the capability of LES to solve complex flow problems and to identify areas of sensitivity in terms of obtaining useful results (Rodi *et al.*, 1997). The conclusions are fairly predictable in that LES is sensitive to many parameters (e.g. sub-grid scale model, numerical methods, grid resolution etc). Of some interest here, however, is the use of symmetry planes (not periodic boundaries) at the spanwise ends of a square-based prism to truncate an otherwise continuous domain. The results of this exercise indicate a particular sensitivity to both the distance between the symmetry planes and the grid resolution in this spanwise direction. It should be noted, however (and this is not considered in the paper), that the spanwise boundaries are likely to impose limitations of the flow development near these walls as they are imposing a zero-flux condition on an otherwise three-dimensional, turbulent flow. Having said that, and despite periodic boundary conditions not being used in this case, the observations regarding wall-sensitivity are useful.

An LES simulation about the same square-based prism test geometry used in Rodi *et al.* (1997) was undertaken by Brady, Gaston and Reizes (2007). Two simulations were performed; one with a spanwise depth between symmetry planes of  $9.75s$ , where  $s$  is the side length of the square, and a much narrower model in the spanwise direction of  $4.0s$ , where the spanwise boundaries employed the periodic condition. The first model (numerically, much

more demanding) matched the experimental results used for validation and the second model was employed to ascertain the validity of the simplification. Both models performed well in terms of replicating experimental data and comment was made that the distance between the periodic boundaries may not have been sufficient “to develop an adequate region of uncorrelated flow.” The main purpose of the work, however, was to assess the validity of using a second-order unwinding scheme as a means to generate sub-grid turbulent diffusion instead of employing a sub-grid scale turbulence model for this purpose and this will be discussed further in Sec. 2.8.5.

Young and Ooi (2007) studied the flow over a cylinder using both LES and Unsteady-RANS or URANS solvers (a time-dependant RANS) in order to assess their performance. The domain was three-dimensional with the spanwise extent of the domain, bounded by periodic boundary conditions, located  $\pi D$  apart where  $D$  is the diameter of the cylinder with the cylinder axis in the spanwise direction. The effect on the LES solution of the number of cells used in the spanwise direction was tested through varying this number between 4, 16, 32 and 48. The URANS results were also tested in this way, but the 48 cell grid was not used with the URANS solver. The spanwise resolution was found to be a very important factor that determined how successful the LES solution would be. The spanwise-spatially-unresolved LES flow solution was little better than the inadequate URANS results but did improve markedly with improved resolution.

Further weight in the literature to underline the general acceptance of the use of periodic boundary conditions, in order to allow the truncation of an otherwise continuous domain, was gleaned from one recent peer-reviewed conference (Burattini, Lavoie and Antonia, 2007; Hutchins *et al.*, 2007; Burattini *et al.*, 2007; Mattner, 2007; Kitsios, Ooi and Soria, 2007; Hawkes, Sankaran and Chen, 2007; and Williamson *et al.*, 2007). These examples showcase either LES or DNS simulations and they all employ periodic boundary conditions in either one-, two- or three-dimensions.

An LES investigation of the flow over a NACA4415 aerofoil at a stalling incidence and at a  $Re = 1 \times 10^5$ , employed spanwise periodic boundary conditions (Eisenbach and Friedrich, 2008). The spanwise extent of the model was 1.0 chord length, greater than all other such cases in the literature. An iso-surface plot of the pressure fluctuations about the suction surface of the aerofoil (undergoing significant separation) showed that, although the scale of the turbulent structures toward the front of the aerofoil were small, the spanwise length-scales grew larger toward the trailing edge – to as large as about two-thirds of the chord length.

These results indicate that a narrow spanwise domain that features periodic boundary conditions is unlikely to capture the full extent of large scale turbulent structures.

Periodic boundaries are employed heavily in this research programme as a suitable means to dramatically reduce the size of the computational grid required, while also allowing an increase in grid resolution to retain more of the flow's turbulent features in the resulting simulation. A thorough validation programme was undertaken in Sec. 4.3 to approve the use of such a boundary condition. Consequently, the periodic boundary condition was employed for all the definitive simulations discussed in Chapter 7.

### **2.8.5 *Pseudo-Direct Numerical Simulation***

Pseudo-Direct Numerical Simulation, or P-DNS, is an alternative CFD solution process that has recently been assessed by Brady, Gaston and Reizes (2007). Their work examined the validity of using a second-order unwinding scheme as a means to generate sub-grid turbulent diffusion instead of employing a sub-grid scale turbulence model for this purpose. The results proved very effective, as already discussed in Sec. 2.8.4.

As discussed in Sec. 2.7, P-DNS was investigated during this research programme (see Sec. 4.3.2 for details of this project) and the results of Brady, Gaston and Reizes (2007) add weight to this admittedly young and relatively unproven theory.

### **2.8.6 *Grid Structure***

Murayama and Yamamoto (2006) undertook a thorough grid dependency study on two- and three-element aerofoil configurations – in both two- and three-dimensional cases – in order to assess the suitability of using an unstructured mesh around the aerofoil configuration. This study found that, for the two-dimensional case, the unstructured mesh can perform as well as the structured mesh provided that the grid resolution is adequate both close to and also further away from the aerofoil, so as to be able to capture the wake region and the significant circulation around the aerofoil configuration.

The three-dimensional case modelled a full wing with a tip at one end, a fuselage at the other, and a few different flap settings. Similar results were again achieved between the structured mesh and the unstructured mesh – but care was needed to ensure the resolution was adequately high in areas such as the trailing edge to capture separation behaviour, the tip to capture the shedding vortices and the wing-fuselage interaction region to capture the complex behaviour there.

The findings of Murayama and Yamamoto (2006) support the use of well developed unstructured grids and such grids have been used throughout this research programme. Care

was taken in the grid development for this programme that, wherever an unstructured grid was used (around the aerofoil for both 2D and 3D simulations), it always featured a high grid resolution and a very slow reduction in this resolution with distance from the aerofoil (if a reduction at all). The grid design is discussed in detail in Chapter 4.

# Chapter 3: Experimental Programme

## 3.1 Introduction

The experimental programme undertaken for this Ph.D. project was conducted primarily as a validation tool for the numerical work discussed in Chapters 6 and 7. This experimental work is significant in aiding the two primary aims of these chapters.

The first, discussed in Chapter 6, is to compare the ability of several numerical simulation techniques to model the flow over an inverted wing in unsteady, quasi-two-dimensional, extreme ground effect flow. The experimental results obtained, as described in this chapter, form the key benchmark in determining how well these various numerical methods perform.

The second objective that this experimental work underpins is the validation of the definitive numerical model that will be used to thoroughly investigate the development of flow separation in extreme ground effect, as discussed in Chapter 7.

This chapter will describe the facilities used, the experimental technique, as well as the specific details of the experiments conducted.

## 3.2 Wind Tunnel Models and Facilities

The wind tunnel utilised for this experimental programme was the low-speed, moving-ground wind tunnel located in the School of Mechanical and Manufacturing Engineering at the University of New South Wales, Sydney, Australia.

The wind tunnel is of open-circuit design, powered by a 10 kW vacuum box at its downstream end. The tunnel's test-section measures approximately  $287 \times 227$  mm (height  $\times$  width) at the model installation and the entire test section is 1020 mm in length. The width and height of the test-section increases slightly down the length of the tunnel by  $0.15^\circ$ , to account for the development of boundary layers on the side walls and the tunnel roof. The test-section also features a floor boundary layer extraction duct which diverts the initial ground boundary layer below the test-section, just upstream of the commencement of the moving ground belt. An elevation of the test section is shown in Figure 3.1 and the whole tunnel is shown in Figure 3.2, where the inlet to the test-section (left of the figure) precedes a 7.8:1 contraction inlet. At the front of the contraction inlet are two flow conditioning screens.

The screens remove the larger scale turbulent eddies from the inlet flow and the contraction reduces the size of the remaining eddies before the flow is introduced to the test-section. The tunnel, running at 10 m/s and with the moving ground on, produces a turbulence intensity of approximately 3.0 % at the entrance to the test section.

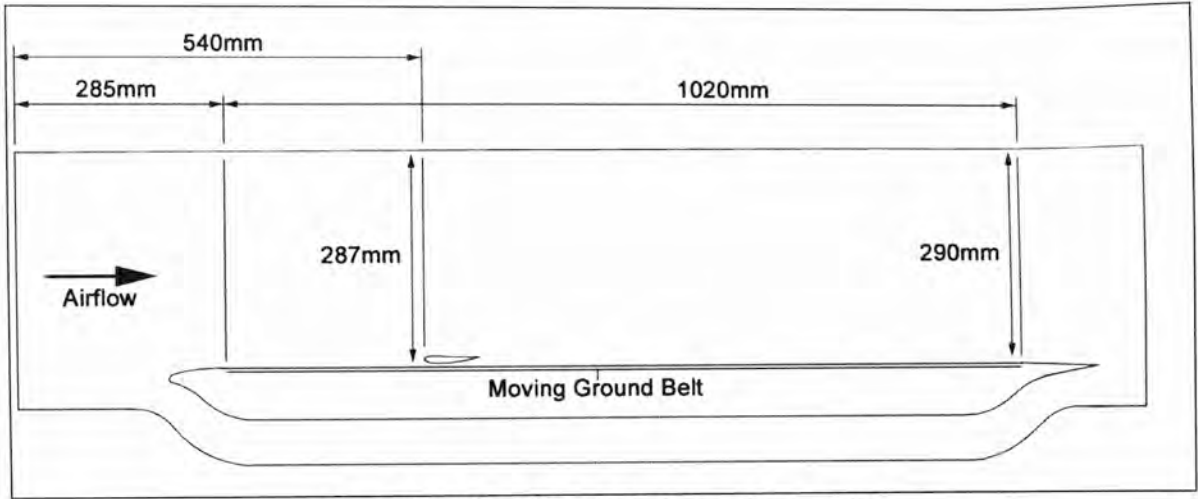


Figure 3.1: Elevation of wind tunnel test section

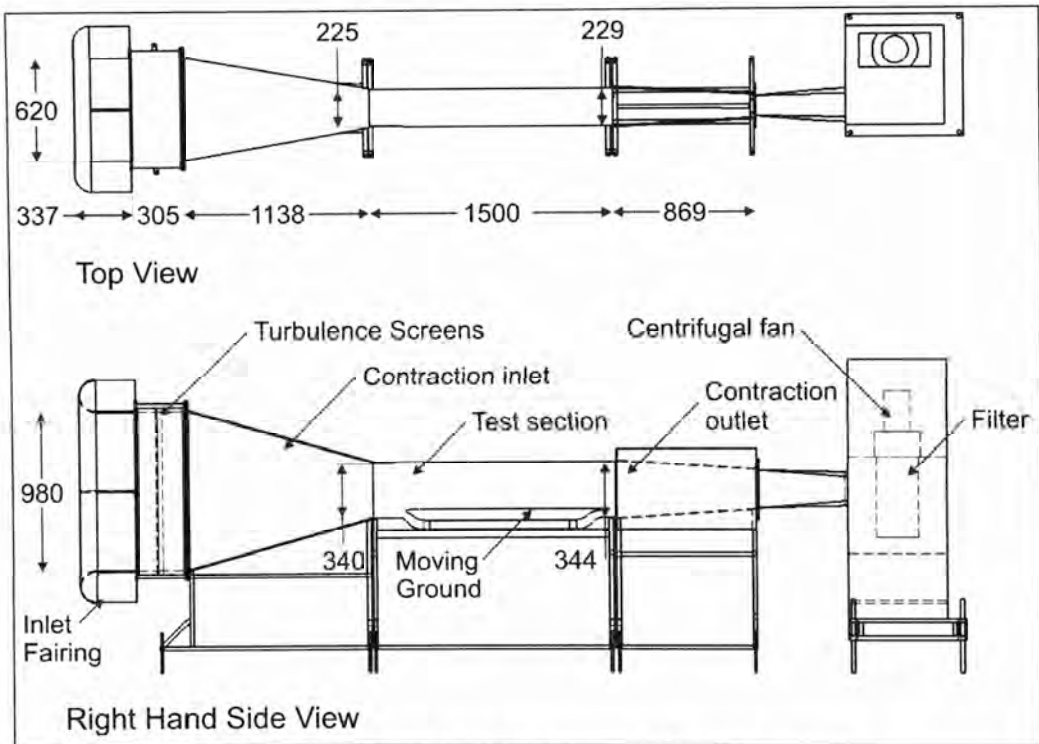


Figure 3.2: Elevation of wind tunnel (Diasinos, 2009)

Turbulence intensity throughout this work is defined as follows

$$T.I. = \frac{\sqrt{\frac{1}{3}(\overline{u_x'^2} + \overline{u_y'^2} + \overline{u_z'^2})}}{U_\infty} \quad (26)$$

where  $u_x'$  is the fluctuating component of velocity and  $U_\infty$  is the reference velocity which in this case is the freestream velocity (10 m/s). Additionally, given the following

$$u_{x-RMS} = \sqrt{u_x'^2} \quad (27)$$

$$u_{x-RMS}^2 = u_x'^2$$

then the squared RMS quantities can be substituted into Eqn. 26:

$$\text{T.I.} = \frac{\sqrt{\frac{1}{3}(u_{x-RMS}^2 + u_{y-RMS}^2 + u_{z-RMS}^2)}}{U_\infty} \quad (28)$$

The turbulence intensity as defined in Eqn. 28 is used throughout this research programme and is quoted as a percentage.

One of the side walls and the roof of the tunnel are manufactured from clear acrylic in order to allow non-intrusive observation of the flow field via optical methods. Wind tunnel models are installed in and secured by the other side wall which is painted matte black in order to absorb laser light and avoid overexposing optical instruments. A photo of the tunnel's test section and LDA probes during operation is presented in Figure 3.3.

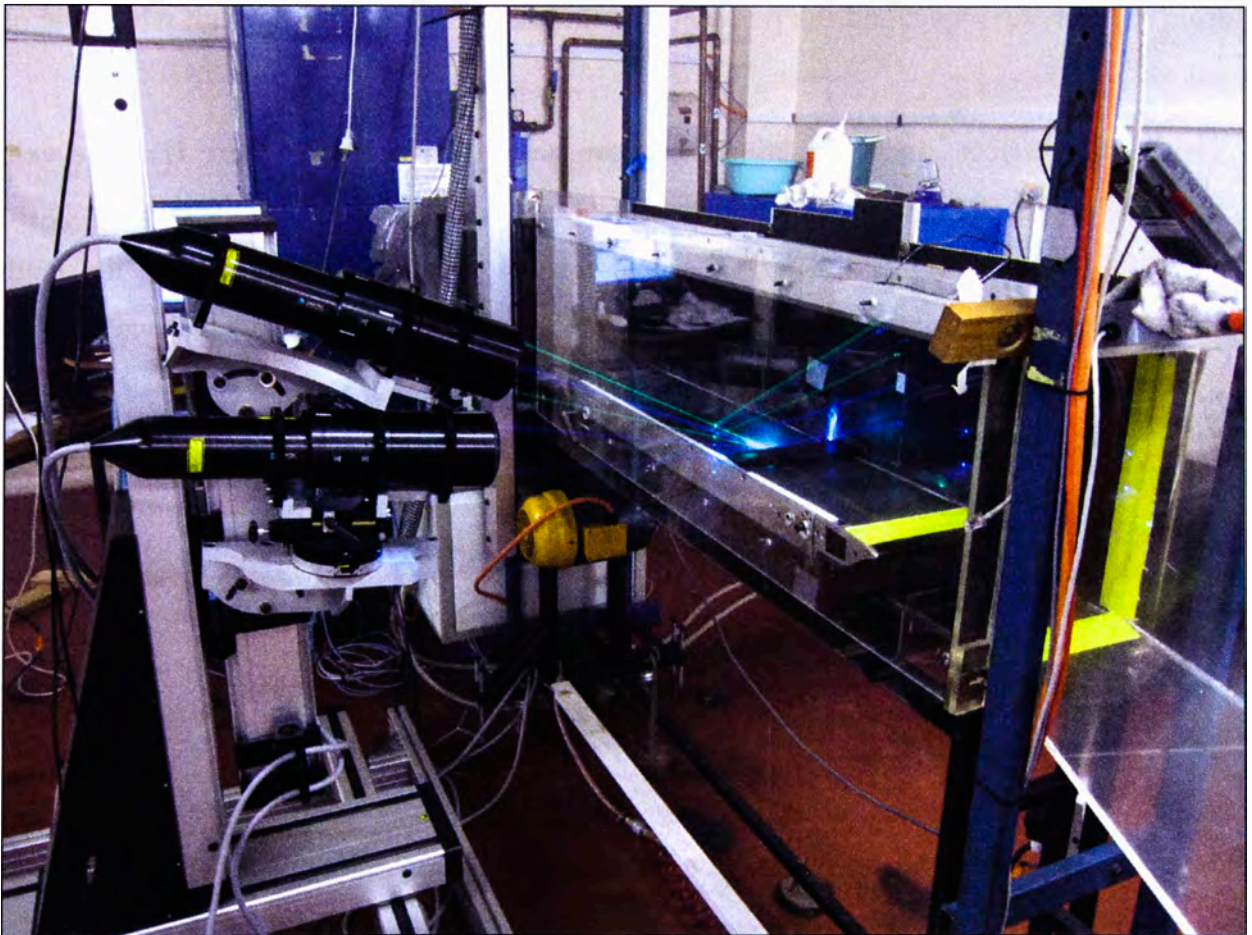


Figure 3.3: Wind tunnel and LDA system

The wind tunnel model used in the experiments is a scale model of the Tyrrell wing which was the main-plane of the front wing assembly of the 1998 Tyrrell Formula 1 car. Its chord measured 75 mm which, with a freestream velocity of 10 m/s, achieved a Re of approximately 53,000. The wing was machined from aluminium and anodised to produce a matte black

finish in order to minimise laser light reflections. When installed in the tunnel, the wing spanned the whole test section to minimise three-dimensional flow and ensure that the spanwise mid-plane of the tunnel achieved quasi-two-dimensional flow.

### 3.3 Laser Doppler Anemometry Technique

Laser anemometry allows the measurement of flow velocities without disturbing the fluid flow itself. The theoretical principles of LDA are discussed in Sec. 3.3.1 and the specific details of how the system was setup and run are given in Sec. 3.3.2. The information covered in the following two sections are based on the Dantec Dynamics' LDA software user's guide (BSA Flow Software, 2006). If further information is required on any of these topics, the reader is referred to this document.

#### 3.3.1 Doppler Effect

LDA systems make use of the Doppler effect to determine the velocity of a moving object (in this case a seeding particle) by measuring the difference between the scattered light frequency from the moving object and the frequency of the emitted laser light through which the object passes.

The Doppler effect can be explained with the help of Figure 3.4, where  $\mathbf{U}$  is the velocity vector of a particle,  $\mathbf{e}_i$  is the unit vector indicating the direction of the incident wave (in the case of LDA, laser light) and  $\mathbf{e}_s$  is the unit vector indicating the direction of the scattered wave, from the particle, that reaches the receiver (which measures the scattered wave frequency).

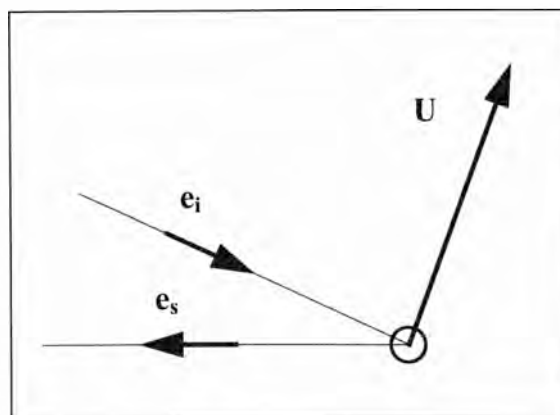


Figure 3.4: Doppler frequency measurement

The incident light has a frequency of  $f_i$ , however, because the particle is moving, it experiences the incident light at a different frequency (due to the Doppler effect) and reflects (scatters) that light at the frequency which is measured by the receiver. It can be shown then (if  $\mathbf{U}$  is much, much smaller than the speed of light  $c$ ), that the scattered frequency is

$$f_s = f_i \left[ 1 + \frac{\mathbf{U}}{c} \cdot (\mathbf{e}_s - \mathbf{e}_i) \right] = f_i + \frac{f_i}{c} \mathbf{U} \cdot (\mathbf{e}_s - \mathbf{e}_i) = f_i + \Delta f \quad (29)$$

Theoretically, the velocity  $\mathbf{U}$  may be determined from Eqn. 29 by measuring the change in frequency  $\Delta f$ . However, this is only practically possible for extremely high velocities and so, LDA systems employ two intersecting lasers (which constructively and destructively interfere) and the receiver measures the beat frequency of the scattered intersecting light, which is much smaller than  $f_s$  from Eqn. 29, and is thus capable of measuring much smaller velocities accurately. The LDA arrangement is show in Figure 3.5. The frequency detected  $f_D$  is the difference between the scatter frequencies from both incident waves,  $f_{s1} - f_{s2}$ . It should also be noted that the incident frequency of both waves are equal (in the simplest case, anyway) as they are supplied by the same laser, whose beam is split;  $f_1 = f_2 = f_i$ .

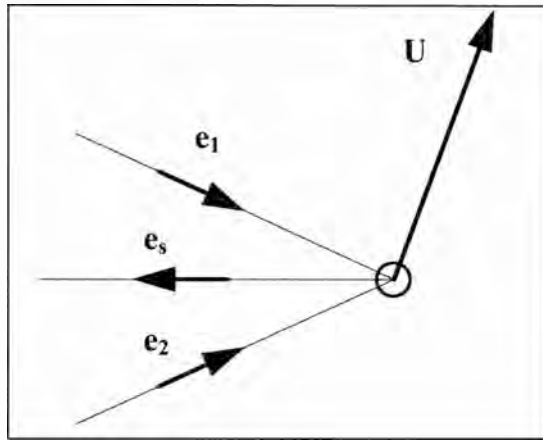


Figure 3.5: LDA Doppler frequency measurement

The detected beat frequency  $f_D$  is related to the incident beams thus:

$$\begin{aligned} f_D &= f_2 \left[ 1 + \frac{\mathbf{U}}{c} \cdot (\mathbf{e}_s - \mathbf{e}_2) \right] - f_1 \left[ 1 + \frac{\mathbf{U}}{c} \cdot (\mathbf{e}_s - \mathbf{e}_1) \right] \\ &= f_i \left[ \frac{\mathbf{U}}{c} \cdot (\mathbf{e}_1 - \mathbf{e}_2) \right] \\ &= \frac{f_i}{c} [|\mathbf{e}_1 - \mathbf{e}_2| \cdot |\mathbf{U}| \cdot \cos(\varphi)] \\ &= \frac{1}{\lambda} \cdot 2 \sin(\theta/2) \cdot u_x = \frac{2 \sin(\theta/2)}{\lambda} u_x \end{aligned} \quad (30)$$

where  $\varphi$  is the angle between the vector  $\mathbf{U}$  and the velocity component measured by the lasers (which would lie on a vertical axis in Figure 3.5) and  $\theta$  is the angle between the two vectors  $\mathbf{e}_1$  and  $\mathbf{e}_2$ . Eqns. 30 yields an expression for velocity component  $u_x$  given the angle between the lasers and their wavelength, having measured the beat frequency  $f_D$ . The last line of Eqns. 30 is thus rearranged to solve for  $u_x$  in Eqn. 31.

$$u_x = \frac{\lambda}{2 \sin(\theta/2)} f_D \quad (31)$$

A physical interpretation of the constructive and destructive interference between the two lasers is also useful. This interference creates parallel planes of light and dark regions as shown in Figure 3.6.

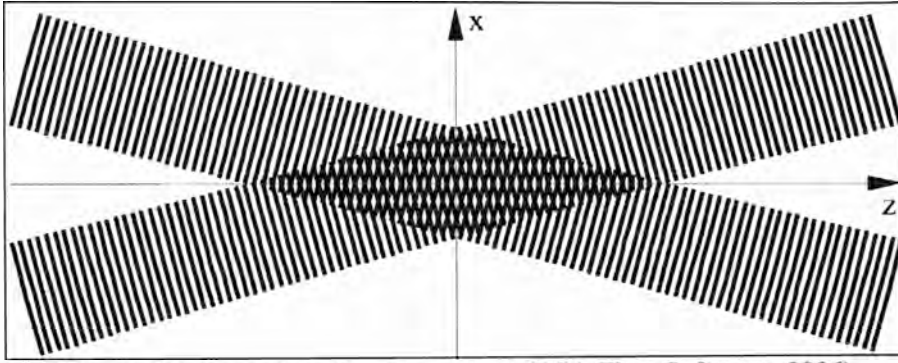


Figure 3.6: Laser interference pattern (BSA Flow Software, 2006)

As the particle moves through the measurement volume, it is illuminated (and thus scatters light to the detector) each time it passes through one of the fringes of light (a plane of constructive interference). If we know how the distance between the light fringes, we can thus determine the particle's velocity by measuring the frequency of the bursts of scattered light from the particle – which is the quantity  $f_D$  that was being measured in Eqns. 30.

With the help of Figure 3.7, the distance between the fringes  $\delta_f$  may be determined.

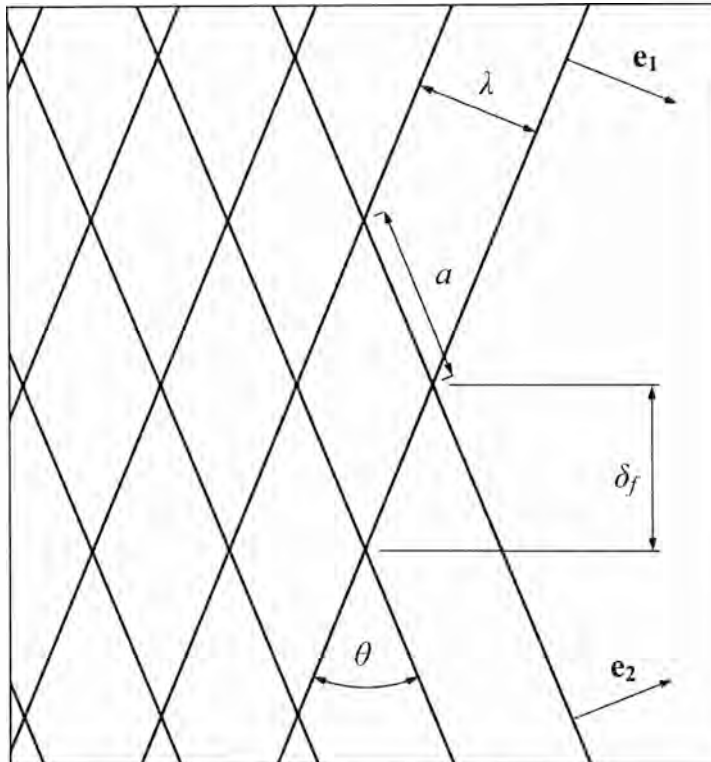


Figure 3.7: Determination of fringe spacing

$$\begin{aligned} \delta_f &= a \cos(\theta/2) \\ \sin \theta &= \lambda/a \rightarrow a = \lambda/\sin \theta \\ \delta_f &= \frac{\lambda \cos(\theta/2)}{\sin \theta} = \frac{\lambda \cos(\theta/2)}{2 \sin(\theta/2) \cos(\theta/2)} = \frac{\lambda}{2 \sin(\theta/2)} \end{aligned} \quad (32)$$

The velocity component normal to the fringes  $u_x$  is then equal to the measured scatter frequency  $f_D$  (number of times the particle travels the distance  $\delta_f$  per second) multiplied by the distance between fringes  $\delta_f$ .

$$u_x = \delta_f f_D = \frac{\lambda}{2\sin(\theta/2)} f_D \quad (33)$$

This result is the same as that in Eqn. 31.

There is a problem with this solution, however, which is that negative  $u_x$  velocity components would require a negative  $f_D$  reading. The LDA system is not capable of differentiating between a positive and negative  $f_D$  reading and so a Bragg cell must be introduced to the system to account for this problem. A Bragg cell is a glass prism through which one of the two laser beams is passed before it is sent to the measurement volume. This glass prism has a series of moving acoustic waves travelling through it generated by a small oscillator. The laser is directed through this prism at an angle and is diffracted by the moving wave fronts to produce intensity maxima at various angles. The first intensity maxima features a slightly increased frequency compared to the input laser beam and this diffracted beam is utilised as one of the incident beams to the measurement volume.

This additional frequency  $f_0$  is 40 MHz and changes Eqns. 30 thus

$$f_D = (f_i + f_0) \left[ 1 + \frac{\mathbf{U}}{c} \cdot (\mathbf{e}_s - \mathbf{e}_2) \right] - f_i \left[ 1 + \frac{\mathbf{U}}{c} \cdot (\mathbf{e}_s - \mathbf{e}_1) \right] \quad (34)$$

which can be shown to equal to the following (after discarding a negligible term, see BSA Flow Software (2006))

$$f_D = f_0 + \frac{2\sin(\theta/2)}{\lambda} u_x \quad (35)$$

This result is very similar to the original equation for  $f_D$  (last of Eqns. 30), but for the addition of  $f_0$ . The significance of this alteration is presented graphically in Figure 3.8. An LDA system not equipped with a Bragg cell would not be able to differentiate between  $u_x$  velocities  $-k$  and  $+k$  (the blue plot), whereas the Bragg cell shifts this function line upward (the red plot) which allows the smaller  $f_D$  measurements to correspond to negative velocity components – and can thus easily differentiate the difference between  $-k$  and  $+k$ , in this case. Depending on how negative a velocity value one expects to encounter during a measurement, the value of  $f_0$  may be tuned by varying the input angle of the laser beam into the Bragg cell.

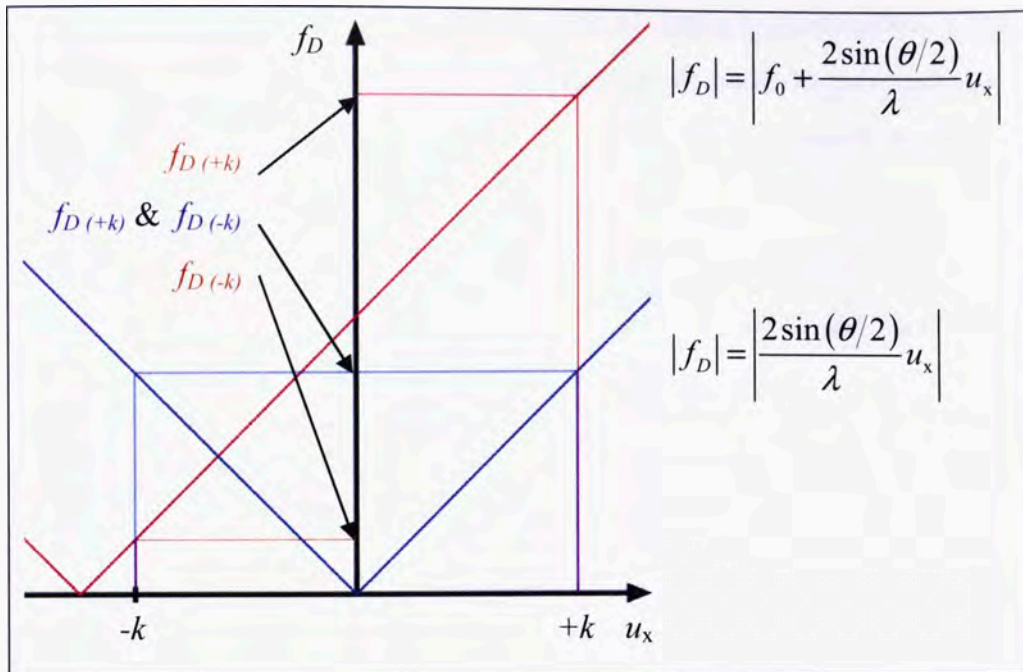


Figure 3.8: LDA velocity measurement with a Bragg cell

Physically, the additional 40 MHz frequency in one of the laser causes the light fringes to scroll along the x-axis in the negative direction. Thus, as can be seen in Figure 3.8, a particle that is not moving at all will still be passing through fringes (as the fringes are moving past the particle), inducing a Doppler frequency  $f_D$  in the detector and so will be measured. If the particle is moving at a negative velocity (moving in the same direction as the fringes), it will pass through fewer fringes and induce a lower Doppler frequency.

### 3.3.2 System Setup

This section briefly explains how the LDA system was configured. A schematic of the system is presented below in Figure 3.9.

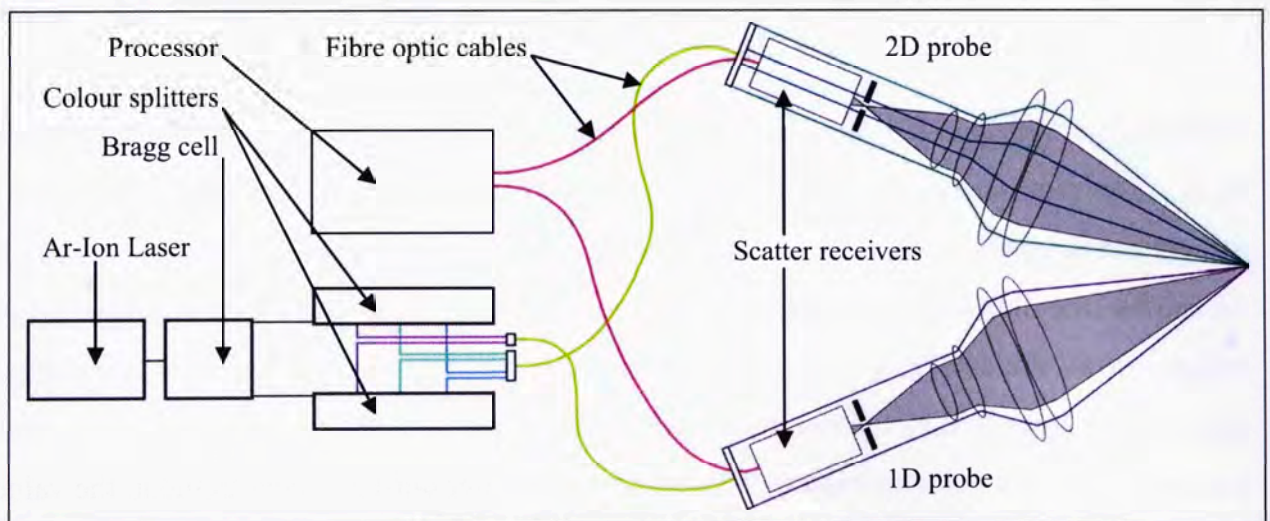


Figure 3.9: Schematic of LDA system

The Doppler principle described in the previous section is employed in three different arrangements concurrently, in order to measure different velocity components at the same location. Although not apparent in Figure 3.9, the measurement volume for each set of

intersecting lasers is positioned in the same location so that the measured velocity components may be used to fully describe the three-dimensional velocity vector at that location. The arrangement used by this three-probe LDA system (one 1-D probe and one 2-D probe) is shown in Figure 3.10.

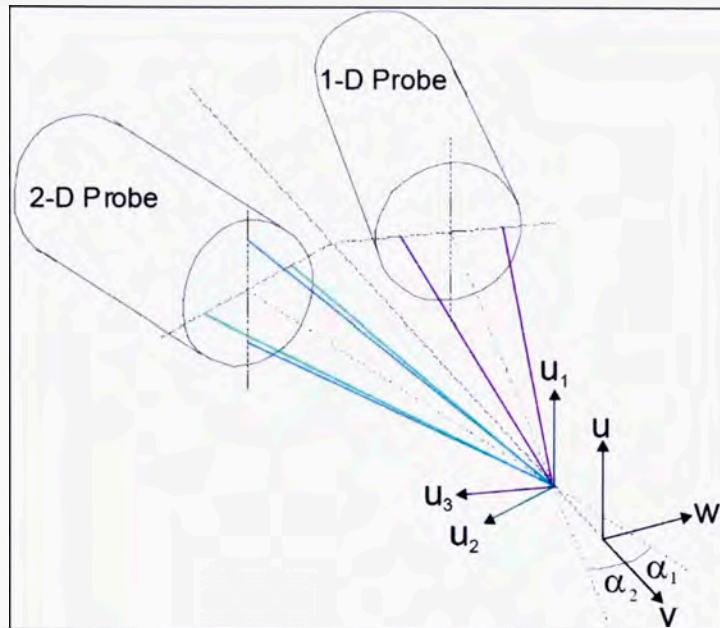


Figure 3.10: Setup for LDA probes (modified from BSA Flow Software, 2006)

As schematically demonstrated in Figure 3.9, the laser is first directed through the Bragg cell which splits the beam into two; the first is the unaltered transmitted beam, the second beam, as was described earlier, had its frequency increased by 40 MHz. Both beams are then refracted into three different colours; green ( $\lambda_g = 514.5$  nm), blue ( $\lambda_b = 488.0$  nm) and purple ( $\lambda_p = 476.5$  nm). Different coloured lasers are required so that each probe can measure the light scattering off the particles without any disturbance from the other two probes' lasers. The six laser beams are then directed into fibre optic cables connecting to the probes. The scattered light from the particles moving through the measurement volume is collected by the large detector optic (large, in order to capture as much scattered light as possible) which then concentrates this signal into a beam. This detected beam is fed via optic cable back to the processor unit, which interprets the Doppler frequency from this signal.

Figure 3.10 shows the coordinate system used for the LDA system (the x-, y- and z-axes correspond to the velocity components  $u$ ,  $v$  and  $w$ ). The positive x-axis points downstream in the tunnel, the positive y-axis points toward the portside, from the perspective of looking into the wind on the installed model (left-pointing spanwise direction), and the positive z-axis points downward.

The velocity components measured by the LDA system are  $u_1$ ,  $u_2$  and  $u_3$ . The  $u_1$  velocity component measures the x-component of velocity  $u$  directly. The  $u_2$  and  $u_3$  components do

not measure the  $y$ - or  $z$ -components directly and, therefore, must be processed using a transformation matrix to yield the desired  $v$  and  $w$  velocity components. The derivation of the transformation matrix employed may be found in Appendix C. The transformation matrix employed is displayed below.

$$\begin{Bmatrix} u \\ v \\ w \end{Bmatrix} = \begin{bmatrix} 0 & 1 & 0 \\ \frac{-\cos \alpha_2}{\sin(\alpha_1 - \alpha_2)} & 0 & \frac{\cos \alpha_2}{\tan(\alpha_1 - \alpha_2)} - \sin \alpha_2 \\ \frac{-\sin \alpha_2}{\sin(\alpha_1 - \alpha_2)} & 0 & \frac{\sin \alpha_2}{\tan(\alpha_1 - \alpha_2)} + \cos \alpha_2 \end{bmatrix} \cdot \begin{Bmatrix} u_2 \\ u_1 \\ u_3 \end{Bmatrix} \begin{matrix} u_{green} \\ \leftarrow u_{blue} \\ u_{purple} \end{matrix} \quad (36)$$

Referring to Figure 3.10, for this LDA setup,  $\alpha_1 = 21.32^\circ$  and  $\alpha_2 = 6.78^\circ$ . Substituting these values into the transformation matrix above yields the following:

$$\begin{bmatrix} 0 & 1 & 0 \\ -3.95427 & 0 & 3.70954 \\ -0.46998 & 0 & 1.44793 \end{bmatrix} \quad (37)$$

At the front end of each of the probes, the laser beams are expanded to be further apart (and a greater beam diameter), thereby inducing a larger separation angle  $\theta$  between them. This is achieved using an optical device called a beam expander and is done for a few reasons. The first is to maximise the detector's ability to collect scattered light by having a larger collection area for the scattered light. The beam expander, by virtue of the greater angle  $\theta$ , reduces the size on the measurement volume which increases the intensity of the light in the volume. The larger angle also produces more light fringes in the measurement volume. The processor calculates the Doppler frequency based on the various pulses it receives from the particle as it travels through the light fringes (one period per pulse of scattered light). The more fringes the particle passes through, the more accurately the processor can calculate the particle's velocity. It can be shown that the number of fringes across the measurement volume is given by

$$N_f = \frac{d_w \tan(\theta/2)}{\lambda} \quad (38)$$

where  $d_w$  is the beam waist or the diameter of the laser at its narrowest point, which is deliberately positioned at the measurement volume. This value may be determined from the following equation:

$$d_w = \frac{4l_f \lambda}{\pi d_i} \quad (39)$$

where  $d_i$  is the diameter of the laser as it leaves the laser probe (which is 2.2 mm for the current LDA system) and  $l_f$  is the focal length of the laser beams (the perpendicular distance

from the laser probe to the measurement volume, which is 500 mm in this case). The waist diameter for each colour laser in the LDA system is thus;  $d_{w-green} = 148.8 \mu\text{m}$ ,  $d_{w-blue} = 141.2 \mu\text{m}$  and  $d_{w-purple} = 137.9 \mu\text{m}$ .

Thus, substituting Eqn. 39 into Eqn. 38, the number of fringes may be calculated as follows:

$$N_f = \frac{4l_f \tan(\theta/2)}{\pi d_i} \quad (40)$$

Thus, for the current LDA system,  $d_i = 2.2 \text{ mm}$ ,  $l_f = 500 \text{ mm}$  and  $\theta = 9.15^\circ$ , which yields  $N_f = 23$  at the widest point of the measurement volume, for all laser colours.

The LDA probes were mounted on a Dantec 41T333 three-axis traverse which allowed positioning of the measurement volume to a precision of 0.01 mm. The coordinates of all the points to be measured are typically entered into the control software and, during operation, the system will collect the required amount of velocity measurements at a point, the traverse will move to the next location and the system will pause for 1.0 s before new measurements are taken to allow for the damping of any transient vibrations.

The seeding required for the LDA system must represent the velocity of the flow field. As such, the seeding particle must be small enough so that it follows the direction of local flow field – it will be swept along by the flow. However, the particle is also required to scatter as much light as possible back toward the receiver in order to achieve the best possible signal to noise ratio for the signal processor. The seeding employed throughout this project was atomised vegetable oil on the order of  $1 \mu\text{m}$  in diameter. Various seeding methods were tested by Coray (2005) during the development of the PIV system for this wind tunnel and the atomised vegetable oil solution was found to be the most effective. Given the similarity between the operating principles of PIV and LDA systems, the same seeding solution has since been utilised also for the LDA system.

### 3.3.3 Sources of Error

The sources of error encountered with an LDA system fall into one of the following three categories; velocity bias, statistical uncertainty of the measurements and beam-waist misalignment.

Velocity bias comes about because the detector sees a larger proportion of fast travelling particles than it ought. Of a theoretical flow field with 50 % slow-moving particles and 50 % fast moving-particles, a correct mean velocity would be calculated based taking the same number of measurements of each speed of particle. However, because one is moving faster than the other, more particles of that speed will pass through the measurement volume in a

given period of time, thus biasing the mean velocity calculation toward a higher, incorrect value. This bias is taken account of in LDA system software by multiplying each velocity measurement  $u_i$  by a weighting factor  $\eta_i$  which is defined as

$$\eta_i = \frac{t_i}{\sum_{j=0}^{N-1} t_j} \quad (41)$$

where  $t_i$  is the transit time of the  $i^{\text{th}}$  particle – the time taken for it to travel through the measurement volume – and the denominator is the summation of all the transit times for all  $N$  particles measured. The mean velocity is then calculated thus:

$$\bar{u} = \sum_{i=0}^{N-1} \eta_i u_i \quad (42)$$

The LDA software assumes that the quantities being measured are normally distributed and thus calculates a statistical confidence error for the mean and root-mean-squared (RMS) velocities, which was developed by Benedict and Gould (1996). For a 95 % confidence level in the mean and RMS velocity components, the following two equations are applied, respectively, in order to obtain the uncertainty of those values in units of m/s.

$$\begin{aligned} \text{Mean velocity} &= \pm 1.96 \times \sqrt{\frac{u^2}{N}} \\ \text{RMS velocity} &= \pm 1.96 \times \sqrt{\frac{u^2}{2N}} \end{aligned} \quad (43)$$

Finally, if the beam waist is not properly located on the measurement volume, the beam will be expanding or contracting (depending on where the beam waist is) as it passes through the measurement volume. Consequently, the incident wave fronts from the beam will not be flat and will not be normal to the beam direction in the measurement volume. This means that the light fringes in the measurement volume will be curved and thus will not be a consistent distance apart. The software assumes the fringes are a consistent distance apart, and so will incorrectly measure the velocity of any particle that passes through fringes that do not have the correct separation distance. It is important, therefore, to ensure that the beam waist is located in the measurement volume for both lasers in a probe.

However, due to the importance of maximising the beam intensity in the measurement volume (which is another reason why the beam waist is located there), if the beam waist is not located correctly, one is not likely to generate an acceptable data-rate anyway. Therefore, any properly functioning system will have mitigated this potential error.

### 3.4 CFD Validation Experiment

The LDA technique described in Sec. 3.3 was used to undertake two experiments whose purpose was to validate the numerical model developed for use in Chapter 7. The validation of this model, using the resulting data from this experimental work, is discussed in detail in Chapter 6 and, therefore, most results will not be presented here. Rather, the remainder of this chapter will deal primarily with how the results were obtained.

#### 3.4.1 Velocity and Boundary Layer Profiles

Given that the primary purpose of the investigation in Chapter 7 is to observe the onset of flow separation, the most important characteristic of the flow that the numerical model must demonstrate an ability to predict is the boundary layer behaviour. Additionally, given this flow field features large adverse pressure gradients, correctly modelling the flow field behaviour further away from the surface of the aerofoil is also of significant importance.

As such, velocity profiles through the flow field and also through the boundary layer were obtained from the experimental setup through a series of vertical LDA sweeps on the spanwise mid-plane of the wind tunnel. The LDA sweeps are shown in Figure 3.11.

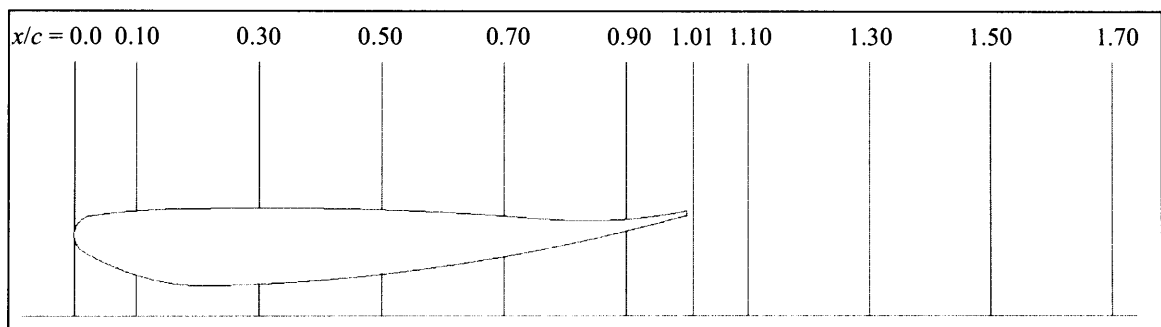


Figure 3.11: LDA velocity profile sweeps,  $h/c = 0.05$ ,  $\alpha = 2^\circ$

The sweeps in Figure 3.11 extend to the ground plane, however, due to the alignment of the lasers and the geometry of the aerofoil, measuring underneath the aerofoil ( $x/c = 0.0, 0.1, 0.3, 0.5, 0.7$  and  $0.9$ ) was impossible. Additionally, the LDA was only able to measure slightly below the trailing edge height at  $x/c = 1.01$ , as the upstream blue incident laser eventually intercepts the trailing edge preventing any further measurement. All downstream LDA sweeps ( $x/c = 1.1, 1.3, 1.5$  and  $1.7$ ) were able to record data almost all the way down to the moving ground plane. As the reflections from the moving ground belt are quite strong at extremely low clearances (within about 1 mm of the belt) the intensity of the reflections into the receiver optic was too strong to operate without risk of damaging the system. This problem was not apparent with the anodised aluminium wing which, subject to sufficient seeding, allowed measurements all the way down to the surface of the wing.

The geometry chosen for the experiment was an extremely low clearance of  $h/c = 0.05$  where the ground effect phenomenon is at its peak strength. A model validated in this configuration should be able, therefore, to simulate configurations down to this extremely low clearance. The angle of attack was chosen to be  $\alpha = 2^\circ$ , which was chosen primarily because a larger angle of attack would induce larger turbulent fluctuations in the wake flow which would require a longer solution time in CFD to obtain statistically-steady flow.

The sweeps were taken at the spanwise mid-plane of the tunnel as only the quasi-two-dimensional flow field was of interest. This is the case for two reasons. Firstly, the flow situation in the real world obviously would not include the three-dimensional flow features present in this wind-tunnel (wall-wing interference effects). Secondly, as discussed in Sec. 4.3, the CFD models that were compared with this experiment did not simulate the three-dimensional flow present at the side-walls of the tunnel as they utilised the more computationally efficient ‘sliver’ model, which features periodic side-wall boundary conditions. The rationale behind the use of periodic boundary conditions is discussed in Sec. 2.8.4. As such, only the quasi-two-dimensional flow at the centre of the tunnel needed to be validated against.

The datum for the traverse system was set to the top edge of the trailing edge of the wing. This point was obtained precisely by moving the measurement volume in increments of 0.01 mm, with the wind tunnel and seeding operational, and finding the location (vertically and horizontally) where the data-rate of the lasers would fall to zero. This was the indicator that the measurement volume had intercepted the wing.

Once the datum had been established, the clearance of the wing could then be very accurately controlled via a similar technique. This was necessary as, while in operation, the moving ground belt was raised slightly from its stationary resting position and this needed to be accounted for. Note that at  $h/c = 0.05$  and with a chord of  $c = 75$  mm, ground clearance  $h = 3.75$  mm. This is quite a small value and so it was very important that the height of the wing from the ground be controlled very precisely. With knowledge of the geometry, the desired distance from the trailing edge to the ground was known and, observing when the data-rate again went to zero, this distance was measured by moving the LDA measurement volume. If this value was, for example, 0.05 mm too small, than the wing needed to be raised 0.05 mm to obtain the correct ground clearance. The measurement volume would then be moved to a position 0.05 mm above the datum and the wing would be very slightly shifted up until the data-rate again went to zero. The clearance was tested once more to confirm the correct value had been achieved.

The sweeps were controlled by entering a spreadsheet with the coordinates of each point to be measured into the control software. The resolution of the measurement points along a sweep was varied with the amount of expected spatial variation in the flow field. In a similar manner to a CFD mesh's spatial resolution, many points are concentrated in the boundary layer (measurement points are only 0.1 mm apart [0.13 % of  $c$ ]) but are much more sparsely separated away from the wing. This extremely fine experimental examination of the boundary layer in the ground effect regime has not been performed before in the literature.

At each measurement location, the LDA control software was set to collect coincident velocity measurements – only those where the same particle has been detected by all three laser probes, thus yielding a full description of the three-dimensional velocity vector at that point in time. Each probe typically detects a great deal more particles than those that are concurrently detected by all three and, thus, the data-rate in coincident mode is usually considerably less than if only single velocity components are sought.

In coincident mode, the data-rate usually varies between 2,000 Hz and 4,000 Hz in good seeding. This value is also dependant on the quality of the alignment of the lasers. As the probes are moved around by the traverse, the lasers slowly become unaligned and the data-rate slowly reduces as the measurement volumes shift apart. This does not affect the accuracy of the gathered data, only the rate at which the data is obtained. Eventually the data-rate falls to a point at which realignment is necessary. The typical data-rate for individual probes is on the order of 30,000-40,000 Hz for the green laser, 15,000-20,000 Hz for the blue laser and 6,000-8,000 Hz for the purple laser.

At each measurement point in this experiment, the time-averaged velocity data was sought and so 5000 coincident measurements were taken at each point to ensure good statistical results before moving onto the next point. At the coincident data-rate mentioned above, each point typically took between 1.25-2.5 seconds. However, in the boundary layer and in the wing's wake, the concentration of the seeding particles reduces quite dramatically, and the data-rate can reduce to as low as about 250 Hz which would take 20 s to record all 5000 measurements. In extremely poor data-rate situations, the system cannot be allowed to sit in one location indefinitely, very slowly collecting data, and so a limit of 30 s was imposed on the data-collection period at each location. This limit was almost never needed during the experiment, however.

The measurement locations specified in the spreadsheet did not cover the whole boundary layer sweep as much care needs to be taken when measuring very close to a solid surface. These near-wall measurements were conducted manually while closely observing the anode

current on the photo-collector, where the detected scattered light signal is directed and converted from a light signal into an electrical signal. If too much light is scattered to the detector, the anode current may exceed its safe operating range and damage the photo-collector. This problem is caused when laser reflections from a solid surface increase the noise in the detected signal. This problem is mitigated by employing a matte black surface finish on the wing surface but this does not completely eliminate the problem. Consequently, when the anode current starts to exceed the safe operating range, the input power of the laser is reduced so that this current is returned to a safe operating condition. The downside of the reducing the laser power is a reduction in data-rate and so this is only performed when necessary.

To demonstrate that the wind tunnel achieves an adequately uniform velocity distribution upstream of the wing, a vertical LDA sweep was conducted at  $x/c = -1.0$  and the results are shown below in Figure 3.12. The streamwise x-velocity component achieves a value close to 10 m/s for most of the clearance except near the ground where it falls before it reaches 10 m/s at the ground (not captured). This dip is probably the remainder of the boundary layer from the tunnel floor upstream of the moving ground.

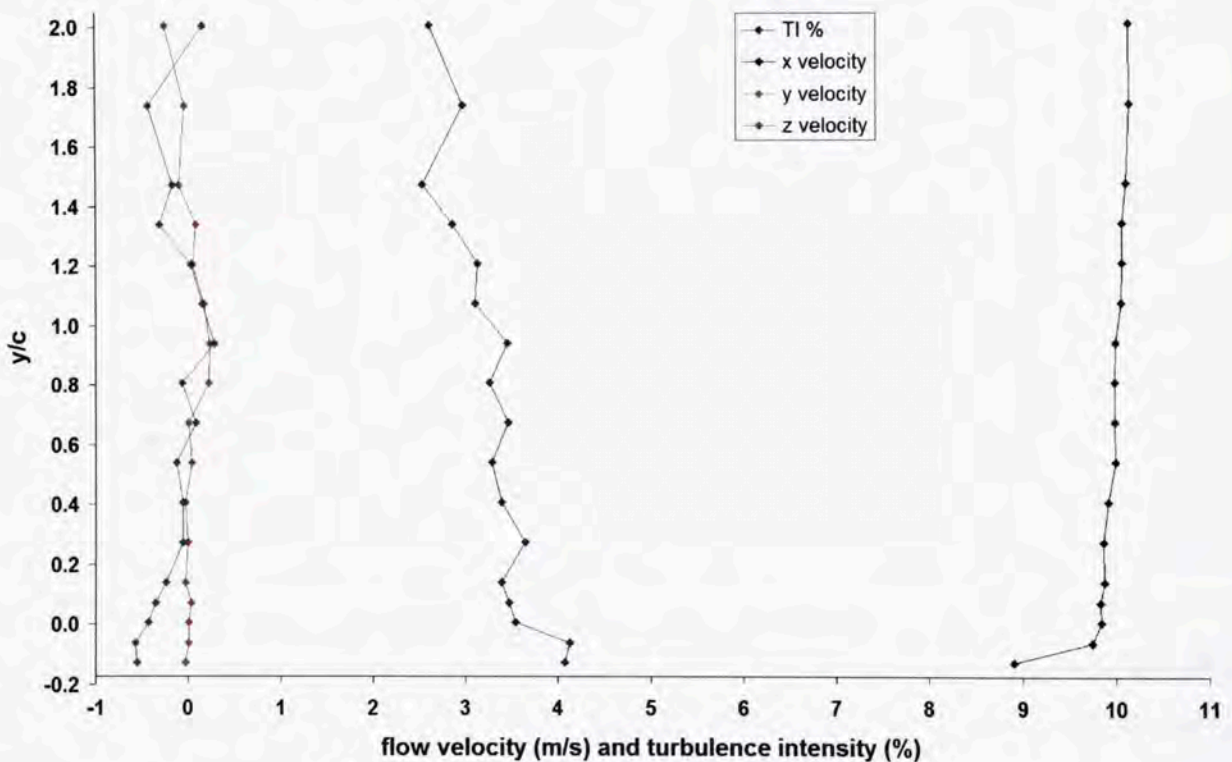


Figure 3.12: Wind tunnel input velocity profile

The vertical y-velocity and the spanwise z-velocity components are both quite close to zero, though the z-velocity does indicate a slight cross-flow in the tunnel. The turbulence intensity increases as it starts to interact with the seeding in the lower reaches of the sweep. The TI

also increases when very close to the ground – this is due to the ground belt moving up and down slightly while in operation. The average TI value from the sweep is 3.3 %.

The relevant data obtained from the LDA measurements were:

- Position of measurement location
- Time of start of data collection
- Number of measurements taken
- Validation rate of measurements
- Mean x-, y- and z-velocity components
- RMS x-, y- and z-velocity component fluctuations
- 95 % confidence uncertainties in mean and RMS velocity components

An example plot of the experimental data for mean x-velocity is shown below in Figure 3.13.

A full exposition of the experimental data may be found in Chapter 6.

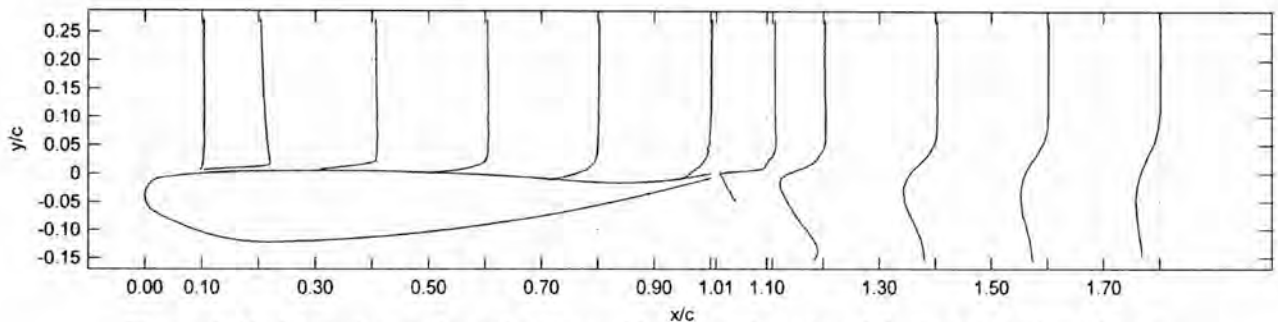


**Figure 3.13: Experimental x-velocity profiles at  $x/c$  locations labelled;  $0.1 x/c = 10$  m/s**

### 3.4.2 Frequency Analysis

A useful tool in demonstrating whether a numerical model accurately represents turbulent flow behaviour is to conduct a frequency analysis of the turbulent flow field. Such an analysis was undertaken in the wind tunnel using the LDA system and this was used to validate numerical models against.

A frequency analysis requires the collection of data of a variable as it changes over time. This data is then transformed, using spectral methods, into the frequency domain which yields a plot of the turbulent energy in the flow field verses the frequency at which it occurs. This technique is discussed and employed in Sec. 6.3. In this experiment, 50,000 readings of the velocity component  $u$  were recorded at five different near-wake locations in the wind tunnel. These locations are presented in Figure 3.14.

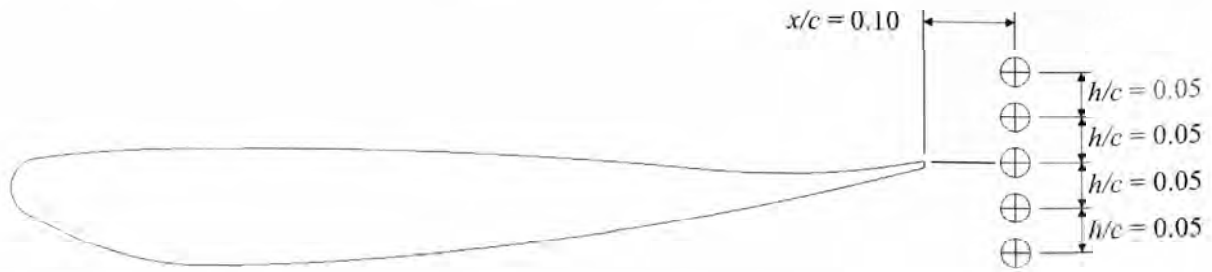


**Figure 3.14: LDA frequency analysis points,  $h/c = 0.05$ ,  $\alpha = 2^\circ$**

50,000 measurements of  $u$ , which is measured directly by the blue laser LDA probe, were recorded in non-coincident mode in order to maximise the data-rate achieved. An average data-rate of 15,000-20,000 Hz was achieved which allowed the data at each point to be collected in no more than 3.5 s.

A high data-rate is required for a frequency analysis in order that the higher frequencies (corresponding to the smaller eddies in the turbulent decay process) are resolved. The turbulent energy decay, which occurs throughout a range of relatively high frequencies, is of critical importance in correctly modelling the turbulence in the flow, and so the experimental data-rate must be maximised.

Consequently, the experimental  $v$  and  $w$  velocity components could not be collected for a frequency analysis as, when running in coincident mode in order to obtain these components through transformation, the data-rates achievable are not high enough. A total of 50,000 data points are required so that sufficient signal information is available such that, when transformed to the frequency domain, the results will represent to true flow behaviour over time. This point is particularly so for low frequency behaviour which needs a greater data-collection time in order to be well resolved in the frequency domain. An example of the raw signal and its transformed Power Spectral Density (PSD) function are shown below in Figure 3.15 and Figure 3.16.

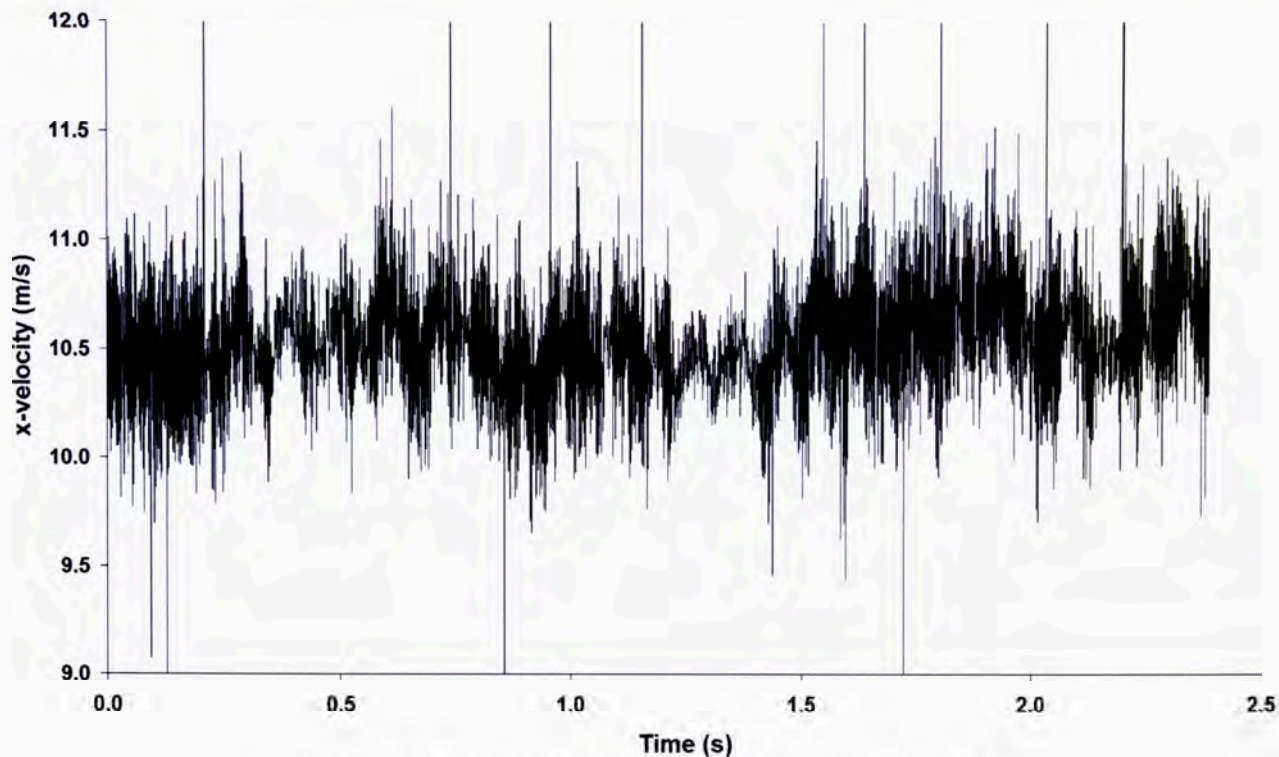


Figure 3.15: Example of raw signal for frequency analysis

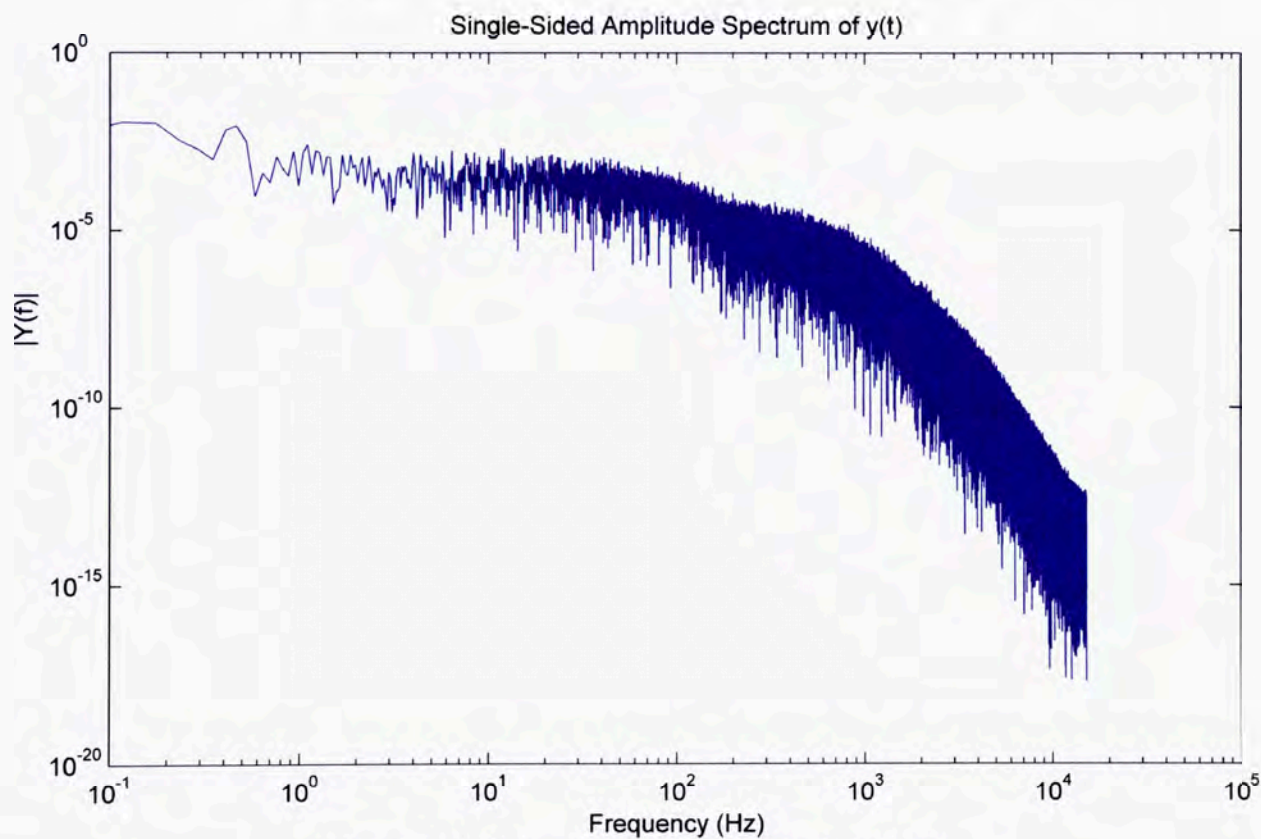


Figure 3.16: Example PSD from frequency analysis

The frequency analysis process will be discussed in more detail in Sec. 6.3.

# Chapter 4: Development and Description of Computational Fluid Dynamics Models

## 4.1 Introduction

This chapter presents the development of two CFD models. The development, verification and validation of a two-dimensional ‘free-air’ model of an aerofoil in ground effect is discussed in Sec. 4.2. The model developed in that section is used for the research project discussed in Chapter 5.

Considered in Sec. 4.3 are the requirements of a model to simulate the quasi-two-dimensional flow over a wing in ground effect. Two general modelling approaches are developed – a large eddy simulation model and pseudo-direct numerical simulation model. This section discusses the development of these models and their verification. The validation of these models is investigated in Chapter 6 where the best performing is selected then applied to the research project in Chapter 7.

## 4.2 Development of Two-Dimensional ‘Free-Air’ Condition Model

A two-dimensional, steady-state RANS model has been developed to simulate the ‘free-air’ condition experienced by bodies operating in ground effect – that is, bodies operating near the ground yet, otherwise, free from the influence of any other boundaries.

### 4.2.1 *Description and Verification of Model*

As mentioned, this model is utilised in two very similar studies discussed in Chapter 5 but it was developed, initially, for the first of those studies (Sec. 5.2). The purpose of the first study was to examine and understand the different ground effect phenomena that occur about a cambered aerofoil in two different configurations – the first in the upright, lift-producing, position and the second in the inverted, downforce-producing, position. The aerofoil is placed at a constant angle of attack of  $6^\circ$  and its height above the ground is varied. The investigation is restricted to the two-dimensional case in order to simplify the study. The aerofoil modelled is the Tyrrell aerofoil which, in its original inverted form, was the cross-section of the main-

plane of the 1998 Tyrrell Formula 1 racing car (Zerihan, 2001). The second study in Chapter 5 (Sec. 5.3) uses the same unaltered model described here but for the different purpose of examining the effect of small changes in aerofoil geometry.

The computational grid was constructed of three primary elements: a structured boundary layer around the surface of the aerofoil and the ground boundary, consisting of 20 rows of expanding thickness with a total height of  $0.031c$  (normal to the boundary surface); a rectangular box surrounding the aerofoil and containing very fine unstructured triangular cells and the remainder of the domain (outside the rectangular box) was composed of structured quadrilateral cells of slowly expanding volume. The unstructured section of the mesh was designed as such to maximise the ease with which the mesh could be adapted when changing the ground clearance of the aerofoil. The mesh was designed to concentrate the cells around the aerofoil and also near the ground.

The structured boundary layer mesh surrounding the aerofoil contained 16,900 cells in total. This value is quite large in order to adequately resolve the boundary layer. The dimensionless wall distance  $y^+$  achieved (in the worst cases) values between 0 and 5 for most of the boundary layer but where the wall shear stress was extremely high at the leading edge, this value was higher. Standard wall functions were employed throughout in view of the sufficiently low  $y^+$  values achieved.

Grid convergence was assessed by constructing two new grids with varying refinements that are otherwise identical to the baseline case discussed thus far; a coarse grid with approximately half the number of cells of the 365,000 cell baseline case, at 184,000; and a fine grid with roughly double the cells of the baseline case at 682,000. The grid structure (including the boundary layer mesh) was refined or coarsened proportionally to achieve the new grids. The coarse grid generated  $C_l$  and  $C_d$  values that were in very close agreement with the standard mesh. The  $C_l$  value for the coarse mesh exceeded that of the standard mesh by 1.052 % and the  $C_d$  exceeded the standard mesh value by only 0.112 %. The fine mesh presented very similar results with the  $C_l$  value exceeding the baseline case by only 0.014 % and the  $C_d$  value also exceeding the baseline case by 0.078 %. These results are summarised in Table 4.1. These very consistent results indicated that the performance of the simulation varied little with changing grid refinement about the baseline case. Despite achieving good agreement with even the coarse grid, as it was feasible to do so with the resources available, the baseline grid was retained so as to more accurately resolve the flow features of the more extreme geometries under investigation (low  $h/c$  cases).

**Table 4.1: Grid convergence comparison of  $C_l$  and  $C_d$  values for coarse, baseline and fine grids**

Grid (cells)	Drag coefficient, $C_d$	Lift coefficient, $C_l$
Coarse (184,000)	0.03485	-1.4514
Baseline (365,000)	0.03481	-1.4363
Fine (682,000)	0.03508	-1.4365

The inlet, outlet and upper boundaries were all positioned away from the aerofoil at values of  $+15c$ ,  $+20c$  and  $+15c$ , respectively. The upper boundary was designated a symmetry plane which specified no fluxes (of any variable) across the top boundary, thus ensuring a physically representative horizontal vector field at the upper boundary. The model's sensitivity to the displacement of the symmetry boundary condition was examined by increasing the distance to the upper symmetry boundary from  $15c$  to  $25c$  – all other boundaries were held constant. This new model with a further displaced symmetry boundary yielded a 0.011 % increase in  $C_d$  and 0.028 % decrease in  $C_l$ . These numbers indicate that the model is not sensitive to the symmetry boundary location and the baseline symmetry boundary position was, therefore, considered boundary-location independent.

For the various ground clearances modelled, the ground plane was moved below the aerofoil to accommodate the change in ground clearances between the extremes to be simulated of  $h/c = 0.03$  and 3.00. The turbulence intensity value was set to 0.1 % because the free-air condition ordinarily features very minimal turbulence at ground level as, in the absence of wind gusts, the flow is completely stationary. Given the fine resolution of the model, it was thought that flow transition to turbulence would be adequately captured by the simulation without the use of a specific transition model and so one is not utilised.

Boundary independence was assessed by testing a model with all boundaries (except the ground) extended by a further 5 chord lengths away from the aerofoil (inlet  $+20c$ , outlet  $+25c$  and upper boundary  $+20c$ ). In comparison to this extended boundary case, the baseline model, with the aerofoil positioned at  $h/c = 0.20$ , saw an insignificant 0.034 % increase in  $C_n$  and a 0.051 % increase in  $C_d$ . The standard model was thus deemed sufficiently boundary independent.

The mesh size ranges from 246,000 cells at  $h/c = 0.03$  to 854,000 cells at  $h/c = 3.00$ . This large increase is due to the high concentration of cells in the additional space under the aerofoil (and also upstream and downstream of this location) at higher clearances. The concentration of cells in the boundary layer remained constant. A typical mesh, in the immediate vicinity of the aerofoil, is shown in Figure 4.1.

All simulations were conducted using an implicit, steady, RANS solver utilising double-precision accuracy. The QUICK discretisation scheme was used for all flow variables and

turbulent quantities in order to best minimise numerical diffusion. The SIMPLEC pressure-velocity coupling was employed for all cases, as was the RSM turbulent closure model.

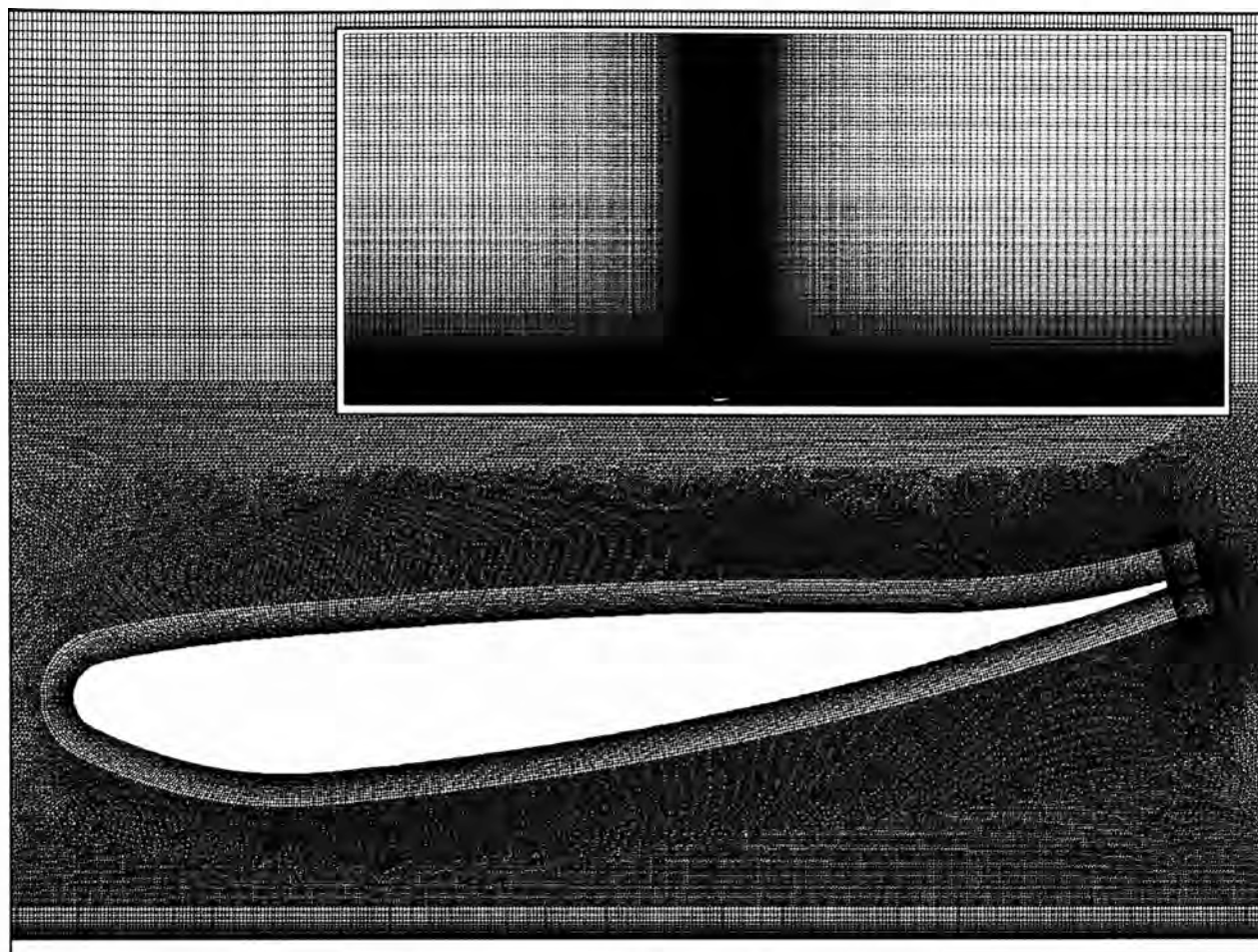


Figure 4.1: Mesh structure about inverted Tyrrell aerofoil,  $h/c = 0.15$ ,  $\alpha = 6^\circ$  (inset) entire domain mesh

#### 4.2.2 Validation of Model

The numerical model was intended to reproduce the experimental conditions from which the data in Mahon and Zhang (2005) were obtained. This was done such that the numerical model could be validated against this data and be used for a ground effect analysis. This data was chosen for three reasons: firstly, it was a moving-ground ground effect experiment employing the correct ground representation method (Barber, Leonardi and Archer, 2002); secondly, the experiment featured a highly cambered inverted aerofoil that was specifically designed to exploit ground effect phenomena and finally, although not achieving a Re of a racing car wing in service, this was the highest Re of any such study performed and is typically about 20% greater than the Re achieved by Formula One teams in their own wind tunnels (Zerihan and Zhang, 2000).

The validation model was created to simulate a two-dimensional mid-plane cut of the wind tunnel facility used by Mahon and Zhang (2005). The Tyrrell aerofoil, with a chord  $c = 0.2234$  m was placed at a clearance of  $h/c = 0.224$  and angle of attack,  $\alpha = 3.6^\circ$ . The boundaries were located to replicate the wind tunnel conditions with the upper boundary

defined as a no-slip wall  $6.78c$  above the ground plane and the ground plane was defined as a moving no-slip wall with a velocity of 30 m/s (the freestream value). Mahon and Zhang (2005) did not specify where the wing was placed in the test-section of their tunnel for their experiments but the entire length of the test-section, at 3.4 m, was known from Zerihan (2001). A location for the aerofoil of 1.0 m downstream of the start of the test section was deemed reasonable and thus the inlet was located  $4.47c$  upstream and the outlet  $9.74c$  downstream of the trailing edge. The surface of the aerofoil was set to a no-slip wall. With the ground moving at the same velocity as the freestream air, there will be no boundary layer development thus the velocity profile will be constant at the inlet. A freestream value of 30 m/s and an inlet TI of 0.3 % was set, which corresponded to that of the experiment of Mahon and Zhang (2005). The velocity outlet was modelled as an outflow boundary condition which extrapolates the flow properties at the exit boundary from the interior of the grid.

Simulations were conducted using this mesh to validate the model's ability to adequately predict the two-dimensional flow behaviour about this aerofoil. The Reynolds Stress turbulence model (RSM), standard  $k-\varepsilon$ ,  $k-\varepsilon$  realisable and  $k-\varepsilon$  RNG models were tested with regard to their ability to simulate the flow around these highly cambered aerofoils. The RSM model produced an excellent, and superior, match to the experimental data, both in terms of pressure coefficient ( $C_p$ ) plots and near-field velocity-deficit wake readings, at  $x/c = 1.2$ , and was used for all cases.

When compared against the experimental and computational  $C_p$  results presented in Mahon and Zhang (2005), see Figure 4.2(a), the present validation model agrees with the experimental results extremely well. It should be noted that the suction spike near the leading edge, identified in both sets of CFD results, is not well represented by the experimental data in Figure 4.2(a). However, the experimental work in Zhang and Zerihan (2003b), using the same aerofoil (but now with a flap), has more pressure tapings in the region  $0.00 < x/c < 0.03$  (Zerihan, 2001) and thus clearly identifies the leading edge spike – albeit a stronger one due to the additional under-wing suction from the flap.

Similarly, with regard to the near-field velocity-deficit wake readings, see Figure 4.2(b), the present work's agreement with the experimental results is excellent. The sectional lift coefficient for the experimental case, integrated over the pressure tapings (Zerihan, 2001), was reported in Mahon and Zhang (2005) to be about  $C_l = 1.4$ . The lift coefficient obtained in the present validation study was  $C_l = 1.43$  which is in close agreement with the experimental case. No sectional drag coefficients were reported but the very good agreement in the near-field velocity-deficit data suggest that the drag values should be in reasonable agreement.

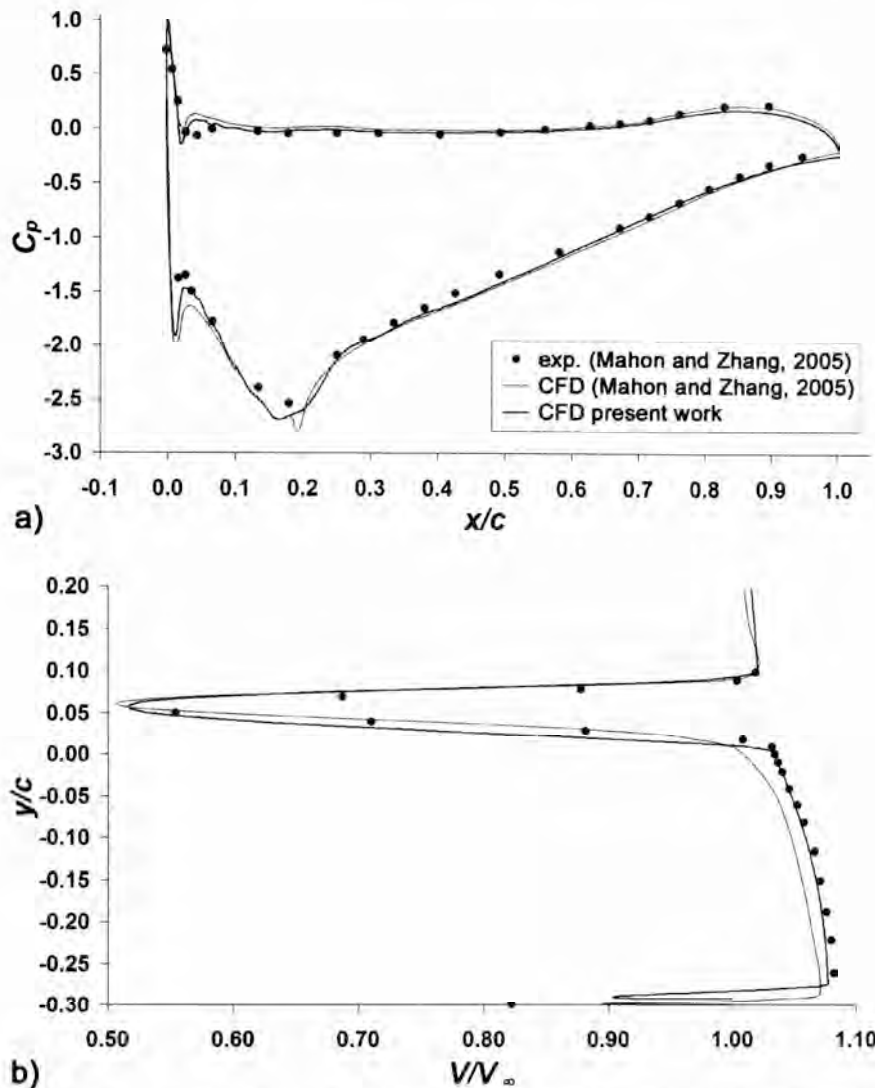


Figure 4.2: Validation case; (a)  $C_p$  plot for  $h/c = 0.224$ , (b) velocity deficit in wake flow at  $x/c = 1.2$

The good performance of the model in the validation process allows the model to be used to examine ground effect behaviour in Chapter 5 with confidence.

### 4.3 Development of Quasi-Two-Dimensional Wind Tunnel Condition Models

Unlike Sec. 4.2, which concerned only one model, this section of work concerns the development of two separate numerical models for the purpose of determining which is most adept at simulating the quasi-two-dimensional flow in the School's moving ground wind tunnel. The most effective model of those discussed in this section, determined by comparisons to the validation wind tunnel experiments (Chapter 6), was used for a definitive quasi-two-dimensional examination of the onset of flow separation, which is discussed in Chapter 7.

For an understanding of the physical system that these models are intended to simulate, the reader is referred to Sec. 3.2, where the wind tunnel facility is discussed, and Sec. 3.4 where the validation experiment is explained in detail.

In summary however, the models developed in this section are intended to model a low speed, moving ground wind tunnel. A model of the Tyrrell wing was installed across the entire test-section, from wall to wall, so as to minimise three-dimensionality in the flow field. The geometry of the wind tunnel test section, with the Tyrrell wing installed, is presented in Figure 4.3. The dimensions of the mesh domain are presented in Table 4.2.

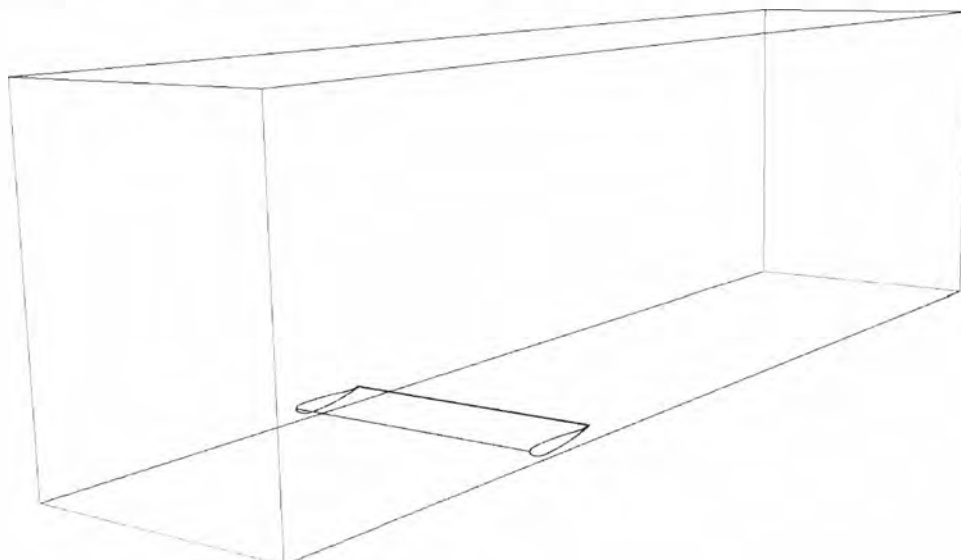


**Figure 4.3: Geometry of wind tunnel test-section to be simulated by numerical models**

**Table 4.2: Boundary locations for three-dimensional numerical model**

Dimension	Distance
Leading edge to inlet	3.40 $x/c$
Trailing edge to outlet	9.20 $x/c$
Floor to ceiling	3.83 $y/c$
Sidewall to sidewall	3.03 $z/c$

It should also be noted that efforts were made to produce as low turbulence as possible within the wind tunnel, which was required for the reproduction of the aerodynamic flow around an inverted aerofoil in ground effect operation. These devices are usually attached to racing cars which move through stationary air that, in the absence of wind gusts, features zero turbulence.

To better understand the flow environment that these numerical models are intended to simulate, a simple flow visualisation experiment was conducted early in the experimental programme using an otherwise identical Tyrrell wing made of transparent acrylic. The spanwise-midplane of the wind tunnel was illuminated with a green laser sheet and the flow was seeded with a smoke machine. Digital photos were taken of the illuminated flow structures about the wing. A summary of this visualisation experiment is shown below in Figure 4.4, for various angles of attack and at clearances of  $h/c = 1.00$  and  $0.05$ .

What is clear from the images in the figure is that for a low ground clearance, even when employing a low angle of attack, the flow is very unsteady and non-periodic in nature. This suggested that a steady-state modelling technique would not be capable of adequately

reproducing this highly turbulent behaviour. Consequently, techniques that are able to more effectively simulate unsteady turbulent behaviour were investigated. The two techniques investigated (and models developed) in the following sections are; a Large Eddy Simulation model and a Pseudo-Direct Numerical Simulation model.

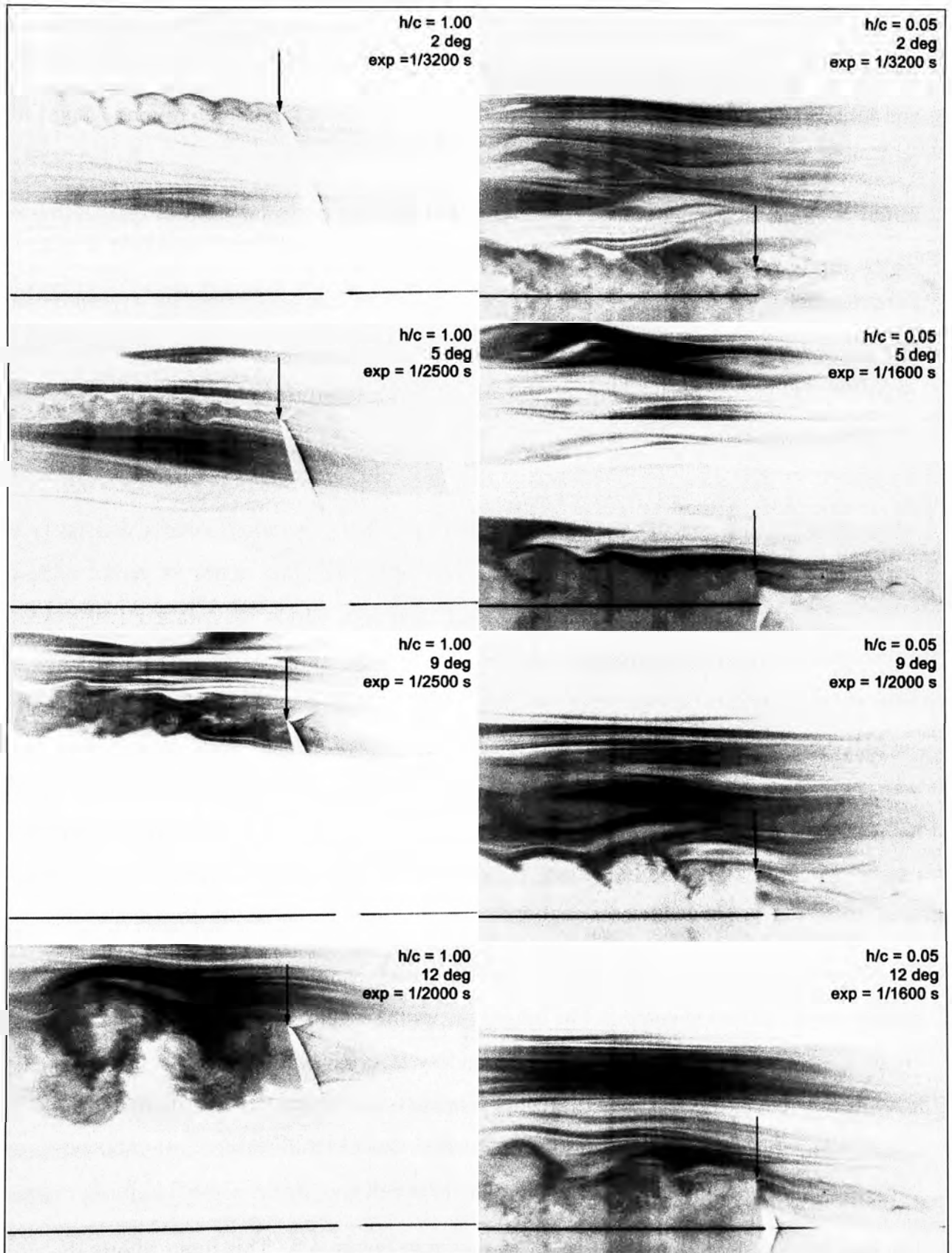


Figure 4.4: Flow visualisation images about Tyrrell wing; arrow indicates trailing edge

### 4.3.1 *Large Eddy Simulation Model*

The verification of the LES model required a large number of test models with slightly varied characteristics, to be simulated and compared. There were limitations placed on this project due to the amount of time a simulation would take to solve, as the simulations were very large. If the computational grid was too fine (the number of cells too large), the job would take too long to solve. Thus, a trade-off between spatial resolution (and potentially, accuracy) and turn-around time had to be made – and this trade-off had to be determined as part of the project.

Initial attempts to generate a grid for the model centred on using the full test-section wind tunnel geometry that is shown in Figure 4.3. These meshes were created using the Harpoon pre-processor by Sharc Ltd. This program allowed the generation of a predominantly structured mesh whose refinement could be controlled (to some extent) by the user. The user specifies the desired refinement in volumes, surfaces and along lines and the program attempts to automatically generate a fully structured mesh that accommodates these requirements.

The advantage of using this software was that the mesh generation process was fairly swift and also the cell size expansion is implemented using hanging nodes (a vertex node on a smaller cell that is situated somewhere other than at a vertex on a larger cell – see cell transitions in Figure 4.5) allowed refinement to be concentrated to the areas of most need. This last advantage was significant as structured meshes generated in programs that do not support hanging nodes require refined mesh regions to propagate out to the grid boundaries, which often massively increases cell counts in regions where a large mesh resolution is not necessary. This is a serious concern for three-dimensional models and models with regions requiring high spatial resolution – this model satisfies both of these criteria.

A significant disadvantage incurred by using Harpoon was an inability to import surface meshes for the Tyrrell wing surface (though Sharc claim otherwise). Consequently, the surface mesh resolution could not be biased across the wing surface. Another disadvantage of the program was that when generating a boundary layer mesh, the total depth of the boundary layer mesh could not exceed the approximate side length of the neighbouring cells. Consequently, any boundary layer mesh generated was too thin and the cell volume transition from the outer boundary layer mesh cell to the next cell was unacceptably (and very) large.

The first mesh generated using harpoon is shown in Figure 4.5. This figure shows the surface mesh generated on the Tyrrell wing and the volume mesh on the spanwise mid-plane cut of the model geometry. This model had 3.4 million cells and did not feature a boundary layer

mesh. As is clear from the image, the mesh refinement away from the wing reduced quickly and initial results showed this model to be highly ineffective at capturing anything other than the largest eddies.

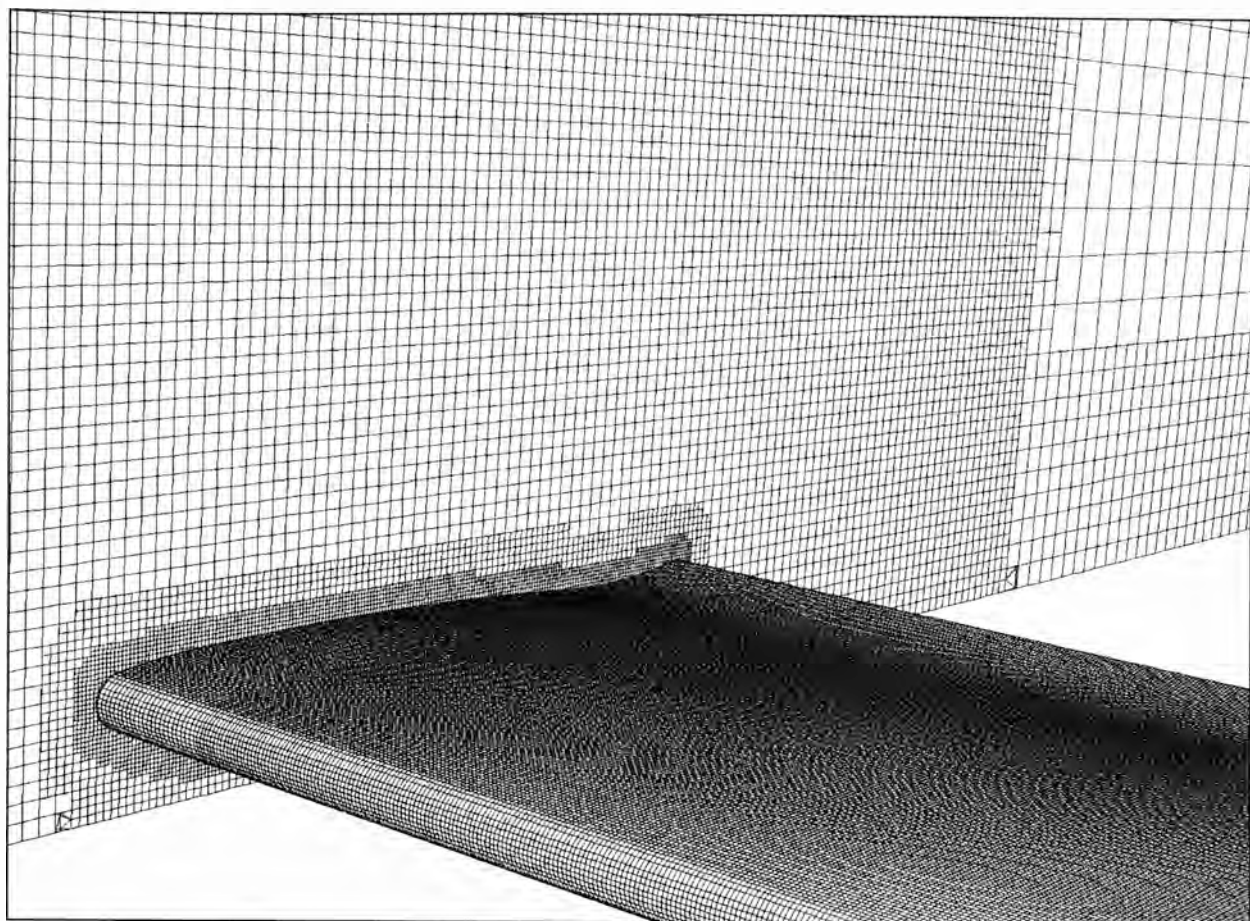


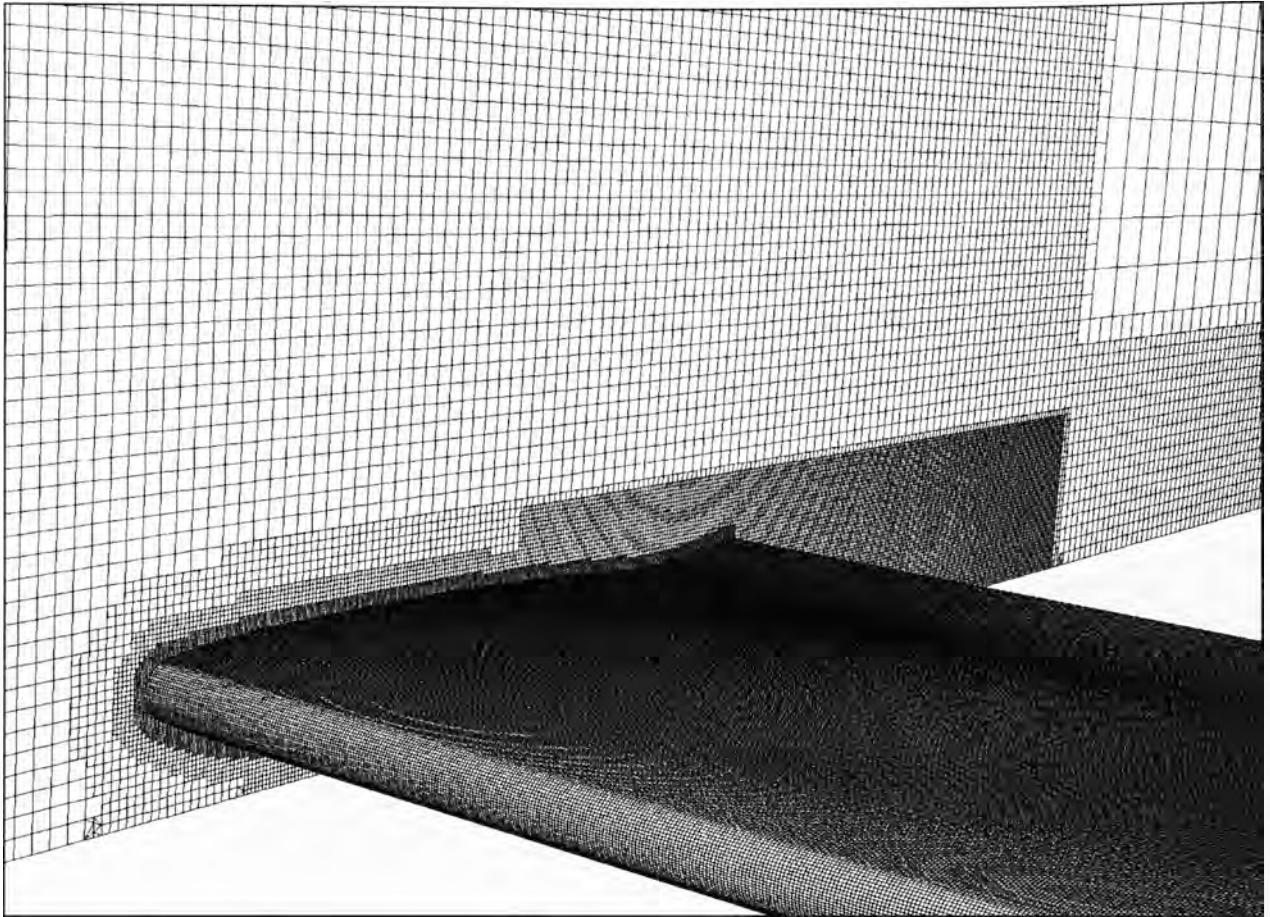
**Figure 4.5: First-generation Harpoon mesh (3.4 million cells)**

A second mesh was developed with the aim of achieving a much greater spatial resolution about the wing in the near wake region so that much smaller eddies may be captured in the flow. This second generation mesh is shown in Figure 4.6. This mesh utilised an additional refinement box region in the very near wake and over the top of the wing and the mesh also employed a further level of refinement about the wing surface. These improvements came at the cost of a significant larger cell count at 14.9 million. This large mesh proved to increase the turn-around time of the simulations to such an extent that it was subsequently deemed unworkable.

An attempt to achieve a trade-off between the two meshes is shown in Figure 4.7. The refinement box in the very near wake region was reduced in refinement and, additionally, a small boundary layer mesh was added to the surface of the wing. The resulting mesh was composed of 13.7 million cells. A brief summary of the three meshes is provided in Table 4.3.

**Table 4.3: Summary of Harpoon meshes**

Harpoon model	Cell count	Comments
Coarse	3.4 million	Baseline case
Intermediate	13.7 million	Improved refinement at wing (incl. boundary layer) and near-wake
Fine	14.9 million	No boundary layer mesh, improved refinement in near wake

**Figure 4.6: Second-generation Harpoon mesh (14.9 million cells)**

The intermediate Harpoon mesh from Table 4.3 was subject to a series of verification evaluations in order to ascertain the appropriate numerical settings for a simulation. As mentioned earlier, the coarse mesh was quickly deemed to be ineffective and the fine mesh was deemed impractically large to solve, particularly as this mesh did not yet include a boundary layer mesh, which was considered very important.

A temporal-dependence study was conducted on the intermediate mesh and the results are presented in Figure 4.8 and Figure 4.9 for  $C_L$  and  $C_D$ , respectively. There are notable differences between the plots of different time-steps and these differences indicate that complete temporal-independence was not achieved even at a time-step as low as  $10^{-5}$  s. (Lower time-steps were not pursued however, as this approach to modelling the wind tunnel was abandoned in favour of the more promising ‘sliver’ approach, which will be discussed shortly.)

A sample of the results obtained from the intermediate model is shown below in Figure 4.10, to demonstrate its spatial inadequacy. The figure shows a comparison between spanwise vorticity contours of the current model and the ‘sliver’ model which was spatially well resolved. The inadequacies of the spatial resolution achieved by the intermediate Harpoon mesh are clear to see. The cause of most alarm, however, was that the refinement box visible in the figure (though, itself, already inadequately refined) terminated well before vortical structures in the wake collapse. It was not possible to extend the refinement box further downstream as the solution time would have been prohibitive. Consequently, a new modelling solution was required.

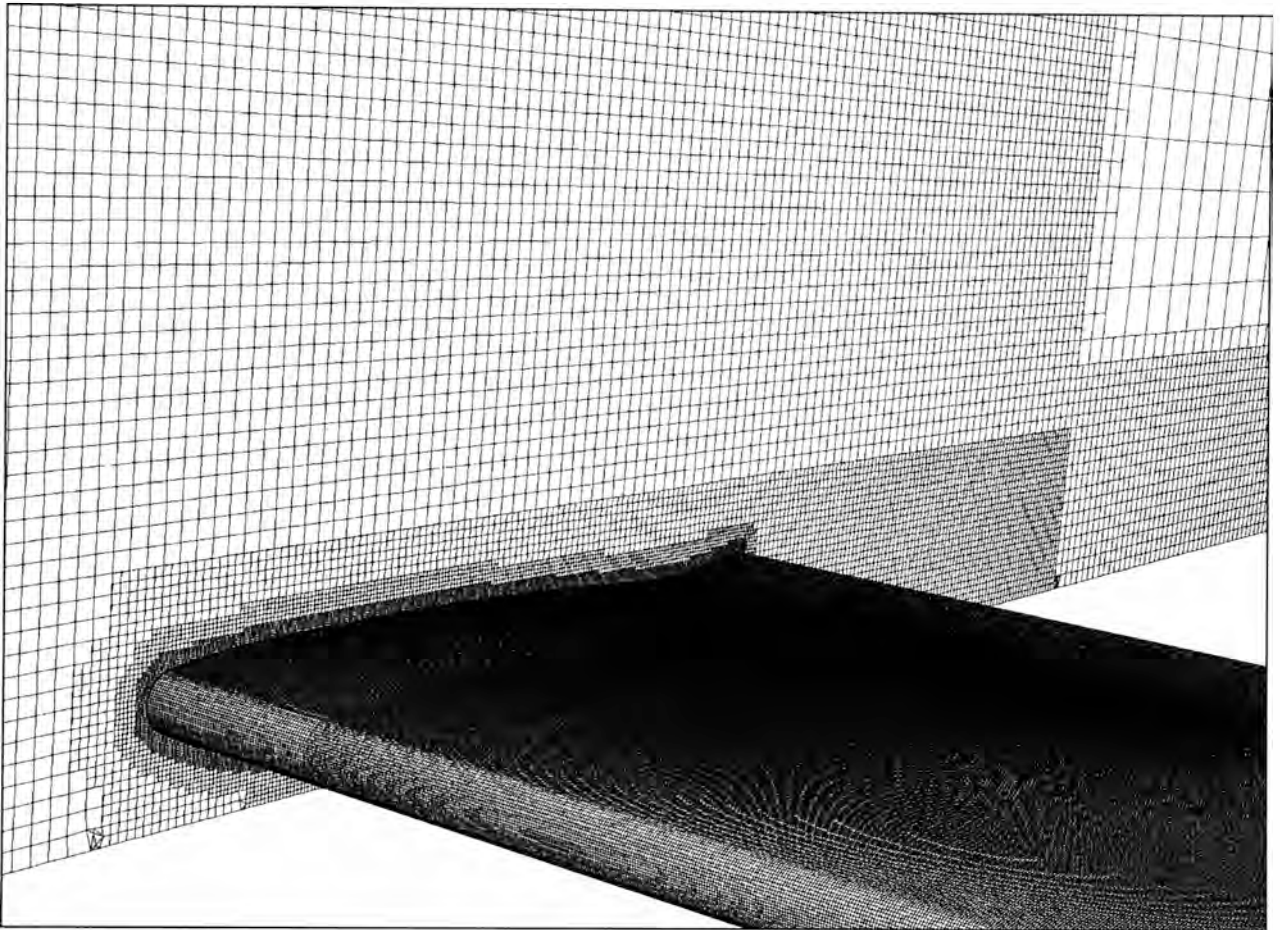


**Figure 4.7: Third-generation Harpoon mesh (13.7 million cells)**

An alternative modelling approach was sought because it became apparent that modelling the full test-section of the wind tunnel, as described thus far in this section, would not provide the desired accuracy, nor would it be able to be solved in a sufficiently timely manner. The ‘sliver’ model employs periodic boundary conditions on spanwise-normal planes near the centre of the wind tunnel in order to create a thin sliver cut of the test section geometry. The geometry is shown below in Figure 4.11.

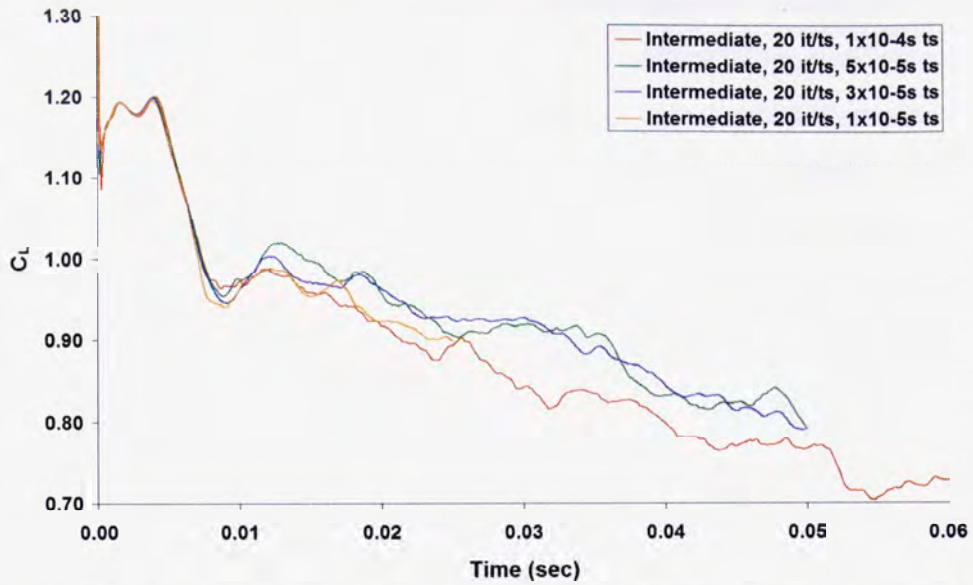


Figure 4.8: Lift coefficient plots of intermediate Harpoon grid at various time-step sizes

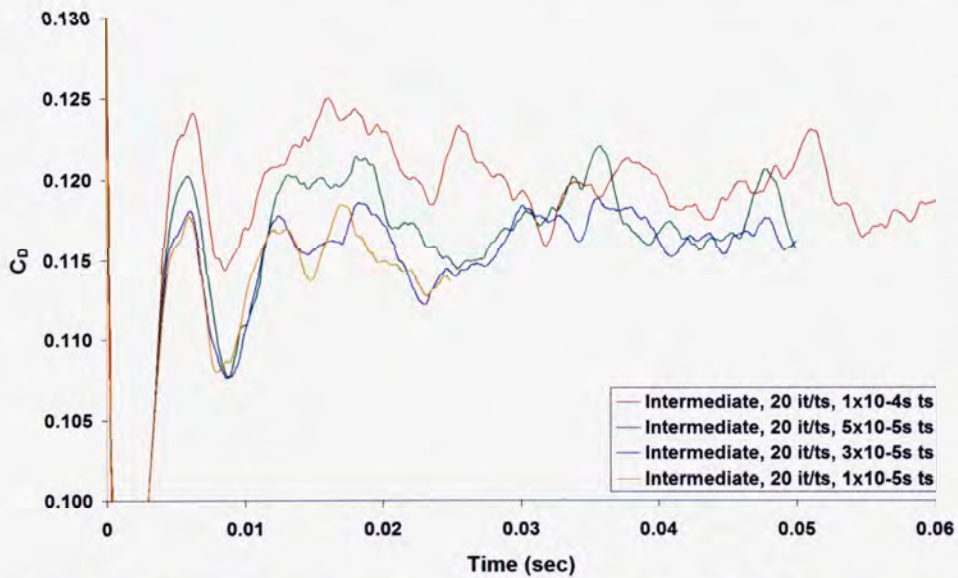


Figure 4.9: Drag coefficient plots of intermediate Harpoon grid at various time-step sizes

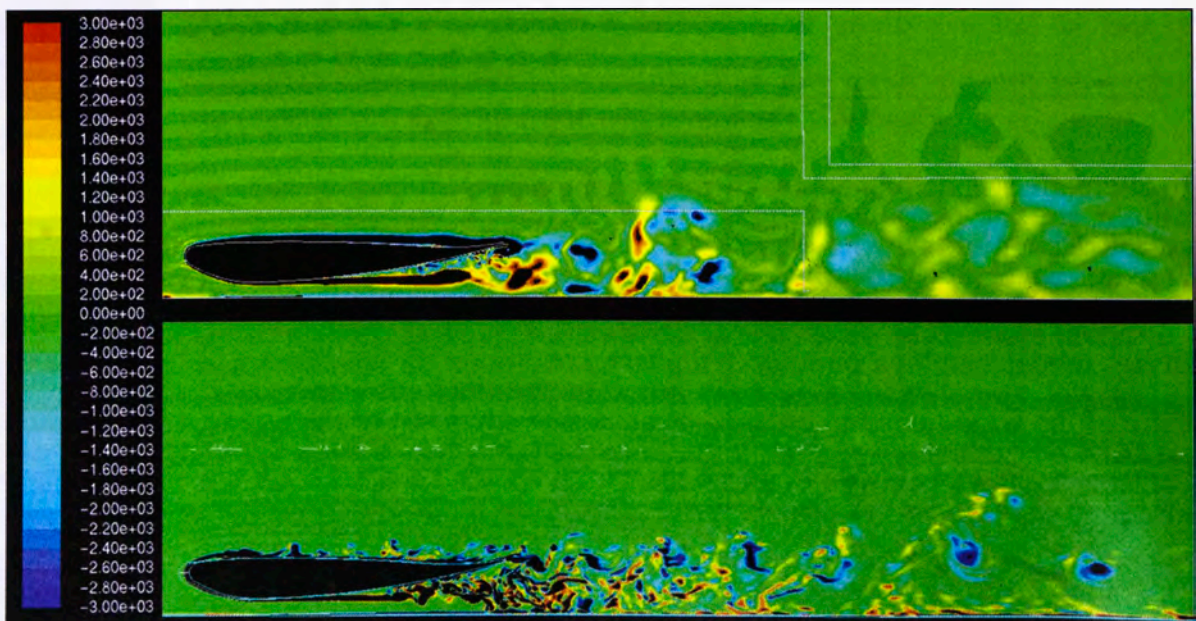
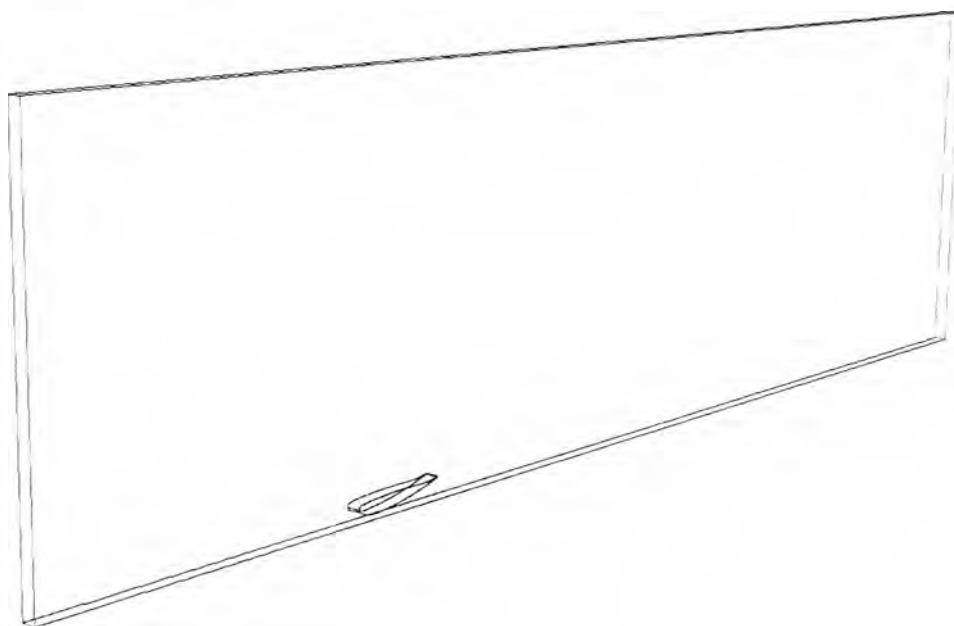


Figure 4.10: Spanwise vorticity contours comparison between intermediate Harpoon mesh and sliver mesh on spanwise midplanes

The literature precedent and justification for the use of such a technique has been discussed earlier in Sec. 2.8.4. The thickness of the sliver model was 10 mm or  $0.133c$ . This value is slightly larger than the  $0.1c$  value used by Shan, Jiang, and Liu (2005) in their DNS evaluation of the turbulent flow over an aerofoil, however, it has been established by Brady, Gaston, and Reizes (2007) and Eisenbach and Friedrich (2008) that the performance of periodic boundary conditions is influenced by the distance between these boundaries and so, care must be taken in their use. In fact, Eisenbach and Friedrich (2008) demonstrated, through the use of periodic boundaries separated by  $1.0c$  for an aerofoil simulation, that a separation of  $0.133c$  as employed in this sliver model, for all cases, will be compromising accuracy to some extent.



**Figure 4.11: Sliver model geometry**

The sliver mesh will be discussed shortly, however, it will be noted here that the total cell count of the sliver model was 5.6 million – 41 % of the size of the intermediate Harpoon mesh developed above.

Table 4.4 summarises the verification tests that were conducted on the sliver model to ensure its adequacy for use. The verification process was not exhaustive as there were insufficient resources to allow such an approach. However, despite only a few tests being conducted, it is still obvious from the results obtained that the adequacy of the model was verified. Each test will be discussed below.

All tests were conducted using the simplest sub-grid turbulence model, the Smagorinsky-Lilly model, SIMPLEC pressure-velocity coupling and the bounded central-differencing discretisation scheme. Further work examining the performance of other sub-grid turbulence

models is discussed later in Chapter 6 where various sliver models based on the one developed here are evaluated against each other and the experimental results.

Additionally, all models employed no velocity perturbations at the inlet and this was done for two reasons: firstly, these aerofoils do not encounter turbulent oncoming air as the air is actually stationary and does not feature turbulence; and secondly, the P-DNS model discussed next in Sec. 4.3.2 requires the use of a laminar solver which precludes the use of inlet turbulence in the numerical settings – thus, if inlet turbulence were specified for the LES models, a direct comparison of the methods would not be possible.

**Table 4.4: Summary of verification of sliver model**

Test	Mesh	Cell count	Time step	Iterations / time step	Notes
1	Sliver	5.6 million	$5 \times 10^{-6}$	20	Periodic boundary results qualitatively realistic; turbulence better resolved*
2	Sliver	5.6 million	$2.5 \times 10^{-6}$	20	Did not improve over test 1
3	Sliver	5.6 million	$5 \times 10^{-6}$	40	Did not improve over test 1
4	Coarse sliver	3 million	$5 \times 10^{-6}$	20	Did not sufficiently capture flow features
5	Fine-span sliver	10 million	$5 \times 10^{-6}$	20	Tangible improvement but insufficient to justify additional computational cost

\* Comparison made to intermediate Harpoon mesh

The solution process for the sliver LES models was quite lengthy. Firstly the model was run for 1200 iterations using a steady-state RANS solver and the simple, but numerically stable,  $k-\epsilon$  turbulence model in order to quickly achieve a ball-park representation of the flow field. The model was then switched to the LES solver and reinitialised with this RANS-determined flow field. This process (which is Fluent's recommended best-practise) does not compromise the overall result and allows one to achieve a developed flow far more quickly than the very slowly developing, time-dependant, LES solver. The model was then run until statistical steadiness was achieved before data-taking was commenced. Statistical steadiness is the point at which the initial (and non-physical) transient behaviour in the model has passed and the model has 'settled' into a quasi-periodic behaviour. This could only be assessed by inspection of the  $C_l$  and  $C_d$  curves. When the quasi-periodic behaviour appears to have been comfortably established, data-taking is commenced, as is show below in Figure 4.12 for the baseline sliver case, test 1.

As shown in the figure, the model was run until the air had flowed over the length of the wing about nine times (0.0675 s of flow time) before it was deemed statistically steady. To reach this point took 13,500 time steps and, with 20 iterations per time step, a total of 270,000 iterations. The metric used on the  $x$ -axis is based on the freestream speed (flow at 10 m/s takes 0.0075 s to travel a chord of 0.075 m) and is used merely for convenience as it allows a better intuitive understanding of how the flow is developing as it travels over the wing.

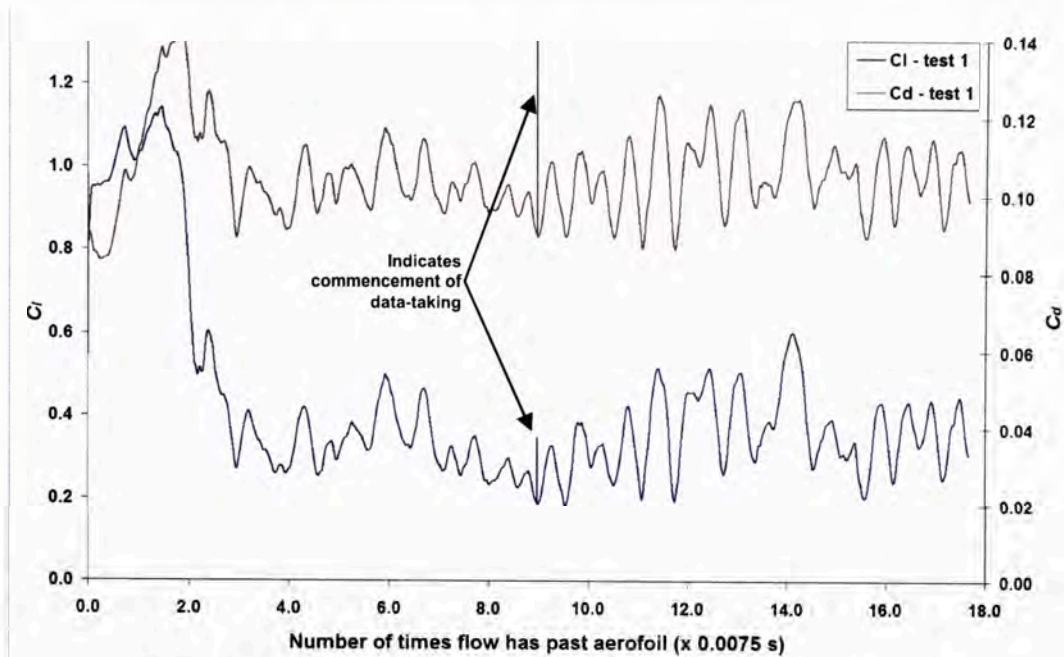


**Figure 4.12: Temporal  $C_l$  and  $C_d$  plot of baseline sliver model, test 1**

At statistical steadiness, data-taking was enabled and the model was run for almost another nine periods of flow past the wing. The total of about 17.5 periods of flow past the wing accounts for 0.13125 s of flow time, 26,250 time steps, 525,000 iterations and, with a timestep typically taking about 2.5 minutes, a total computation time (not including the initial 1200 RANS iterations, file reading/writing or job queue time [which was often multiple days]) of almost 46 days. The simulations were periodically stopped and saved to minimise data loss in the case of system glitches.

The simulations were run on an SGI Altix 4700 machine consisting of 128 dual-core 1.6 GHz CPUs. The computer employed 64-bit architecture and had 1 TB of RAM. Simulations conducted for this project typically used 32 processors, required 20 GB of RAM and were limited to a wall-time of 240 hours, thus requiring a restart every 10 days.

The coarse mesh model and the fine-spanwise model, tests 4 and 5, both followed the same solution procedure as explained above. The half-time step and double iterations per time step models, tests 2 and 3, were commenced from a statistically steady point of the baseline sliver model by simply changing the numerical setting and allowing the model to continue to run. These models were then compared against the trend of the baseline model. This approach saved a great deal of computation time.

Test 1 from the table above was run to establish a baseline model for further verification tests but also to assess the general behaviour and capabilities of the sliver model concept. As has already been shown in Figure 4.10, the much greater spatial resolution of this model allowed it to reproduce the turbulent features in the flow much more finely. It should be noted, however, that the accuracy of this improved turbulent resolution was not at this stage yet

validated. Additionally (but also not yet validated), the periodic boundary conditions appeared to perform very well by producing qualitatively realistic results. Given that the flow field on one spanwise boundary of the model is identical to that of the other spanwise boundary, this did not seem to generate any obviously non-physical results in the flow field, as can be seen in Figure 4.13. In this figure is shown an iso-surface of the magnitude of vorticity and contour plots of spanwise vorticity and instantaneous velocity at the sliver midplane.

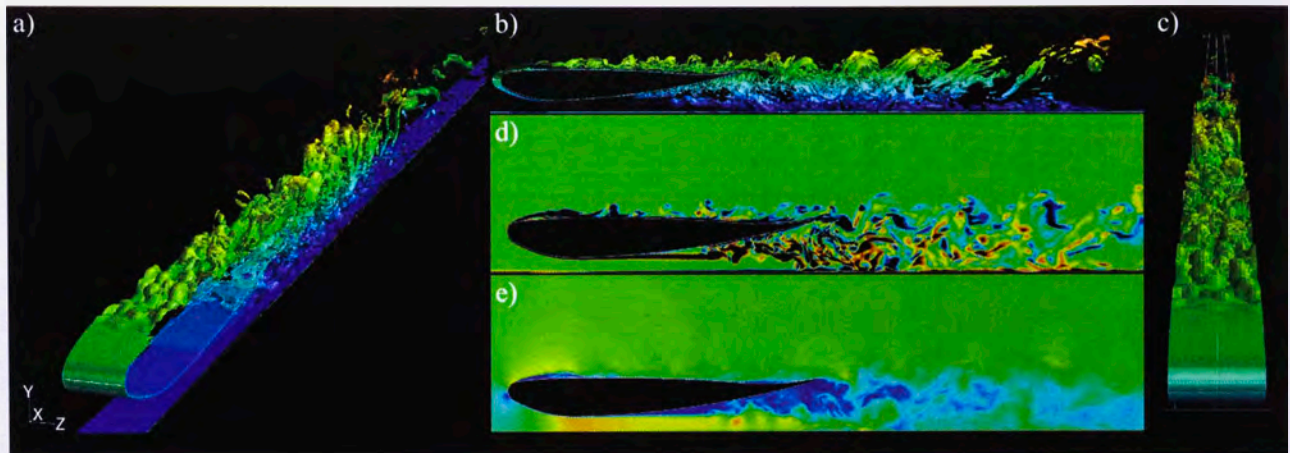


**Figure 4.13: Qualitative results from sliver model test 1; a-c) iso-surface of vorticity magnitude = 3000 /s coloured by vertical position, d) contours of spanwise vorticity at midplane, e) contours of instantaneous velocity magnitude at midplane**

This much smaller mesh allowed an improvement in the temporal resolution over the Harpoon mesh. As was demonstrated in Figure 4.8 and Figure 4.9, temporal resolution was not achieved on the Harpoon mesh with a time step of  $10^{-5}$  s. Two finer time steps –  $5 \times 10^{-6}$  s (test 1) and  $2.5 \times 10^{-6}$  s (test 2) – were assessed for the sliver model. Test 1, with the larger time step, was run until statistical steadiness was achieved – that is, fully developed turbulent flow – and then the two time steps were assessed back-to-back for 1,000 iterations of test 2 (500 iterations of test 1). The  $C_L$  and  $C_D$  results, when plotted in Figure 4.14, show almost no variation at all between the two time steps, as the trends completely overlap. The time step  $5 \times 10^{-6}$  s was adopted and considered to achieve temporal-independence.

Test 3 from Table 4.4 was conducted to determine if an increase in the number of iteration per time step was warranted. A setting of 40 iterations per time step was tested but the result indicated no change in model performance. Thus for all subsequent sliver cases, 20 iterations were used. A typical residual plot is shown in Figure 4.15. After 20 iterations, the worst performing variable, continuity, achieves a residual of about  $10^{-6}$ . All the velocity components are well below  $10^{-8}$  after 20 iterations. The accuracy improvement that can be achieved with additional iterations is extremely minimal and not worth the additional computation time.

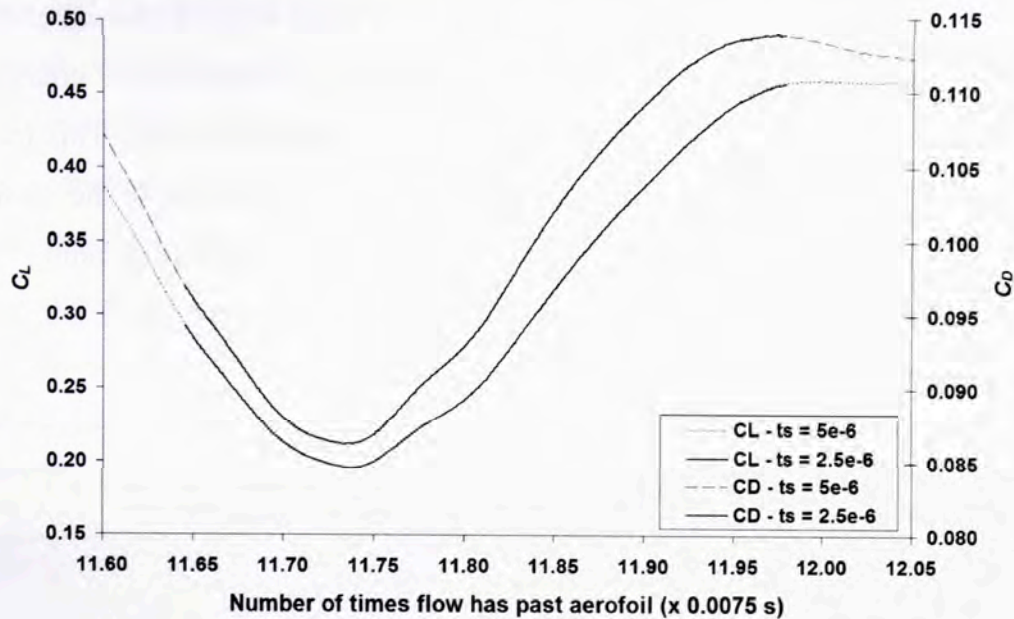


Figure 4.14: Time step size comparison for sliver model (tests 1 and 2)

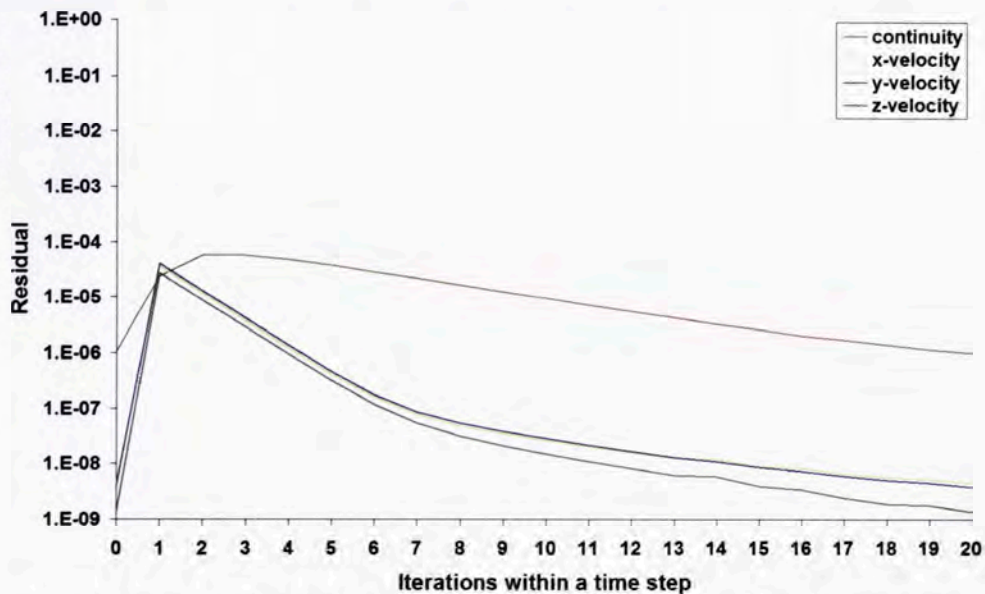


Figure 4.15: Sample residual plot for a single time step of an LES sliver model simulation

The sliver mesh consists of a combination of cell types, both structured and unstructured, in order to facilitate the most efficient use of resources. As has been discussed in Sec. 2.8.6, the use of unstructured cells in CFD analyses is capable of producing accurate results provided a high resolution is employed. A schematic of the sliver model grid structure is presented in Figure 4.16. For clarity, this figure is not to scale. Details regarding the various zones identified in this figure are given in Table 4.5.

All the grids produced for the sliver model were created in Fluent's standard pre-processing package, Gambit. Unlike Harpoon which was used for the full 3D cases, Gambit gives the user very precise control over the makeup and structure of the grid. As shown in Figure 4.16, that capability was used extensively here. Zones A, B, C and D are designed to feature a highly resolved mesh which is well able to resolve the larger turbulent eddies. Zones G, H

and I are of much coarser resolution but are located in areas where turbulent eddies either are not present or should have more-or-less already collapsed. Zones E and F creates a transition between the two sections of mesh by primarily using tetrahedral cells. This transition from fine to coarser mesh also includes a transition in spanwise resolution of the mesh (across the thickness of the sliver) from 20 or 40 cells across on the finer mesh (depending on the model) to 10 cells across in the coarser regions. This transition is presented graphically via an exploded view of the mesh in Figure 4.17.

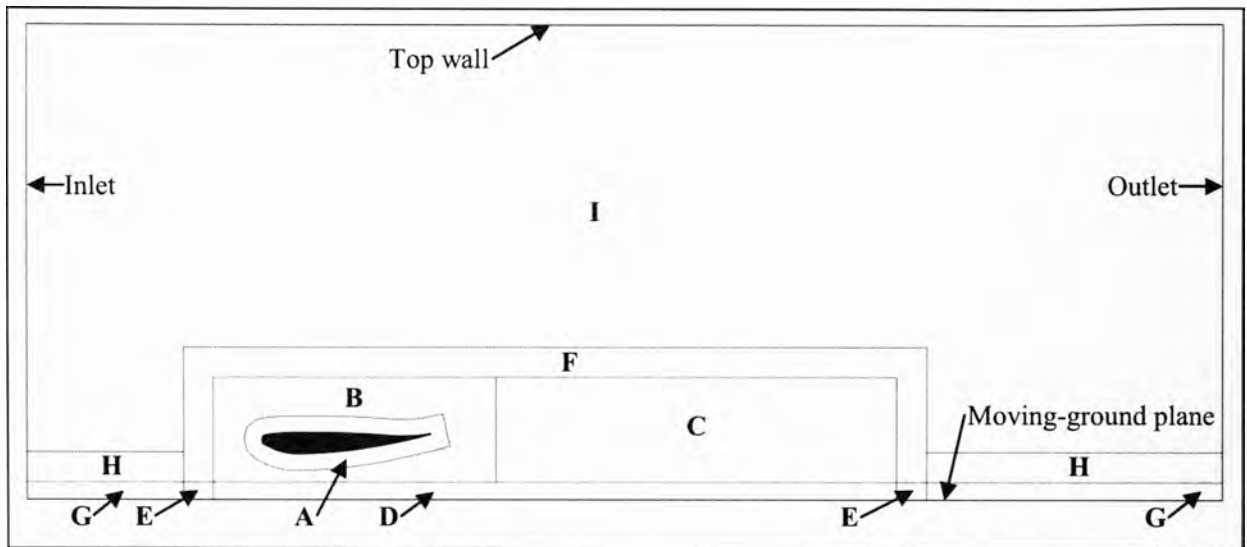


Figure 4.16: Sliver model mesh schematic (not to scale)

Table 4.5: Sliver model mesh zone details

Zone	Structure	Cell type	Note
A	Structured	Hexahedrons	Expanding normally from wing surface
B	Semi-unstructured	Triangular-based prisms (spanwise axis)	
C	Structured	Hexahedrons	Slowly expanding downstream
D	Structured	Hexahedrons	Expanding normally from ground surface
E	Semi-unstructured	Triangular-based prisms (almost vertical axis)	Expanding normally from ground surface and achieves transition*
F	Unstructured	Tetrahedrons and square-based pyramids	Achieves transition*
G	Structured	Hexahedrons	Expanding normally from ground surface
H	Structured	Hexahedrons	Expanding normally from zone G
I	Structured	Hexahedrons	

\* Refers to transition from spanwise grid resolution of 20 or 40 cells down to 10 cells away from wing.

For the baseline sliver mesh, the boundary layer mesh in zone A features 30 cells of expanding thickness with about 800 cells along the surface of the wing, totalling 522,000 cells. The semi-unstructured mesh in zone B is characterised as such because, although it is unstructured in the x- and y-directions, in the z-direction (spanwise), it is structured, as can be seen in Figure 4.17. Zone B has about 2.4 million cells in total (depending on the wing placement). The fully structured mesh in zone C extends the highly refined region of the mesh out to a total of 4.0c behind the wing. It features 1.125 million cells. The baseline sliver mesh is shown in Figure 4.18.

Test cases 4 and 5 were used to examine the mesh sensitivity of the model. Test 4 employed a coarse mesh construction which doubled the cell side length in all locations in the x- and y-directions but maintained the mesh resolution in the spanwise z-direction. This allowed a significant reduction in cell count of 46 % down to 3 million cells. Test 5 was used to examine the mesh's sensitivity to spatial resolution in the spanwise direction. Zones G, H and I of the mesh remained unchanged but the high resolution zones A – D had their spanwise resolution doubled from 20 to 40 cells. Various comparisons between the results of tests 4 and 5 and the baseline test 1 are shown in the figures that follow. A brief summary of the boundary layer mesh for the test cases 1, 4 and 5 is presented in Table 4.6.

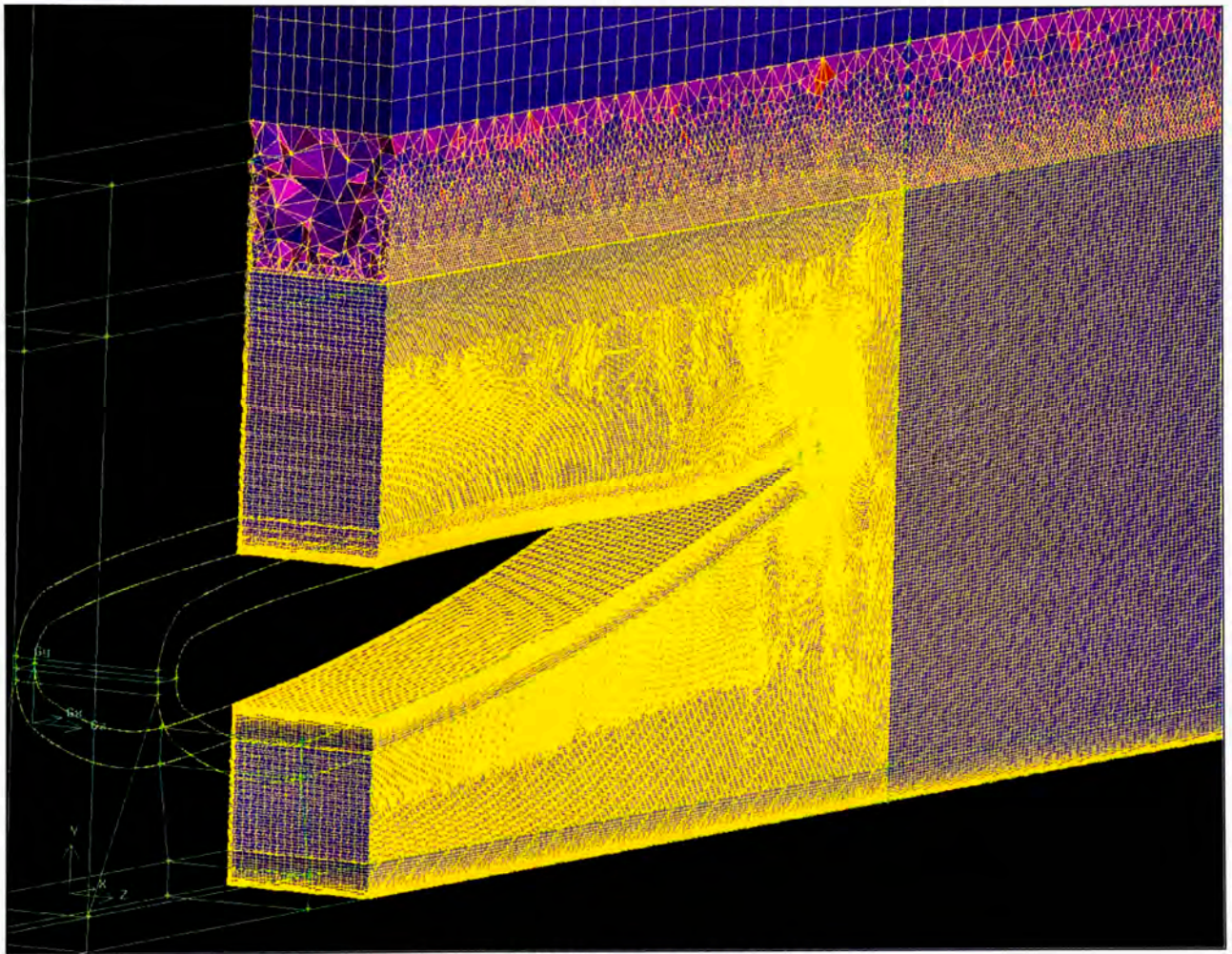


Figure 4.17: Sliver mesh explosion

Table 4.6: Summary of sliver model boundary layer meshes for test cases 1, 4 and 5

Test	Description	Cell count along wing surface (top + bottom)	Cell count of boundary layer mesh depth	Spanwise cell count at wing surface
1	Baseline	800	30	20
4	Coarse	400	15	20
5	Double-span res.	800	30	40

In order to facilitate a comparison between the test 1, 4 and 5, Figure 4.19 shows the RMS velocity magnitude, instantaneous velocity magnitude and the spanwise (out-of-page)

component of vorticity, all at the midplane cut of the sliver model and Figure 4.20 displays the iso-surface of vorticity magnitude at 3000 /s.

The coarse mesh, when compared against the baseline mesh, demonstrates some inadequacies. Most clearly evident in the spanwise vorticity contours in Figure 4.19, the coarse mesh's resolution of the vortical structures in the wake, and indeed around the wing, is inferior to the baseline case. In the same figure this can be seen to some extent in the lack of small fluctuations in the instantaneous velocity magnitude contours. Due to the lack of resolution, the velocity fluctuations in the immediate wake (RMS velocity) are slightly lower. Additionally, the separated shear layers off both surfaces of the wing are thicker and take longer to collapse into shedding vortices on the coarse mesh – although, this last observation must be considered carefully given the instantaneous nature of the vorticity contour plots. Finally, the lack of vortical structure captured by the coarse mesh is further emphasised in Figure 4.20, particularly over the top surface of the wing.

All these observed differences between the two meshes are considered erroneous on the part of the coarse mesh because, primarily, any variation observed in a mesh-dependence study indicates that the mesh resolution is still influencing the solution. However, it should be noted that, although the coarse mesh from test 4 has demonstrated an inferior ability to capture the flow features, compared to the baseline mesh of test 1, the accuracy a large eddy simulation ultimately achieves depends primarily on how finely one wishes to model the flow field. There will be observed differences in the flow features with increases in spatial resolution all the way until a DNS solution is performed. So, in reality, achieving complete mesh-independence is simply not possible unless one is prepared to perform a DNS solution (Geurts, 2004). Consequently, the spatial resolution chosen for an LES simulation is in practice determined by the accuracy the user feels is necessary to achieve in order to faithfully reproduce the flow field in question. The coarse mesh has demonstrated that its results are probably not sufficient for this task but the baseline model appears to produce the turbulent features quite well.

The comparison between the baseline case, test 1, and the fine spanwise mesh case, test 5, revealed some improvement in the simulation through the doubling of the spanwise resolution. The RMS velocity plots in Figure 4.19 are very similar with the velocity variation slightly lower in the immediate wake and slightly higher at the collapse of the separated shear layer on the top surface. The instantaneous velocity contours do not show any obvious differences in performance, however, the spanwise vorticity contours do show that the resolution of the vortical behaviour is improved slightly, particularly over the top surface of

the wing. The improved modelling over the top of the wing is more clearly defined by the high angle shots of the vorticity iso-surfaces in Figure 4.20 where the additional spanwise resolution has allowed smaller vortical structures to be resolved.

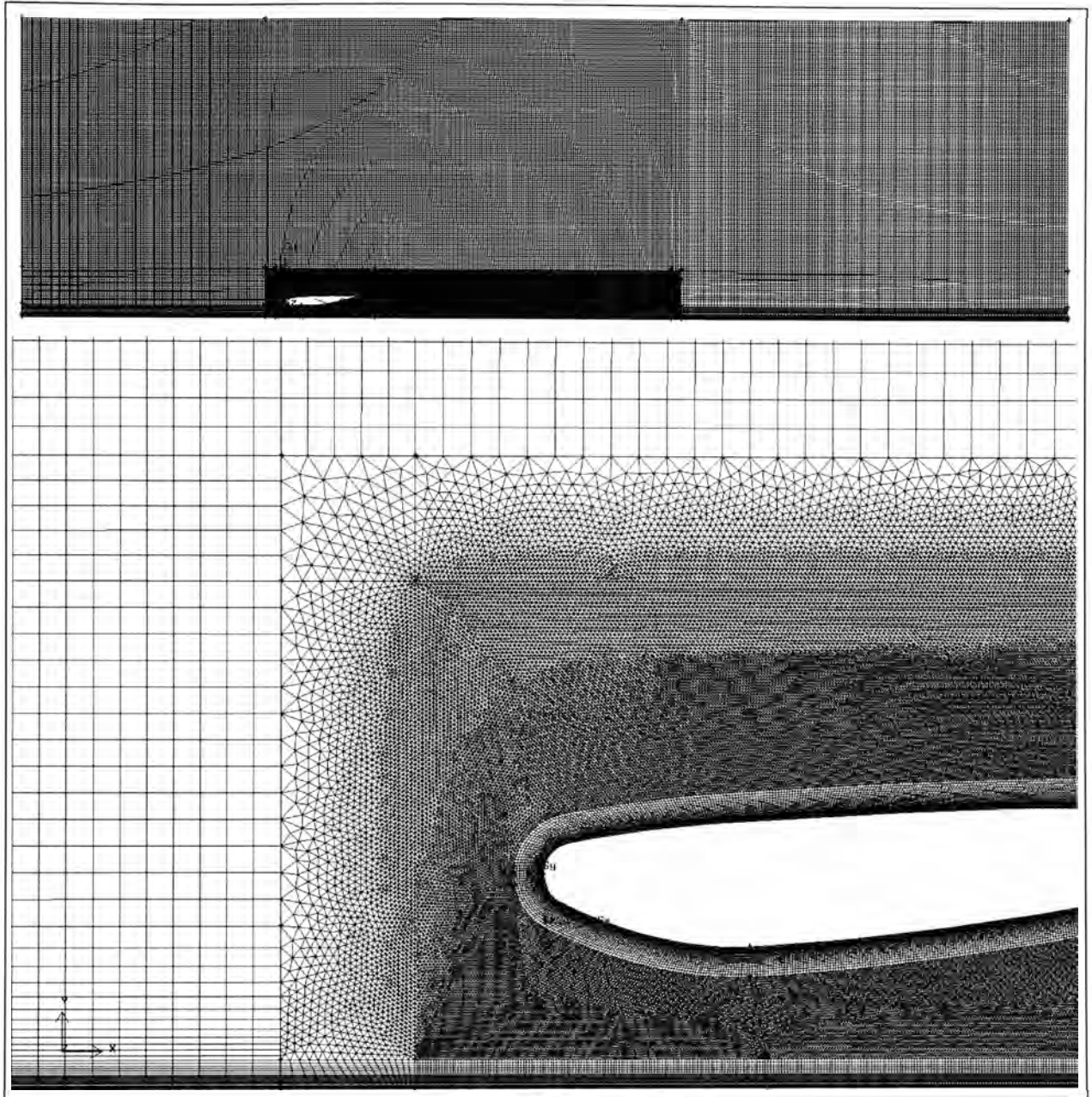


**Figure 4.18: Sliver mesh**

Despite the fact that the finer spanwise resolution yielded some tangible improvements to the turbulent modelling, the improvement observed was not very significant considering the spanwise resolution had to be doubled in order to achieve it. Regardless of these results, the baseline sliver mesh would be retained over the fine spanwise mesh as the latter is too computationally expensive for insufficient gain.

From the work presented in this section, the sliver model was considered able to simulate the flow phenomena in question while also doing so in an economical way.

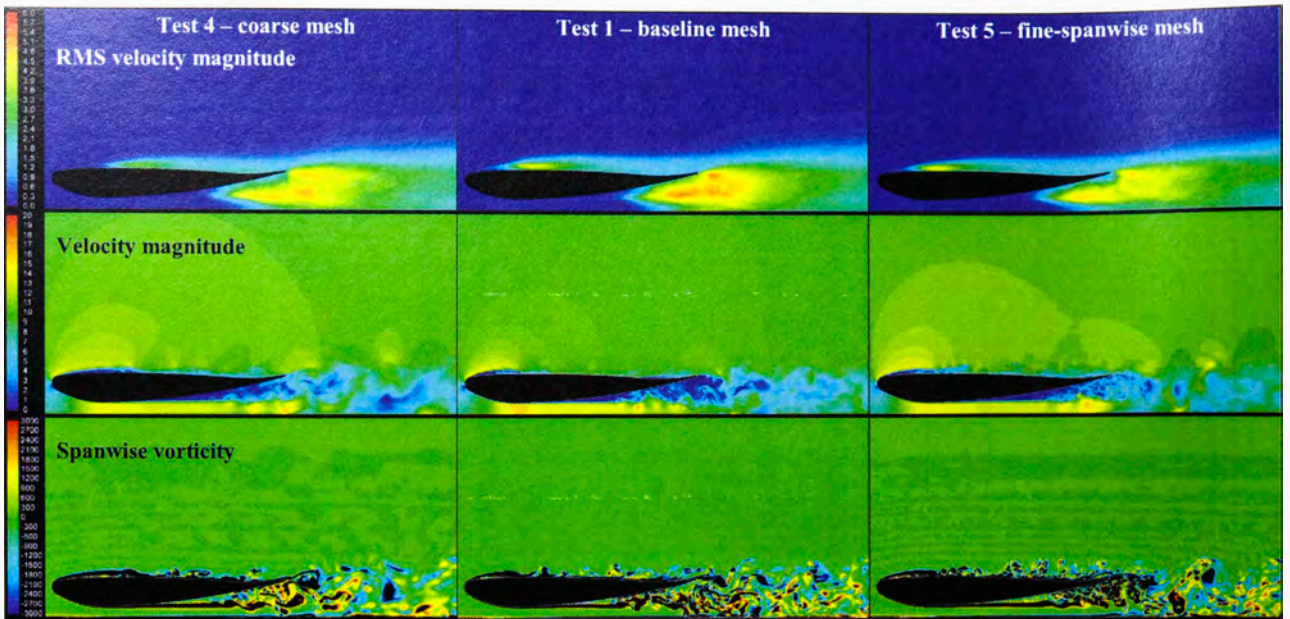


Figure 4.19: Grid comparisons; column 1) test 4 coarse mesh, column 2) test 1 baseline mesh, column 3) test 5 fine spanwise mesh, row 1) RMS velocity magnitude, row 2) velocity magnitude and row 3) spanwise vorticity

### 4.3.2 Pseudo-Direct Numerical Simulation Model

In most respects, the P-DNS model is identical in practical application to an LES model. This is advantageous as the development work in the preceding section for the LES model is applicable to this model also.

The mesh requirements, for example, are the same for the two methods because, like LES, the P-DNS model directly resolves the larger of the turbulent structures and relies on a sort of ‘model’ to account for the smaller turbulent scales. Thus, P-DNS is intended to function using an LES-type mesh geometry.

What is not known about the P-DNS model regarding mesh refinement is how its ability to capture the turbulent flow features changes with spatial resolution. Although this may vary from the LES analysis above, such knowledge would not change the ultimately-chosen geometry for two reasons: a) the finest practical grid would still be employed (making such knowledge superfluous for this particular application) and, as the computational demands of P-DNS is quite similar to LES, the same mesh as that used for LES would also be chosen here; and b) in order to facilitate a fair comparison between LES and P-DNS, as is discussed in Chapter 6, the same mesh should be used for both.

The time step of  $5 \times 10^{-6}$  s used for the LES model was retained for the P-DNS model; however, the number of iterations per timestep was increased from 20 for the LES case to 30 for P-DNS. This roughly increased the solution time by 50 % but this was deemed necessary for the model to achieve residuals of the same order as those achieved by the LES model. It was thought that this measure was important in order to facilitate a fair comparison between

the two models despite the large difference in computation time. This does, of course, negate one of the perceived advantages of this approach mentioned in Sec. 2.7 – that it should solve more quickly than an LES model. A typical residual plot from one time step during the P-DNS solution process is shown in Figure 4.21. It should be noted that the same under-relaxation factors were employed for both LES and P-DNS models.

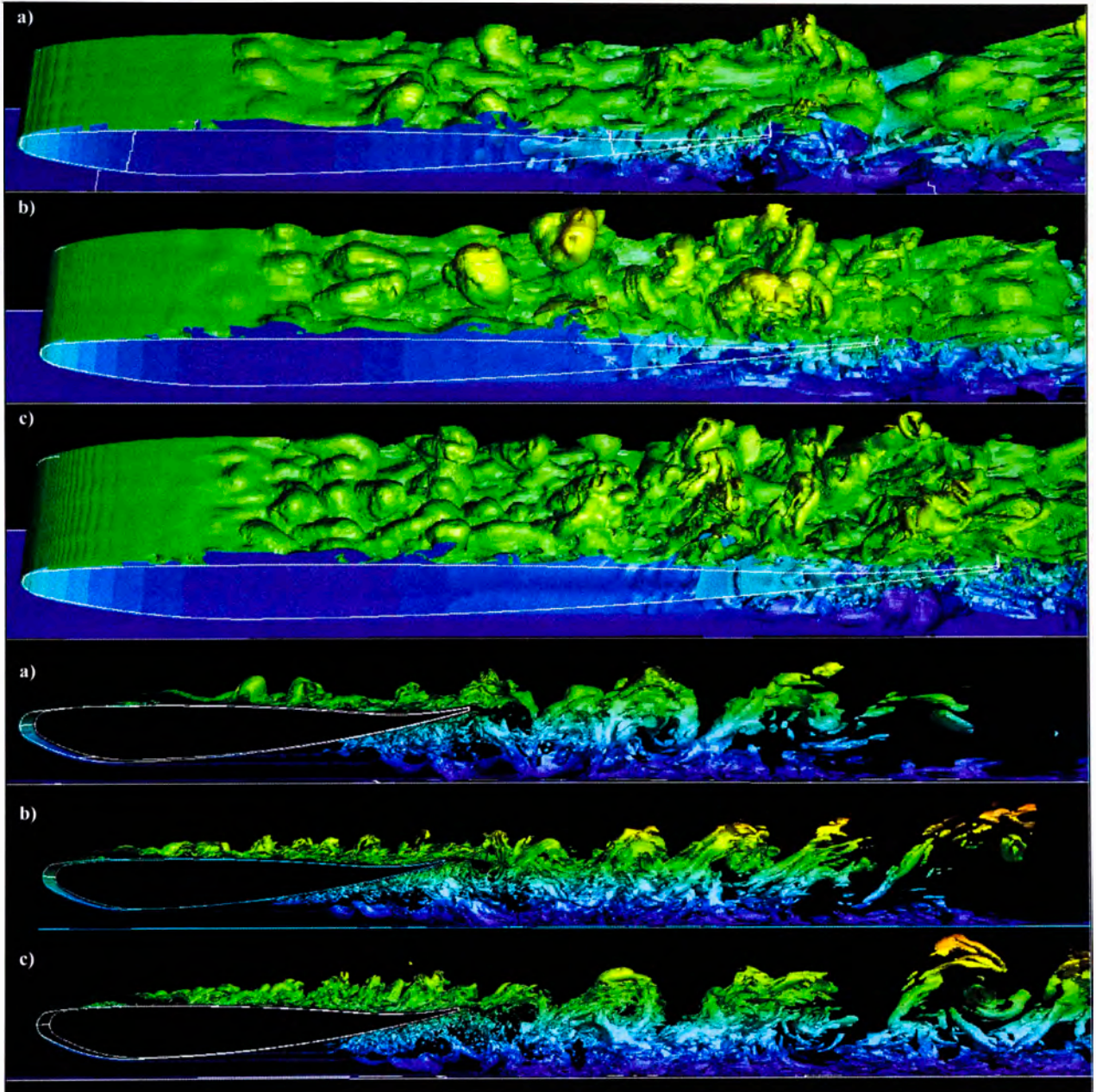


**Figure 4.20:** Comparisons of iso-surface of vorticity magnitude: a) test 4 coarse mesh, b) test 1 baseline mesh and c) test 5 fine-spanwise mesh

The solution process for the P-DNS model was identical to the LES model (though lengthier) and its performance, measured against the LES and the experimental validation data may be found in Chapter 6.

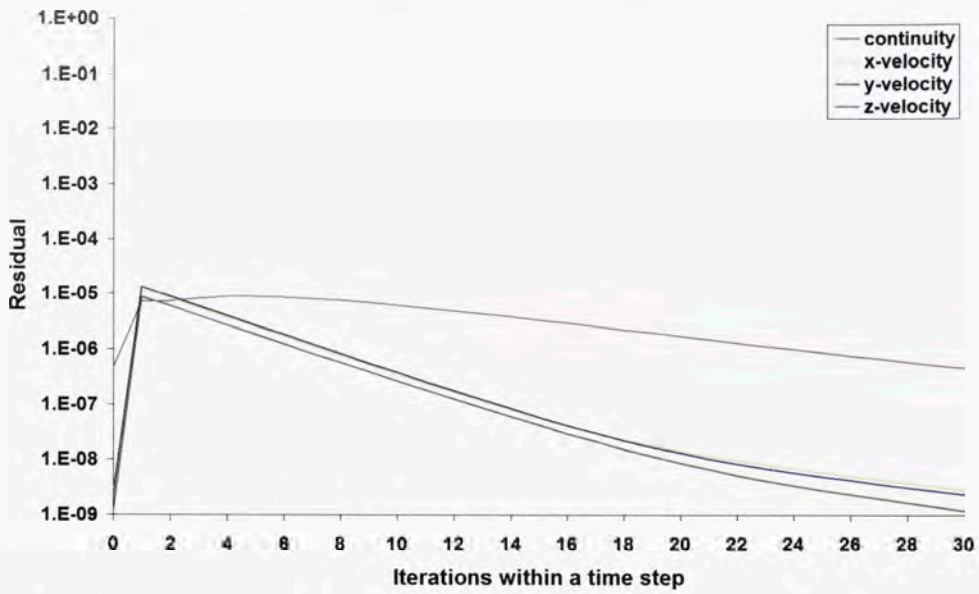


Figure 4.21: Sample residual plot for a single time step of an P-DNS sliver model simulation

# Chapter 5: Results and Discussion 1: Two-Dimensional Steady Simulations of Inverted Aerofoils in Ground Effect

## 5.1 Introduction

Examined in this chapter are the findings of a ground effect study that was undertaken using the CFD model developed in Sec. 4.2. The broad purpose of the study was to examine, in the two-dimensional regime, the workings of ground effect phenomena. Observed in the first part of the work, in Sec 5.2, is the ground effect behaviour about both upright and inverted aerofoils. This work seeks to clearly explain how ground effect works in both cases. The second part in Sec. 5.3 is a closer assessment of the inverted aerofoil case which examines the influence on ground effect of changes to the geometric properties of the aerofoil and thus sheds light on how ground effect may be better exploited.

## 5.2 Ground Effect Phenomena about Lift and Downforce Generating Cambered Aerofoils

Investigations into ground effect phenomena about aerofoils are typically conducted on either an upright (lift-producing) or inverted (downforce-producing) configuration, in isolation. This limited approach does not promote a holistic understanding of how ground effect influences aerofoils. In this study a two-dimensional CFD investigation is undertaken of the highly cambered Tyrrell aerofoil, in both its upright and inverted configurations, in order to better understand ground effect phenomena by observing how it influences each configuration.

Various studies have been undertaken in the past to examine and explain the effect of ground effect on upright (lift generating) wings or aerofoils, through analytical, numerical and experimental methods (Coulliette and Plotkin, 1996; Hsiun and Chen, 1996; and Ahmed and Goonarate, 2002). Additionally, various studies have sought to explain ground effect about inverted (downforce generating) wings or aerofoils, mainly through numerical and

experimental means (Ranzenbach, 1995; Zerihan and Zhang, 2000; Zhang and Zerihan, 2003b; Beves, Barber and Leonardi, 2005; Mahon and Zhang, 2005; and Mokhtar, 2005).

The investigation in this section reveals the different ways in which ground effect manifests about the two configurations and also uncovers some general mechanisms that are at play on both configurations. Two primary questions were studied regarding the general behaviour. Firstly, why do the dividing streamlines of both configurations become less deflected (or angled) in close ground proximity? Secondly, why does the stagnation point of both configurations shift downward over the leading edge in close ground proximity? These behaviours are non-intuitive and this study seeks to uncover the physics that causes them.

A two-dimensional CFD study, using a steady RANS solver, was conducted at a representative Reynolds number of 458,800 using the Tyrrell aerofoil. The investigation is restricted to the two-dimensional case in order to simplify the study. The numerical model was designed to simulate the open air condition – that is, there was no solid wall at the top of the domain. This open air condition was used because it creates a better representation of the conditions the airfoil would encounter in service. The aerofoil was tested in both its upright and inverted configuration and was set at an angle of  $\alpha = +6^\circ$  to the horizontal in both cases. Additionally, both aerofoil configurations were simulated at the following ground clearances:  $h/c = 3.00, 2.00, 1.50, 1.00, 0.75, 0.50, 0.40, 0.30, 0.20$  and  $0.15$ .

The upright aerofoil was simulated at the additional ground clearances of  $h/c = 0.10, 0.05$  and  $0.03$ . However, lack of numerical stability, brought on by inherent unsteadiness in the flow, prevented the inverted aerofoil simulations from converging at these additional very low clearances. In order to model this inherently unsteady flow, a more powerful technique like LES would need to be used, at considerable additional expense. As the phenomena investigated in this study predominately occurs about the both aerofoils in a quasi-steady fashion, It was decided that the additional expense to model inherently unsteady flow, only to gain the extremely low clearance configurations, was unnecessary. Therefore, fully unsteady flow at extremely low clearances (for the inverted aerofoil) is beyond the scope of this work.

The simulation was stopped when convergence was considered achieved for both the  $C_n$  and  $C_d$  values. The normal force and drag force coefficients,  $C_n$  and  $C_d$ , were considered converged when plots of these quantities (with iterations on the ordinate) levelled out such that their variation per iteration was consistently below 0.01 %.

The applicability of this numerical model is limited to quasi-steady-state cases and, as such, not all ground clearances could be computed while maintaining a steady flow solution.

### 5.2.1 Force Behaviour

The normal force, in the context of this thesis, is defined as the component of generated force that acts perpendicular to the direction of travel of the aerofoil (or in a wind tunnel context, the direction of travel of the freestream air). The sense of this force vector is considered positive under normal operation of the given aerofoil configuration (downward for inverted, upward for upright). It is convenient to consider the force behaviour of both aerofoil configurations in terms of the normal force  $n$  as the performance of both aerofoils can then be directly compared despite the lift vector of each aerofoil pointing in the opposite direction to that of the other. This convention allows ease of comparison of the two aerofoils.

The normal force coefficient  $C_n$  for both the upright and inverted Tyrrell aerofoils is shown in Figure 5.1. The freestream result is also plotted on this figure (as a discontinuous data point) and, without the influence of the ground, is the same value for both aerofoil configurations. Both aerofoils exhibit a large increase in  $C_n$  at low ground clearances.

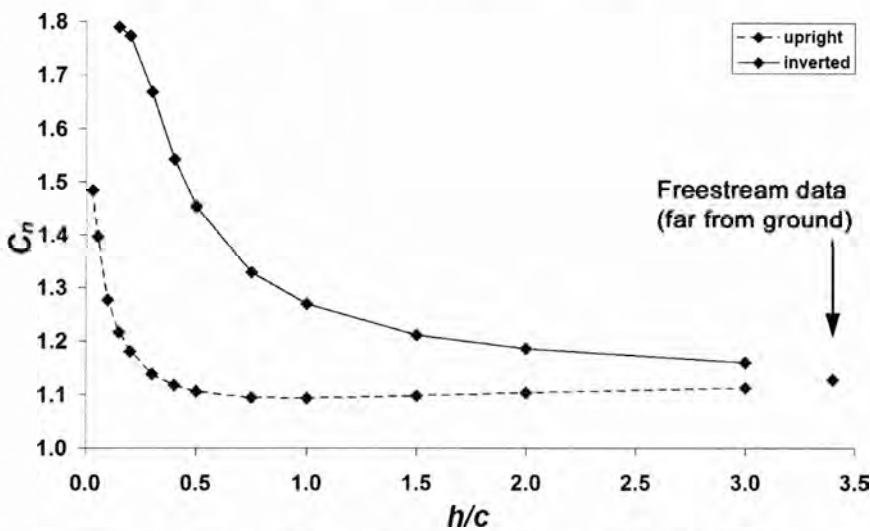


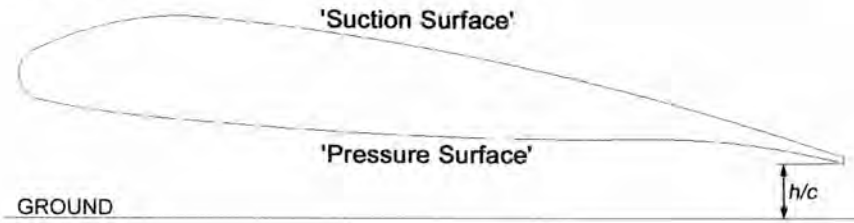
Figure 5.1: Coefficient of normal force vs. ground clearance

In addition to the inverted aerofoil producing a large increase in  $C_n$ , the rate at which  $C_n$  increases is of interest. Decreasing  $h/c$  from freestream,  $C_n$  of the inverted aerofoil increases very slowly until about  $h/c = 1.0$ – $1.5$  whereupon its normal force starts to increase more steeply until its maximum is reached. The upright aerofoil, as  $h/c$  is reduced, shows a slight decrease in  $C_n$ , of similar but opposite rate to the increase seen for the inverted case. This decrease in  $C_n$  continues down to a minimum at about  $h/c = 1.00$  and then  $C_n$  starts to increase rapidly (more so than the inverted case) from about  $h/c = 0.50$  downwards.

For each aerofoil, the highly cambered side which features an accelerated flow (and associated suction force) is called the ‘suction side’ of the aerofoil. The other side is called

the 'pressure side'. These terms will be used hereafter and are presented graphically in Figure 5.2.

### Upright Aerofoil



### Inverted Aerofoil

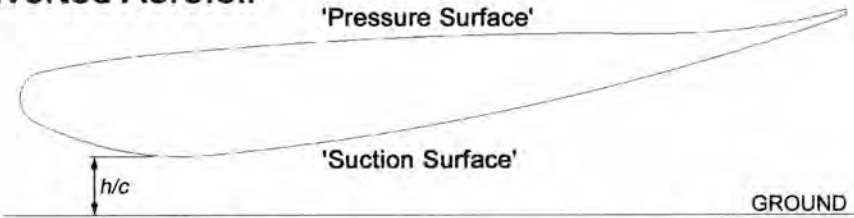


Figure 5.2: Aerofoil surface name convention

Figure 5.3(a) and Figure 5.3(b) show the various components of normal force coefficient that contribute to the total normal force coefficient on the inverted and upright aerofoil, respectively. Figure 5.3(a) indicates that the increase in  $C_n$  is entirely attributable to an increase in pressure force on the suction side of the aerofoil. The normal force due to pressure on the pressure side decreases with ground clearance and the viscous components of the normal force are negligible. Figure 5.3(b) shows that the pressure force on the underside of the upright aerofoil increases and that the pressure force on the suction side slowly diminishes. Again, the viscous components are negligible.

The drag force coefficient  $C_d$  is presented in Figure 5.4. The  $C_d$  of the inverted aerofoil increases slowly at high clearances and then more quickly at low and very low clearances. The  $C_d$  trend of the upright aerofoil, however, decreases slightly all the way down to  $h/c = 0.05$  and then increases slightly at the lowest clearance of  $h/c = 0.03$ .

Figure 5.5(a) and Figure 5.5(b) show the various components of drag coefficient that contribute to the total drag coefficient for the inverted and upright aerofoils, respectively. Figure 5.5(a) shows an increase in pressure drag, on the suction surface of the aerofoil, as  $h/c$  is reduced. This component of drag is of some interest as, at higher clearances above about  $h/c = 0.2$ , this component force is actually negative and, therefore, reducing the overall drag force. This negative drag phenomenon can be explained by plotting the pressure force normal to the surface of the aerofoil, indicating the direction in which the pressure force acts. Figure 5.6 demonstrates this by presenting the pressure coefficient  $C_p$  about the inverted aerofoil at  $h/c = 1.00$ . It can be seen that an integration of the pressure force on the lower surface of the

aerofoil could yield a forward-facing net force. The same could not be said of the upper surface.

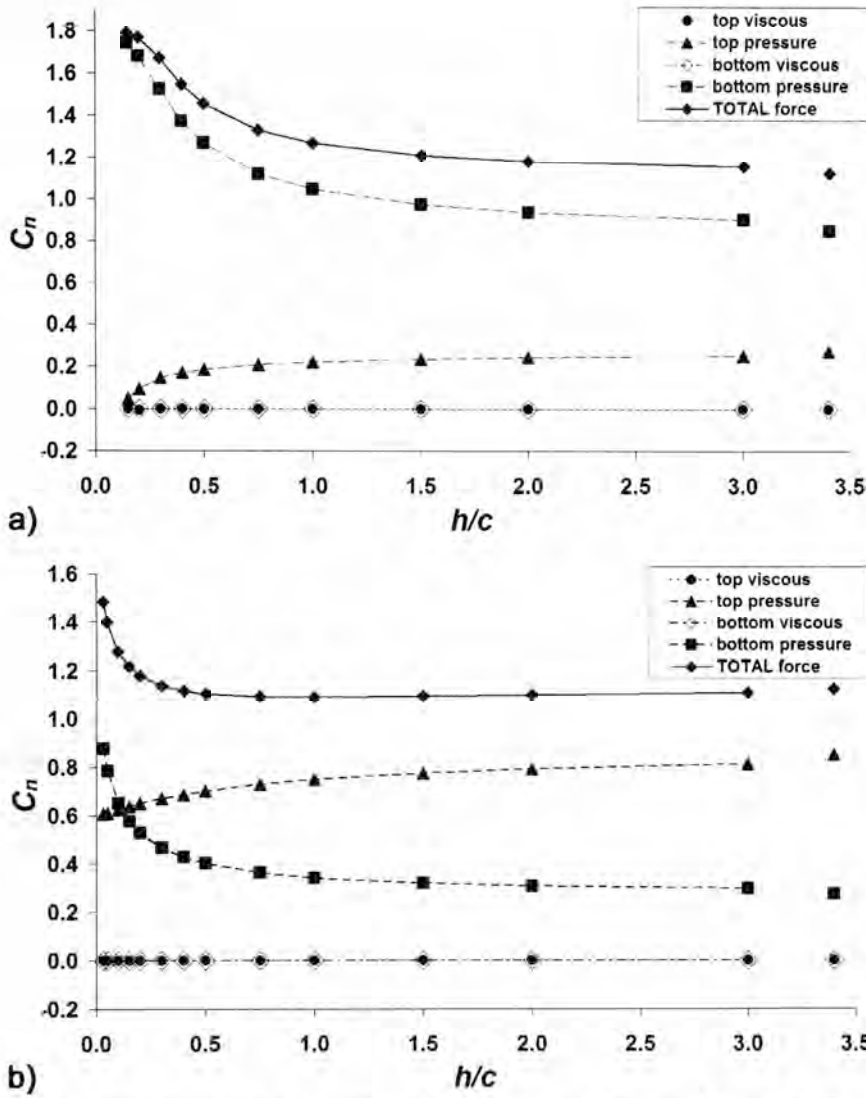


Figure 5.3: Normal force components vs. ground clearance; (a) inverted aerofoil, (b) upright aerofoil

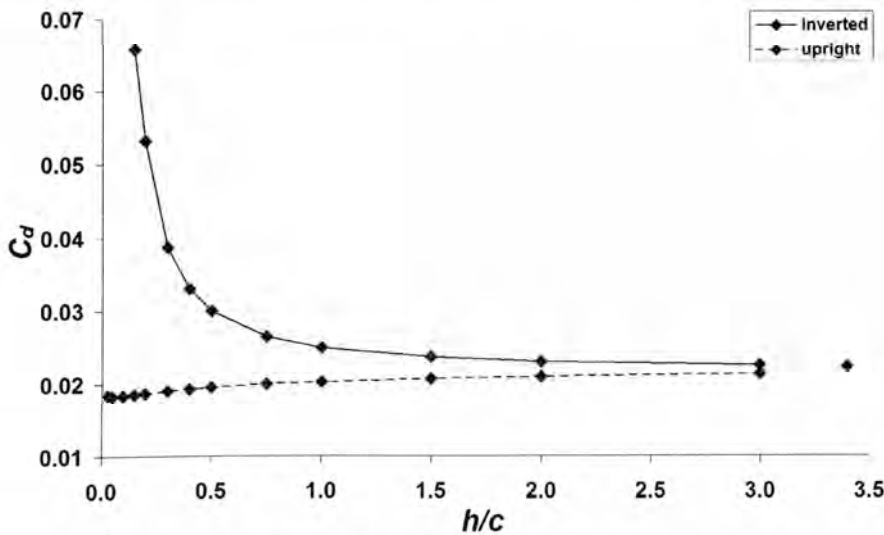


Figure 5.4: Coefficient of drag vs. ground clearance

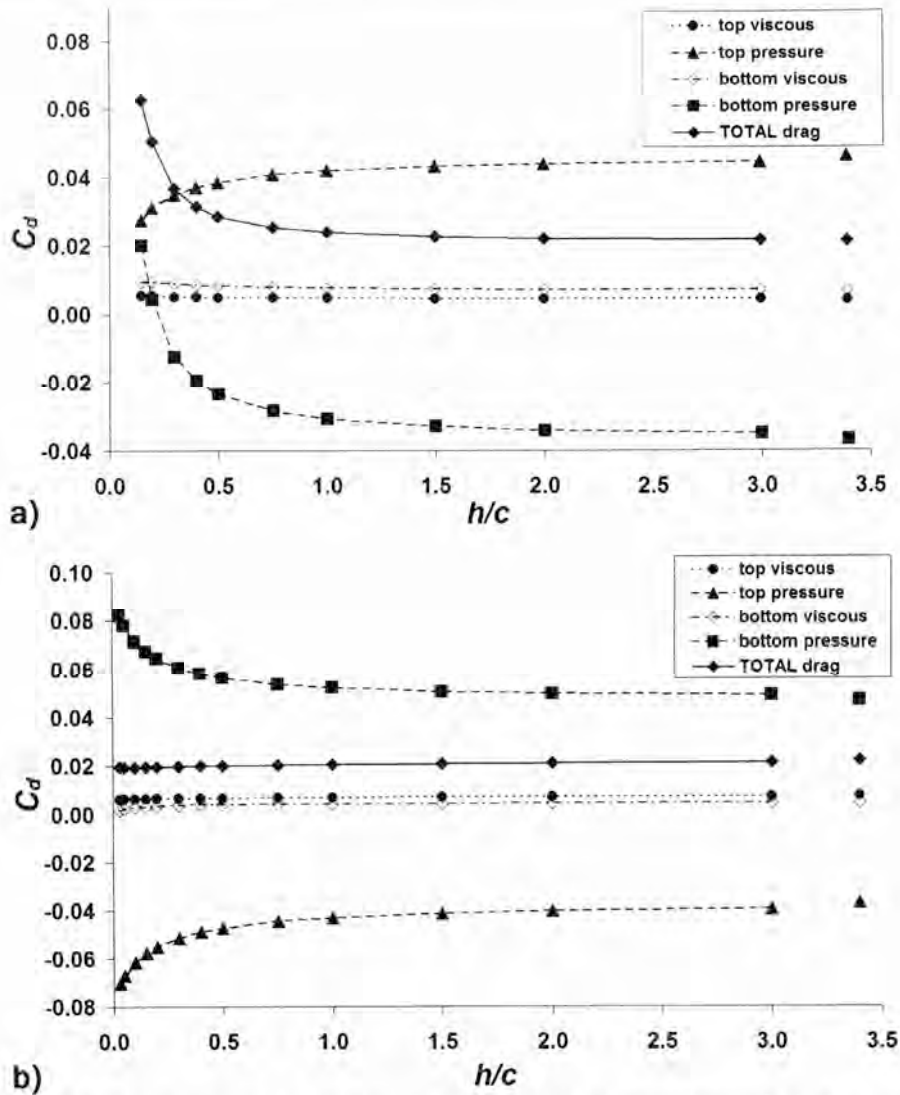


Figure 5.5: Drag force components vs. ground clearance; (a) inverted aerofoil, (b) upright aerofoil

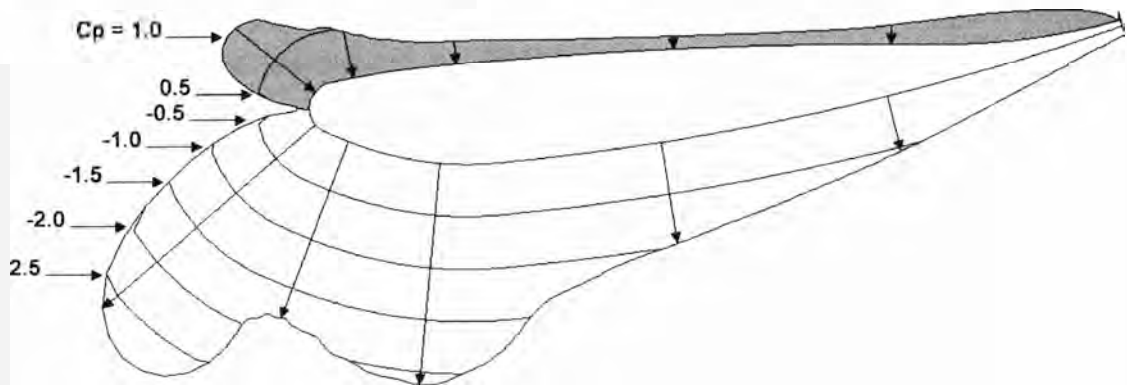


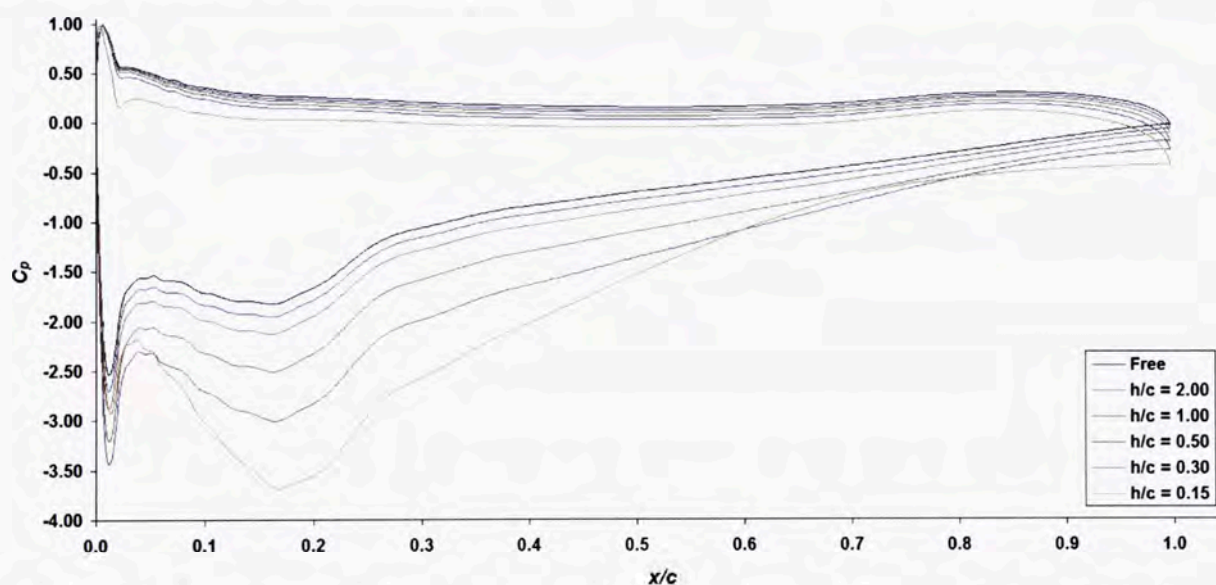
Figure 5.6: Plot of pressure coefficient  $C_p$  about inverted aerofoil at  $h/c = 1.00$

Figure 5.5(b) shows that, although the overall drag coefficient of the upright aerofoil does not change greatly with height, the pressure components of the drag coefficient do change notably. As  $h/c$  is reduced, the pressure drag attributable to the pressure surface of the aerofoil increases. However, in contrast, the pressure drag on the suction surface is always negative and decreases, effectively giving the aerofoil thrust and reducing the overall drag.

Finally, regarding the force behaviour of the aerofoils, the normal force-to-drag ratio,  $n/d$ , behaves oppositely for each case.  $n/d$  increases for the upright aerofoil from the freestream value of 50.82 to 80.29 at  $h/c = 0.03$  (58% increase).  $n/d$  initially increases very slightly for the inverted aerofoil to a maximum at approximately  $h/c = 3.00$  of about 52.3 and then declines to a minimum of 27.23 at  $h/c = 0.15$  (46% reduction from freestream). This is accounted for due to the large increase in drag seen on the inverted aerofoil and the reduction in drag seen on the upright aerofoil.

## 5.2.2 Pressure Coefficient Distributions

The  $C_p$  distributions, at selected clearances, for the inverted aerofoil are shown in Figure 5.7. A characteristic of the Tyrrell aerofoil, are the relatively sharp curves on both the pressure and suction surfaces, near the leading edge. As can be seen in Figure 5.7, these sharp curves result in a localised decrease in pressure as the flow speeds up around these corners. These features are referred to as ‘suction spikes’.



**Figure 5.7: Pressure coefficient distributions for inverted aerofoil at various ground clearances**

As the inverted aerofoil is brought closer to the ground, suction increases over the suction surface, particularly in the maximum suction region of  $0.1 < x/c < 0.2$  where  $C_p$  changes from about -1.8 to -3.7. This increased suction results in an increased pressure recovery demand. As  $h/c$  is reduced, the pressure slightly, yet consistently, decreases over the whole pressure surface. Below  $h/c = 0.75$  (not shown in the figure), the suction strength, on the bottom surface, and the accompanying adverse pressure gradient, increase at a greater rate, resulting in a large adverse pressure gradient and the onset of flow separation at  $h/c = 0.15$ . As shown in the close-up of the leading edge region, in Figure 5.8, decreasing clearance also strengthened the suction spike, on the suction surface, from -2.5 to down to -3.4 at  $h/c = 0.3$ ,

below which the suction spike decreases in strength back to -2.9. Below this same clearance, the pressure surface suction spike begins to increase in strength.

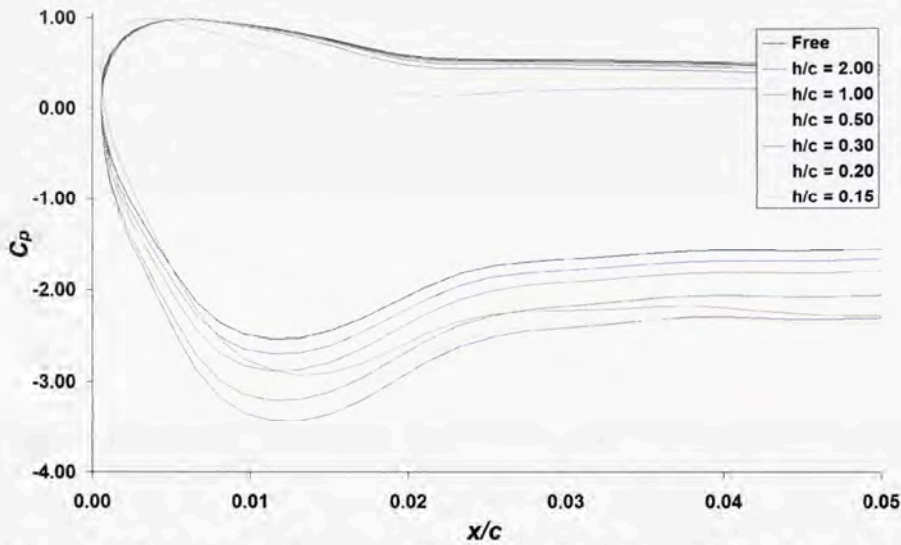


Figure 5.8: Leading edge region from Figure 5.7 about inverted aerofoil

Figure 5.9 shows the  $C_p$  plots for the upright aerofoil. As  $h/c$  is reduced, a slight yet consistent increase in pressure can be seen on both the suction and pressure surfaces down to a clearance of  $h/c = 0.75$  (not shown). Below this height, the pressure on the pressure surface (surface facing the ground) increases more rapidly. Below  $h/c = 0.15$ , the suction spike on the suction surface, having previously decreased in strength with reduced clearance, starts gaining strength, as shown in Figure 5.10). The suction spike on the pressure surface is continually weakened with decreasing  $h/c$  as the pressure continues to increase on that surface.

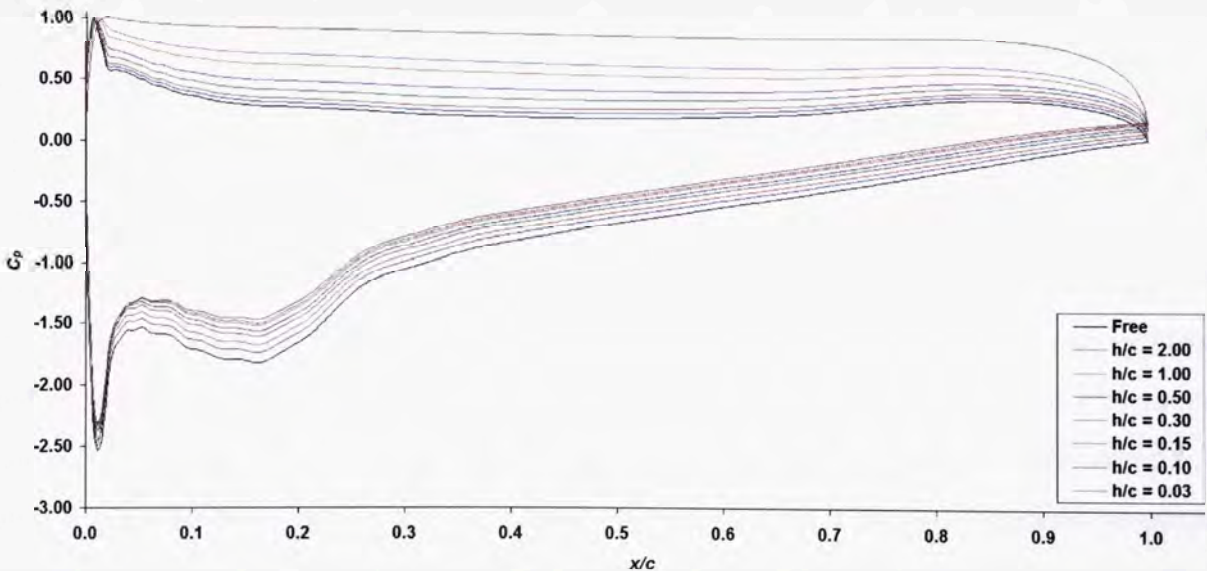


Figure 5.9: Pressure coefficient distributions for upright aerofoil at various ground clearances

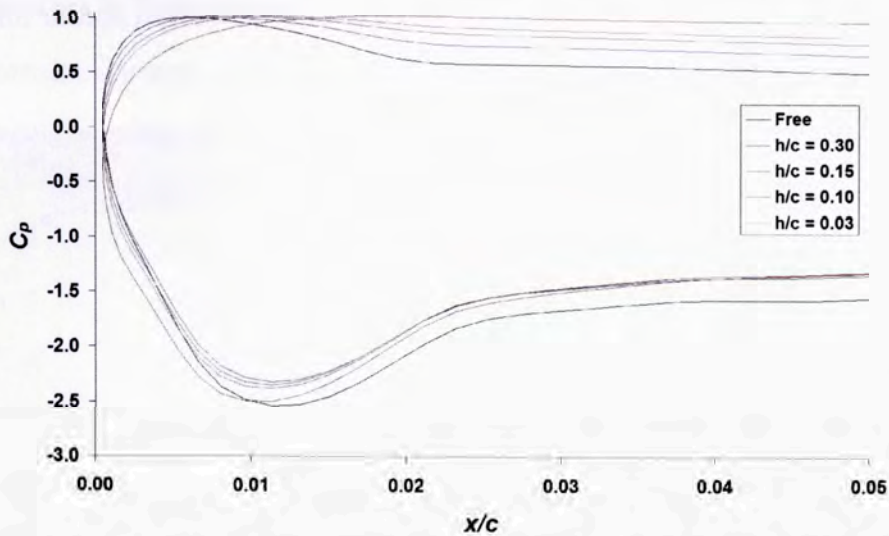


Figure 5.10: Leading edge region from Figure 5.9 about upright aerofoil

The pressure coefficient plots emphasise that the flow behaviour is altered about the inverted and upright aerofoils in distinctly different ways. The large increase in suction seen under the inverted aerofoil is the only contributor to the aerofoil’s increase in  $C_n$  at low  $h/c$ . The contribution from the pressure surface all but disappears as the pressure on this surface reduces to approximately the freestream static value by  $h/c = 0.15$ . The increase in adverse pressure gradient is clear to see in Figure 5.7. The adverse pressure gradient on the suction surface of the upright aerofoil remains predominantly unchanged. Unlike the inverted aerofoil, both sides of the upright aerofoil continue to contribute to  $C_n$  down to very low  $h/c$ . The flow speed over the suction surface does decrease, however, even at its lowest contribution, the suction surface still produces 40.8% of total  $C_n$  at  $h/c = 0.03$ .

### 5.2.3 Flow Field

#### 5.2.3.1 Velocity Contours

A selection of velocity contour maps are presented in Figure 5.11. Figure 5.11(a-c) show the change in the velocity field around the inverted aerofoil as it approaches the ground through  $h/c = 1.00, 0.30$  and  $0.15$ , respectively. At  $h/c = 1.00$ , the boundary layer on the suction side of the aerofoil is still relatively thin, though turbulent, beyond about  $x/c = 0.20$ , and the wake is not yet significant. The turbulent nature of the flow is evident from the sudden increase in the rate of boundary layer growth downstream of  $x/c = 0.20$ . As the aerofoil is brought down to  $h/c = 0.30$ , the boundary layer thickness increases on the suction side feeding into a, now, quite large and less deflected wake region. At  $h/c = 0.15$ , the boundary layer now spans about one-third of the distance to the ground at the trailing edge and the wake is thicker still. The flow through the throat region is now moving rapidly with its average speed now about double the freestream speed. The velocity field about the pressure side of the aerofoil

remains quite consistent with minimal change in overall velocity contour and boundary layer thickness.

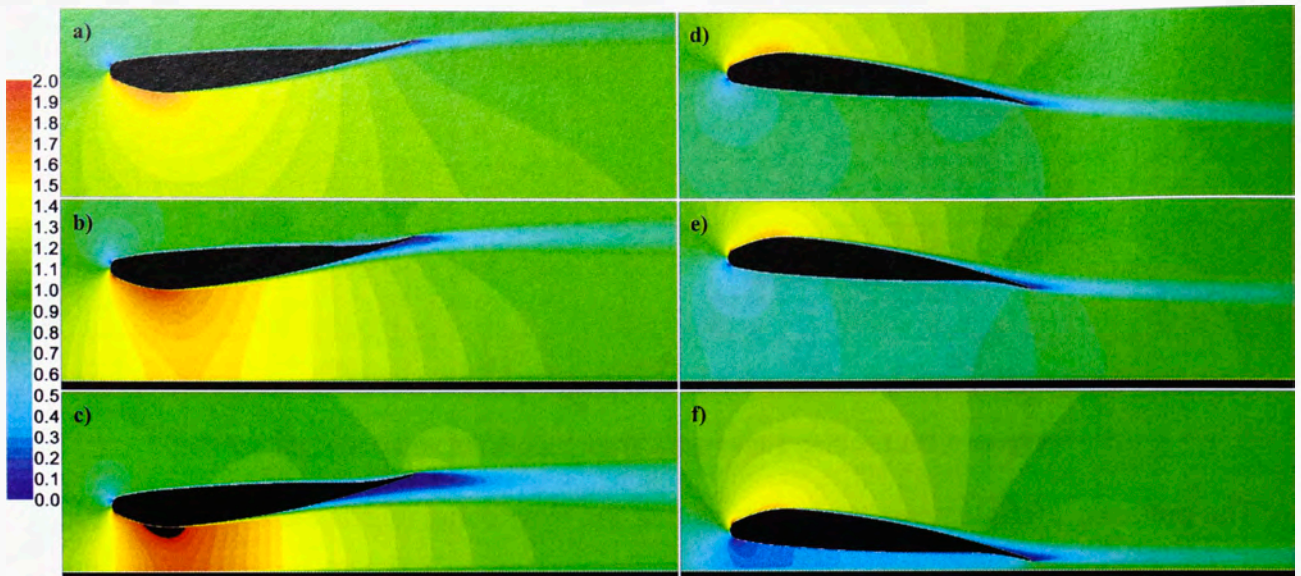


**Figure 5.11: Velocity contours ( $V/V_\infty$ ) about inverted aerofoil at; (a)  $h/c = 1.00$ , (b)  $h/c = 0.30$  and (c)  $h/c = 0.15$ , and upright aerofoil at; (d)  $h/c = 1.00$ , (e)  $h/c = 0.30$  and (f)  $h/c = 0.03$**

Figure 5.11(d-f) shows the variation of the velocity contours around the upright aerofoil for ground clearances of  $h/c = 1.00$ ,  $0.30$  and  $0.03$ , respectively. At  $h/c = 1.00$ , the boundary layer on the suction surface (upper surface) is still thin, leading to a fairly small wake – similar to the suction surface of the inverted aerofoil at this clearance. The flow speed over the top surface is slightly reduced in comparison to the freestream case, which is not shown here. The boundary layer on the suction surface increases in thickness only marginally as the aerofoil is brought down to  $h/c = 0.30$ . The wake is slightly thicker and less deflected and the flow speed over the top of the wing is reduced in comparison to the  $h/c = 1.00$  case. At  $h/c = 0.03$ , the suction surface boundary layer has grown further, leading again to a slightly larger wake region, but the boundary layer growth is insignificant compared to the inverted aerofoil, whose boundary layer thickness even at  $h/c = 0.15$  ( $0.12c$  further from the ground than this case) is noticeably larger.

The variation in the flow field about the pressure surface is of primary interest for the upright aerofoil. At  $h/c = 1.00$ , the velocity field around the pressure surface is starting to be impeded and, with no adverse pressure gradient, the boundary layer remains very thin to the trailing edge. At  $h/c = 0.30$ , the nozzle effect formed between the pressure surface and the ground is now clearly apparent. The flow is starting to be slowed toward the front of the nozzle section. The boundary layer remains very thin. Finally, at  $h/c = 0.03$ , the nozzle effect is now strong with the flow speed at the entrance to the nozzle highly restricted by the limitations imposed on the mass flow rate out of the rear of the section.

### 5.2.3.2 Turbulence Intensity

Turbulence intensity contours about the inverted and upright aerofoils are presented in Figure 5.12 at each aerofoil's lowest ground clearance. The inverted aerofoil shows a significant development of turbulence within the suction surface boundary layer, downstream of the throat, and a highly turbulent wake. The pressure surface, however, shows a far lower level of turbulence within its boundary layer. The maximum TI value for the inverted aerofoil was 20.34 % in the near wake and the maximum wall TI value was 19.42 % at the 'suction spike' on the suction surface.

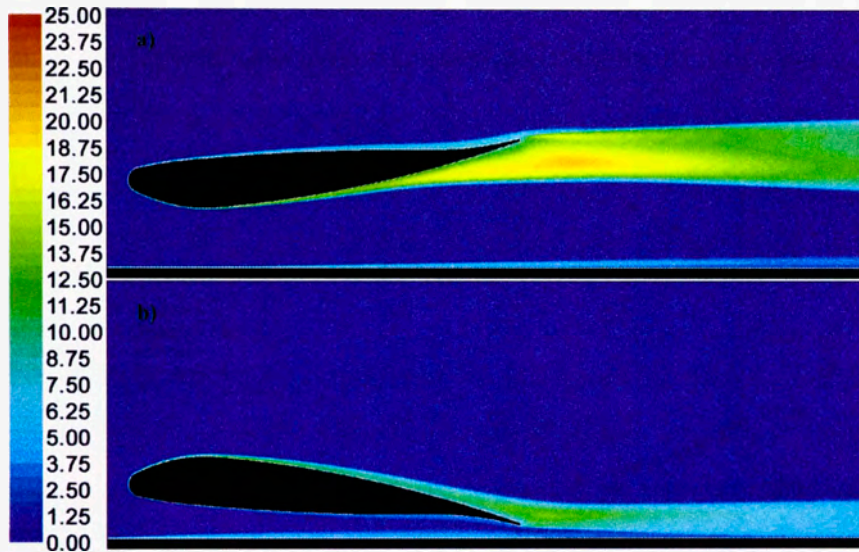


Figure 5.12: Contours of turbulence intensity percentage; (a) inverted aerofoil at  $h/c = 0.15$ , (b) upright aerofoil at  $h/c = 0.03$

The TI values around the upright aerofoil indicate an overall lower level of intensity with the maximum wake value about 13.3 % – 34 % lower than the inverted aerofoil. The maximum TI value appeared at the aerofoil surface, again at the suction surface suction spike, at 18.18 %. The pressure surface, like the inverted case, showed minimal turbulent growth. The suction surface shows a much higher turbulent growth within the boundary layer, in comparison to the pressure side, but this is still insignificant when compared to the suction surface turbulent growth on the inverted case.

## 5.2.4 Dividing Streamline Movement as Part of General Ground Effect Mechanism

### 5.2.4.1 Dividing Streamline movement

The trends in the behaviour of the close-range flow upstream and downstream of both aerofoils were observed. The dividing streamline terminates at the stagnation point at the leading edge and effectively divides the flow into that going over the aerofoil and that going under it. Similarly, the dividing streamline downstream emanates from the trailing edge and similarly divides the flow. The position of the dividing streamline, relative to the leading

edge of the aerofoil, was recorded three chord lengths upstream and downstream of the aerofoil. This is demonstrated graphically in Figure 5.13, and the results over the clearance range are presented in Figure 5.14.

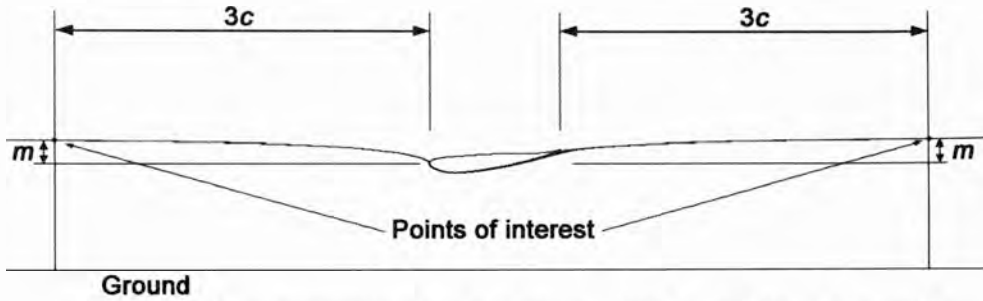


Figure 5.13: Dividing streamlines on inverted aerofoil at  $h/c = 1.00$ ,  $\alpha = 6^\circ$

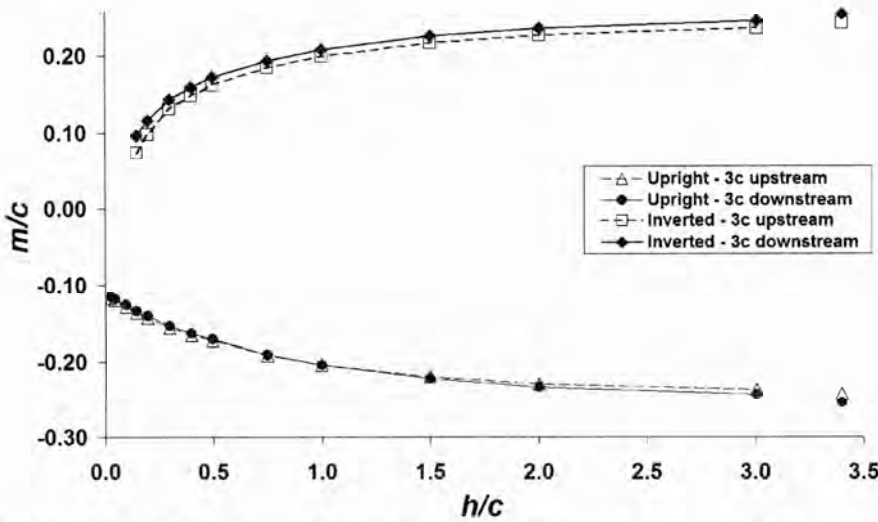


Figure 5.14: Position of dividing streamline at 3.0 chords distance from aerofoils vs. ground clearance

The upstream dividing streamline for the inverted aerofoil moves slowly downward, toward the leading edge, as the aerofoil approaches the ground. At lower clearances this trend becomes more pronounced. The upstream dividing streamline is consistently lower than its downstream counterpart and the gap between them remains fairly constant over the clearance range.

The upright aerofoil case demonstrates a similar but opposite trend as the dividing streamlines initiate below the leading edge at freestream (a mirror image of the inverted case) and moves up toward the leading edge with reduced clearance. The total movement of the upstream and downstream streamlines is less than the inverted case – even including the upright case’s larger range of  $h/c$ . Additionally, the downstream dividing streamline, which is below the upstream trend at freestream, eventually crosses over the upstream trend between  $h/c = 0.75$ – $1.00$ . Below this height, it remains slightly above the upstream trend.

### 5.2.4.2 *Dividing Streamline Relationship to General Ground Effect Mechanism*

As mentioned earlier, the upright aerofoil experiences a decrease in  $C_n$  as ground clearance is reduced from freestream down to about  $h/c = 1.00$ . Given that a sizable increase in  $C_n$  is achieved at low clearances, this opposite trend through medium clearances was unexpected. However, a similar phenomenon has previously been observed by Coulliette and Plotkin (1996) about a cambered arc using a discrete vortex method. A close inspection of the  $C_p$  plots, about the upright aerofoil (Figure 5.9 and Figure 5.10), indicates that for  $h/c$  down to 1.00, the pressure on the pressure surface increases at quite a low rate. However, the increase in pressure on the suction surface (less suction) is more significant. This shows that at high and medium clearances, before the effect of the increased pressure under the wing becomes predominant, a general reduction in flow speed over the top of the aerofoil causes it to decrease in  $C_n$  throughout this height range. The net result is a loss in lift ( $C_n$ ) in this height range as the loss in suction on the top surface is greater than the marginal increase in pressure on the bottom surface.

This loss in performance can be characterised as a decrease in circulation about the upright wing due to a gradual decrease in the effective angle of attack, as ground clearance is reduced. This is a general ground effect phenomenon and can be seen through the trends of the dividing streamlines. In the freestream condition, the dividing streamlines (3c upstream and downstream of the aerofoil) are located at  $y/c = -0.24$  and  $-0.25$ , respectively. A rough estimate of the effective change in angle of attack  $\Delta\alpha$  due to the oncoming flow direction may be considered the angle of the flow from this dividing streamline position to the leading edge, which in this case is approximately  $4.6^\circ$ . This additional incidence angle will result in a higher  $C_n$  value than if the incident flow was merely horizontal. The wake flow behind the aerofoil exhibits similar behaviour with the flow heading downward at an estimated angle of  $4.8^\circ$ . The angle of the wake flow can not be considered downwash due to tip vortices, as three dimensional effects have not been considered in this CFD analysis. Rather, it is likely the result of momentum considerations with the aerofoil acting much like a turning vane.

As the aerofoil is brought closer to the ground, the effective angle of attack,  $\alpha_{eff} = \alpha + \Delta\alpha$ , reduces due to a continual reduction in  $\Delta\alpha$ . This reduction is caused by the upward movement (relative to the aerofoil) of the dividing streamline. With a reduced  $\alpha_{eff}$ , the aerofoil experiences less circulation and produces less  $C_n$  and  $C_d$ . Additionally, the deflection of the flow in the wake reduces, in kind. At low clearances,  $\Delta\alpha$  continues to diminish toward zero, however, this becomes insignificant in comparison to the now dominant nozzle effect that stifles the flow under the aerofoil.

This general phenomenon can also be seen about the inverted aerofoil, however, unlike the upright aerofoil, its  $C_n$  value does not reduce as clearance is reduced through medium clearances. This is the case because the negative (or counter-productive) effect of the reduction in  $\alpha_{eff}$  is outweighed by the positive (downforce increasing) effect of the diffuser, which starts to noticeably influence  $C_n$  at much higher clearances than the nozzle effect for the upright aerofoil. This is evident by observation of the  $C_p$  plots which show an immediate and tangible increase in suction under the inverted aerofoil, as clearance is initially reduced from freestream. This is contrasted by the lack of significant change in the pressure on the pressure side of the upright aerofoil until below  $h/c = 1.00$ .

### 5.2.5 Stagnation Point Movement as Part of General Ground Effect Mechanism

#### 5.2.5.1 Stagnation Point Movement

Figure 5.15 shows the trend of the vertical position of the stagnation point on both aerofoils. Both aerofoils' stagnation point originates at  $y/c = \pm 0.0224$  at freestream. The stagnation point for the upright aerofoil slowly shifts downward over the leading edge. The rate of change of this stagnation point movement increases significantly once below  $h/c = 0.50$  and the minimum value, achieved at  $h/c = 0.03$ , was  $y/c = -0.0343$ . This is a downward movement of  $y/c = 0.0119$ .

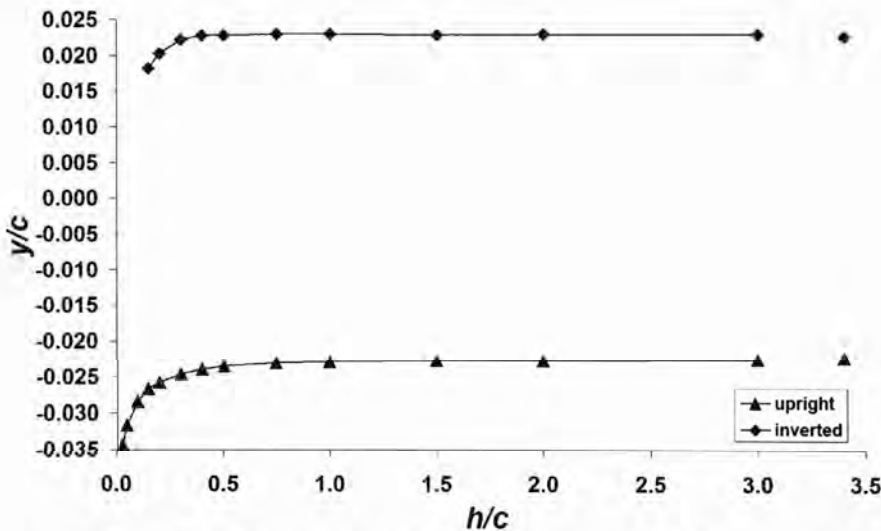


Figure 5.15: Stagnation point position vs. ground clearance

The inverted aerofoil stagnation point initially shifts very slowly upward until a maximum of  $y/c = 0.0229$  is achieved at  $h/c = 0.75$ . Following this maximum, it follows a similar trend to the upright aerofoil with the rate of change increasing with decreased clearance and also moving downward. However, the slope of this curve is greater than the upright aerofoil. The lowest value, at  $h/c = 0.15$ , was  $y/c = 0.0182$  which indicated an overall downward movement of  $y/c = 0.0042$ . This total movement represents only 35% of that of the upright aerofoil,

however, down to  $h/c = 0.15$ , the total stagnation point movement for both aerofoils is almost identical.

### 5.2.5.2 Stagnation Point Relationship to General Ground Effect Mechanism

One of the most unintuitive observations from this investigation is that the stagnation point moves down toward the ground for both the upright and inverted aerofoil, as ground clearance is reduced. In the low clearance regime, the upright aerofoil's stagnation point moves toward the high pressure region of the flow and on the inverted aerofoil, it moves toward to the low pressure region of the flow.

This behaviour is the result of a general ground effect mechanism that affects the stagnation point location in two ways. The first is the fairly global effect of the normalised flow rate observed under the aerofoils and the second is the local flow behaviour about the stagnation point, which is caused by the first.

Figure 5.16 shows a plot of the volume flow rate passing between the ground plane and the trailing edge of each of the aerofoils as the ground clearance of the trailing edge  $y/c$  is changed. Superimposed on this figure is the 'ideal' flow rate defined as the flow rate of uninterrupted freestream air which would be seen through the same size channel. With a freestream velocity of 30 m/s, this value is  $30 [m^3/s] / k [m^2]$ , where  $k = y/c [m] \times \text{unit depth [m]}$ . This ideal flow rate increases linearly with  $y/c$ . This figure demonstrates that for most of the ground clearances under consideration, the flow rate under the inverted aerofoil is enhanced due to the diffuser effect and the flow under the upright aerofoil, for all clearances, is below the ideal flow rate and is thus being constricted. It is helpful to recast this figure with the flow rates normalised by the ideal flow rate, as shown in Figure 5.17. The flow physics for each configuration is explained below.

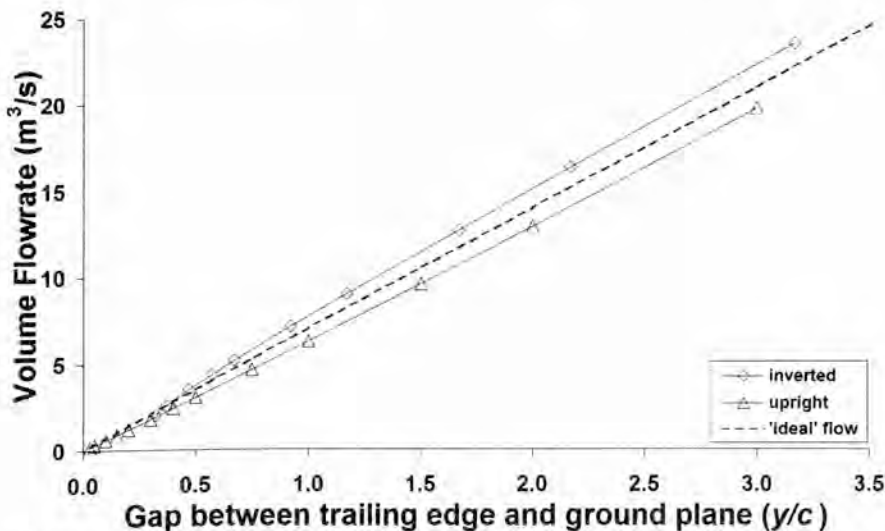


Figure 5.16: Volume flow rate under aerofoil vs. clearance between ground and trailing edge

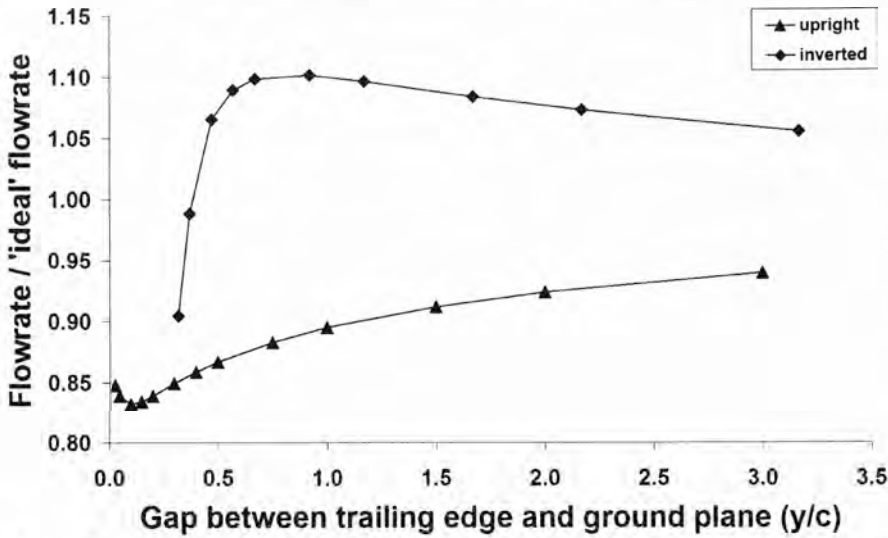


Figure 5.17: Volume flow rate under aerofoil normalised by 'ideal' flow rate at given ground clearance

**Inverted Aerofoil:** The normalised flow rate increases to a maximum of 1.103 (110.3% of the idealised flow rate) at  $y/c = 0.92$  (this corresponds to  $h/c = 0.75$ ). It then reduces dramatically to 0.904 at  $y/c = 0.32$  ( $h/c = 0.15$ ). Figure 5.17 indicates that as the inverted aerofoil moves toward the ground, the volume flow rate under the aerofoil is initially increased. This necessitates a diversion of more flow under the wing at the leading edge and will thus induce a slightly upward movement of the stagnation point, as the ground is approached. This is because the stagnation point represents the termination point of the dividing streamline. If more of the available flow must be diverted under the aerofoil, the stagnation point will move upward and thus supply more flow under the aerofoil.

Below  $h/c = 0.75$ , however, the expansion ratio of the diffuser section between the aerofoil and the ground becomes so large to the extent that, despite highly accelerated flow under the aerofoil, the flow rate through the expanding section cannot be maintained and so the normalised flow rate starts to reduce. This reduction indicates that some flow now has to be diverted over the top of the wing and so the stagnation point will start to move downward to accommodate this. The start of the steep downward slope in Figure 5.17 at  $y/c = 0.67$  ( $h/c = 0.50$ ) indicates the onset of significant diversion of flow over the top of the aerofoil and matches quite closely to the start of the rapid downward movement of the stagnation point at about  $h/c = 0.40$ , in Figure 5.15.

The effect of this flow diversion on the stagnation point and the local flow field is clarified in Figure 5.8 where, below  $h/c = 0.3$ , the pressure at the suction spike on the suction (bottom) surface starts increasing quite rapidly. This change is caused by the downward movement of the stagnation point as it reduces the flow rate and flow speed in the local region. A similar effect can also be seen at the suction spike on the pressure surface where the pressure reduces

dramatically. The downward stagnation point movement increases the flow rate and flow speed into this region.

**Upright Aerofoil:** From freestream down to  $y/c = 0.10$  ( $h/c = 0.10$  as well), the flow is progressively more constricted as the increasing nozzle effect further hampers the flow under the aerofoil. This trend will divert flow over the top of the aerofoil, shifting the stagnation point downward. Below  $y/c = 0.10$ , the normalised flow rate starts to make a small recovery. This small recovery is indicative of a strong nozzle effect rather than any tangible increase in flow under the aerofoil, which is why the stagnation point continues to fall rapidly in Figure 5.15.

The effect of the flow diversion on the stagnation point and the local flow field is clarified in Figure 5.10. As the clearance is reduced for the upright aerofoil, the suction (top) surface pressure at the suction spike remains constant down to below  $h/c = 0.10$ , below which the suction then increases as the stagnation point moves downward and flow is diverted into this region. Down to about  $h/c = 0.15$ , the suction spike on the pressure surface gradually increases in pressure as the flow rate is stifled and the stagnation point slowly moves down. Below  $h/c = 0.15$ , the pressure increases more quickly with the suction spike eliminated completely at the lowest clearance.

Despite the inverted and upright aerofoils both exhibiting extremely different ground effect phenomena – the former generating a strong diffuser section and the latter generating a nozzle section – both configurations featured the same stagnation point behaviour. This was found to be due to another general ground effect mechanism that diverts flow over the top of the body (regardless of the configuration) at sufficiently low clearances.

### 5.3 Variation of Ground Effect Phenomena about Downforce Generating Aerofoils Caused by Changes in Aerofoil Shape

Ground effect phenomena, and the resulting aerodynamic behaviour of ground effect bodies, are influenced by changes to the combined geometry of the body and ground combination. In terms of aerofoils, this geometry variation can be investigated in several ways; (a) a constant aerofoil shape varying in ground clearance, (b) a constant aerofoil shape varying in angle of attack and, (c) variation of the shape of the aerofoil. Cases (a) and (b) have both been investigated previously (Ranzenbach, 1995; Zerihan and Zhang, 2000; Mokhtar, 2005; and Mahon and Zhang, 2005). Case (c) has not been investigated to any great extent. The distinctly different behaviour between an upright (lift-producing) aerofoil and an inverted (downforce-producing) aerofoil has just been investigated in depth in Sec. 5.2, however, little attention has been paid to understanding the influence on ground effect phenomena of more

subtle changes in the geometry of an aerofoil. This is the purpose of this current investigation.

Two distinctly different aerofoils, the inverted Tyrrell (Zerihan, 2001) and the inverted NACA4412, were chosen for a CFD investigation where the ground effect behaviour of both aerofoils were observed and compared over a range of different ground clearances. This was done to ascertain the differences in ground effect phenomena apparent, due to the geometric differences between the two aerofoils. As mentioned earlier, the Tyrrell aerofoil is the cross-section of the main-plane of the 1998 Tyrrell Formula 1 racing car and, as such, was specifically designed to operate in a ground effect environment. The NACA4412, a common aerofoil used in aerodynamic research, was not designed for use in a ground effect environment.

Comparing two distinct aerofoils is useful in determining the more general performance consequences of using one aerofoil instead of another. However, it is difficult to determine the reasons behind the observed differences in behaviour as there are many variables that change from one aerofoil to the other. It is, therefore, desirable to be able to change only one key performance variable at a time in order to ascertain the causes of the change in performance.

With the above in mind, at a constant ground clearance in the strong ground effect clearance region ( $h/c = 0.30$ ), three additional aerofoils were initially studied to investigate more precisely the influence on ground effect phenomena of three geometric features representing the key differences between the Tyrrell and NACA4412 aerofoils. These three new aerofoils were based on the Tyrrell aerofoil and were designed to replace one feature of the Tyrrell with the corresponding feature of the NACA4412. The three features tested on the modified Tyrrell aerofoils were the leading edge shape, the camber on the top surface (pressure surface) and the camber on the bottom (suction) surface. These modifications will be discussed in more detail in Sec. 5.3.1. Latterly, as a result of this comparison work, two more aerofoils were created to more precisely explain the phenomena in play. This will be discussed in Sec. 5.3.2.2.

Like the prior study in Sec. 5.2, the two-dimensional CFD investigation used a steady RANS solver. The restriction to the two-dimensional case was done in order to highlight the fundamental flow phenomena without the added complexity of wing-tip vortices and other three-dimensional effects.

The model simulated the various aerofoils which could be located at several heights above the ground plane. All aerofoils had a chord  $c = 0.2234$  m and were positioned with an angle of

attack  $\alpha = 6^\circ$  (an increase in the angle of attack indicates an elevation of the trailing edge (TE)). The height above the ground  $h$  was measured from the lowest point of the aerofoil. The freestream velocity was set to a constant 30 m/s at the inlet, achieving a racing car representative Reynolds number of  $Re = 458,800$ . The turbulence intensity (TI) at the inlet was set to 0.1 %. The ground plane was defined as a moving no-slip wall with a velocity equal to the freestream value. The velocity outlet was modelled as an outflow boundary condition which extrapolates the flow properties at the exit boundary from the next upstream interior cell of the grid.

The Tyrrell and NACA4412 aerofoils were simulated at the following ground clearances:  $h/c = 3.00, 2.00, 1.50, 1.00, 0.75, 0.50, 0.40, 0.30, 0.20$  and  $0.15$ .

Finally, it should be noted that the applicability of this numerical model is limited to steady-state cases and, as such, extremely low ground clearances could not be computed while maintaining a steady flow solution – clearances below  $h/c = 0.15$  are inherently unstable and thus could not be simulated.

### 5.3.1 Modified Tyrrell Aerofoils

This section details how the Tyrrell aerofoil was modified to create the three new aerofoils. Figure 5.18: NACA4412 and Tyrrell aerofoils at incidence of  $6^\circ$  shows the Tyrrell and NACA4412 aerofoils at the incidence of  $6^\circ$ . The three main geometric distinctions between the two (leading edge shape, top surface camber and bottom surface camber) are clear to see in the figure.

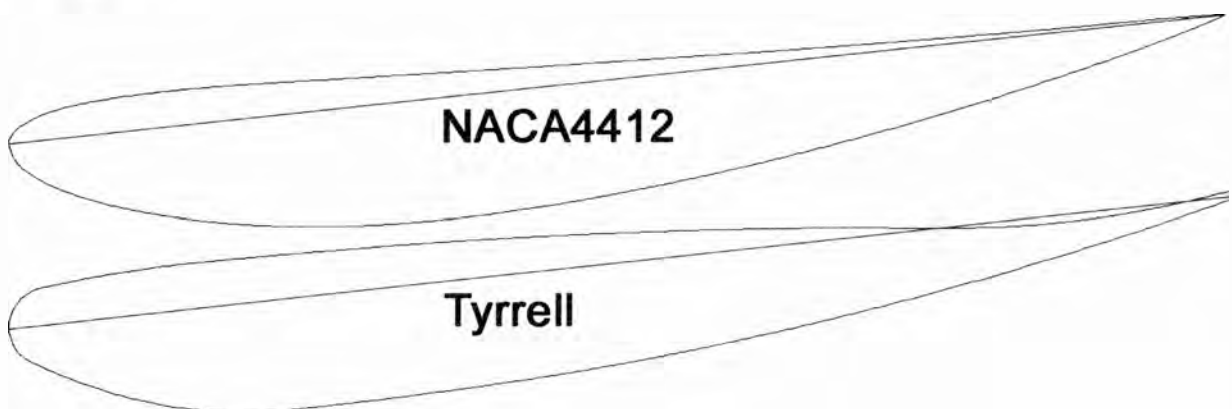


Figure 5.18: NACA4412 and Tyrrell aerofoils at incidence of  $6^\circ$

#### 5.3.1.1 Leading Edge Modification

As can be seen from Figure 5.18, the leading edge (LE) of each aerofoil is quite different. The Tyrrell leading edge features two areas of sharp curvature on the top and bottom surface, between which is a fairly blunt face almost perpendicular to the oncoming airflow. The

NACA4412, by contrast, has a smooth sweeping curve throughout the leading edge region with its sharpest curvature at the front tip of the chord line.

The leading edge modification, or ‘LE Mod’ aerofoil, replaced the leading edge of the Tyrrell with that of the NACA4412. This was achieved by slicing vertically through both aerofoils (whilst set at zero incidence) in the same  $x/c$  location and substituting the leading edge. As the aerofoils are of different shape, much care was taken to choose an  $x/c$  location where the slopes of the aerofoil surfaces were very similar (in order to maintain the slope) and also where the vertical position of the curves were also quite close. This last consideration helped to minimise the required vertical scaling of the NACA4412 leading edge section to fit onto the remaining Tyrrell section and thus helped to maintain the original NACA4412 leading edge geometry, as best as was possible.

Figure 5.19 shows the assessment process for the leading edge cutting location. The slopes of the two aerofoils’ top and bottom surfaces (in degrees) are closest at the location  $x/c = 0.12$ . The distance between the aerofoil surfaces at this location was very close to the minimum values and so  $x/c = 0.12$  was chosen as the cutting location.

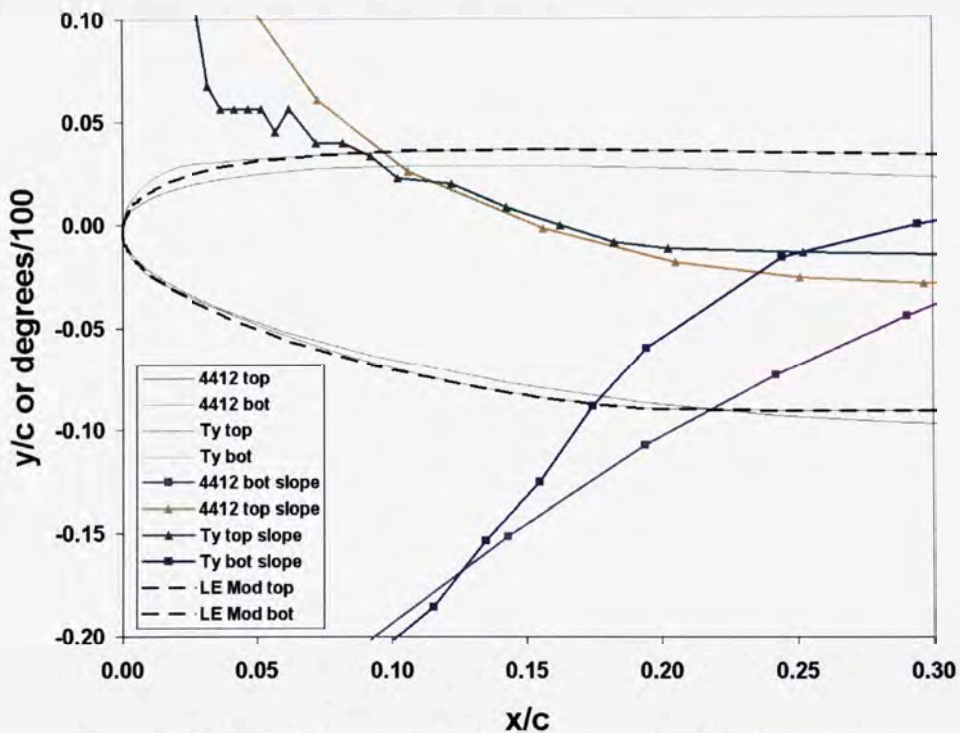


Figure 5.19: LE Mod cutting location assessment and final curvature

The leading edge of the NACA4412 was cut into the top and bottom surfaces and scaled independently to match up with the cutting points on the Tyrrell aerofoil. Both scaling operations were anchored at the tip of the chord line. The resulting aerofoil is shown (partially) in Figure 5.19 and also in Figure 5.20.

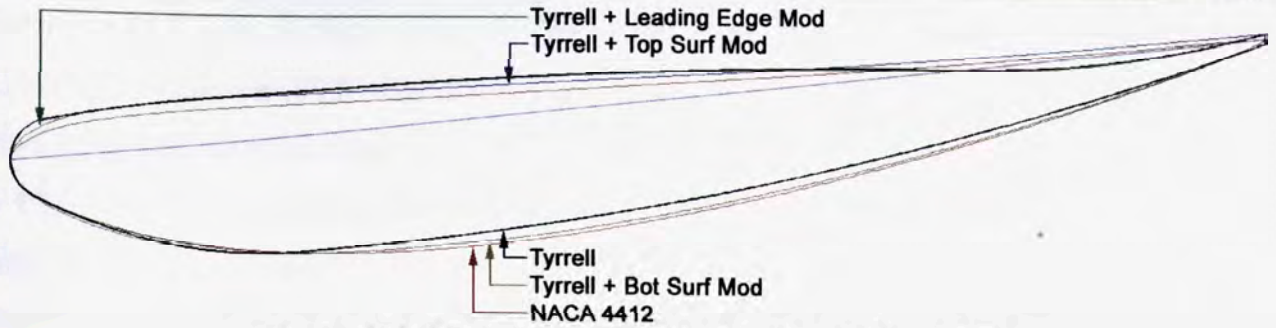


Figure 5.20: Superposition of original and modified aerofoils

### 5.3.1.2 Top Surface Modification

The top surfaces of the aerofoils are very different. The NACA4412 top surface, shortly downstream of the leading edge, forms a long, consistent yet only slight positive camber (concave) all the way to the TE. The Tyrrell aerofoil's top surface maintains a fairly small negative camber (convex) down much of the top surface before switching to a sharp positive camber region about where the top surface passes over the chord line.

The top surface modification, or 'Top Surf Mod' aerofoil, was created in a similar way to the LE Mod aerofoil. With both aerofoils set to zero incidence, an  $x/c$  cutting location for the top surface was chosen where the slope of both Tyrrell and NACA4412 top surfaces were close to zero. This cutting location was chosen to be  $x/c = 0.15$ . The NACA4412 top surface downstream of this location was substituted into the remaining Tyrrell section and was scaled vertically (anchored at the top surface at  $x/c = 0.15$ ) to touch the top of the finite thickness trailing edge of the Tyrrell aerofoil (which was retained). The resulting aerofoil is shown in Figure 5.20.

### 5.3.1.3 Bottom Surface Modification

There are two features of the bottom surface of the Tyrrell aerofoil that differ from the NACA4412 when both aerofoils are set at an incidence of  $6^\circ$ . The first is the location of the lowest point of the aerofoil which was located at  $x/c = 0.20$  for the Tyrrell and  $x/c = 0.25$  for the NACA4412. The second feature of difference is the curvature encountered in the vicinity of and downstream of this point. The Tyrrell curves up quite sharply immediately downstream of its lowest point and then steadily curves up with positive camber until the TE. The NACA4412's lowest point is in the midst of a long gentle curving concave section, with no abrupt changes in curvature downstream of this point. Its curvature further downstream to the TE is similar to the Tyrrell with a consistent positive camber.

Unlike the other modified aerofoils, the bottom surface modification, or 'Bot Surf Mod', was carried out on the Tyrrell aerofoil while set to a  $6^\circ$  incidence, as the position of the lowest point was under consideration. Firstly, the bottom surface of Tyrrell was cut at its lowest

point ( $x/c = 0.20$ ) and the surface downstream of this point was removed. The remaining section of Tyrrell bottom surface, from the leading edge to  $x/c = 0.20$ , was scaled horizontally (anchored at the leading edge of the chord line) so that the new lowest point would be located at  $x/c = 0.25$ . Finally, the bottom surface of the NACA4412 downstream of  $x/c = 0.25$  was substituted into place, anchored at the new lowest point, and scaled vertically so that it touched the bottom of the Tyrrell’s finite thickness TE (which was again retained). This arrangement allowed the lowest point and smooth curvature to mirror that of the NACA4412, while maintaining the Tyrrell leading edge curvature. This modified aerofoil is shown in Figure 5.20.

### 5.3.2 Results and Discussion

#### 5.3.2.1 Tyrrell and NACA4412 Aerofoil Comparison

##### 5.3.2.1.1 Force Behaviour

The results of the normal force coefficient  $C_n$  for both aerofoils is presented in Figure 5.21. It should be reiterated that the data points not linked to a trend line indicate the ‘freestream’ performance, far from the ground. As such, these data points are located at in the figures at  $h/c = 3.4$  merely for convenience – they were simulated at freestream. This practise is used throughout.

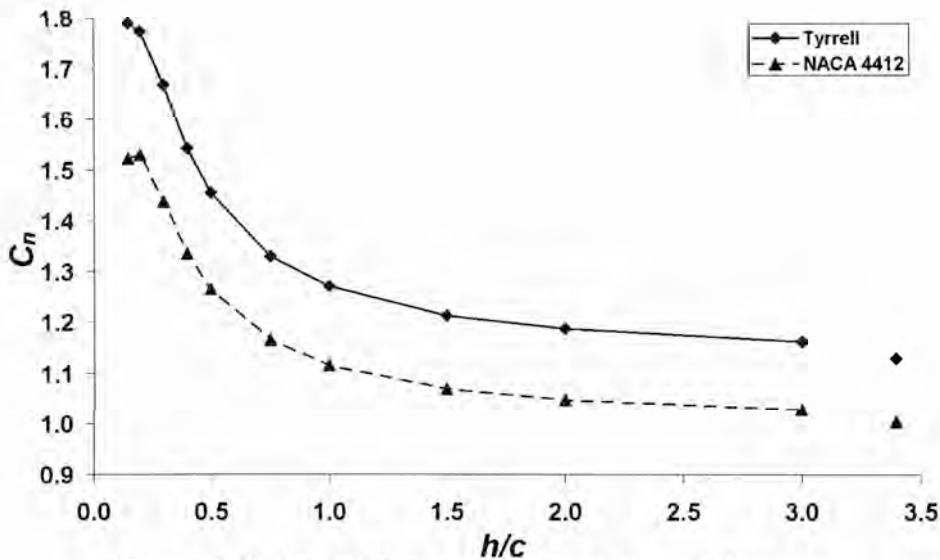


Figure 5.21: Normal force coefficients vs. ground clearance

As the ground clearance of the aerofoil is reduced, an increasingly more aggressive diffuser configuration is formed between the bottom of the aerofoil and the ground. This has been shown to bring about significant changes in aerodynamic performance and this is visible in Figure 5.21 as both aerofoils exhibit an increase in downforce as their clearance is reduced.

The Tyrrell aerofoil consistently produces more downforce than the NACA4412 and this gap is widened at lower clearances. This result indicates that the Tyrrell aerofoil’s geometry

allows it to benefit from the diffuser configuration to a greater extent than the NACA4412 geometry, as the diffuser configuration is the only variable changing for both aerofoils. Additionally, by  $h/c = 0.15$ , the NACA4412 appears to have stalled as its normal force increase (with decreasing clearance) abruptly disappears with the aerofoil producing less downforce than at the next lowest clearance. This is a sharp stall which appears to be more aggressive than the plateau developing on the Tyrrell aerofoil's normal force trend at this lowest clearance. Without more data points, it is difficult to establish how quickly the stalling behaviour would develop on the Tyrrell aerofoil below this point, suffice to say that it appears to be less aggressive than the NACA4412 case, as the NACA4412 peak in Figure 5.21 is more abrupt than the Tyrrell peak.

The drag coefficient  $C_d$  data presents a similar story to the normal force data and is presented in Figure 5.22. The Tyrrell consistently produces more drag than the NACA4412 and this gap is again enlarged at low clearances. The development of the diffuser section, and the associated strengthening of this ground effect phenomenon, clearly constitutes a significant drag component as well as a downforce component. The drag force, being an element of this ground effect phenomenon, is clear as the NACA4412 (which appears to experience the phenomenon less strongly than the Tyrrell) features a smaller increase in drag.

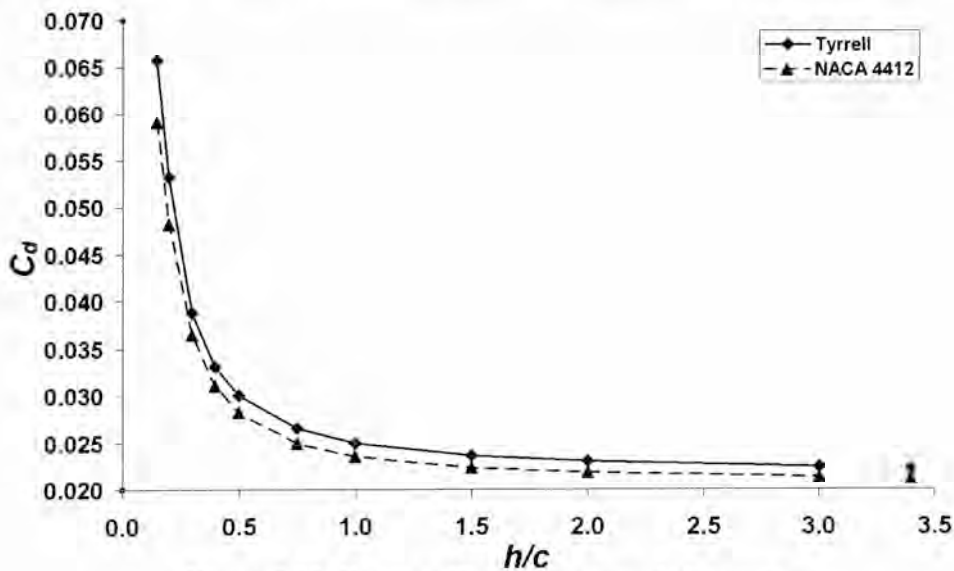


Figure 5.22: Drag coefficient vs. ground clearance

For increased clarity as to what is contributing to the force behaviour changes on the aerofoils, the force data were broken down into top and bottom surface components and also friction and pressure subcomponents. The normal force coefficients from Figure 5.21 are replotted in component form in Figure 5.23. Similarly, the drag coefficient data from Figure 5.22 are replotted in Figure 5.24.

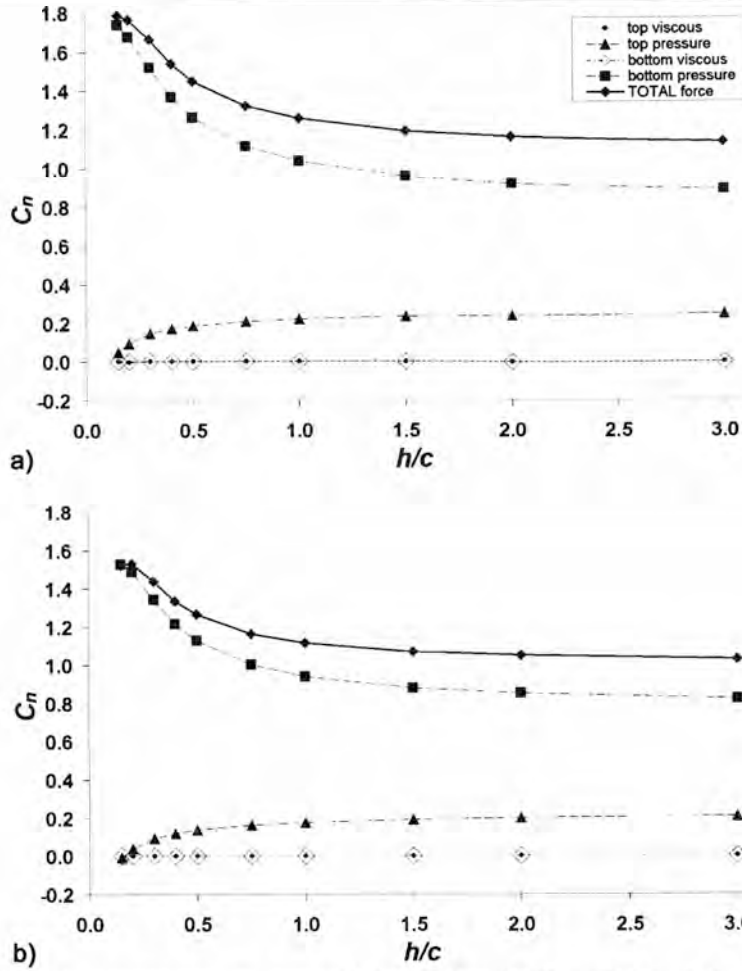


Figure 5.23: Normal force components vs. ground clearance; (a) Tyrrell aerofoil, (b) NACA4412 aerofoil

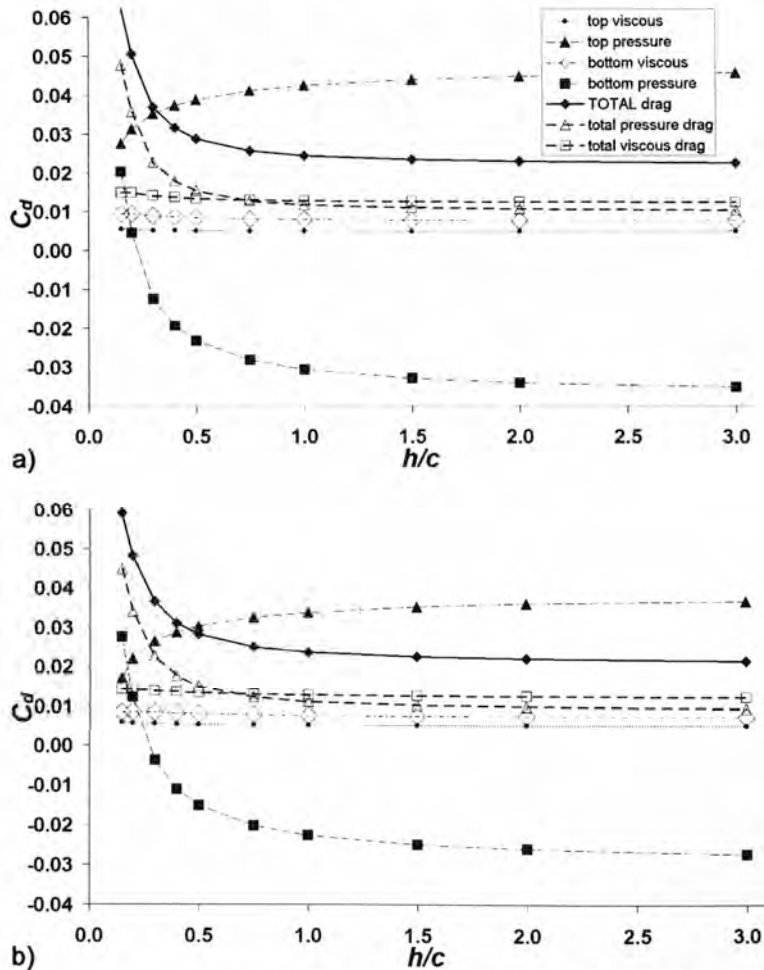


Figure 5.24: Drag force components vs. ground clearance; (a) Tyrrell aerofoil, (b) NACA4412 aerofoil

From Figure 5.23, it is clear that the top surface pressure component of normal force follows a very similar trend for both aerofoils, albeit in slightly different positions with the NACA4412 trend at a consistently lower position. The bottom surface pressure component shows a different relationship where the Tyrrell trend is a magnification of the NACA4412 trend. Its displacement from the NACA4412 trend enlarges with decreased clearance. These results indicate that the flow over the top of both aerofoils is not influenced to any great extent by the diffuser effect developed under the wing as both aerofoils (experiencing different levels of the diffuser effect) show a very similar top surface trend. As we shall see in Sec. 5.3.2.2, however, the same cannot be said of the reverse situation – the top surface flow’s influence on the diffuser effect.

The drag force components in Figure 5.24 present an unintuitive pressure force component trend, with a highly negative (thrust producing) bottom surface and a highly positive top surface, for most of the clearance range. This is mainly due to the location of the stagnation point (see Sec. 5.2.5), but is not of primary importance here. For clarity, therefore, total pressure and total viscous force trends are included in this figure in order to present their overall effect.

The drag force pressure components trends are similar between the two aerofoils. They follow the same trend but are slightly different with the Tyrrell bottom surface pressure drag more negative than its NACA4412 counterpart. The opposite is true for the top surface pressure drag trends. Despite these obvious differences, the superposition of the top and bottom pressure force components results in a similar trend for both aerofoils. The Tyrrell aerofoil exhibits a higher pressure thrust from its bottom surface than the NACA4412, however this is countered by a greater positive pressure drag contribution from the Tyrrell’s top surface compared to the NACA4412 top surface. The net results are quite similar with the Tyrrell showing slightly higher drag values.

The reason for the bottom surface thrust seen on both aerofoils (and the subsequent reduction at low clearances) is demonstrated in Figure 5.25 where the pressure coefficient distribution  $C_p$  for two ground clearances, is plotted normal to the surface of both the Tyrrell and NACA4412 aerofoils, in order to indicate the direction of the resulting pressure force at each location on the aerofoil. At  $h/c = 1.00$ , on both aerofoils, the sections of the lower surface whose normal vector points (in part) upstream, feature greater suction than those sections whose normal vector points downstream. This is particularly so for the Tyrrell aerofoil. At the lower clearance of  $h/c = 0.15$ , this phenomena is much reduced with the partially-

downstream facing surfaces having gained significantly more suction. Consequently, the thrust produced at the higher clearance, on the lower surface, is now significantly reduced.

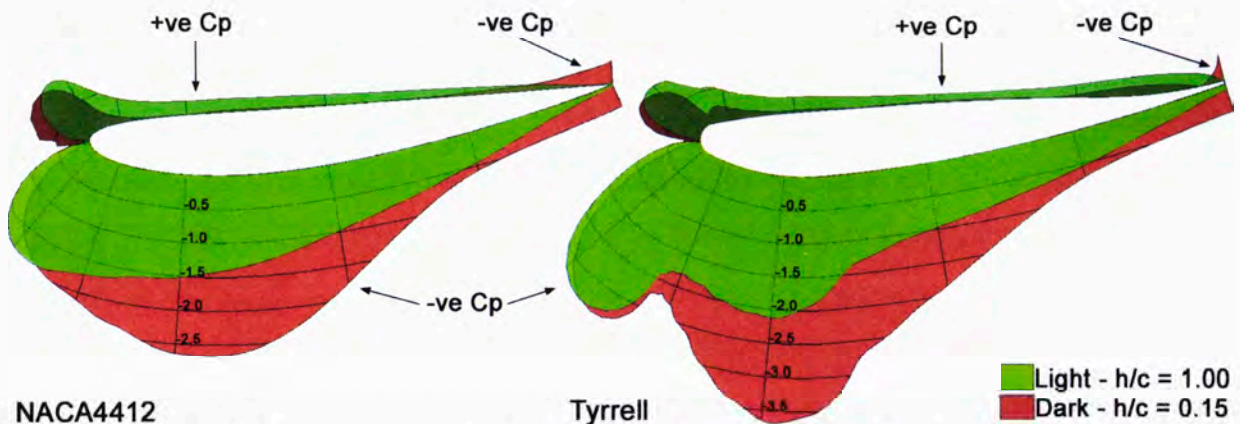


Figure 5.25: Pressure coefficient distributions plotted perpendicular to aerofoil surface

### 5.3.2.1.2 Pressure Coefficient Distributions

The  $C_p$  distribution for the Tyrrell is shown in Figure 5.26(a) and the NACA4412 distribution in Figure 5.26(b). One of the most obvious points of difference between the two distributions is the presence of leading edge ‘suction spikes’ on the Tyrrell distribution, located on both the top and bottom surfaces. These are visible on the figure as sudden negative dips near the leading edge and are the result of sharp increases in velocity due to the strong curvature at these locations.

Another distinction between the two configurations is the shape of the ‘maximum suction region’ between about  $0.1 < x/c < 0.2$  for the Tyrrell and between about  $0.2 < x/c < 0.3$  for the NACA4412 (this term is used despite the fact that at several clearances it is lower in magnitude than the bottom surface suction spike). Downstream of the suction spike, the Tyrrell shows an increase in suction to a maximum (minimum  $C_p$ ), followed by an abrupt increase in pressure which then settles into a consistent adverse pressure gradient region. This behaviour is maintained for all clearances with the suction strengthening with reduced clearance.

The NACA4412 aerofoil behaves quite differently. The maximum suction region doesn’t exist until very low clearances and, even then, the  $C_p$  values achieved are much less negative than those seen on the Tyrrell. At high clearances, the suction is at its greatest near the leading edge and then starts to deteriorate downstream through a consistent adverse pressure gradient region. As clearance is reduced, the suction around the leading edge increases, resulting in a slightly steeper adverse pressure gradient. For  $h/c = 0.75$  and below, however, the increase in suction, observed relative to the next higher clearance, shows a maximum change in the region between  $0.2 < x/c < 0.3$ . This change in the general shape of the pressure

coefficient distribution is something that was not observed on the Tyrrell aerofoil. This change in behaviour occurred because the diffuser/venturi affected throat region ( $0.2 < x/c < 0.3$ ) strengthened at a faster rate than the leading edge region. The suction trend near the leading edge reverses and starts to decrease through the lowest two clearances shown in Figure 5.26(b). This is brought on by the increasing constriction of the flow under the aerofoil at extremely low clearances. In this situation, the stagnation point progressively moves downward and the flow in the vicinity of the bottom surface leading edge is slowed, reducing suction.

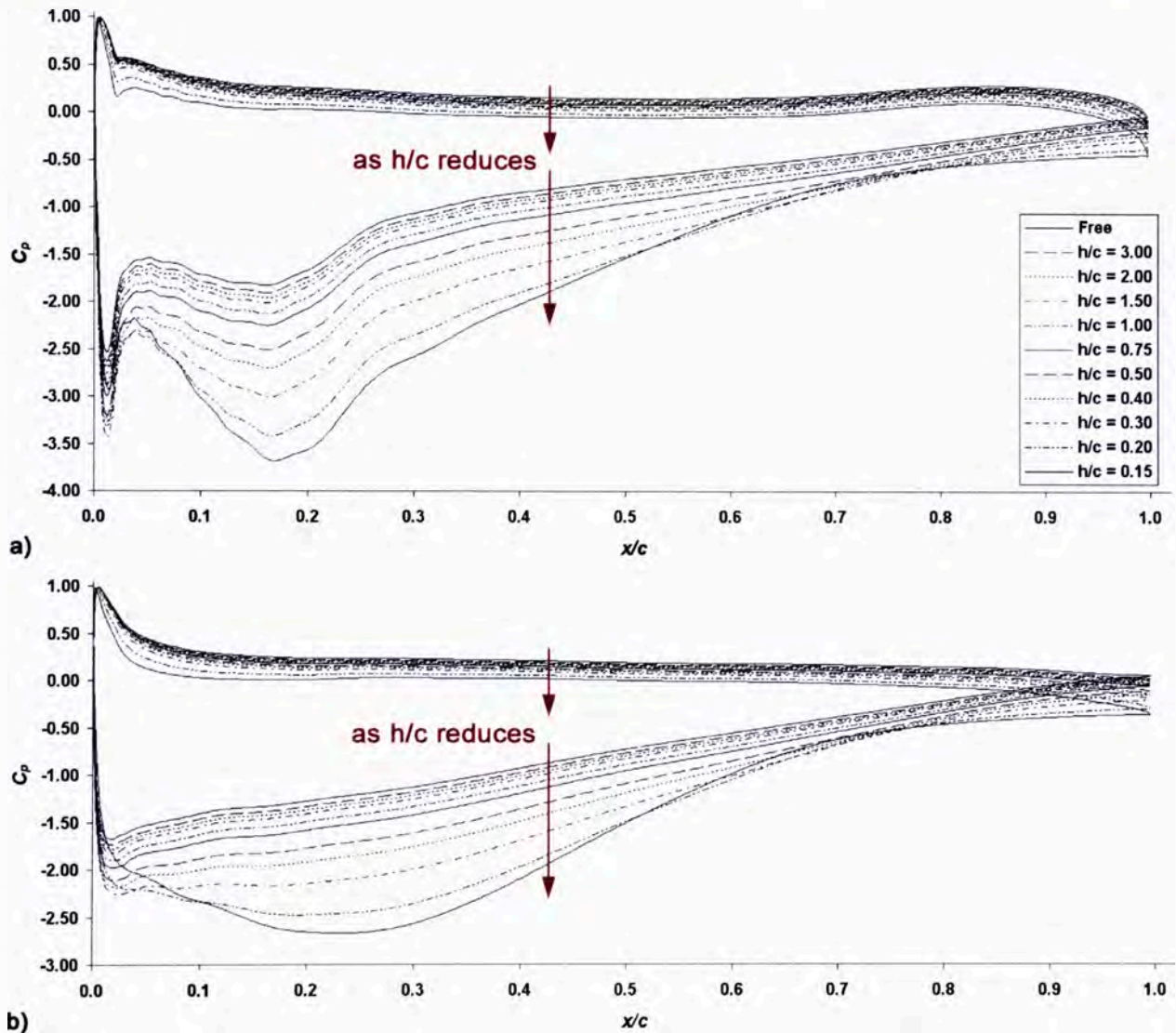


Figure 5.26: Pressure coefficient distributions at various ground clearances; (a) Tyrrell aerofoil, (b) NACA4412 aerofoil

Another point of difference is the lack of a sudden increase in pressure as seen on the Tyrrell aerofoil. Downstream of  $x/c = 0.3$ , both aerofoils show similar adverse pressure gradient trends except that the NACA4412 trend, at any given clearance, is slightly steeper. This results in the NACA4412 featuring greater flow separation at the lowest clearances.

The final feature of difference between the two aerofoils is a localised pressure increase on the top surface of the Tyrrell aerofoil near the TE. This feature remains consistent throughout the clearance range and is absent from the NACA4412 aerofoil.

The explanations for the various different pressure coefficient plot characteristics were not immediately apparent from this analysis. Consequently, the modified aerofoils were created in order to isolate the geometric features thought to be causing these distinct behaviours and so, identify the cause of the behaviours noted above. These analyses are discussed in Sec. 5.3.2.2.

### 5.3.2.1.3 Dividing Streamlines

An analysis of the dividing streamline position, as previously discussed in Sec. 5.2.4 is performed here for the Tyrrell and NACA4412 aerofoils. The results are shown in Figure 5.27.

Both aerofoils follow the same trend where the upward deflection of the dividing streamline from the leading edge datum, up and downstream, is reduced with clearance. This is caused by the reducing volume of air that is able to be directed under the aerofoil with reduced clearance (which is not sufficiently offset by the increased flow speed under the aerofoil). For a full explanation of this downward movement phenomena about inverted aerofoils, see Appendix B.

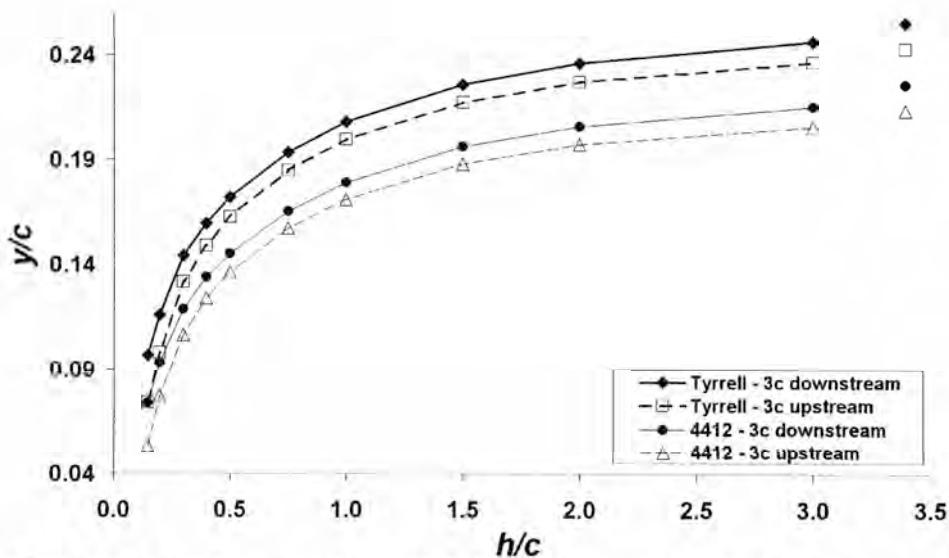


Figure 5.27: Position of dividing streamlines at 3 chords distance from aerofoils vs. ground clearance

Both aerofoils show that the downstream flow is slightly more deflected than the upstream flow and that this difference is magnified slightly at low clearances. Additionally, the Tyrrell aerofoil's flow deflection is consistently greater than the NACA4412, indicating that the Tyrrell is more highly cambered than the NACA4412. The gap between the aerofoil trends

reduces at low and very low clearances which suggests that the additional flow volume that is sucked under the Tyrrell (relative to the NACA4412) diminishes at low clearances.

### 5.3.2.1.4 Stagnation Point

The vertical stagnation point position, relative to the leading edge position, is plotted in Figure 5.28: Stagnation point position vs. ground clearance against ground clearance. The stagnation point position is of some interest as it is the termination point of the dividing streamline and thus represents the point at which the oncoming flow is dividing between that travelling over and under the aerofoil.

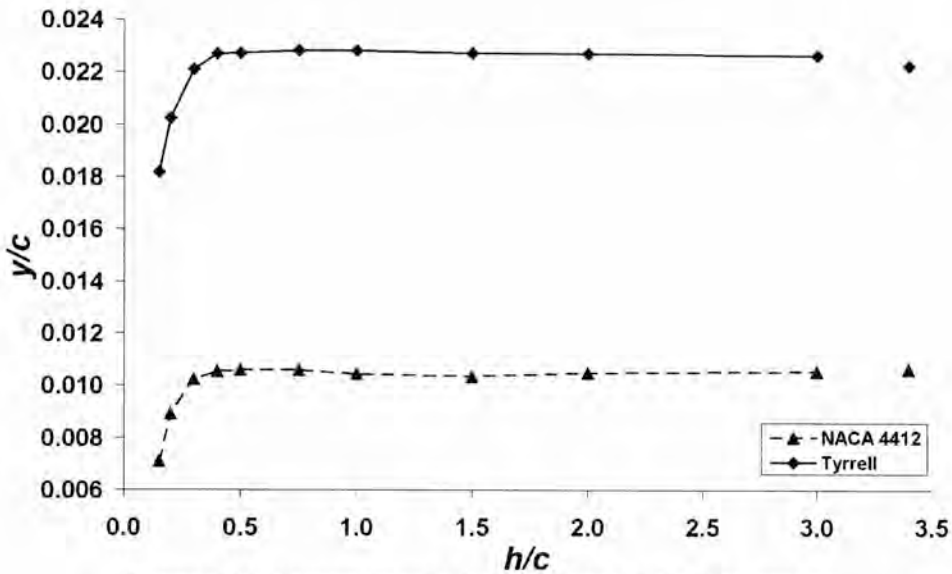


Figure 5.28: Stagnation point position vs. ground clearance

The trends of both aerofoils are similar but displaced vertically from each other. The stagnation point of both trends remains fairly steady down to  $h/c = 0.40$ . Below this height, both trends start to move downward rapidly. The Tyrrell aerofoil's downward movement is more pronounced than the NACA4412's.

As argued in Sec. 5.2.5, the movement of the stagnation point, under the influence of ground effect, is influenced primarily by both the constriction of the flow under the aerofoil (which occurs at low clearances) and by the influence of the local flow field, controlled by the suction spike behaviour. The constriction of the flow at low clearances is demonstrated in Figure 5.29 where the volume flow rate passing under the two aerofoils is normalised by the 'ideal' flow rate that would be expected from an uninterrupted (freestream) flow through a channel the same height as the trailing edge height above the ground (at the given clearance). If a value in Figure 5.29 is greater than 1.0, the average flow under the aerofoil is faster than freestream, pumping through more volume than would an uninterrupted channel of the same size. If the value is less than 1.0, the flow is being constricted by the space limitations under the aerofoil. The former case ( $>1.0$ ) necessitates more flow to be diverted under the aerofoil

and results in an upward positioning of the dividing streamline and a slight upward positioning of the stagnation point. The latter case induces the opposite.

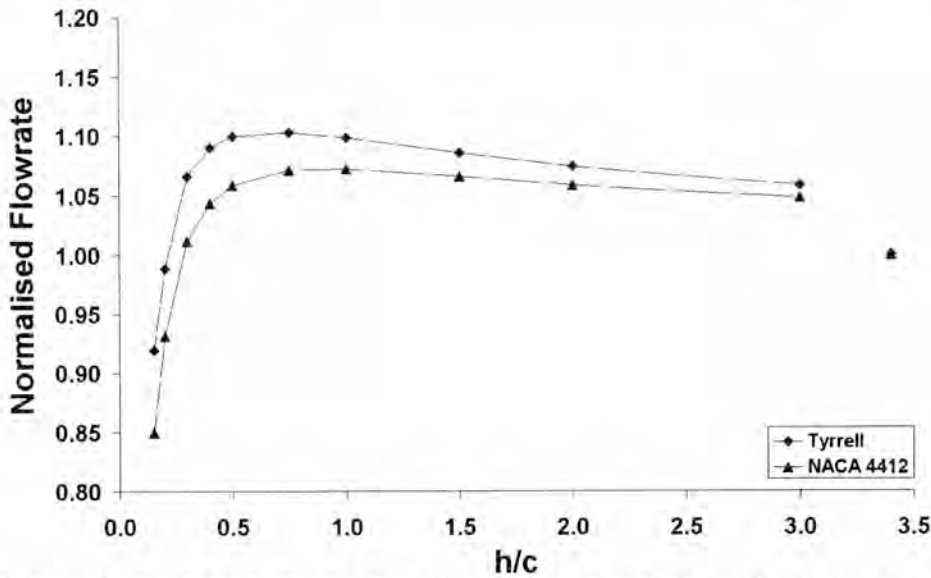


Figure 5.29: Volume flow rate under aerofoils, normalised by ‘ideal’ flow rate at given ground clearance vs. ground clearance

Figure 5.29 shows that the normalised flow rate under both aerofoils is increased above ‘ideal’ conditions for much of the clearance range. The flow starts to be limited by  $h/c = 0.75$  and the normalised flow rate falls dramatically below clearances of about  $h/c = 0.40$ . This constriction of the flow, in part, induces the downward shift in stagnation point observed in Figure 5.28, due to the diversion of air over the top of the aerofoils, shifting the stagnation point (and dividing streamline) downward.

Additionally, the local flow field influences the stagnation point position. For the Tyrrell aerofoil at low clearances, the strengthening of the suction spike on the top surface and the weakening of the suction spike on the bottom surface, both induce a downward movement of the stagnation point. For the NACA4412 aerofoil, the local flow has less of an impact on stagnation point position as the top surface does not feature a dramatic local flow feature (suction spike) in the vicinity of the stagnation point. The bottom surface is also less likely to shift the stagnation point as much as the Tyrrell, as it also lacks a suction spike but the pressure variations near the stagnation point at the lowest clearances are similar to those of the Tyrrell bottom surface.

The influence of the local flow field helps explain why, although the Tyrrell encounters less flow constriction, its stagnation point movement is larger. The consistently superior normalised volume flow rate enjoyed by the Tyrrell in Figure 5.29, shows how the diffuser effect is utilised more effectively to take advantage of ground effect. Additionally, the Tyrrell’s superior resilience to flow constriction in Figure 5.29 may also be a contributing reason to its more gradual stalling behaviour in Figure 5.21.

Finally, the displacement between the Tyrrell and NACA4412 plots in Figure 5.28: Stagnation point position vs. ground clearance is an indication of the greater camber and induced flow circulation about the Tyrrell aerofoil. At low clearances, the downward movement of the stagnation point about both aerofoils, is an indication of the reduction in circulation suffered by the aerofoils due to the flow constriction.

### 5.3.2.2 Modified Tyrrell Aerofoils Comparison

#### 5.3.2.2.1 Pressure Coefficient Distributions

Presented in Figure 5.30 are the pressure coefficient distributions for the five primary aerofoil configurations considered in this work: the Tyrrell aerofoil, its three modified forms and the NACA4412 aerofoil. All are presented at a high ground effect clearance of  $h/c = 0.30$  and an incidence of  $\alpha = 6^\circ$ . This figure is very useful as it allows the influence of various geometric features on the pressure coefficient plots to be isolated.

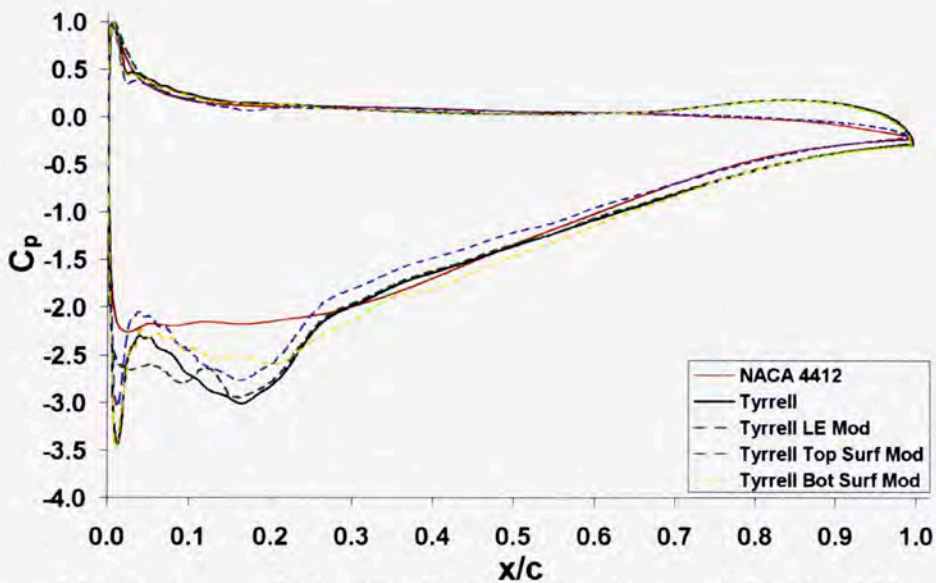


Figure 5.30: Pressure coefficient distributions for various aerofoils;  $h/c = 0.30$ ,  $\alpha = 6^\circ$

The leading edge modified (LE Mod) aerofoil removes the sharp curvature from the top and bottom of the Tyrrell's leading edge (replacing it with the more consistent curve of the NACA4412) but maintains the rest of the original Tyrrell geometry. Figure 5.30 shows that the result of this modification is the absence of a suction spike on either the top or bottom surface near the leading edge, with the  $C_p$  plots following the general form of the NACA4412 in this region (which is logical as it features its leading edge geometry here). Of particular interest on the LE Mod plot is that the absence of the leading edge suction spikes do very little to change the  $C_p$  plot further downstream. The maximum suction region does not appear to be influenced to any great extent by the flow features preceding it. As shown in Table 5.1, the downforce and drag produced by the LE Mod configuration is only very slightly below that of the Tyrrell aerofoil.

**Table 5.1: Downforce and drag coefficients;  $h/c = 0.30$ ,  $\alpha = 6^\circ$ , T = Tyrrell, N = NACA4412**

	<b>Tyrrell</b>	<b>NACA4412</b>	<b>BS Mod</b>	<b>TS Mod</b>	<b>LE Mod</b>
$C_n$	1.6687	1.4375	1.6584	1.4559	1.6531
		T -13.86 %	T -0.62 %	T -12.75 %	T -0.93 %
	N +16.08 %		N +15.37 %	N +1.28 %	N +15.00 %
$C_d$	0.03883	0.03651	0.04097	0.03512	0.03872
		T -5.97 %	T +5.51 %	T -9.55 %	T -0.28 %
	N +6.35 %		N +12.22 %	N -3.81 %	N +6.05 %
$n/d$	42.97	39.37	40.48	41.46	42.69
		T -8.38 %	T -5.79 %	T -3.51 %	T -0.65 %
	N +9.14 %		N +2.82 %	N +5.31 %	N +8.43 %

The top surface modified (TS Mod) aerofoil features a far less cambered top surface compared to the Tyrrell and, as such, the pressure increase toward the trailing edge on the Tyrrell aerofoil top surface is not present on this modified version. Rather, it follows the trend of the NACA4412 in this region. Despite the fact that the remainder of the geometry (leading edge and entire bottom surface) is identical to the Tyrrell geometry, this aerofoil functions far less well with a consistent reduction in suction over all of these areas. It follows the same trend as the Tyrrell in all these areas but with a lesser magnitude indicating that the same flow mechanisms are present but are simply less effective. This would appear to be because of the reduction in circulation caused by the lack of camber present on the top surface. This aerofoil produces 12.8 % less downforce than the Tyrrell aerofoil, simply because it lacks the upper surface camber. Because of its reduction in suction, this aerofoil also sees a fairly significant reduction in drag as well, at 9.6 %. The upper surface camber, therefore, appears to be of great importance in the overall production of downforce in the ground effect regime.

The bottom surface modified (BS Mod) aerofoil maintains the top and bottom surface suction spikes near the leading edge, as it maintains the Tyrrell leading edge geometry. The maximum suction region of this aerofoil is significantly weaker than the equivalent Tyrrell region, however, is it also a fair bit stronger than the NACA4412 trend in this region. This latter comparison is significant as it is the NACA4412 geometry that is in place in this region and also downstream to the trailing edge. The curvature immediately downstream of the lowest point is smoother than the Tyrrell's and consequently, the  $C_p$  trend sees a less abrupt increase in pressure through this region as one would see on the Tyrrell trend. From this point back to the trailing edge, the adverse pressure gradient region follows the NACA4412 trend, albeit at a slightly higher suction. Despite a reduced maximum suction region, this modified aerofoil regains sufficient suction over the adverse pressure gradient region to produce almost as much downforce as the original Tyrrell aerofoil (only 0.6 % less). However, this aerofoil also suffers a 5.5 % increase in drag.

A few conclusions can be drawn at this stage about the effect of aerofoil geometry on ground effect behaviour:

- (1) The LE Mod aerofoil results indicate that the leading edge spike has no notable influence over aerofoil performance. This is likely because the high speed throat flow immediately downstream of the suction spike essentially maintains the flow through this region as laminar.
- (2) The TS Mod aerofoil results shows that the absence of camber on the top surface significantly reduces suction on the bottom surface and slightly increases suction on the top surface – both detrimental to performance and indicative of a reduction in circulation. This reduction in circulation reduces the effectiveness of the diffuser effect.
- (3) The BS Mod aerofoil showed a much improved performance on the bottom surface compared to the NACA4412 bottom surface and this was exclusively due to the presence of the top surface camber (point 2) as the other geometric difference to the NACA4412, the suction spike, was determined to have no effect (point 1).
- (4) Additionally, the BS Mod aerofoil showed that the NACA4412 bottom surface is less effective at producing a large suction region under the aerofoil, when compared to the Tyrrell.

The underlying cause for this last observation in point 4 was hard to determine and so an additional modified aerofoil, the ‘New Mod’ aerofoil, was developed to help answer this question. This aerofoil maintained the  $x/c$  position of the lowest point of the Tyrrell aerofoil (whereas the BS Mod shifted it back to the NACA4412 lowest point position) and incorporated the smoother curve of the NACA4412 bottom surface (like the BS Mod, but starting further forward). This was achieved by retaining the Tyrrell geometry from the leading edge to its lowest point ( $x/c = 0.20$ ) and replacing it downstream with the NACA4412 geometry (scaled slightly to extend forward to the Tyrrell’s lowest point) which continues to the trailing edge. The Tyrrell top surface remained. This New Mod geometry compared with the Tyrrell is shown in Figure 5.31, a comparison of  $C_p$  plots is shown in Figure 5.32 and the downforce and drag results are shown in Table 5.2.

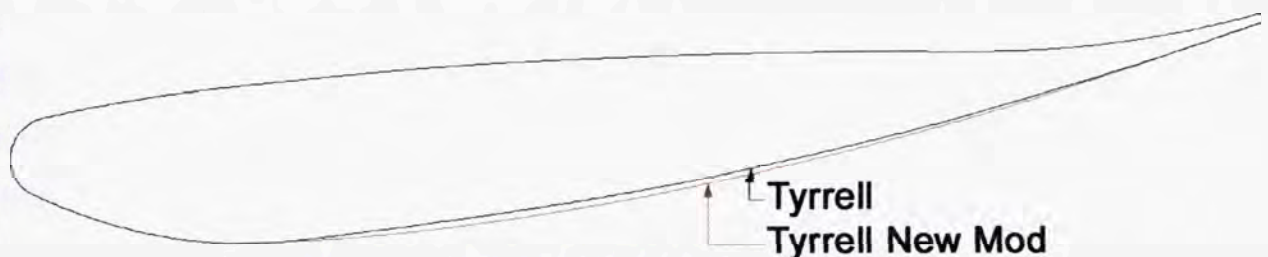


Figure 5.31: Tyrrell and New Mod geometry comparison

When the New Mod aerofoil is compared to the BS Mod in Figure 5.32 – bearing in mind that the only difference between these aerofoils is the location of the lowest point – it is clear that the more forward location of the lowest point causes a significant enhancement to the suction in the maximum suction region and also causes a similarly large increase in the sudden jump in pressure immediately downstream of this region. The differences in Figure 5.32 are quite significant considering the lowest point was only moved forward by  $x/c = 0.05$ .

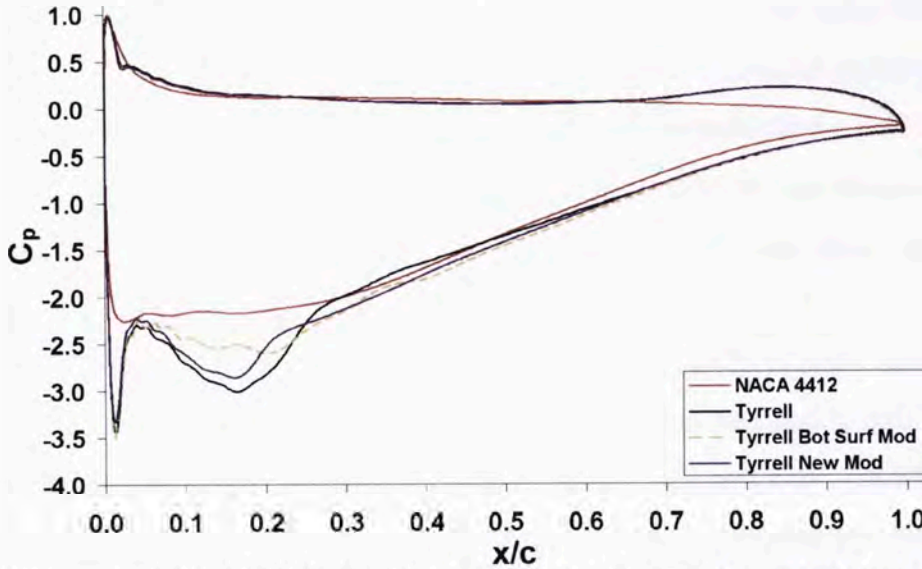


Figure 5.32: Pressure coefficient distributions for New Mod and comparison aerofoils;  $h/c = 0.30$ ,  $\alpha = 6^\circ$

Table 5.2: Tyrrell New Mod results and comparison;  $h/c = 0.30$ ,  $\alpha = 6^\circ$ , T = Tyrrell

	Tyrrell	BS Mod		New Mod	
$C_n$	1.6687	1.6584	T -0.62 %	1.6665	T -0.13 %
$C_d$	0.03883	0.04097	T +5.51 %	0.03996	T +1.03 %
$n/d$	42.97	40.48	T -5.79 %	41.70	T -2.96 %

When compared to the original Tyrrell aerofoil, it appears that using the NACA4412 bottom surface on the New Mod aerofoil (with its smoother upward curve, see Figure 5.31) actually stifles the diffuser effect resulting in lower suction in the maximum suction region. This also results in a less sudden jump in pressure. It is argued here that the smoother upward curve allowed the diffuser less space to take effect and so reduces its effectiveness.

In considering the influence on ground effect performance, it would appear that achieving good suction in the maximum suction region is more effective than achieving a more balanced suction over the entire underside of the aerofoil. The lift to drag ratio ( $n/d$ ) results for the Tyrrell and Bot Surf Mod aerofoils in Table 5.1 indicate this. The reason for this is simply that the vectors of the suction forces in the maximum suction region point either vertically down or slightly forward, whereas the suction of the remaining bottom surface of the aerofoil will have a rearward (drag) component.

Another interesting observation is that the NACA4412 suffers flow separation earlier than the Tyrrell, despite not featuring an abrupt increase in pressure after the maximum suction region. It may be the case that employing a sudden increase in pressure, as on the Tyrrell, is actually advantageous by ensuring that the downstream adverse pressure gradient region will be less strong (smaller slope) and, thus, less likely to cause separation. Additionally, the sudden pressure increase, although sucking a large amount of energy from the flow, may be tapping the flow in such a high energy location that its disturbance would never be sufficient to induce immediate separation (regardless of ground clearance) and thus help protect the aerofoil against separation at low clearances by allowing the flow to transition to a low adverse pressure gradient state without risk of separation in the process. This theory, however, needs further investigation.

### 5.3.2.2 Velocity Contours and Turbulence Intensity

Velocity contour plots for the NACA4412, the Tyrrell and the three primary modified aerofoils are presented in Figure 5.33. It is clear from the figure that there is no significant variation between the aerofoils. Worth noting, however, are: the increased velocity under the Tyrrell compared to the NACA4412; the increased velocity under the BS Mod aerofoil compared to the TS Mod aerofoil, as the former maintains a more consistent suction on its bottom surface; and finally, the notable similarity in the wake flow of all the aerofoils – in terms of thickness, direction and velocity deficit – is indicative that most of the variation in drag observed between these aerofoils is caused by variations in pressure drag.

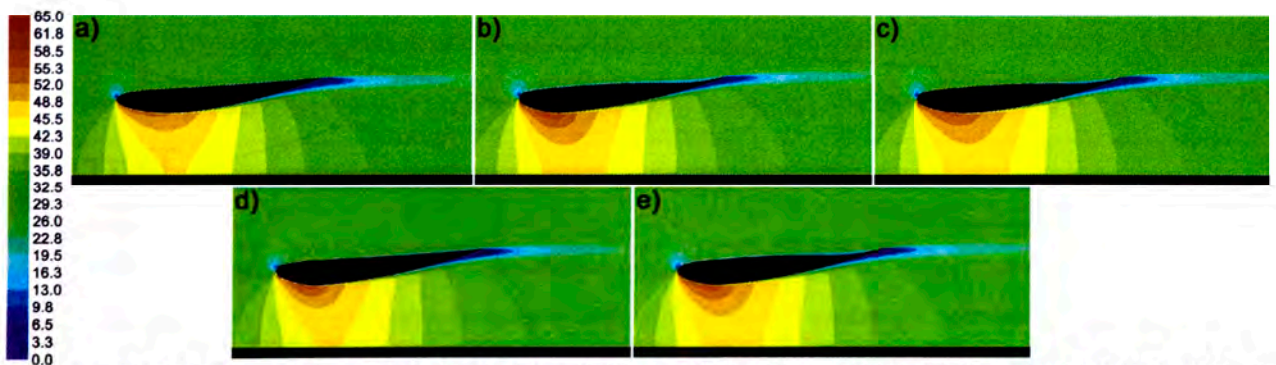


Figure 5.33: Velocity contour plots (m/s),  $h/c = 0.30$ ,  $\alpha = 6^\circ$ ; (a) NACA4412, (b) Tyrrell, (c) Bot Surf Mod, (d) Top Surf Mod, (e) LE Mod

The turbulence intensity plots in Figure 5.34 are also very similar. However, there is a difference in the TI pattern in the wake between the aerofoils that have Tyrrell bottom surfaces (Tyrrell, LE Mod and TS Mod) and those that have NACA4412 bottom surfaces (NACA4412 and BS Mod). The latter cases produce a slightly higher peak TI percentage in the wake compared to the former cases. This observation is interesting as it indicates that the bottom surface geometry is the primary influence on the wake TI behaviour. Although, when

compared to the drag values in Table 5.1, it is evident that these slightly elevated TI values in the wake are not necessarily indicative of higher overall drag values, putting further weight on the argument that drag is more dominated by its pressure component in this ground effect configuration.

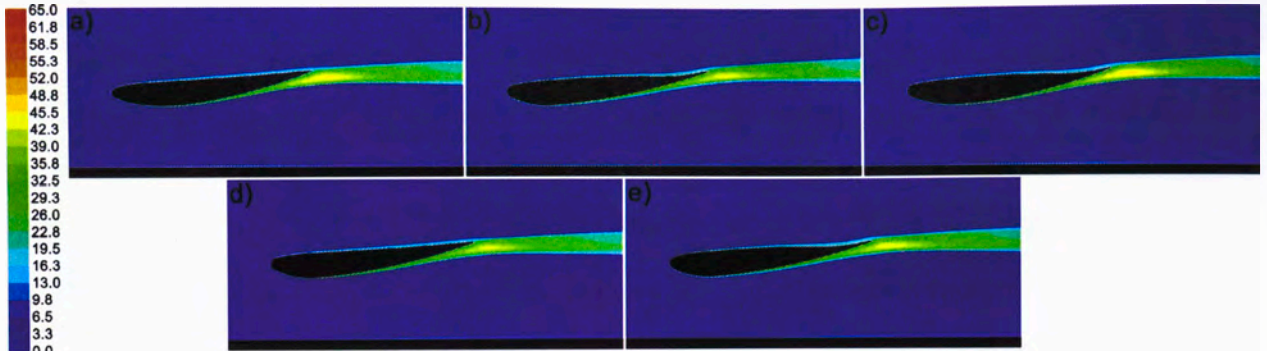


Figure 5.34: Turbulence intensity contour plots (%),  $h/c = 0.30$ ,  $\alpha = 6^\circ$ ; (a) NACA4412, (b) Tyrrell, (c) Bot Surf Mod, (d) Top Surf Mod, (e) LE Mod

### 5.3.2.2.3 Development of New ‘Vogt’ Aerofoil

In order to exploit the ground effect behaviour just discussed, a new aerofoil, again modified from the Tyrrell aerofoil, was developed and dubbed the ‘Vogt’ aerofoil. This aerofoil, shown in Figure 5.35, differs from the Tyrrell in two respects: firstly, the camber on the top surface has been increased significantly (and fairly arbitrarily) in order to increase circulation about the wing and therefore facilitate a strong diffuser effect; secondly, the lowest point on the wing (when held at 6 degrees incidence) was shifted forward from  $x/c = 0.20$  arbitrarily to  $x/c = 0.15$  to promote a greater peak suction region under the wing.



Figure 5.35: Tyrrell and Vogt geometry comparison

A comparison of the  $C_p$  plots of both the Vogt and Tyrrell aerofoils, when operating at 6 degrees and  $h/c = 0.30$ , is shown in Figure 5.36. The increased camber on the top surface had the desired effect in that positive pressure was increased universally on the top surface and particularly near the TE, and also suction was increased near the TE on the bottom surface. The forward placement of the lowest point of the aerofoil induced a modest increase in the suction spike and a large increase in suction in the peak suction region. Additionally, because the steep upward curve of the Tyrrell was maintained on the Vogt aerofoil, the pressure aft of the peak suction region increases rapidly and develops into a steady and not-excessive adverse pressure gradient – a less severe one, in fact, than the Tyrrell.

The force comparison between the two aerofoils is shown in Table 5.3. The Vogt aerofoil outperforms the Tyrrell in downforce by 7.17 %. The drag increases by a similar amount and so the  $n/d$  ratio remains about the same, with a slight reduction. This performance gain is useful in the ground effect regime as a similar downforce increase achieved through increasing the angle of incidence of the Tyrrell aerofoil would put the aerofoil at a greater risk of separation, owing to a larger adverse pressure gradient, and would also come with a larger drag penalty as incidence increases in ground effect invariably (and significantly) reduce the lift-to-drag ratio (Mokhtar, 2005). The Vogt aerofoil, therefore, represents a tangible design improvement when operating in the ground effect regime. It should also be noted that the Vogt aerofoil does not represent an optimised design as, although the modifications made to the Tyrrell design were targeted, the magnitude of those modifications were quite arbitrary.

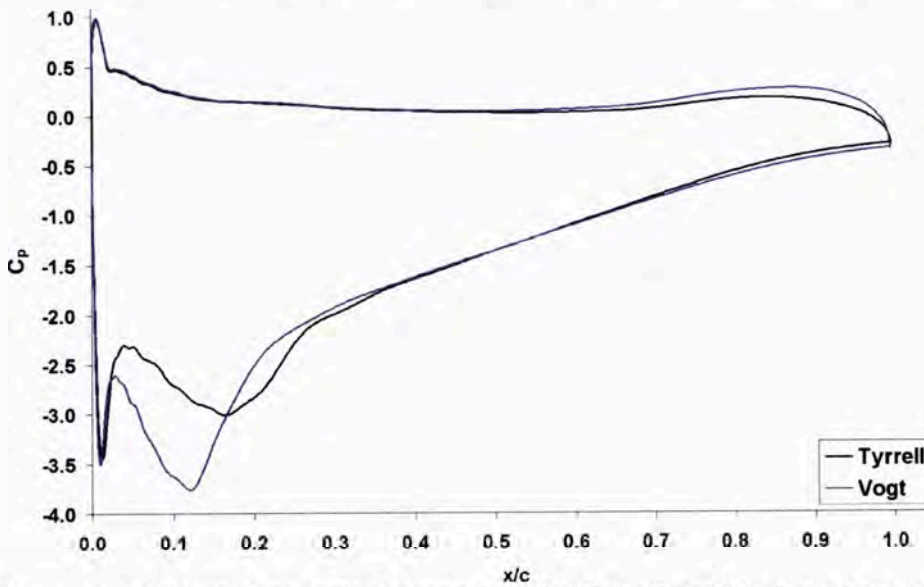


Figure 5.36: Pressure coefficient distribution comparison for Tyrrell and Vogt aerofoils;  $h/c = 0.30$ ,  $\alpha = 6^\circ$

Table 5.3: Tyrrell and Vogt results and comparison;  $h/c = 0.30$ ,  $\alpha = 6^\circ$ , T = Tyrrell

	Tyrrell	Vogt	
$C_n$	1.6687	1.7884	T +7.17 %
$C_d$	0.03883	0.04178	T +7.60 %
$n/d$	42.97	42.80	T -0.39 %

## 5.4 Conclusions

This chapter detailed the findings of a two-dimensional CFD investigation, the purpose of which was to examine and uncover the mechanics behind two-dimensional ground effect phenomena. The first study in Sec. 5.2 closely observed the ground effect behaviour about both upright and inverted aerofoils, in order to clarify and differentiate the workings of ground effect for both cases. The study in Sec. 5.3 considered the inverted aerofoil case more closely by observing the influence of changes to the geometric properties of the aerofoil, which facilitated a more precise understanding of how ground effect mechanisms work and how they may be controlled.

Our understanding of the workings of ground effect phenomena is aided by the following observations from Sec. 5.2:

- (1) The only significant contributor to the increase in downforce seen for the inverted aerofoil was the increase in suction under the aerofoil. Any contribution from the pressure side of the aerofoil diminished in close proximity to the ground. In contrast, the increase in lift seen on the upright aerofoil, when close to the ground, was a combination of a large increase in pressure lift and also due to the suction on its upper surface.
- (2) The normal force increase was significantly higher (85 % higher) for the inverted aerofoil in close ground proximity, however, the drag force for the inverted aerofoil also increased significantly (183 % increase) compared to a slight decrease for the upright aerofoil (reduction of 11.5 %).
- (3) The lift produced by the upright aerofoil slowly diminished down to a clearance of  $h/c = 1.00$ . This decrease was due to a general ground effect flow mechanism which induced a reduction in the effective angle of attack (for both configurations), with decreased clearance, and a consequent reduction in lift. A similar reduction in angle of attack was seen for the inverted aerofoil. However, the beneficial effect of the diffuser, formed between the aerofoil and the ground, more than cancelled this negative effect.
- (4) The stagnation point, on both aerofoils, moved significantly down toward the ground (relative to the aerofoil) at low clearances. This was found to be due to another general ground effect flow mechanism. This behaviour was due to an overall reduction in flow rate under the aerofoil (diverting more flow over the top of the aerofoil) which caused changes to the local flow field in the vicinity of the stagnation point.

The findings of the first investigation were built upon, in Sec. 5.3, in the second investigation concerning inverted aerofoils only. A comparison of the performance of the inverted Tyrrell and NACA4412 aerofoils led to the following conclusions:

- (5) The Tyrrell aerofoil made greater use of ground effect at low clearances than the NACA4412, with a higher production of downforce and associated drag.
- (6) The character of the  $C_p$  plots for the Tyrrell remained consistent with decreasing clearance, whereas the character of the NACA4412  $C_p$  plots changed with decreasing clearance. This behavioural variation on the NACA4412 indicated that a significant change in the encountered aerodynamic phenomena was occurring, as the aerofoil moved into the ground effect regime. This suggests that the NACA4412 aerofoil was ill-equipped to exploit the ground effect phenomena and so, this behavioural change may be considered a qualitative indicator of poor ground effect utilisation.

- (7) Compared to the NACA4412, the Tyrrell aerofoil always produced a larger normalised volume flow rate between itself and the ground and suffered less flow constriction between itself and the ground, at lower clearances.

An investigation of the effect of specific geometric changes to the aerofoil – proven in the development of the Vogt aerofoil – are summarised below:

- (8) The presence of camber on the top surface of an inverted aerofoil significantly increases suction on the bottom surface and slightly increases pressure on the top surface, which indicates an increase in circulation and enhancement of the diffuser effect.
- (9) The more-forward placement of the lowest point on an inverted aerofoil is advantageous in the generation of peak suction under the aerofoil. This effect was not simulated to extremes however, and so this behaviour should be investigated in future, all the way forward to the leading edge.
- (10) The use of a smooth upward curve, downstream of the lowest point (as apposed to the sharper upward curve of the Tyrrell), tended to stifle the diffuser effect, resulting in reduced suction under the aerofoil, and the absence of a sudden pressure increase immediately downstream of the lowest point which is otherwise present on the Tyrrell aerofoil.

Based on the observations and conclusions drawn from the work in this chapter, the following design guidelines should be carefully considered in the design of a high performance inverted aerofoil operating in ground effect.

**Top Surface Camber:** the presence of camber on the top surface of the aerofoil is very important in the generation of circulation about the whole aerofoil, which allows a much more effective diffuser effect under the aerofoil. The design of the top surface of a high performance inverted aerofoil should, therefore, be considered in a holistic sense so as to generate the best possible circulation about the whole aerofoil.

**Bottom Surface Design:** the lowest point of the aerofoil should be positioned close to the leading edge as this appears to benefit performance by inducing a larger peak suction under the aerofoil. Additionally, the surface immediately downstream of this lowest point should transition (curve upward) fairly quickly to form an expanding section in order to promote the best use of the diffuser effect. This practise seems to have the added benefit of changing the flow quickly to a higher pressure state (and lower adverse pressure gradient, thereafter) without unduly risking separation and so, should be replicated.

**Holistic Deign Approach:** regarding the  $C_p$  plot trends for the Tyrrell and NACA4412 aerofoils, the overall character of the NACA4412 plots change as ground clearance is

reduced. This indicates that, as ground effect phenomena intensify at lower clearances, they force the flow field structure about the NACA4412 to adjust quite substantially (forming a peak suction further downstream, see Figure 5.26). The mere fact that an adjustment in the flow field structure about the aerofoil is necessary indicates that the geometry is not ideally suited to the ground effect operational environment and should, therefore, be considered a problem. The Tyrrell, on the other hand, whether in ground effect or not, features the same flow field structure in its vicinity – the same  $C_p$  plot character. This allows ground effect to enhance the Tyrrell's already inherent behaviours, rather than overpowering them and imposing its own.

# Chapter 6: Results and Discussion 2: Comparison of Techniques for Modelling Unsteady Flow over an Inverted Aerofoil in Ground Effect

## 6.1 Introduction

Presented in this chapter are the results of a comparison study, the purpose of which was to establish the most effective numerical modelling technique for simulating the quasi-two-dimensional flow about the Tyrrell wing in extreme ground effect.

Various techniques, which are described briefly in Sec. 6.2, are assessed against the experimental results from Chapter 3 – an experiment they seek to replicate. The techniques are based upon either the large eddy simulation model described in Sec. 4.3.1 or the pseudo-direct numerical simulation model developed in Sec. 4.3.2.

The technique which most faithfully reproduces the experimental results will be utilised for the definitive simulations in Chapter 7, which are intended to examine the onset of flow separation in ground effect.

## 6.2 Techniques Assessed

The techniques assessed in this section are the result of the model development work in Sec. 4.3. That section identified two general modelling approaches which may be able to accurately simulate the strong ground effect required of the definitive model: a large eddy simulation model and a pseudo-direct numerical simulation model. Each of the following five techniques is based on one of these two approaches.

**Smagorinsky-Lilly Large Eddy Simulation:** This technique utilised the sliver LES model from Sec. 4.3.1 and uses the classic Smagorinsky-Lilly sub-grid scale turbulence model to model the effects of the unresolved turbulent eddy scales. This sub-grid model is described in Sec. 2.6.2.1. This LES model, and all of the others compared here, featured zero inlet turbulence intensity.

**Dynamic Smagorinsky-Lilly Large Eddy Simulation:** This LES model is the same as the one described above, but utilised the dynamic extension to the Smagorinsky-Lilly model, as discussed in Sec. 2.6.2.2.

**Dynamic Sub-grid Kinetic Energy Large Eddy Simulation:** This technique utilises the same LES model as above but employs the Dynamic SKE sub-grid model which is discussed in Sec. 2.6.2.3.

**Double-Span Grid Resolution Smagorinsky-Lilly Large Eddy Simulation:** The double-span LES model, which was examined in Sec. 4.3.1, was developed in order to look at the effect of doubling the spanwise grid resolution of the sliver LES mesh from 20 cells to 40 cells. This doubling of the spanwise grid was restricted to the near-wing and wake regions, leaving the spanwise resolution in the outer regions of the mesh unchanged. The jump in cell count as a result of this operation was from 5.6 million to 10.0 million cells – an increase of 78 %.

The possibility of utilising this double-span model for the definitive simulations in Chapter 7 has already been ruled out in Chapter 4 as the computational demands were impractical. Additionally, the apparent performance gains were not significant enough to justify the increase in mesh size (even if the resources to run such a mesh were available). However, the model did perform well and, even though it cannot be used for the definitive simulations, it was thought that the model's performance against the other techniques tested here would be of great interest.

The double-span LES model utilises the standard Smagorinsky-Lilly model.

**Pseudo-Direct Numerical Simulation:** This model utilises the LES sliver mesh used for the Smagorinsky-Lilly, Dynamic Smagorinsky-Lilly and SKE LES models and does so for two reasons; using the same mesh allows a direct back-to-back comparison with the aforementioned models, but additionally, the P-DNS method, as described in Sec. 4.3.2, filters the turbulent scales in a similar way to LES and is well suited to an LES mesh.

## 6.3 Model Selection

### 6.3.1 *Remarks on Experimental Data*

The model selection process is based upon a comparison of the components of velocity and RMS velocity fluctuation profile plots of each model compared against the experimental results obtained in Chapter 3. All six of these profile plots are presented in Figure 6.1, Figure 6.2 and Figure 6.3. A more magnified view of all cases is presented in a series of figures in Appendix D.

From these figures it is clear that there is reasonable qualitative agreement between the experimental data and the numerical simulations. There are, however, some clear discrepancies which should be briefly addressed. In Figure 6.1(a) the x-velocity immediately under the trailing edge and slightly downstream into the wake is significantly faster in the data than in any of the simulations. The reason for this discrepancy is not immediately apparent and may be the result of increased turbulent mixing from vibrations of the moving ground belt. However, this requires further investigation. The y-velocity data in Figure 6.1(b) seems to agree in shape if not entirely in magnitude. The z-velocity data in Figure 6.2(a) indicates that there is a systematic error present in the tunnel which results in a cross-flow. The data recordings in this figure are known to be legitimate as the z-velocity returns to zero at the wing surface, as it should. Fortunately, the magnitude of this cross-flow ( $< 0.25$  m/s, at its worst) is not significant.

Similar to the smaller magnitude experimental y-velocity measurements, the RMS-y-velocity measurements in Figure 6.3(a) are similar in shape but the experimental data is of lesser magnitude. The RMS-z-velocity data in Figure 6.3(b) shows a consistent variation in the cross-flow direction not seen in the other two directions. This is probably related to the actual cross-flow noted earlier. Again though, the measurements are not defective as the RMS-z-velocity correlates well with the numerical data inside the boundary layer and in the wake.

It was also noted during the experimentation that the moving ground belt could not be prevented from periodically vibrating vertically, despite significant tensioning. This movement of the ground belt may be contributing to some of the discrepancies noted.

Additionally, the experiment featured higher than anticipated turbulence intensity levels at 3.3 %, whereas the numerical models, as explained in Chapter 4, feature no inlet turbulence. To help quantify how much of the noted discrepancies are due to the additional turbulence, an additional Dynamic Smagorinsky LES model simulation was run which mimicked the inlet turbulence of the experiment through the use of the vortex method, which has been shown by Mathey *et al.* (2006) to be an accurate method of producing a turbulent flow field.

Figure 6.4 shows a comparison between the experimental data and the Dynamic-Smagorinsky LES model with inlet turbulence intensities of 0 % and 3.3 %. Despite some slight variation between the two numerical models, overall the agreement between the two is strong. This result indicates that the effect of this level of turbulence on the flow field is actually quite minimal and so comparing the experimental data against the zero inlet turbulence numerical models is valid.

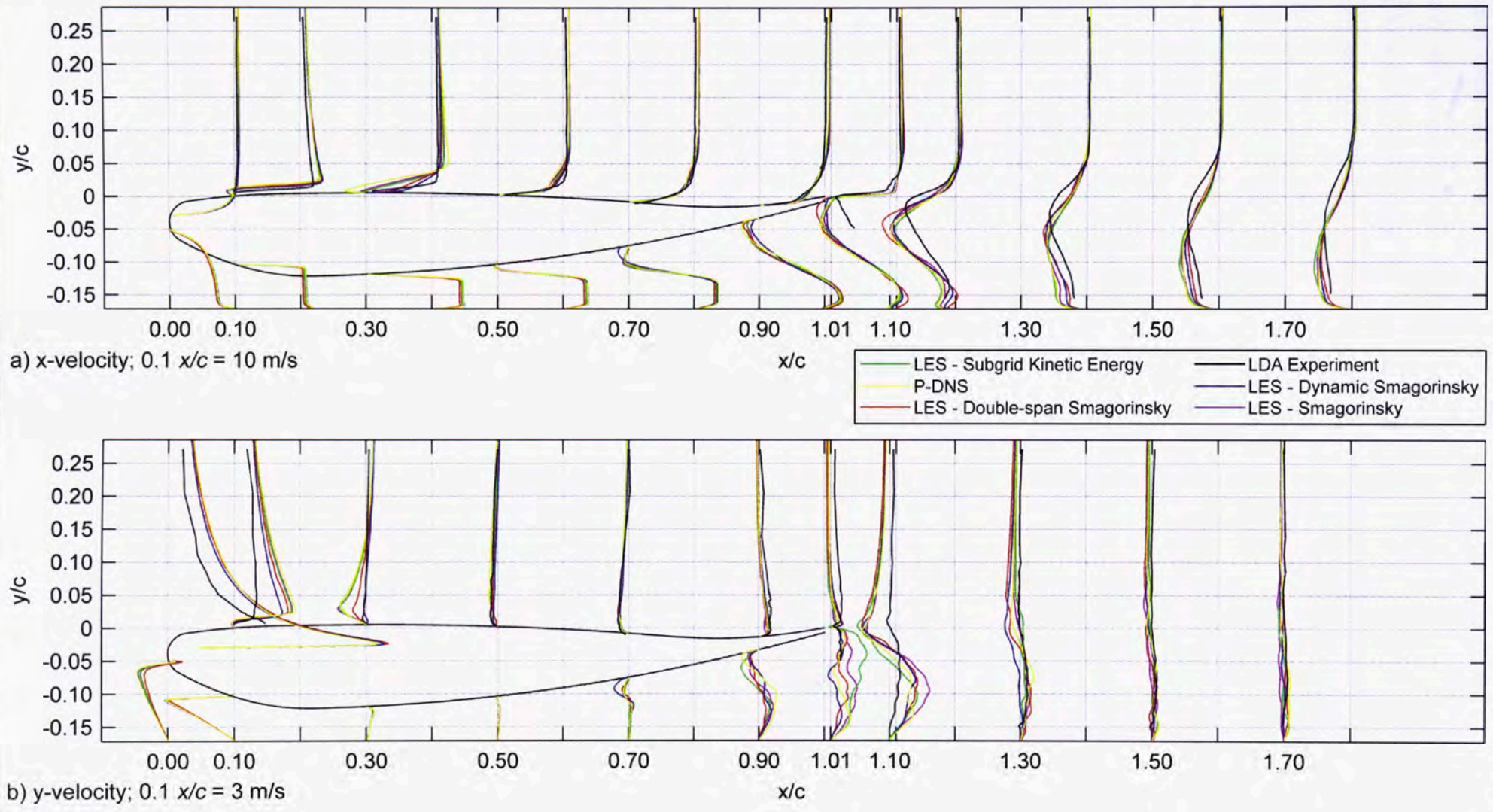


Figure 6.1: Profiles of x-velocity (a) and y-velocity (b) about Tyrrell wing at various  $x/c$  locations;  $0.1 \ x/c = 10 \text{ m/s}$  for x-velocity and  $3 \text{ m/s}$  for y-velocity

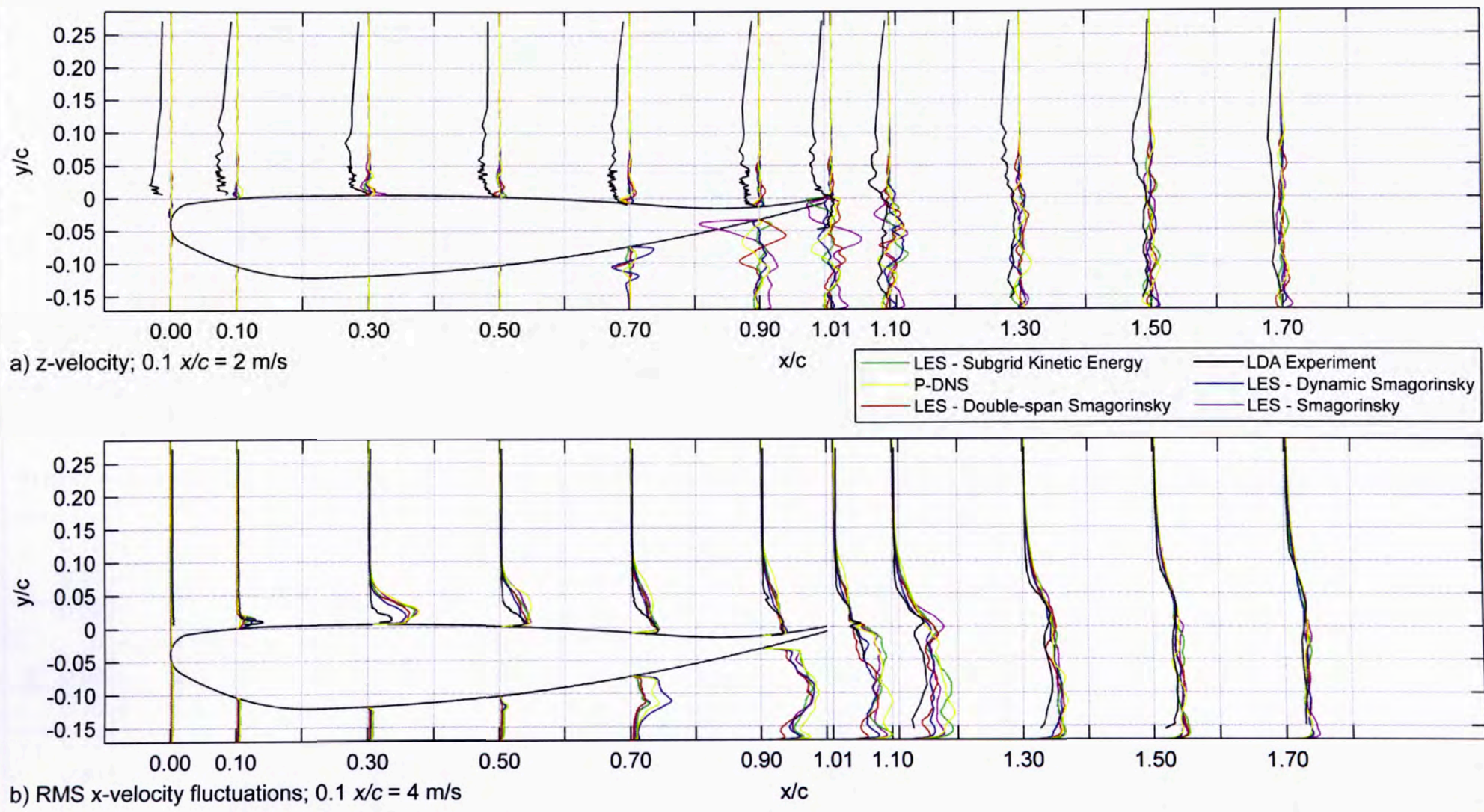


Figure 6.2: Profiles of z-velocity (a) and RMS-x-velocity fluctuations (b) about Tyrrell wing at various  $x/c$  locations;  $0.1 x/c = 2 \text{ m/s}$  for z-velocity and  $4 \text{ m/s}$  for RMS-x-velocity fluctuations

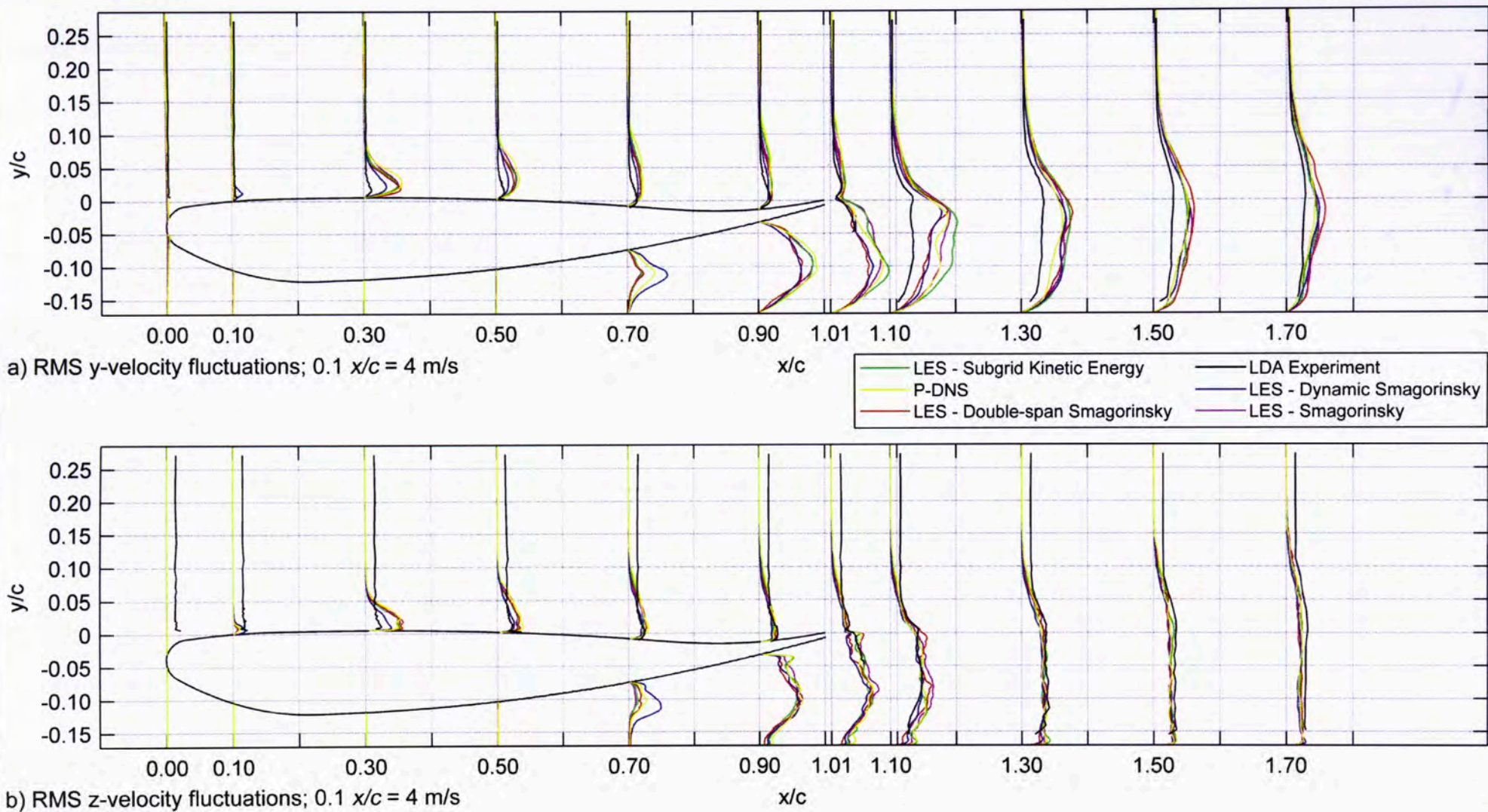
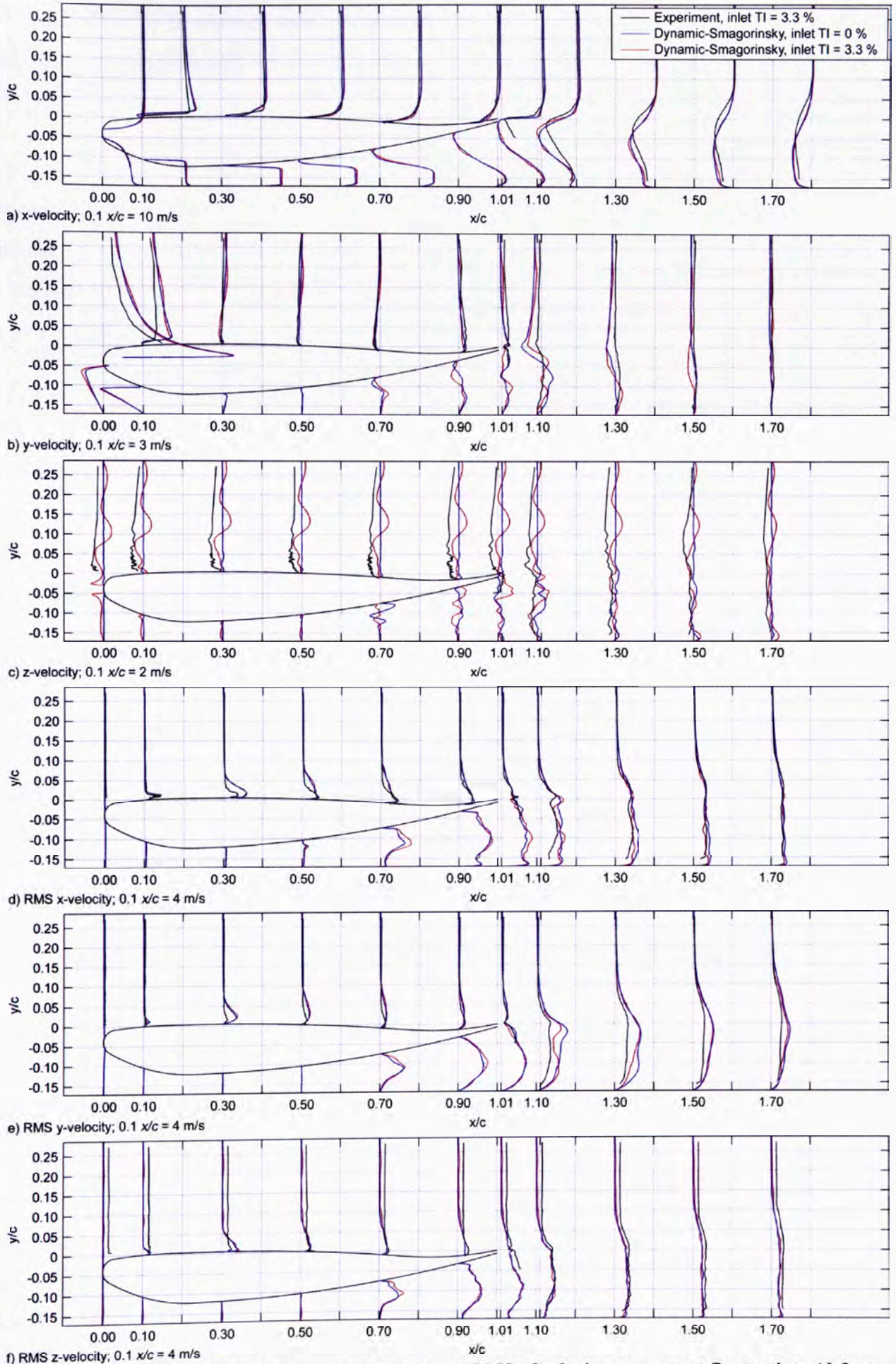


Figure 6.3: Profiles of RMS-y-velocity fluctuations (a) and RMS-z-velocity fluctuations (b) about Tyrrell wing at various  $x/c$  locations;  $0.1 x/c = 4 \text{ m/s}$



**Figure 6.4: Profiles of velocity components (a-c) and RMS of velocity component fluctuations (d-f) at various  $x/c$  locations, comparing the experiment to the Dynamic Smagorinsky LES models with differing inlet turbulence intensities**

Despite the inconsistencies noted above, the experiment was considered of sufficient quality to be used to validate the numerical models listed in Sec. 6.2. This assessment is discussed below.

### 6.3.2 Model Selection

To determine the best performing model, a point-scoring system was developed where each model’s performance was compared against the other models. This system, which is explained below, was intended to establish a criteria-based means to assess the models and thus allow a more objective, quantitative assessment rather than merely a qualitative one that is open to subjectivity.

At the core of the assessment process is a ranking of how well the models perform at one vertical sweep  $x/c$  location and for one flow variable (for example, x-velocity). Consider the example of the profiles of x-velocity at  $x/c = 0.1$  below in Figure 6.5.

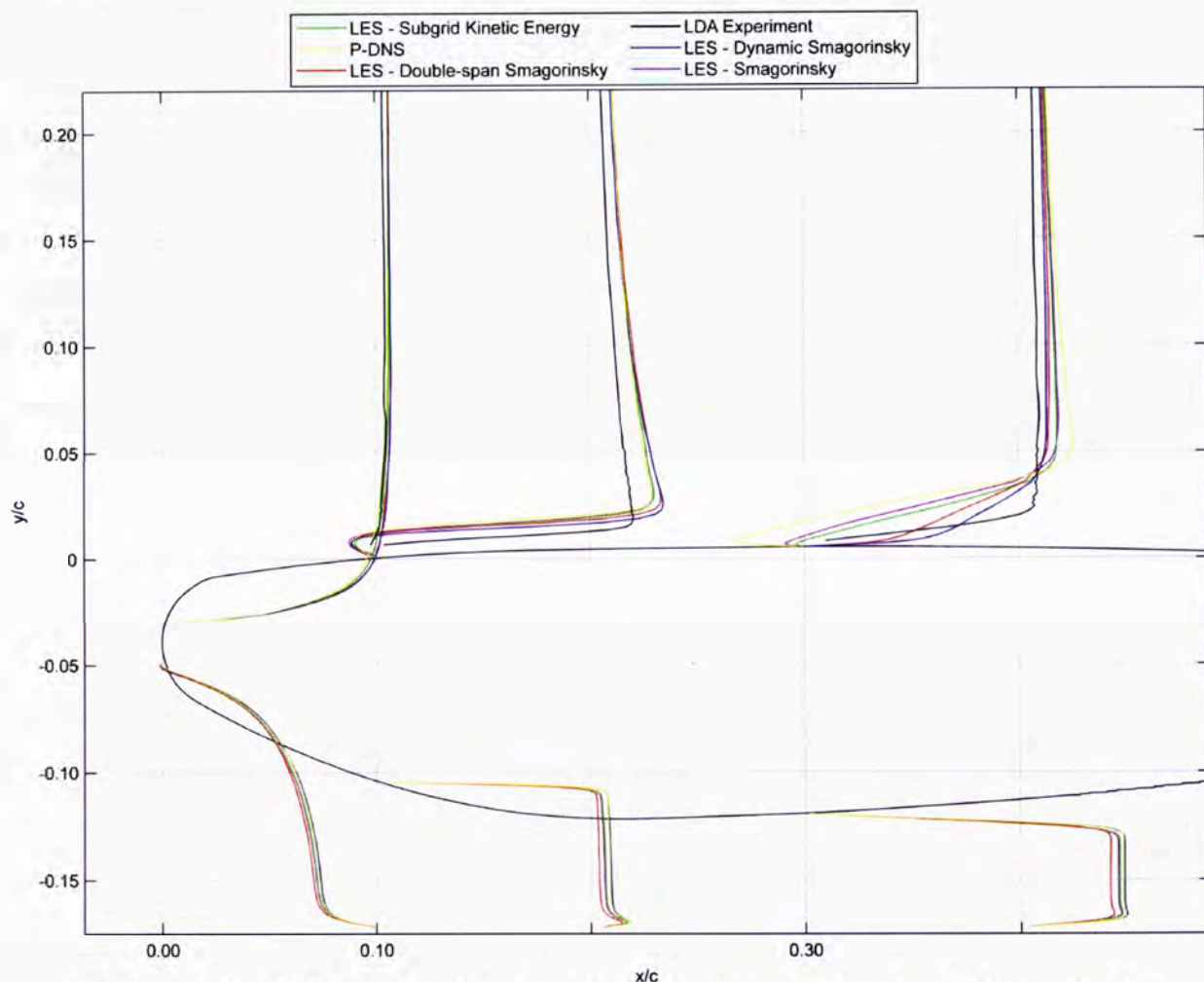


Figure 6.5: X-velocity profiles about Tyrrell wing at various  $x/c$  locations;  $0.1 x/c = 10 \text{ m/s}$

The best performing model with respect to reproducing the experimental profile in black – and this can only be judged in a qualitative sense – is assigned 5 points, the second best, 4; third, 3; fourth, 2; and the worst, 1 point. In this case, the numerical models seem to place the shear layer too far from the wing’s surface and the peak velocity outside the shear layer seems

to be over-predicted. The qualitative assessment deemed the first of these two issues the most important and so the rankings for this location and for the x-velocity variable were as follows in Table 6.1:

**Table 6.1: Model rankings for x-velocity profile at  $x/c = 0.1$**

Model	Ranking / Points awarded
Dynamic Smagorinsky	1 <sup>st</sup> / 5
Double-span Smagorinsky	2 <sup>nd</sup> / 4
Sub-grid Kinetic Energy	3 <sup>rd</sup> / 3
Smagorinsky	4 <sup>th</sup> / 2
Pseudo-Direct Numerical Simulation	5 <sup>th</sup> / 1

To offer the most accurate assessment of the merits of each model, two weighting factors were applied to the points that are awarded. The first of these is the Importance Weighting. This is a scaling factor from 0-10 which ascribes a value to how important this sweep location is, in the context of the rest of the flow. This importance was determined through a qualitative assessment of the flow field, largely based on the experimental results, and was thus determined independently of the performance of any of the CFD models. For example, the  $x/c$  location just discussed is considered very important, as it features a separated shear layer – an important and distinctive flow feature – and so has an importance rating of 10. A location in the wake receives less weighting.

The second weighting factor is the Simulation Variation Weighting. This is a measure of how much the five simulation models vary in relation to each other (not in relation to the experimental results). Thus, if there is great variation between the models, the better performing models' scores should be amplified. Conversely, if there is little or no variation between the models, the difference in the awarded scores will be minimised. Both weighting factors are multiplied together and this is multiplied by the 1-5 score to produce the overall score for each model, for that flow variable and location.

The flow variables x-, y- and z-velocity and RMS-x-, RMS-y- and RMS-z-velocity fluctuations were all assessed at the  $x/c$  locations 0.0, 0.1, 0.3, 0.5, 0.7, 0.9, 1.01, 1.1, 1.3, 1.5 and 1.7. The results of the assessment are presented in Table 6.2. Note that entries for z-velocity are missing in the table because the variation between the numerical simulations was consistently negligible (Simulation Variation Weighting = 0) for all  $x/c$  locations. Similarly, the variation between the simulations for most variables at  $x/c = 0$  was also negligible, as can be seen in the table.

**Table 6.2: CFD model scoring system**

Models Assessed									
Dynamic Smagorinsky	Sub-grid Kinetic Energy	Smagorinsky	Pseudo-Direct Numerical Simulation	Double-Span-Res. Smagorinsky					
Variable	Vertical Sweep Location (x/c)	Importance Weighting (0-10)	Simulation Variation Weighting (0-10)	Total Weighting Multiplier	Score; (best = 5, worst = 1) × Multiplier				
					5	4	3	2	1
x-vel	0	3	0	0	0	0	0	0	0
x-vel	0.1	10	4	40	200	160	120	80	40
x-vel	0.3	6	8	48	240	192	144	96	48
x-vel	0.5	6	5	30	150	120	90	60	30
x-vel	0.7	6	3	18	90	72	54	36	18
x-vel	0.9	9	5	45	225	180	135	90	45
x-vel	1.01	6	10	60	300	240	180	120	60
x-vel	1.1	4	9	36	180	144	108	72	36
x-vel	1.3	4	7	28	140	112	84	56	28
x-vel	1.5	3	6	18	90	72	54	36	18
x-vel	1.7	3	7	21	105	84	63	42	21
y-vel	0	3	1	3	15	12	9	6	3
y-vel	0.1	10	4	40	200	160	120	80	40
y-vel	0.3	6	4	24	120	96	72	48	24
y-vel	0.5	6	1	6	30	24	18	12	6
y-vel	0.7	6	1	6	30	24	18	12	6
y-vel	0.9	9	2	18	90	72	54	36	18
y-vel	1.01	6	4	24	120	96	72	48	24
y-vel	1.1	4	5	20	100	80	60	40	20
y-vel	1.3	4	2	8	40	32	24	16	8
y-vel	1.5	3	1	3	15	12	9	6	3
y-vel	1.7	3	0	0	0	0	0	0	0
RMS-x	0	3	0	0	0	0	0	0	0
RMS-x	0.1	10	2	20	100	80	60	40	20
RMS-x	0.3	6	4	24	120	96	72	48	24
RMS-x	0.5	6	3	18	90	72	54	36	18
RMS-x	0.7	6	3	18	90	72	54	36	18
RMS-x	0.9	9	2	18	90	72	54	36	18
RMS-x	1.01	6	4	24	120	96	72	48	24
RMS-x	1.1	4	3	12	60	48	36	24	12
RMS-x	1.3	4	2	8	40	32	24	16	8
RMS-x	1.5	3	1	3	15	12	9	6	3
RMS-x	1.7	3	1	3	15	12	9	6	3
RMS-y	0	3	0	0	0	0	0	0	0
RMS-y	0.1	10	1	10	50	40	30	20	10
RMS-y	0.3	6	3	18	90	72	54	36	18
RMS-y	0.5	6	3	18	90	72	54	36	18
RMS-y	0.7	6	2	12	60	48	36	24	12
RMS-y	0.9	9	2	18	90	72	54	36	18
RMS-y	1.01	6	3	18	90	72	54	36	18
RMS-y	1.1	4	4	16	80	64	48	32	16
RMS-y	1.3	4	4	16	80	64	48	32	16
RMS-y	1.5	3	3	9	45	36	27	18	9
RMS-y	1.7	3	3	9	45	36	27	18	9
RMS-z	0	3	0	0	0	0	0	0	0
RMS-z	0.1	10	1	10	50	40	30	20	10
RMS-z	0.3	6	3	18	90	72	54	36	18
RMS-z	0.5	6	2	12	60	48	36	24	12
RMS-z	0.7	6	2	12	60	48	36	24	12
RMS-z	0.9	9	1	9	45	36	27	18	9
RMS-z	1.01	6	3	18	90	72	54	36	18
RMS-z	1.1	4	2	8	40	32	24	16	8
RMS-z	1.3	4	1	4	20	16	12	8	4
RMS-z	1.5	3	1	3	15	12	9	6	3
RMS-z	1.7	3	1	3	15	12	9	6	3

When the points awarded for each model are summed, the following results in Table 6.3 are obtained.

**Table 6.3: Summary of Model Performance**

Model	Points Scored	% of Best Possible Score (4425 points)
Dynamic Smagorinsky	3,954	89.36 %
Double-Span-Res. Smagorinsky	2,751	62.17 %
Sub-grid Kinetic Energy	2,496	56.41 %
Smagorinsky	2,165	48.93 %
Pseudo-Direct Numerical Simulation	2,051	46.35 %

The Dynamic Smagorinsky model, in overall terms, consistently outperformed all the other models by a sizeably margin. The Double-span Smagorinsky model was the second best performing model, however, as mentioned earlier, this model was only included in the analysis to establish its capabilities – it was not a candidate for selection. It is interesting to note that despite a very significant increase in cell count associated with the Double-span resolution Smagorinsky model, it still did not outperform the lower spanwise resolution Dynamic Smagorinsky model. This indicates that the addition of the dynamic component to the Smagorinsky model improves performance more effectively than even a vast increase in spanwise resolution. However, the increase in spanwise resolution did enable the basic Smagorinsky model to perform significantly better.

Presented in Figure 6.6 is a bar graph showing the number of times each model scored in each performance category. Made clear in this figure is the Dynamic Smagorinsky model’s prevalence as the best performing model. It achieved the best performance 30 times in 50 opportunities – 22 more times than the next best performer. At the second best position, the double-span-resolution Smagorinsky model performed better than any other. Out of 50 opportunities, the Dynamic Smagorinsky model achieved either the best or second-best performance a total of 38 times – a significant 76 % of cases. At the other end of the performance scale, the P-DNS model was most often the worst performing model and the basic Smagorinsky model was most often the second-worst performing model. These results further confirm the points totals discussed above in Table 6.3.

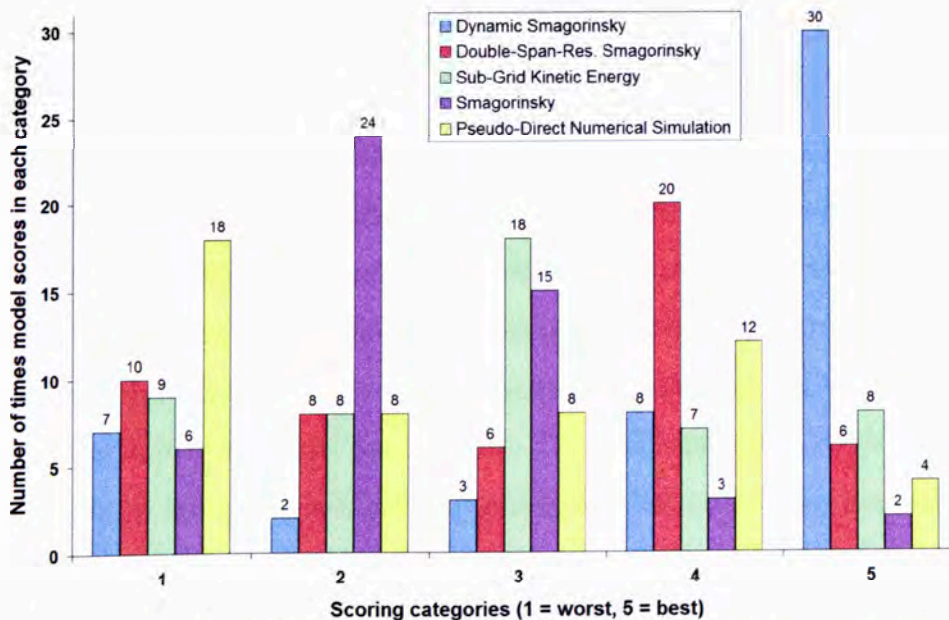


Figure 6.6: Number of times models score in each performance category

It was clear from the analysis that the Dynamic Smagorinsky LES model was the superior model of those tested and so was selected for the definitive set of simulations discussed in Chapter 7.

### 6.3.3 Frequency Analysis

A frequency analysis of the flow was conducted at five locations just behind the trailing edge of the Tyrrell wing, as shown below in Figure 6.7. The analysis compares the LDA experimental data against the Dynamic Smagorinsky model, determined to be the best model in Sec. 6.3.2. The purpose of the analysis was to assess whether the LES model adequately reproduces the turbulent energy cascade.

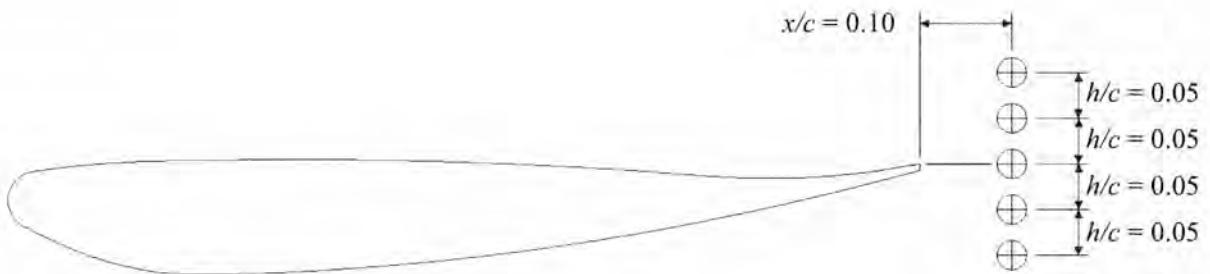


Figure 6.7: LDA Experiment and CFD frequency analysis points,  $h/c = 0.05$ ,  $\alpha = 2^\circ$

The analysis produced Power Spectral Density (PSD) plots of the raw velocity input signals, revealing the frequency behaviour of the velocity signal. This is achieved by taking a Fast Fourier Transform (FFT) of the data and allows one to see how the energy associated with the turbulent eddies is dissipated as the eddies get smaller (that is, as frequency gets higher); this is known as the turbulent energy cascade which presents in the form of an exponential decline, with increasing frequency.

The plots shown in this section were produced in Matlab. For the experimental data, 50,000 velocity readings were taken over a period of as little as 2.0 s to as much as 3.5 s. As the input signal to an FFT must be equally spaced in time, the experimental signal needed to be re-sampled. This process takes the original signal points and interpolates new data points that are equally spaced. It is common when re-sampling to increase the number of points from the original signal for two reasons: firstly, it allows more ‘frequency bins’ to be produced in the resulting FFT and secondly, it allows a more precise representation of the signal. Frequency bins work in a similar way to a histogram where the precision is determined by the range of values each bar of the histogram represents. By increasing the number of points and producing more frequency bins in the FFT, the range of frequencies associated with each bin is reduced and power is, therefore, more accurately assigned across the frequency range. The interpolation method re-sampled the signal using 16 times the original data points (800,000 in

total) and used a piecewise cubic polynomial function to interpolate the signal. A cubic polynomial was used as it is more representative of the signal than would be a linear interpolation as it avoids introducing any sudden (and unrealistic) gradient changes which would increase the noise generated in the final FFT.

In addition to requiring equally spaced input data, the FFT also requires that the length of input data be a power of 2. Thus with an 800,000 data point input, the largest applicable FFT ‘window’ size that could be used was of length 524,288 ( $2^{19}$ ). This meant only about 66 % of the re-sampled input signal was used – the rest of the signal was discarded. Despite this waste of signal however, tests showed that if the data were re-sampled to produce a total data count closer to 524,288 ( $50,000 \times 11 = 550,000$ , for example), then the resample of the raw input signal would be of insufficient smoothness and result in excessive noise in the FFT output.

Before the FFT was generated, a Hamming filter was applied to the re-sampled signal. A Hamming filter scales the re-sampled data proportional to a cosine function whose lowest points are located at the first and last data points, and their magnitude is 0.08 of the peak magnitude in the middle of the signal. This filter thus reduces the magnitude of the start and end regions of the signal. This filtering was necessary because the FFT assumes the input signal is a periodic function and thus considers the first point in the signal to follow on from the last point. This produces a discontinuity in the signal which introduces erroneous frequency information to the FFT. This problem is known as the Gibbs phenomenon. By reducing the magnitude of the signal (and thus the discontinuity) this source of error is minimised.

The numerical data was collected at every time step for 8,705 time steps where each time step was  $5 \times 10^{-6}$  s. The signal was already equally spaced and so did not need to be re-sampled. Additionally, with such a small time step size, the time gap between these data points was on the same order as the re-sample experimental data, so no errors due to sudden temporal signal variations were expected. Due to the much smaller sample size, there were less frequency bins in the final FFT, however, with little noise in the signal, this did not compromise the solution. The window size of the FFT was 4096. This allowed two FFTs to be taken from the numerical data (as  $[2 \times 4096] < 8705$ ) and averaged. The averaging process smooths the resulting FFT plot slightly and is commonly employed in signal analysis. A window size of 8192 was not used as some signal processing problems were encountered. The resulting numerical FFT does, however, produce a good signal with the smaller window size. The Hamming filter was also used for both numerical FFT input data sets.

The results of the analysis, for all five points, are presented in Figure 6.8 through Figure 6.12. Immediately apparent from these plots is the much higher noise content in the experimental PSD in comparison to the numerical PSD, however, given the sources of the data, this was to be expected. The measureable ranges of both data sources are also apparent; the numerical data was collected at an extremely high frequency (200,000 Hz) but only for a short period of flow time (0.0435 s) and with a relatively small amount of data. This allowed it to produce a PSD with a very high upper frequency bound but with a relatively poor resolution at low frequencies. The LDA experimental collected a large amount of data at a reasonably high frequency (between 15,000-20,000 Hz) and over a much longer period of flow time (2.0-3.5 s). This produced a PSD with a lower upper frequency bound but with a better frequency resolution down to much lower frequencies (owing to the longer recording time).

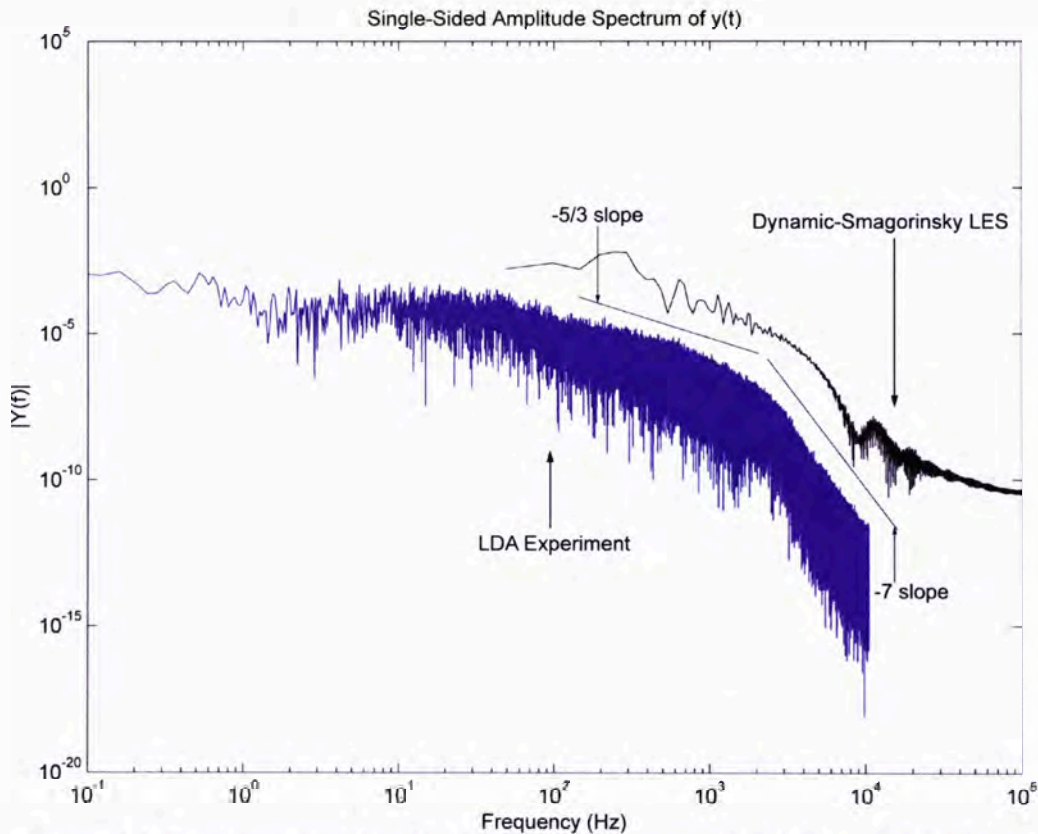


Figure 6.8: Power spectral density of velocity measurements at  $x/c = 1.1, y/c = 0.10$

Although the numerical FFT results appear to routinely produce more power than the experimental results, this is not actually the case. The difference in magnitude between the plots is a function of the window size used, which is significantly larger for the experimental FFT (524,288 vs. 4096 for the numerical FFT). With a larger window size, each frequency bin covers a smaller range of frequencies and so the power value attached to that frequency bin will be lower as it represents the collective power of a smaller frequency range. Thus the power in the experimental FFT case is spread over a large number of discrete frequency bins and so the magnitude of each bin is lower, when compared against the less resolved numerical

FFT. This magnitude change does not affect the slope of the FFT output which is the parameter of interest in this analysis.

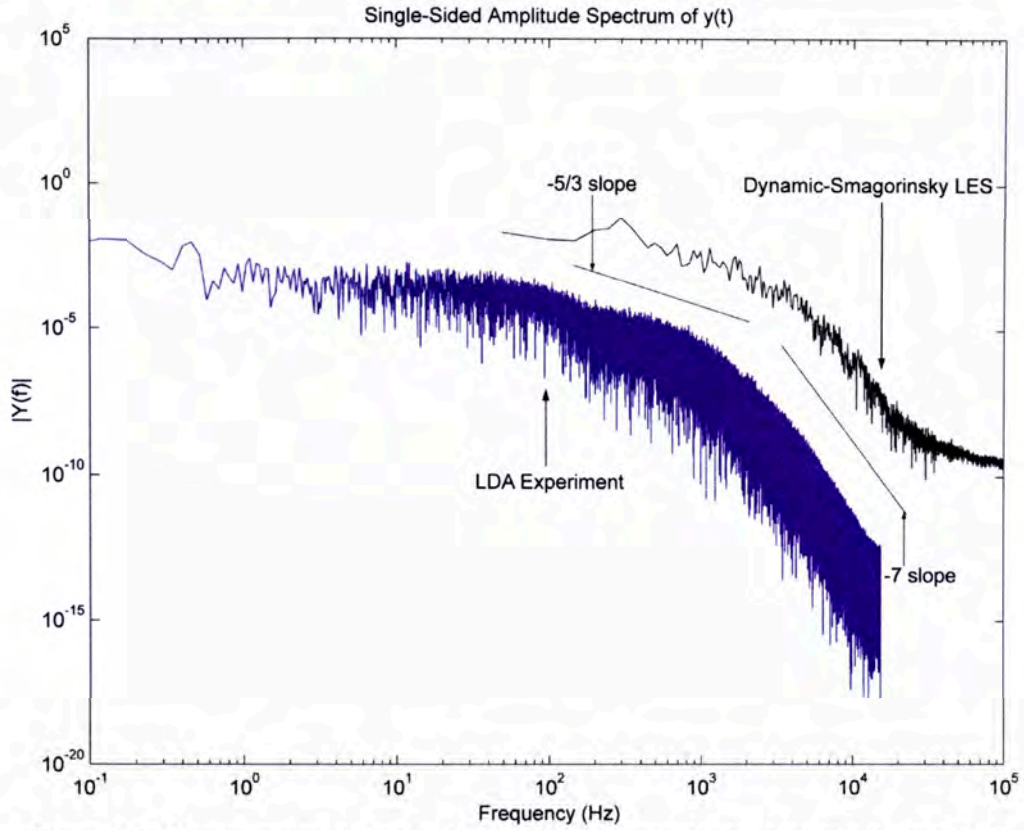


Figure 6.9: Power spectral density of velocity measurements at  $x/c = 1.1, y/c = 0.05$

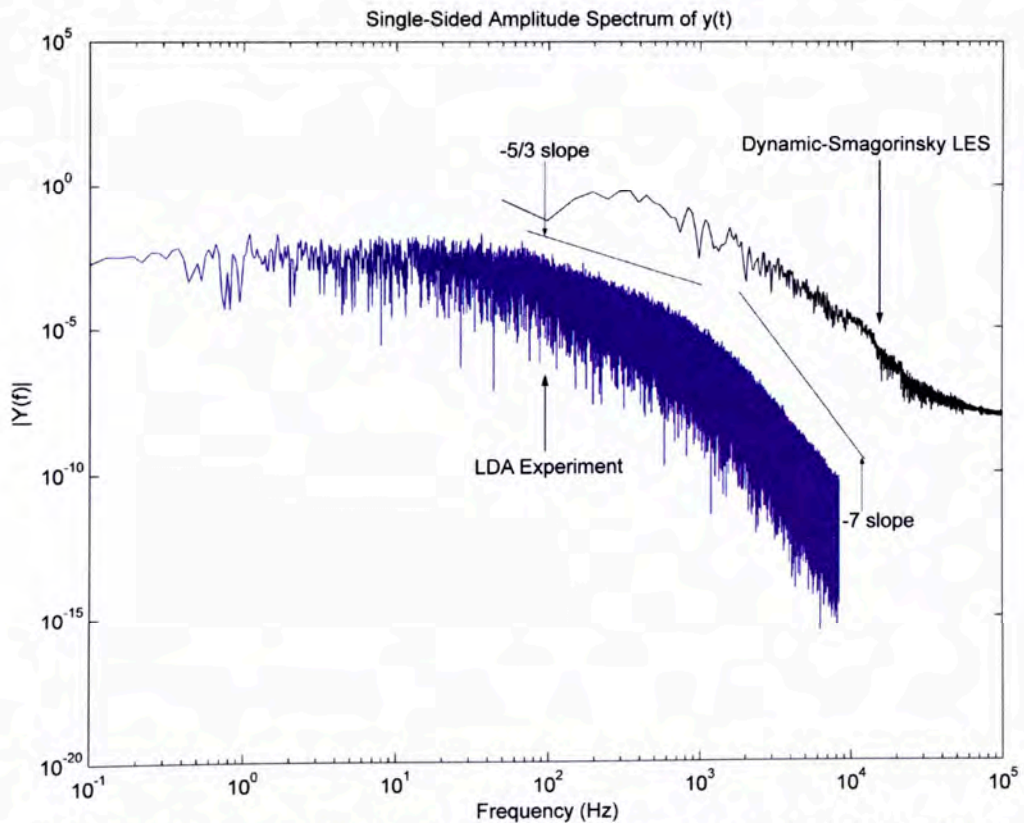


Figure 6.10: Power spectral density of velocity measurements at  $x/c = 1.1, y/c = 0$

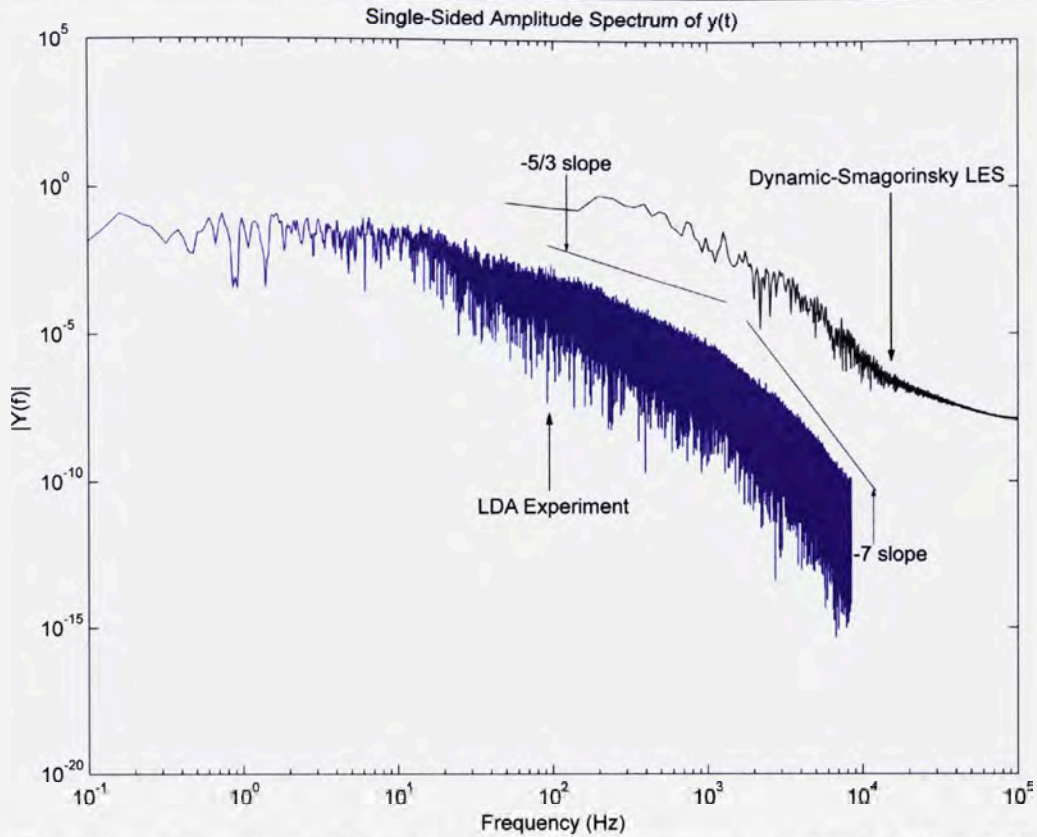


Figure 6.11: Power spectral density of velocity measurements at  $x/c = 1.1, y/c = -0.05$

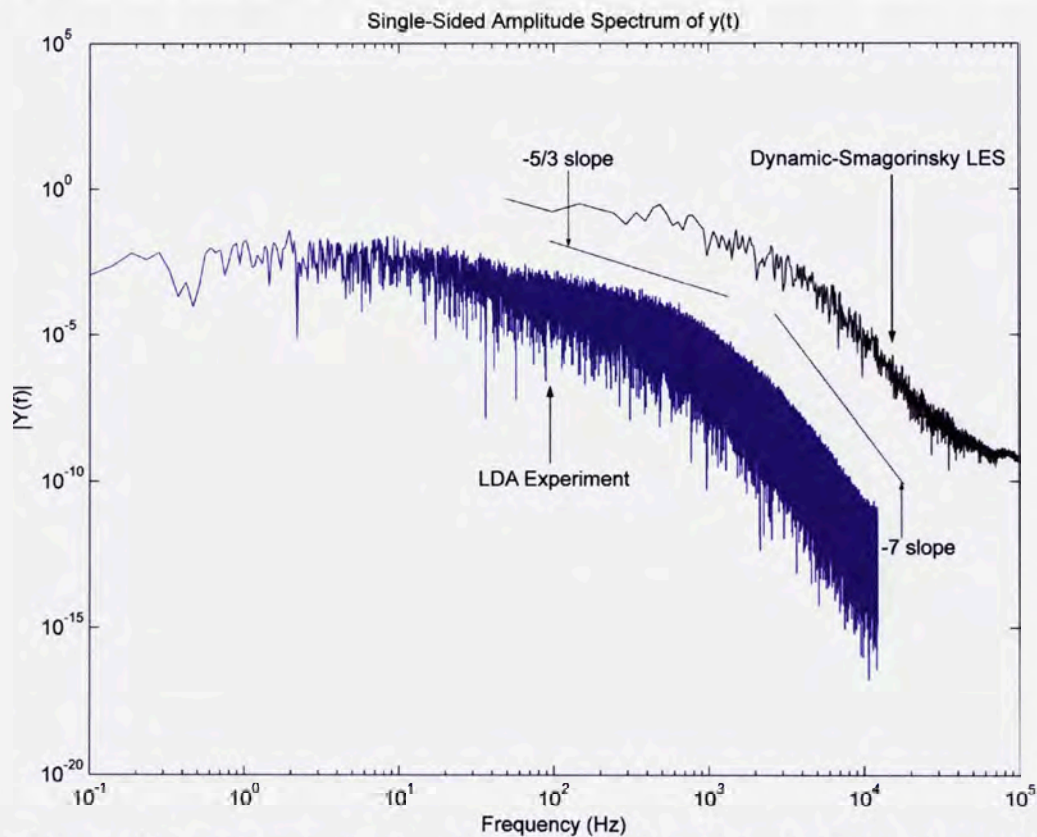


Figure 6.12: Power spectral density of velocity measurements at  $x/c = 1.1, y/c = -0.10$

The frequency data shows that the experiment and the Dynamic-Smagorinsky LES model agree quite well at all five measurement points as, at all points, the turbulent exponential decay is well captured by both. Both the LES and the experiment demonstrate clearly the two components of the turbulent decay slope; the momentum-dominated decay region which

should approximately follow the  $k^{-5/3}$  exponential curve (Wilcox, 2006) and the viscous-dominated decay region which should approximately follow the  $k^{-7}$  exponential curve (Hinze, 1959).

Comparison of the plots over the five  $y/c$  positions tested shows slight variation (with position) in the slope of the turbulent decay. However, the change in slope is fairly minimal and, importantly, the variation in the experimental PSD mirrors that of the numerical PSD; this indicates that the small variation in the flow field between the  $y/c$  locations is being well reproduced by the LES model.

From these results, it is clear that the Dynamic-Smagorinsky model is well able to produce the turbulent decay behaviour present in the flow field.

## 6.4 Conclusions

A study was undertaken to select the most appropriate numerical model with which to conduct a thorough numerical investigation of ground effect about the inverted Tyrrell wing. The five models tested were rigorously assessed using a weighted scoring system designed to highlight the best performing model.

One of the models tested – the double-spanwise-resolution Smagorinsky LES model – was not a candidate for use in the definitive investigation, but was rather included as an exercise to more precisely determine the effect of doubling the spanwise resolution of the LES mesh.

The Dynamic-Smagorinsky LES model was found to be the clearly superior model with an overall performance score comfortably higher than any other model. This model was selected for the definitive investigation in Chapter 7.

The double-spanwise-resolution Smagorinsky LES model was found to be inferior to the Dynamic-Smagorinsky model but superior to the standard (normal resolution) Smagorinsky LES model. This indicates that doubling the spanwise resolution would not offer a sufficiently attractive improvement to the model's predictive power as merely incorporating the dynamic modelling approach to the basic Smagorinsky model produced better results at very little additional computational expense.

A frequency analysis was conducted to compare the chosen model's performance against the experimental results in terms of predicting the turbulent energy cascade. The experiment and the LES model both clearly identified the expected turbulent decay behaviour and how it varied across different  $y/c$  positions behind the wing. The consistency (between the LES and the experiment) in how the decay behaviour varied in space is of particular importance in demonstrating the predictive capability of the Dynamic-Smagorinsky LES model.

# Chapter 7: Results and Discussion 3: Flow Separation about a Highly Cambered Inverted Wing in Ground Effect

## 7.1 Introduction

This chapter utilises the results of Chapter 6, in which the most effective numerical model for simulating the flow over the inverted Tyrrell wing in a low-speed wind tunnel was determined. Using the best performing model – the sliver LES model with the Dynamic Smagorinsky sub-grid turbulence model – a series of different configurations of the Tyrrell wing were modelled in order to examine the onset of flow separation. As the negative effect of flow separation has already been well documented, this study was not intended to cover this same ground again, but rather to consider the process by which ground effect flow separation develops. In so doing, it was hoped to establish a means to mitigate separation development in future inverted aerofoil designs.

As the model was validated against experimental data from the low speed wind tunnel, this set of LES simulations were conducted at the same Reynolds number of 53,000 and assumed a quasi-two-dimensional flow field. The Tyrrell aerofoil was set at a constant angle of attack of  $5^\circ$ , which is greater than a typical ground effect application but was done so in order to accentuate the ground effect phenomena at play. The aerofoil was simulated at various ground clearances in the extreme ground effect and force-reduction height ranges so as to capture the complete transition to flow separation. The clearances tested were:  $h/c = 0.30, 0.26, 0.22, 0.18, 0.14, 0.11, 0.08$  and  $0.05$ .

The boundary conditions used for these simulations were predominantly the same as the sliver LES models in Sec. 4.3.1, with the exception of the upper boundary which, in this instance, no longer seeks to model the top wall of the wind tunnel but, rather, an open air condition; thus the top boundary was set to a symmetry plane, which was established earlier to be appropriate for this purpose (see Sec. 4.2.1). The turbulence intensity level at the inlet was set

to zero as the flow near the ground is stationary and therefore usually completely free of turbulence.

In a similar manner to the sliver LES models evaluated in Sec. 4.3.1, each model was run until quasi-steady-state was achieved, at which point, data taking was initiated. This initial stabilisation period took as little as 0.045s of flow time (9,000 time steps at a time step size of  $5 \times 10^{-6}$  seconds) to as much as 0.105s of flow time (21,000 time steps). Once quasi-stead-state was achieved, each model was then run for a data-taking period of at least 0.06s (12,000 time steps).

## 7.2 Results and Discussion

### 7.2.1 Force Behaviour

The normal and drag force coefficients were recorded at each time step during the 12,000 time step data-taking period. The  $C_N$  plots for each clearance are shown in Figure 7.1, below. As can be seen in the figure, there are a few inconsistencies; the  $h/c = 0.05$  clearance case featured such strong fluctuations that it was thought prudent to run the simulation for an extra 3,000 time steps in the interest of obtaining adequate time-averaging. Additionally, the  $h/c = 0.11$ , 0.18 and 0.30 cases all have sections of missing data which was the result of an intermittent reporting error in the Fluent software. This reporting error, however, did not otherwise affect the simulations. The  $C_D$  plots are of the same character as the  $C_N$  plots and so are not shown here.

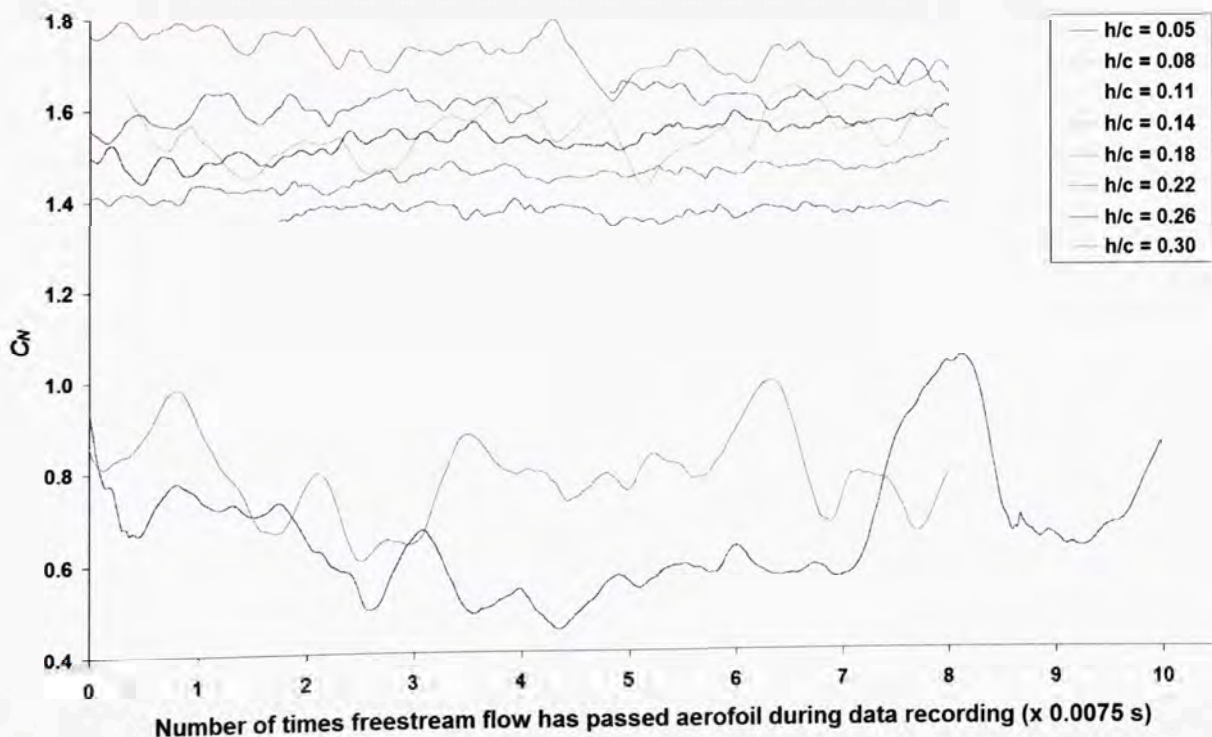


Figure 7.1: Instantaneous  $C_N$  plots of LES simulations during data-taking period

The time-averaged  $C_N$  and  $C_D$  values for each clearance tested are shown in Figure 7.2. This plot clearly shows that the sudden drop-off in normal force (with decreasing  $h/c$ ) has been well captured by the ground clearance extent of the study. The maximum time-averaged normal force was generated at  $h/c = 0.14$ , before a reduction commencing somewhere between  $h/c = 0.14$  and  $0.11$ .

The  $C_D$  values in the graph show an initially exponential-looking increase as the ground is approached, before it starts to plateau at extremely low clearances. This plateau region was not captured in the two-dimensional studies performed in Chapter 5, as those inverted aerofoils could not be simulated at sufficiently low clearances with a RANS solver.

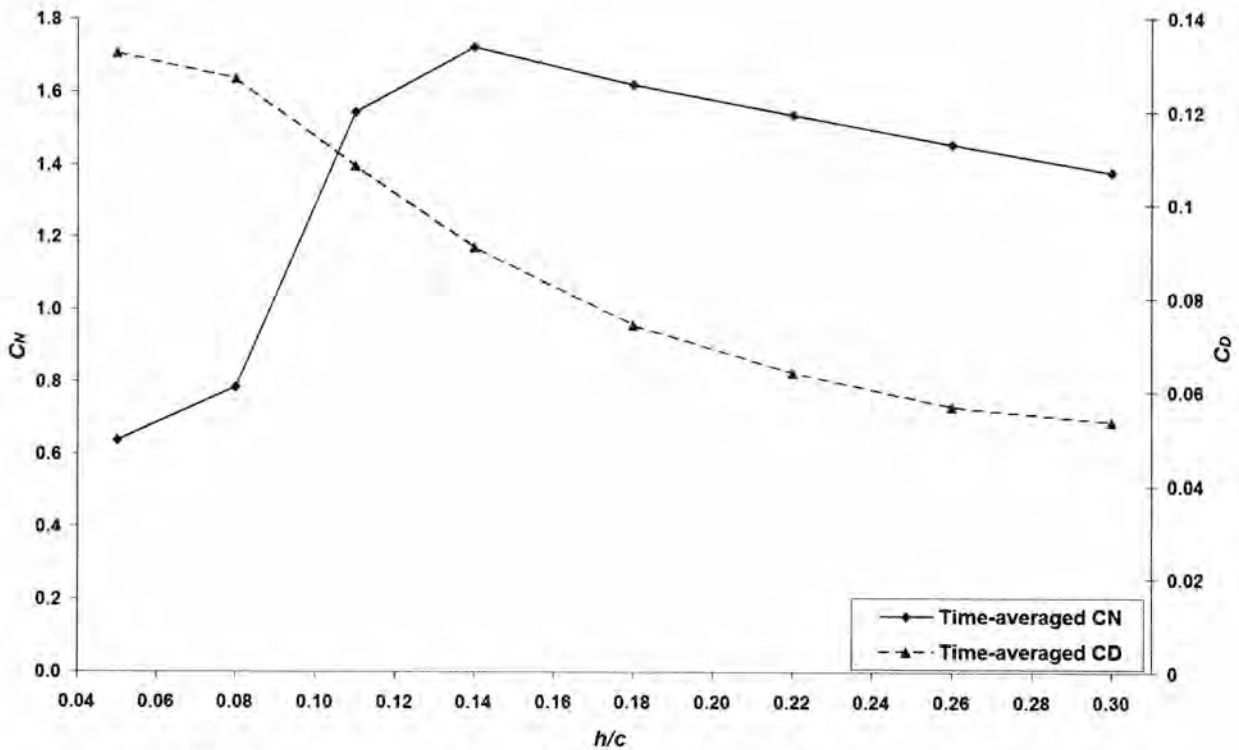


Figure 7.2: Time-averaged  $C_N$  and  $C_D$  plots for LES simulations vs. ground clearance

Using the  $C_N$  and  $C_D$  values from the figure above as the mean values, the RMS values for the fluctuating component of both quantities were calculated in order to demonstrate the changing behaviour of the flow field. This data is presented in Figure 7.3. Both  $C_N$  and  $C_D$  RMS plots show a steady increase in the average fluctuation experienced as the ground is approached, which indicates an increasing level of turbulence brought about by the ground's proximity. However, perhaps unsurprisingly, the average fluctuations increase markedly in the lowest two clearances where, it will be shown, full flow separation has been established. This increase in turbulent behaviour is indicative of a tendency to increasingly less periodic behaviour as is quite clear from an inspection of the temporal behaviour of the two or three lowest clearances in Figure 7.1.

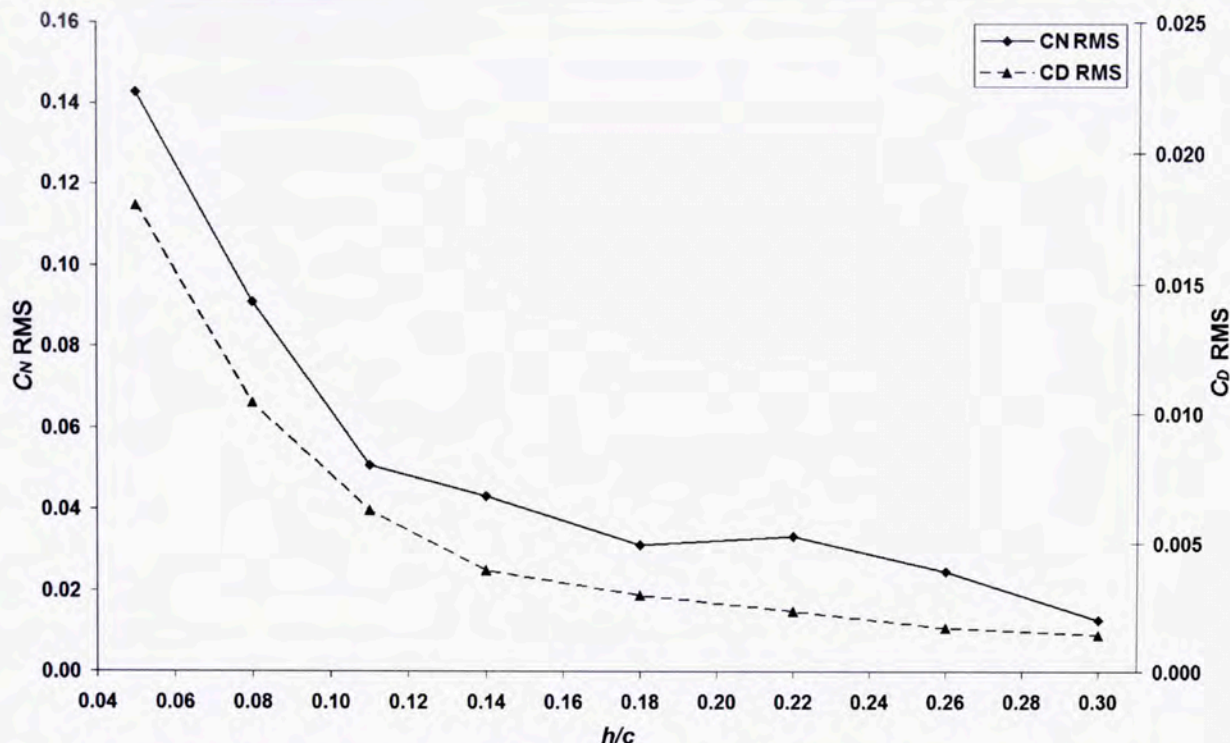


Figure 7.3: Root-mean-squared values for LES  $C_N$  and  $C_D$  quantities vs. ground clearance

### 7.2.2 Pressure Coefficient Plots

Before discussing the pressure coefficient plots, it is necessary to briefly make an observation about the general flow field about the wing; Figure 7.4 shows an instantaneous velocity contour plot of the midplane of the wing at the highest clearance simulated ( $h/c = 0.30$ ). At this clearance and all lower clearances (except those with full flow separation), a laminar separation bubble is present under the wing. Consequently, most of the  $C_p$  plots to follow feature annotated separation and reattachment points, indicating the start and end of this separation bubble. This and other flow field phenomena will be discussed further in the following sections.

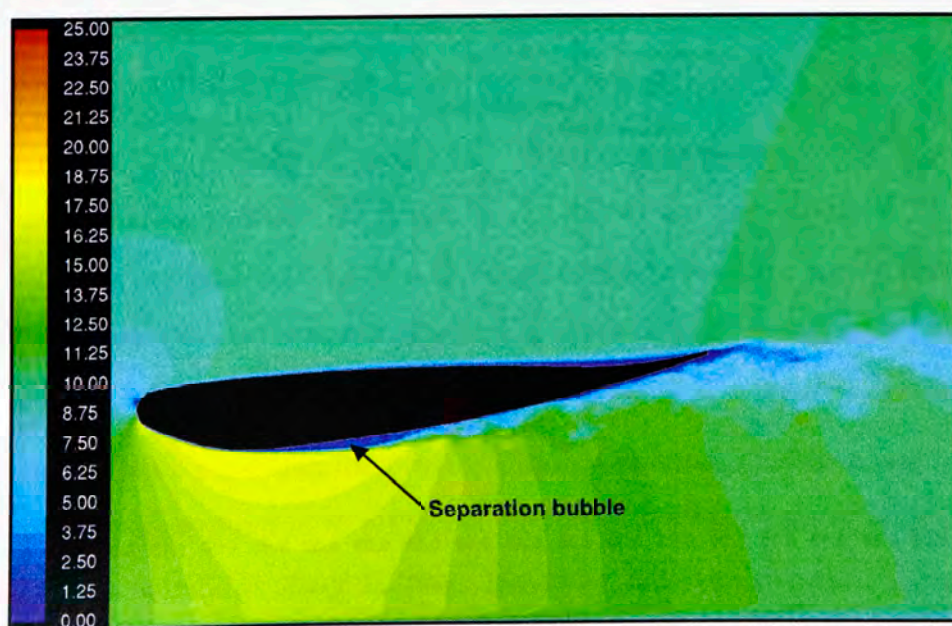


Figure 7.4: Instantaneous velocity contours (m/s) about wing midplane,  $h/c = 0.30$

The pressure coefficient plots were generated by plotting the time-averaged  $C_p$  along the spanwise midplane cut of the wing. The instantaneous  $C_p$  fluctuations were quite significant in regions of turbulent flow but the time-averaged  $C_p$  is quite spatially consistent across the wing span which indicates an acceptable time-averaging period. A demonstration of the instantaneous fluctuations for  $h/c = 0.30$  and  $0.22$  is shown in Figure 7.5 and the time-averaged  $C_p$  plots for all clearances are shown in Figure 7.6.

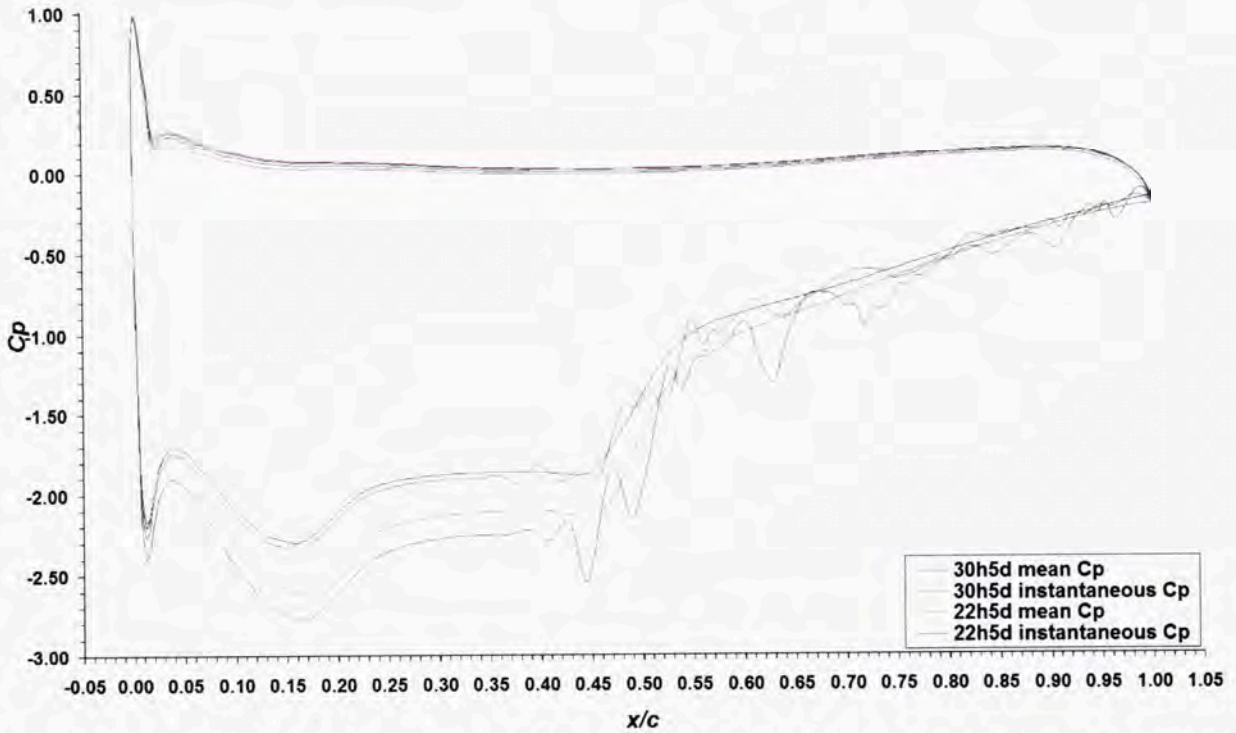


Figure 7.5: Comparison of time-averaged and instantaneous  $C_p$  at wing midplane for ground clearances  $h/c = 0.30$  and  $0.22$ ,  $\alpha = 5^\circ$

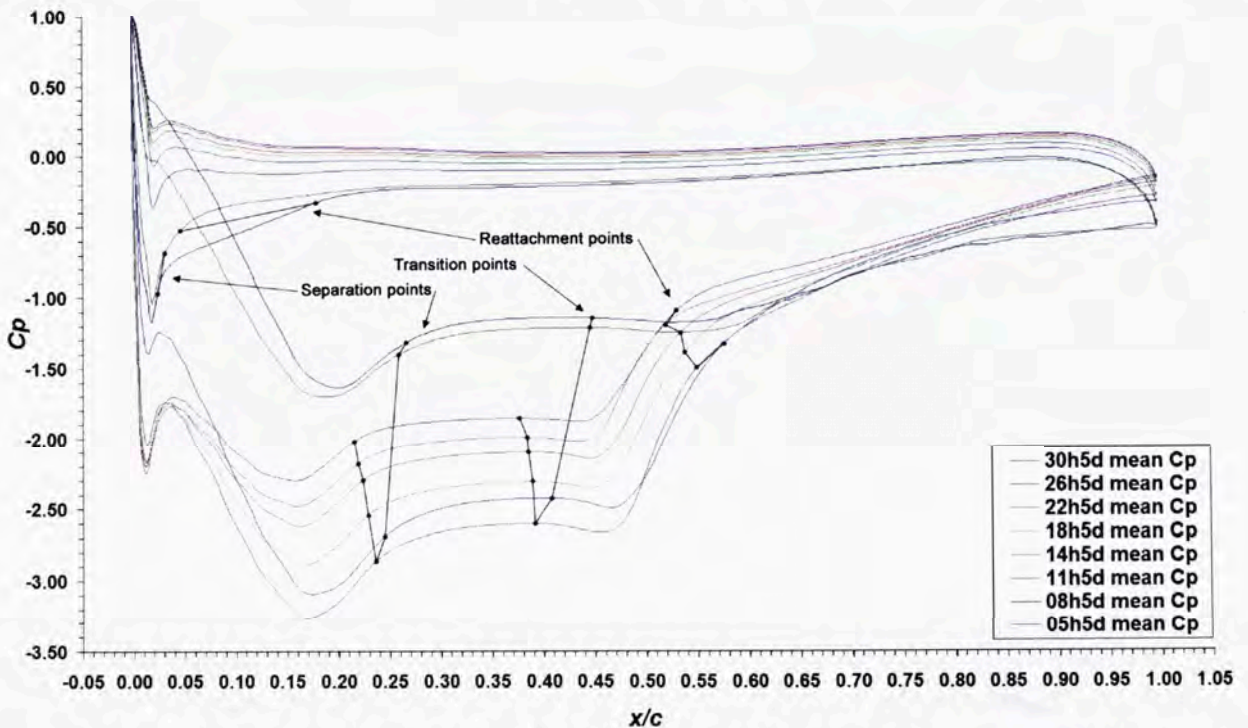


Figure 7.6: Time-averaged  $C_p$  plots at wing midplane for various ground clearances

Included in Figure 7.6 are annotations which indicate the location of the separation, transition and reattachment points of the laminar separation bubble. These points were gleaned from time-average results at the midplane. The separation point is very consistent in both time and space as it is located in a laminar flow region. The time-averaged reattachment point at the midplane is a good indication of the flow across the wing span, though there does exist variation across the span (see Figure 7.13); the means to identify the transition point will be discussed in Sec. 7.2.4. A line is scribed between successive clearance cases to indicate the progression of the separation, transition and reattachment points as the clearance is changed. The line connecting the successive separation points indicates a slow downstream progression with reduced clearance. The transition point line indicates a very similar progression. The reattachment line shows a general downstream progression also, albeit with an upstream exception at  $h/c = 0.26$ .

The plots feature a large plateau in the region of the separation bubble which commences after a short region of adverse pressure gradient which is too great for the laminar flow to withstand without separation. As the wing's clearance is reduced, the maximum under-wing suction increases. The shape of the separation bubble plateau remains fairly constant throughout most of the clearance range; after the flow transitions to turbulence, mixing promotes a rapid pressure recovery before reattachment is achieved. From the reattachment point downstream to the trailing edge, a constant adverse pressure gradient can be seen. This final section of adverse pressure gradient gets slightly stronger with reduced clearance until some flow separation becomes evident near the trailing edge at  $h/c = 0.11$  with the  $C_p$  trend quite curved and approaching zero-gradient at the trailing edge. At the lowest two clearances, the underwing suction has reduced significantly and no flow reattachment was achieved. The separation, transition and reattachment points, generally, all move rearward as clearance is reduced but a more detailed discussion of this is to follow in Sec. 7.2.4.

The pressure on the upper surface reduces with clearance such that, at the lower clearances, the top surface produces positive lift (most, if not all, of the top surface  $C_p$  trend is below zero). Additionally, a significant suction spike generates around the top of the leading edge and, with a steep local adverse pressure gradient, a small separation bubble appears on the top surface as well.

Several important points regarding the progression to separation may be noted from this plot. Firstly, the dramatic deterioration in performance (underwing suction) is associated with the wing's inability to re-establish attached flow. However, the extensive flow separation seen at  $h/c = 0.08$  and  $0.05$  was not caused by an excessive adverse pressure gradient as the gradient

had reduced from  $h/c = 0.14$  to  $0.11$ , indicating something else must have triggered the full separation. Finally, as noted in Chapter 5, as the wing moves toward the ground, the ground constricts the flow under the wing and forces it to be diverted over the top of the wing instead. This can be seen in the reduced overall suction at  $h/c = 0.11$  and below and also the reduced suction at the underwing leading edge suction spike from  $h/c = 0.22$  and below, with larger reductions starting at about  $h/c = 0.14$ . The opposite trend occurs on the upper side of the wing, indicating a rapidly increasing flow speed over the top of the wing.

### 7.2.3 Velocity Contours

The midplane slice of the quasi-two-dimensional flow over the Tyrrell wing forms the basis of most of the following figures which examine the general flow field behaviour. Velocity contours of both mean and instantaneous velocity magnitude are presented in Figure 7.7. As mentioned earlier, a laminar separation bubble is present on the lower surface at all clearances simulated, except the lowest two clearances where reattachment does not occur.

The separation bubble is formed by a laminar separated shear layer which eventually transitions to turbulence and collapses. Turbulent mixing introduces higher energy flow from outside the boundary layer down to the surface and reattachment is then achieved. The turbulent mixing is obvious from an inspection of the instantaneous flow fields in the right column of Figure 7.7.

As the wing moves toward the ground, the average velocity through the throat under the wing increases steadily until a maximum is achieved at  $h/c = 0.14$ . Below this height, the average velocity reduces, first slightly down to  $h/c = 0.11$  and then by much more down to the lowest two clearances. This trend is accompanied by a slow increase in the velocity over the top of the wing which increases markedly around  $h/c = 0.14$  and below. This increase in flow velocity over the wing can be seen by examining the flow near the leading edge on the top surface (the location of the top surface suction spike mentioned earlier). This is shown in Figure 7.8.

This diversion of flow over the wing is further elucidated by examining the normalised volume flow rate under the wing, as was previously done in Chapter 5. The time-averaged velocity data was used to calculate the average volume flow rate through the diffuser section at two locations; under the trailing edge and through the throat section. The volume flow rate was normalised by the 'ideal' flow rate which is equal to the flow rate of an unimpeded freestream flow through the same size channel. The results are plotted in Figure 7.9.

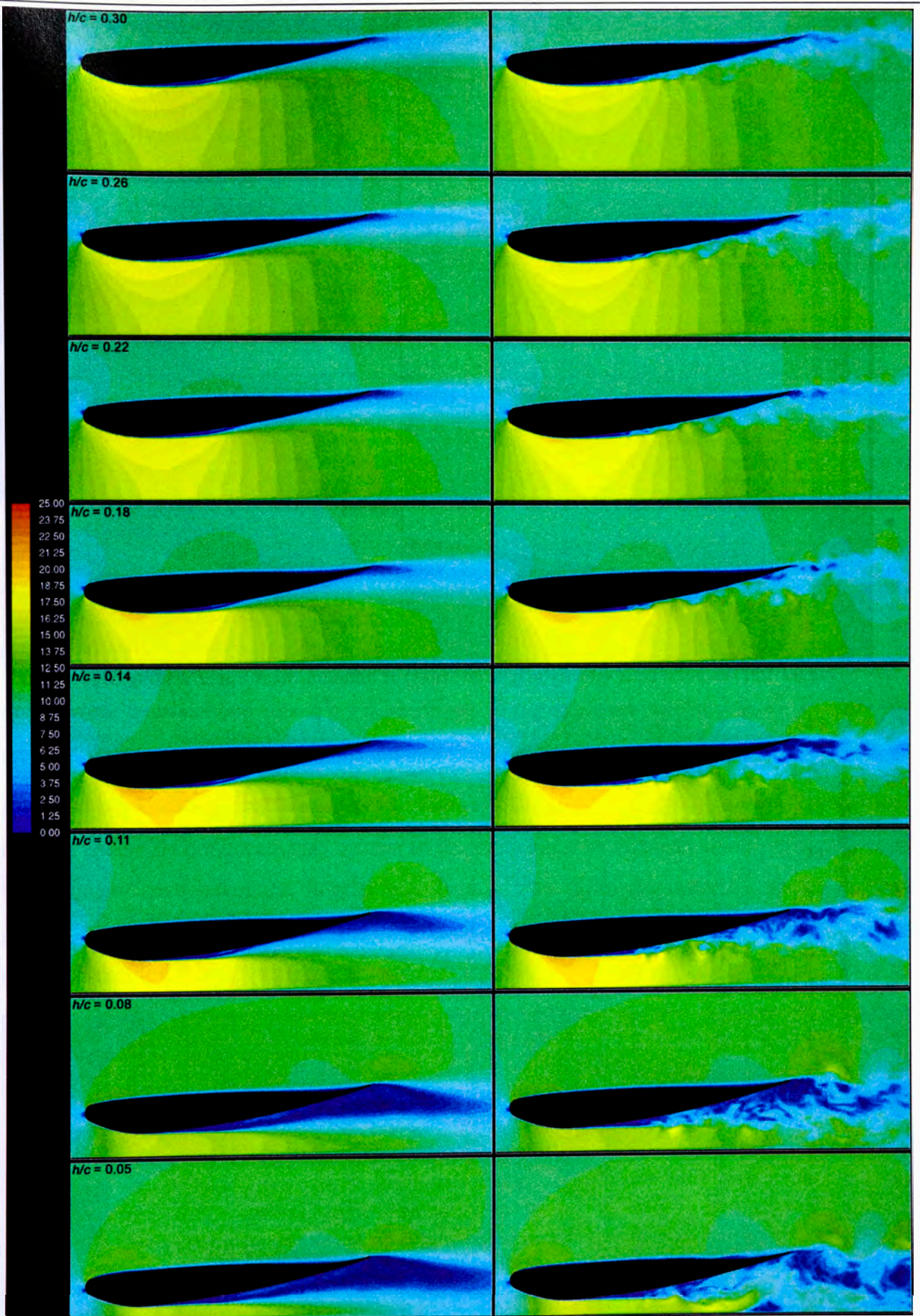


Figure 7.7: Contours of mean velocity magnitude (m/s, left column) and instantaneous velocity magnitude (m/s, right column) at midplane for all clearances, freestream velocity = 10 m/s

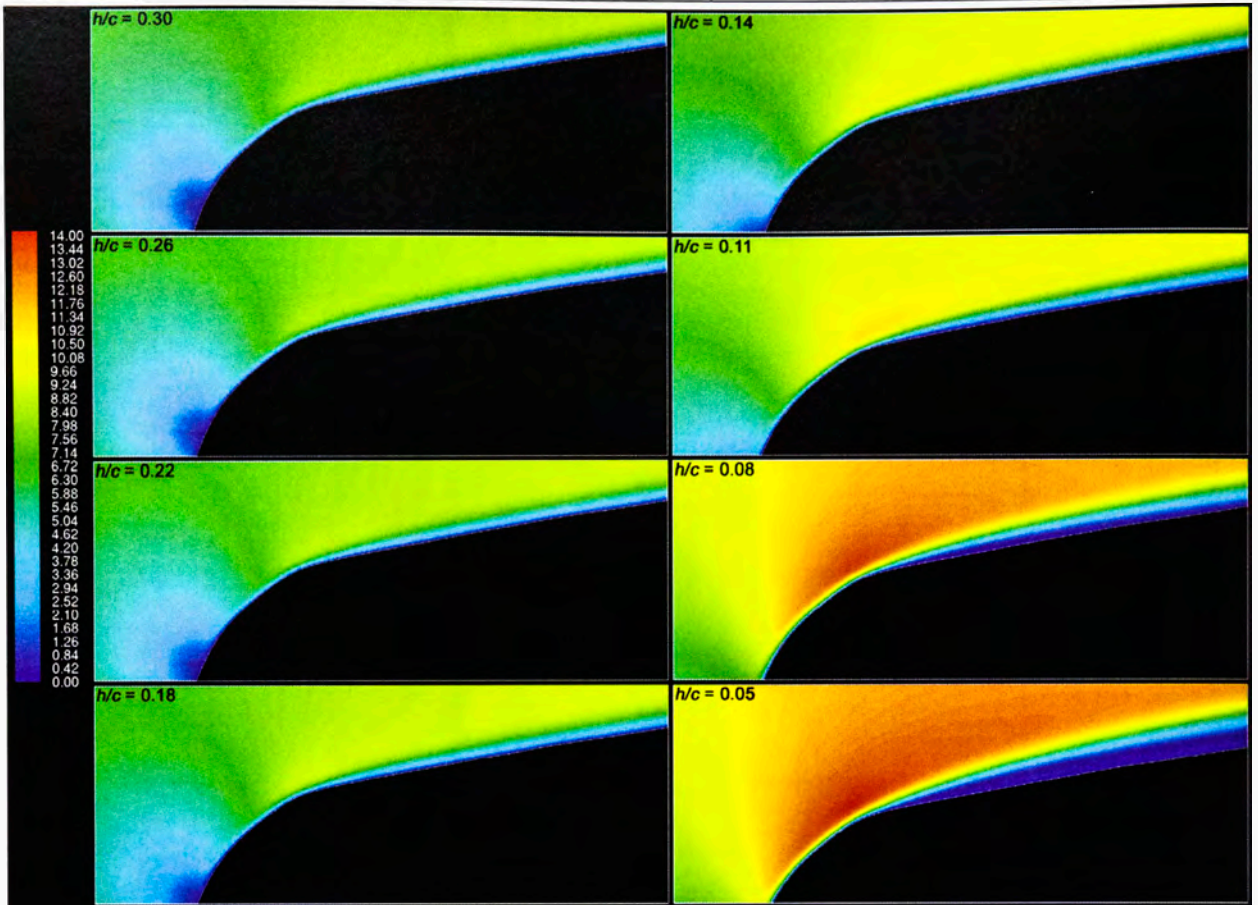


Figure 7.8: Instantaneous velocity magnitude (m/s) at midplane near upper leading edge region

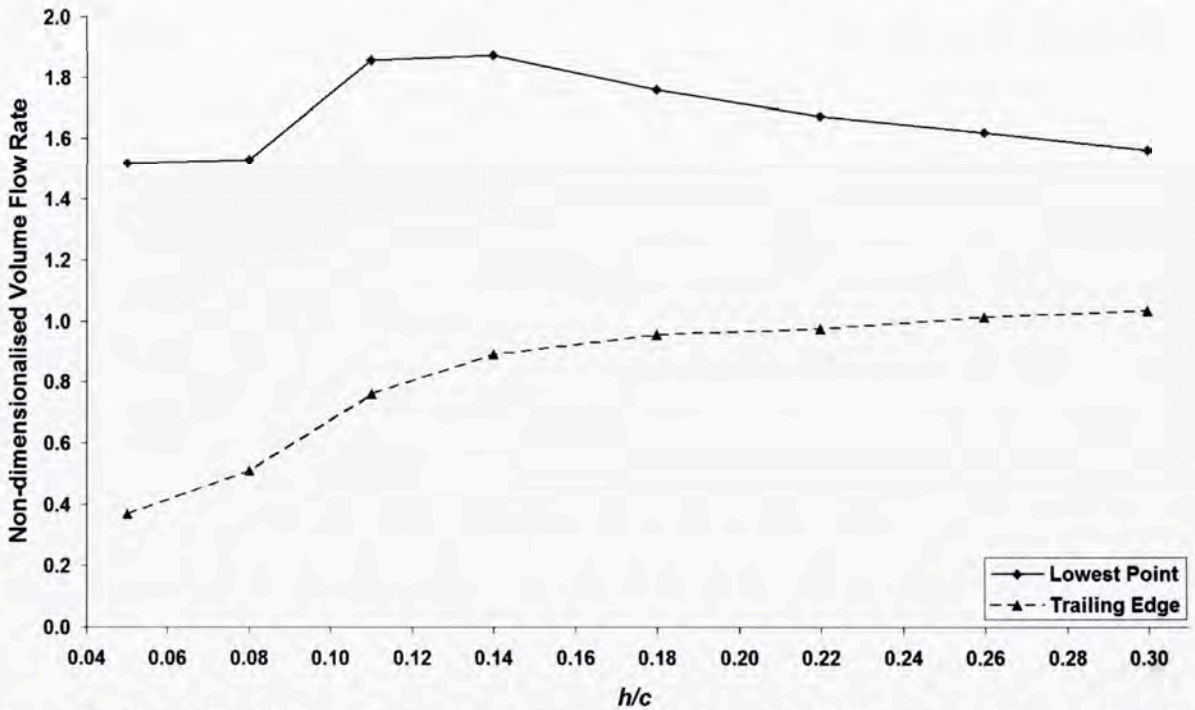


Figure 7.9: Normalised volume flow rate under wing at the lowest point (throat) and the trailing edge; normalised by 'ideal' freestream flow rate through given channel size

The reduction in the normalised flow rate through the trailing edge section of the diffuser, with decreasing clearance, shows the progressive worsening of flow constriction under the wing, which causes the flow to be diverted over the top of the wing. The normalised flow rate through the throat section manages to increase down to  $h/c = 0.14$ , while the overall flow rate

under the wing (see trailing edge trend) is being stifled – this is due to the strength of the diffuser effect. The reduction through the throat section commencing below  $h/c = 0.14$  coincides with a quicker reduction at the trailing edge. This indicates that the reduction seen at the throat is linked to the overall constriction of the flow under the wing.

Also of significance from Figure 7.7 is the shape of the separated shear layer at different clearances. At the higher clearances, the shear layer is quite convex as it leaves the surface of the wing and then progresses back toward the surface along a curved sweeping trajectory. As the wing moves toward the ground, this convex trajectory is flattened as the flow becomes more constricted by the ground's proximity. In free air, the shear layer will be entrained to follow the streamlines of the surrounding flow field which, due to the higher pressure away from the wing, head upward, following the wing's contour. In the constrained diffuser configuration, there is no source of higher pressure below the wing pushing the streamlines upward and, in fact, the widening diffuser will pull the streamlines away from the wing's surface. This change to the streamline behaviour is graphically demonstrated in Figure 7.10 where instantaneous streamlines originating at the midplane (near the leading edge) are compared between  $h/c = 0.30$  and 0.14. To create the figure, vertical strips of the  $h/c = 0.14$  image were overlaid onto the  $h/c = 0.30$  image. This approach allows one to compare the general inclination of the streamlines in both images at any point, with ease.

It should be noted that the streamlines in Figure 7.10 propagate through a three-dimensional domain and so do not necessarily remain in the midplane – particularly those passing through the turbulent sections of the flow field. This is why, from the camera's distant vantage perpendicular to the midplane, some streamlines appear to cross paths when they are, in fact, merely travelling through different spanwise positions.

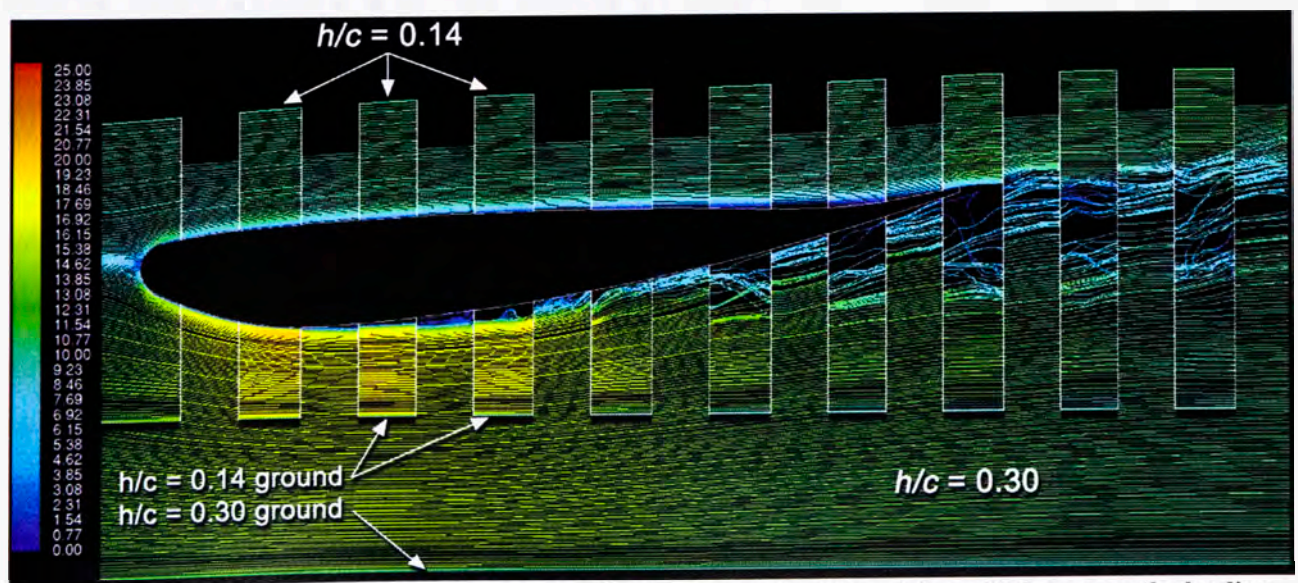


**Figure 7.10:** Instantaneous streamlines emanating from a vertical line at the midplane near the leading edge for  $h/c = 0.30$  and 0.14 (superimposed over  $h/c = 0.30$ ), coloured by instantaneous velocity magnitude (m/s)

Figure 7.10 shows how the underwing streamlines at  $h/c = 0.14$  follow a far more horizontal trajectory compared to the higher clearance case. At low clearances, the separated shear layer no longer curves back toward the wing's lower surface but rather tends to follow a more horizontal trajectory. It will be explained later in Sec. 7.2.7 that this change in behaviour contributes, among other things, to the full flow separation seen at  $h/c = 0.08$  and  $0.05$ .

#### 7.2.4 Separation, Transition and Reattachment

The separation point along the Tyrrell wing surface was defined as the location at which the x-component of velocity (in the wall adjacent cell) changed from positive to negative in the streamwise direction. The reattachment point was similarly defined as the surface location at which the x-component of velocity changed from negative to positive in the streamwise direction. In practise, the separation and reattachment lines over the wing surface were plotted where the x-component of velocity, in the wall adjacent cell, was equal to zero and the wing surface area captured within those lines was considered the separation zone.

The transition point was defined as the  $x/c$  location by which point the  $UV$  Reynolds stress  $\tau_{xy}$ , normalised by  $U_\infty^2$ , first reaches 0.001. This criterion was developed by Ol *et al.* (2005) for use with the transition to turbulence of a laminar separation bubble on a low Re aerofoil, and is applicable for this study. Contours of this normalised  $UV$  Reynolds stress criterion are presented later in Figure 7.20.

The time-averaged separation, transition and reattachment points, at the midplane, are presented below in Figure 7.11. As  $h/c$  is reduced, the separation point is pushed further downstream as the flow becomes more constricted under the wing, forcing flow through the throat region. This rearward movement actually accelerates slightly at the lowest two (full separation) clearances. For most of the clearance range, the transition point location remains fairly steady, albeit progressing downstream slowly. Below  $h/c = 0.14$ , however, the transition point location rapidly repositions from around  $x/c = 0.38$  back to around  $x/c = 0.45$  and seems to steady at this location (with decreasing clearance). The wall shear stress  $\tau_w$  escalation point (often used as an indicator of flow transition) was obtained from inspection of time-averaged wall shear stress plots over the wing's span. For an example of these plots, see Figure 7.12. The increase in  $\tau_w$  (at about 0.0317 m or  $x/c = 0.423$  in the figure) indicates the point on the wing's surface where the turbulent mixing first becomes apparent. The wall shear stress trend in Figure 7.11, though downstream somewhat, follows the transition point well except there is an obvious increase in the distance between the transition point and the wall shear stress spike at the two lowest clearances. Finally, the reattachment point trend

follows the separation, transition and wall shear stress point trends fairly well, though the distance back to the reattachment point grows fairly strongly between  $h/c = 0.14$  and  $0.11$ .

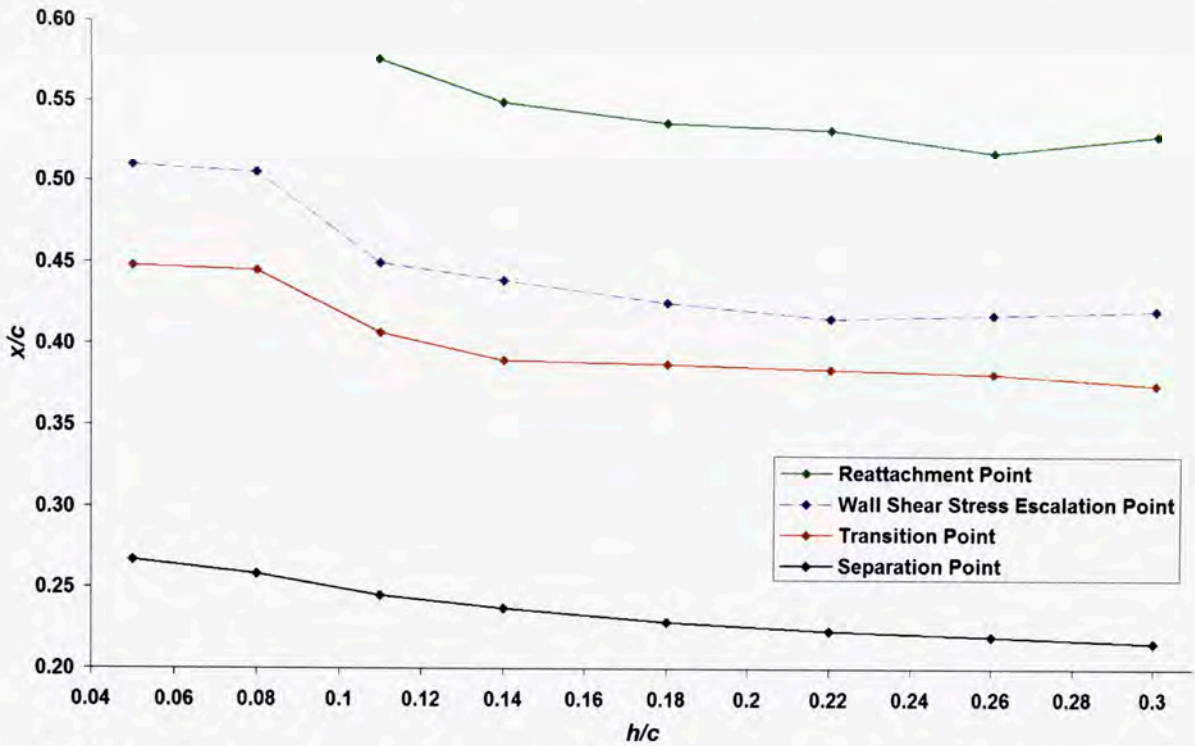


Figure 7.11: Time-averaged separation, transition, wall shear stress escalation, and reattachment points at midplane

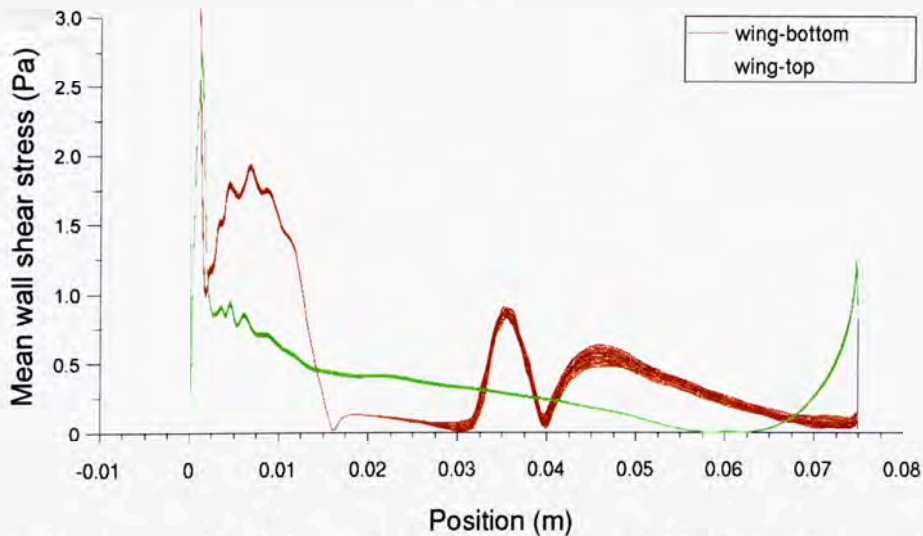
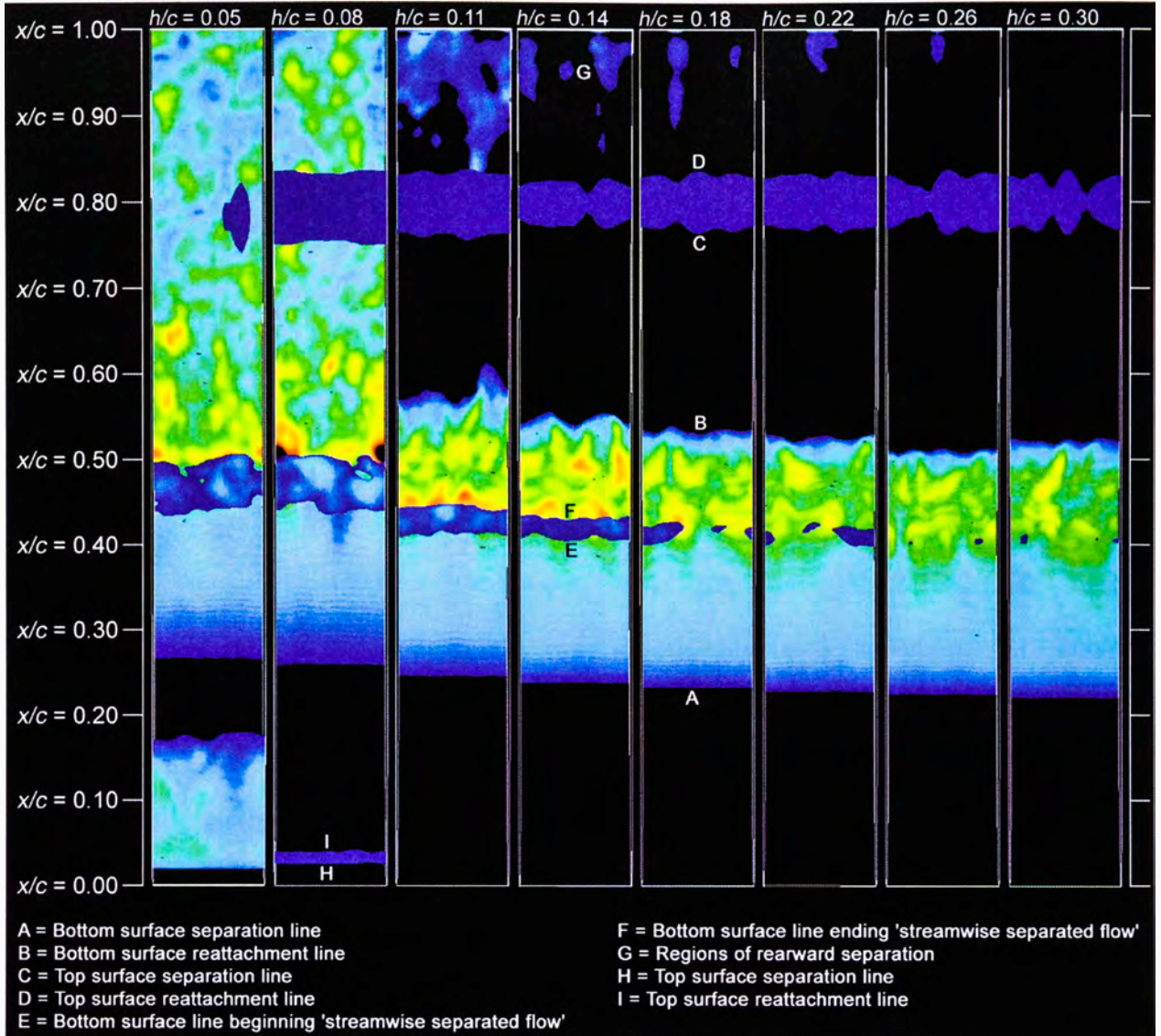


Figure 7.12: Time-averaged wall shear stress across wing span at  $h/c = 0.30$ , wing chord =  $0.075$  m

The wing’s flow separation behaviour is explained further in Figure 7.13. A top-down view of the Tyrrell wing is presented. Also plotted is an iso-surface where the time-averaged  $x$ -velocity component is equal to zero. This iso-surface thus captures the separation zone(s) around the aerofoil. On the iso-surface are plotted contours of average velocity magnitude. The separation line along the span of the wing (point A in Figure 7.13) is very consistent at all clearances as the flow is still laminar in this region. The reattachment lines (B), roughly located between  $x/c = 0.5$  and  $0.6$ , shows more variation across the span, owing to the turbulent mixing. This spanwise fluctuation of the location of the reattachment line gets

greater at  $h/c = 0.14$  and  $0.11$  – particularly the latter case with the maximum variation across the span reaching about  $x/c = 0.05$ . It is clear to see, however, that the trends identified in Figure 7.11 are still well representative of the separation bubble's behaviour.



**Figure 7.13: Time-averaged separation zones captured by iso-surface of zero x-velocity component, coloured by contours of average velocity magnitude**

There are several other features in Figure 7.13 that are quite instructive. Firstly, there is a progression of worsening separation near the trailing edge (with decreasing clearance) (G) as can be seen from the increasing size and upstream extent of the dark and light blue regions downstream of about  $x/c = 0.85$ . This behaviour shows that, despite downforce increasing down to  $h/c = 0.14$ , separation did already exist, and was getting worse, between  $h/c = 0.26$  and  $0.14$ . Below  $h/c = 0.14$ , the rearward separation zone grows quickly before full flow separation eventuates at  $h/c = 0.08$ . It should also be noted that at  $h/c = 0.11$  – where the worst of the rearward separation exists before full separation – the underwing suction and adverse pressure gradient were, in fact, already in decline.

Additionally, the dark blue band across the span, between  $x/c = 0.75$  and  $0.85$  (C and D), is actually located adjacent to the top surface of the wing (which may be apparent through a close inspection of the figure's white line outlines of the wing's geometry). This blue band represents a very shallow, extremely slow moving recirculation zone in the concave section of the wing's top surface. This section remained more-or-less steady through the simulated clearance region but almost completely, and abruptly, disappears at  $h/c = 0.05$ . This is due to the increased local flow speeds over the top of the wing at this extreme ground clearance. Also on the top surface, and located near the leading edge at the lowest two clearances, is a laminar separation bubble (H and I) due to the extra flow velocity travelling around the sharp convex curvature of the leading edge. The flow is much faster at the lowest clearance (see Figure 7.8) and the recirculation zone is thus much larger.

Finally, there is a small region within the bottom surface separation bubble, adjacent to the bottom surface, that is roughly located between  $x/c = 0.4$  and  $0.5$ , at all clearances (E and F). This region is encompassed by a dark-blue iso-surface of zero x-velocity – inside this region the flow features positive streamwise flow, whereas immediately outside it (in the separation bubble-proper) the flow is reversed. This region represents a temporary reattachment zone which is analogous to a recirculation zone, however, the flow within it is actually travelling in the downstream direction. Hence, within this zone, the wall-adjacent flow is in fact 'attached' by the definition set out at the beginning of this section. In reality though, the flow within these regions is of such low kinetic energy that the stability implied by the term 'attached' is in no way apparent. Consequently, it is probably more appropriate to term this type of flow 'streamwise separated flow.' Although this unusual flow phenomena is of some fundamental interest, it would not seem to impose any influence on the greater flow field.

### 7.2.5 Velocity Profiles and Reynolds Stresses

Profiles of the x-velocity component (streamwise) and  $UV$  Reynolds Stress component  $\tau_{xy}$  at various  $x/c$  locations and at all clearances are presented in Figure 7.14, Figure 7.15 and Figure 7.16. The  $UV$  component of Reynolds stress was included in these figures as it is very indicative of the turbulent behaviour about the wing. This will be discussed shortly.

The velocity profiles reveal how the boundary layer is being stressed as it progresses toward the trailing edge – not because of the adverse pressure gradient but because of the diffuser effect and its influence on the flow. Consider the  $h/c = 0.30$  case in Figure 7.14; after reattachment is achieved at  $x/c = 0.54$ , the velocity profiles downstream show that an attached turbulent boundary layer profile is quickly established and then is progressively strained toward the trailing edge, as kinetic energy reduces in the near-wall boundary layer. This

deterioration of the boundary layer gets progressively worse as ground clearance is reduced. It is important to note this trend includes the clearances of  $h/c = 0.14$  and  $0.11$  (the latter showing worse boundary layer deterioration than the former) despite  $h/c = 0.11$  featuring a lower adverse pressure gradient. This indicates that the primary cause of the boundary layer deterioration is not the adverse pressure gradient but the effect of the increasing outlet-to-inlet diffuser ratio.

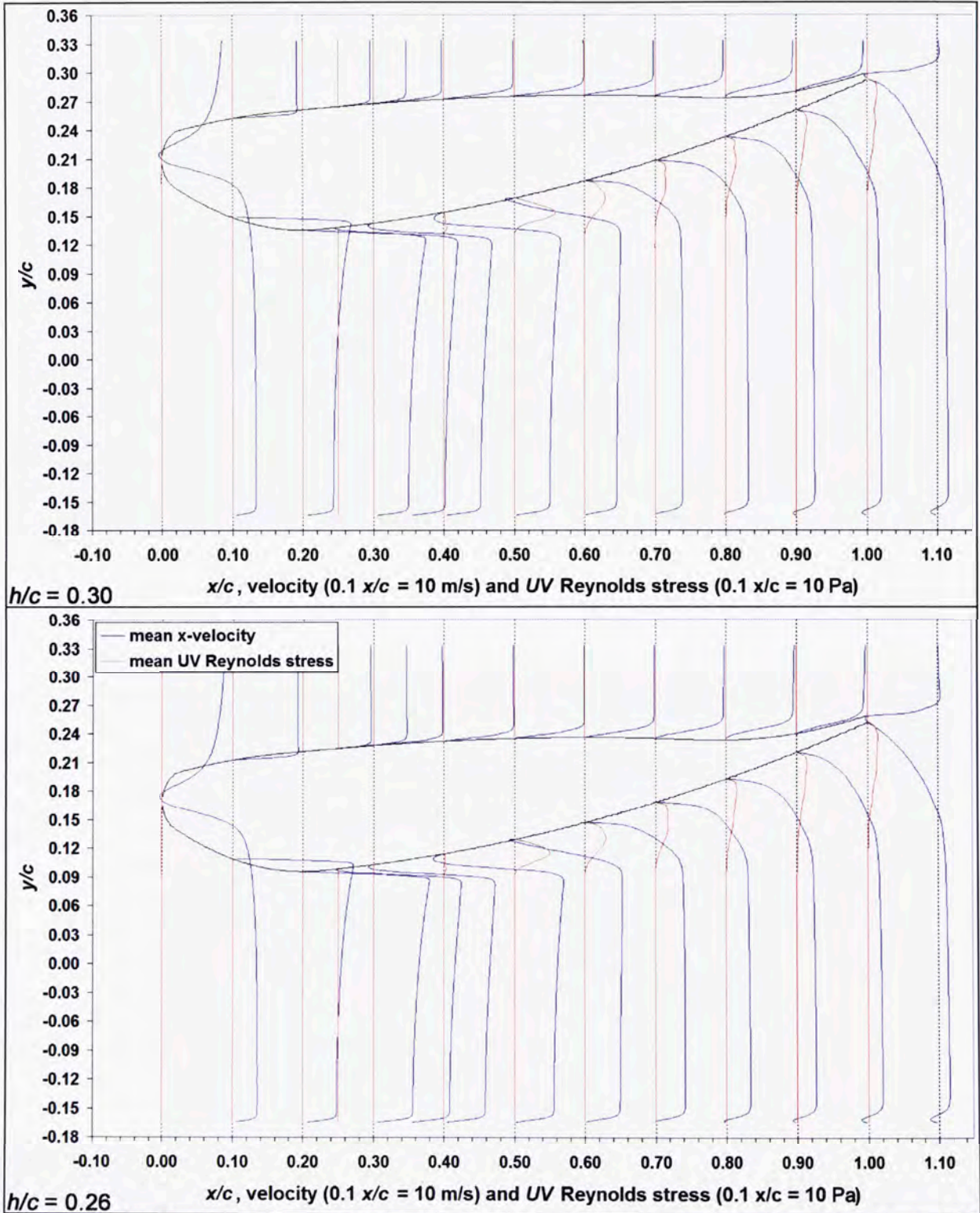


Figure 7.14: Profiles of average x-velocity and  $UV$  Reynolds stress at various streamwise locations at the midplane for  $h/c = 0.30$  and  $0.26$ ;  $0.1 x/c = 10$  m/s and  $10$  Pa

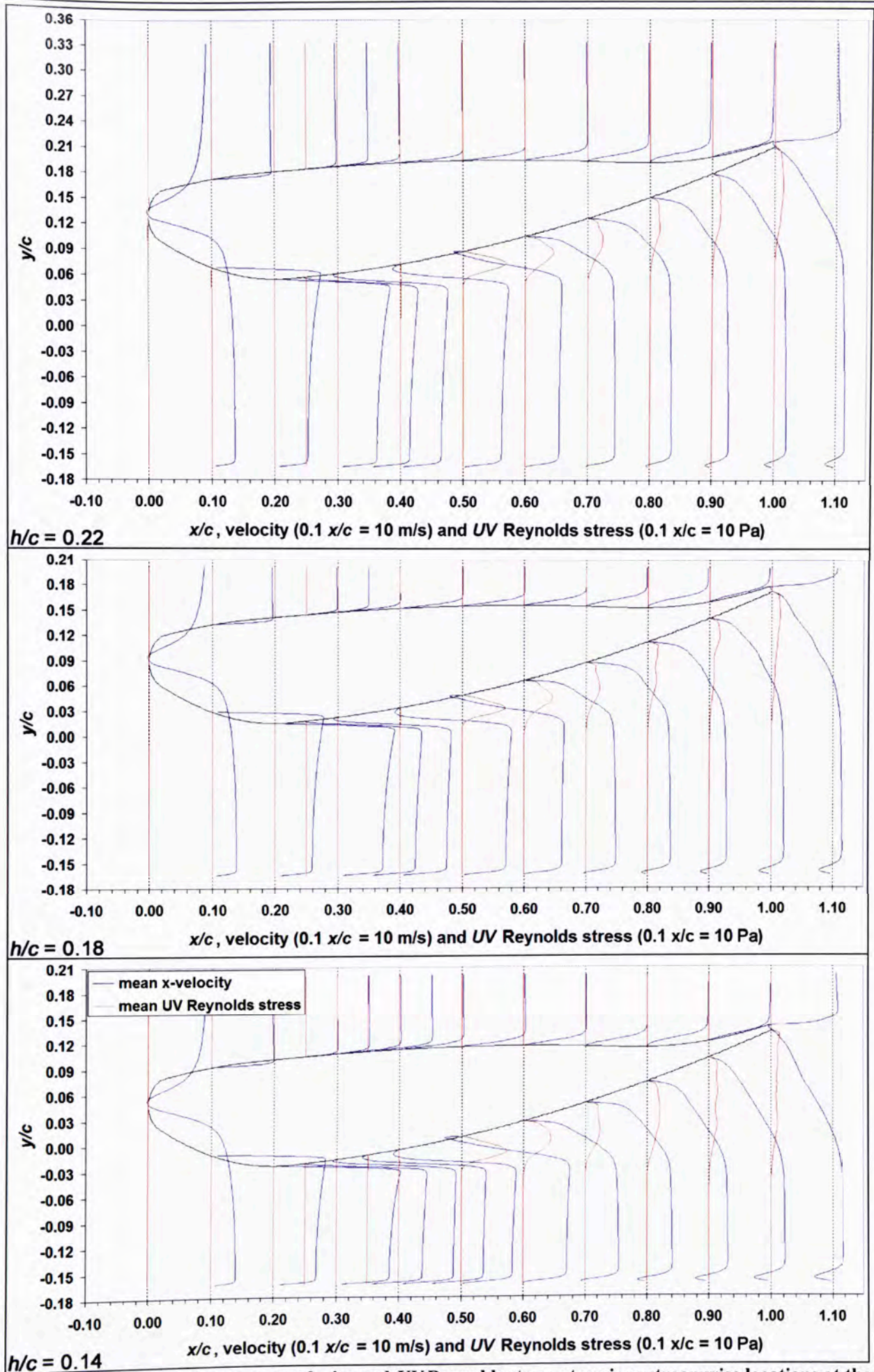


Figure 7.15: Profiles of average x-velocity and UV Reynolds stress at various streamwise locations at the midplane for  $h/c = 0.22, 0.18$  and  $0.14$ ;  $0.1 x/c = 10$  m/s and  $10$  Pa

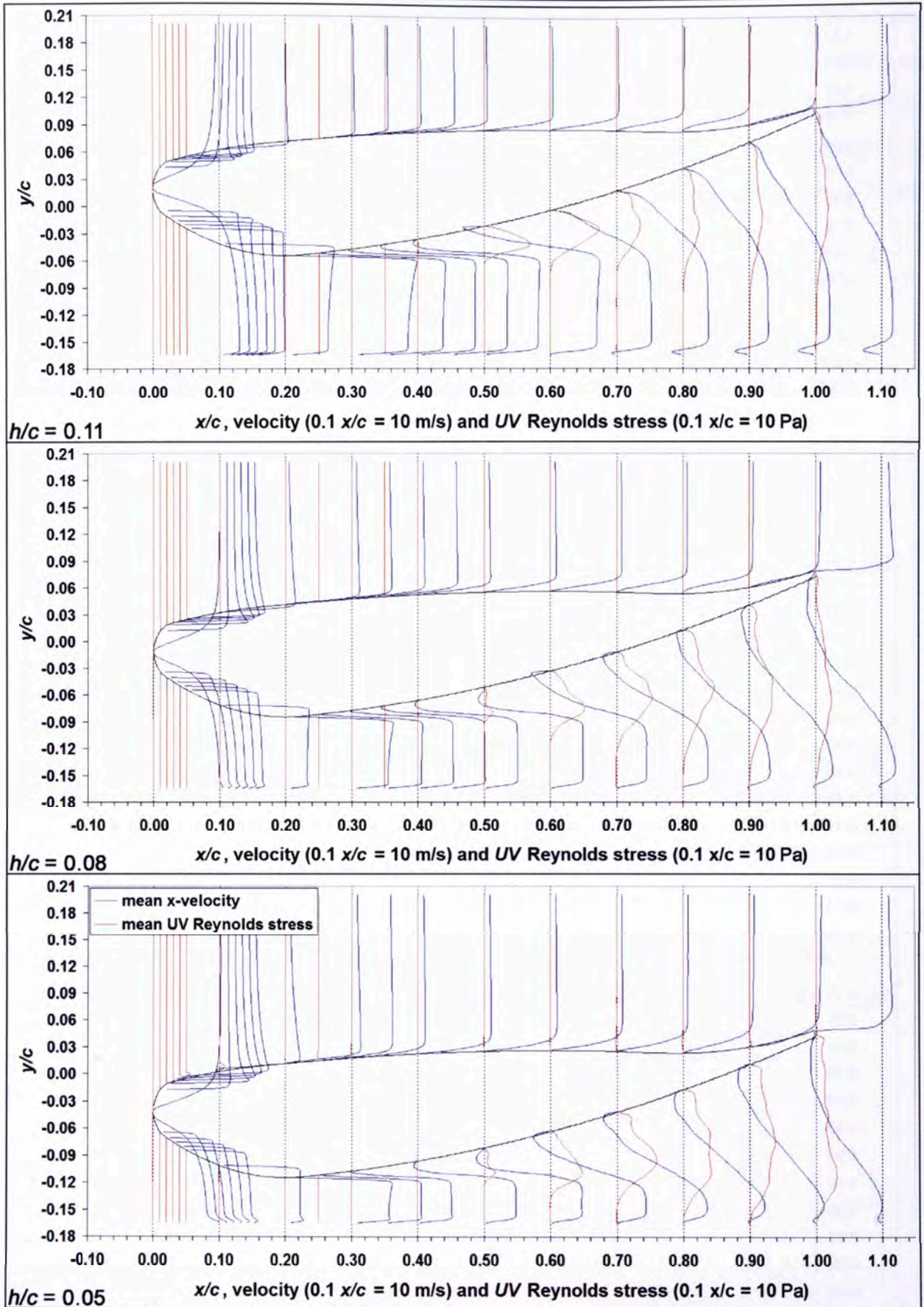


Figure 7.16: Profiles of average x-velocity and UV Reynolds stress at various streamwise locations at the midplane for  $h/c = 0.11, 0.08$  and  $0.05$ ;  $0.1 x/c = 10$  m/s and 10 Pa

As the clearance is reduced, the average flow velocity outside the boundary layer remains fairly steady from  $x/c = 0.60$  to the trailing edge. However, as the wing moves toward the ground, the ratio of the height of the rear of the diffuser section to the throat becomes greater.

This ratio increases the relative volume that the throat flow must fill downstream. However, given that the average velocities outside the boundary layer remain predominantly unchanged, the vertical extent (or width) of this fast flow channel cannot be maintained (while maintaining conservation of mass) and, thus, the depth of the boundary layer increases. Additionally, at lower clearances, the boundary layer features much less energy in the near-wall region, transitioning almost linearly in places from the out-of-boundary flow speed to stationary at the wall (see, for example, the  $x$ -velocity profile at  $x/c = 0.90$  for the clearance  $h/c = 0.11$ ).

The  $UV$  Reynolds stress plots can help to explain this behaviour. At the higher clearance cases ( $h/c = 0.30, 0.26, 0.22$  and  $0.18$ ), the peak values of  $\tau_{xy}$  are located at the wall. This indicates that turbulent mixing is enabling kinetic energy from outside the boundary layer to reach the bottom of the boundary layer. This  $\tau_{xy}$  peak at the wall starts at the reattachment point and continues to peak at the wall all the way to the trailing edge. However, at  $h/c = 0.14$  and below, the peak Reynolds stress starts to shift away from the wall which indicates that less kinetic energy is reaching the wall and placing more strain on the boundary layer. At  $h/c = 0.11$  (in Figure 7.16), the peak Reynolds stress is always toward the outside of the boundary layer, allowing little kinetic energy to stimulate the near-wall region. At  $h/c = 0.08$ , this trend is exacerbated further. Although the peak Reynolds stress at this clearance is actually higher in many places than at  $h/c = 0.11$ , it is located in the outer boundary layer and does not aid the near-wall region which is now completely separated. This complete separation is a result of the wall not having been imparted sufficient energy to regain attachment. The same situation is also seen at  $h/c = 0.05$ .

It is also interesting to note the behaviour of the velocity profiles near the ground as clearance is reduced. At  $h/c = 0.30$ , an effective flow reversal occurs at the ground at about  $x/c = 0.80$ . As the ground plane moves at 10 m/s, the adjacent flow is always well in excess of this and therefore generates a boundary layer at the ground. This flow near the ground remains laminar and, with the adverse pressure gradient from the diffuser effect, eventually suffers relative flow separation from the ground surface. From a stationary reference frame, this flow reversal manifests as a dip below 10 m/s adjacent to the ground surface. This ground separation gets larger with decreased clearance, with separation occurring at  $x/c = 0.70$ , until it stabilises at  $h/c = 0.14$  and  $0.11$ . Below  $h/c = 0.11$ , the ground separation almost disappears with separation occurring now at  $x/c = 0.90$ . The reason for this change in behaviour is because the flow near the ground transitions to turbulence and thus delays separation.

A plot showing the contours of  $UV$  Reynolds stress at the midplane of the wing, at all clearances, is shown in Figure 7.17. The change in behaviour as described above is evident. The turbulent production begins at the breakdown of the separated shear layer and, at the higher clearances, this turbulent production stays close to the wing within the boundary layer, energising the near wall and allowing the boundary layer to reattach, and stay attached.

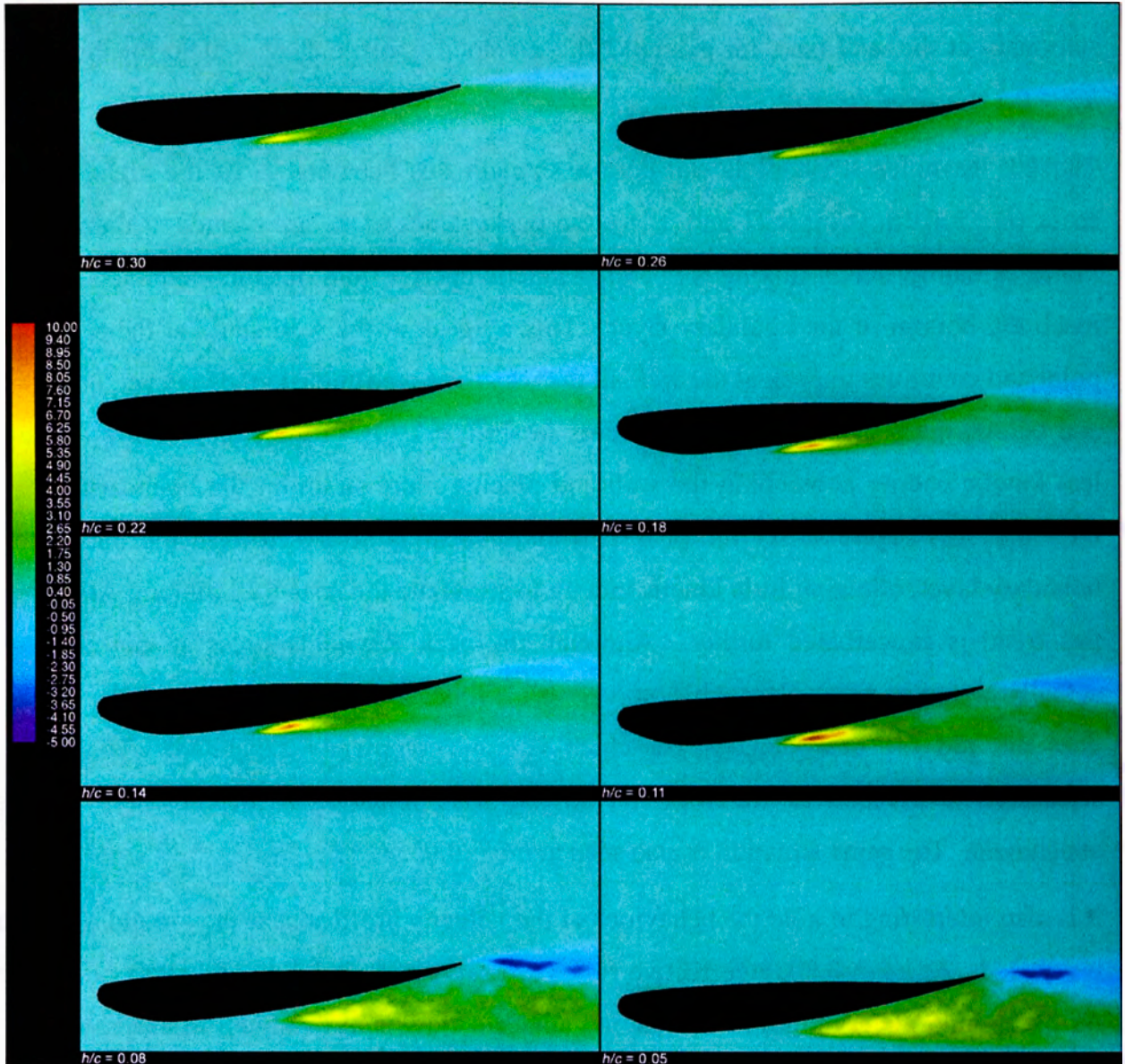


**Figure 7.17: Contour plots of  $UV$  Reynolds stress at midplane for all clearances (Pa)**

The peak  $UV$  Reynolds stress value steadily increases down to the clearance  $h/c = 0.11$ . This increase in peak value can be attributed to the continually increasing flow velocity under the wing. This increased flow velocity feeds more kinetic energy into the energy cascade. However,  $h/c = 0.08$  and  $0.05$  both see a sudden reduction in the peak value which is due to the lower available energy in the, now much slower, underwing flow. Additionally, the  $UV$  Reynolds stresses at the lowest clearances initiate far from the wall such that the turbulent production does not reach the near-wall region, preventing reattachment.

### 7.2.6 Vorticity and Turbulent Wake

Selected vorticity contour plots are presented in Figure 7.18. The right hand column in the figure displays the three components of vorticity at the midplane of the Tyrrell wing at  $h/c = 0.18$ . It can be noted – and this is consistent for all clearances – that the vortical structures about each axis are of a similar strength; this indicates that the generated turbulence is predominantly homogenous. The vortical structures emerging from the collapsing underwing shear layer move down toward the ground for clearances below  $h/c = 0.11$  indicating a change in the turbulent behaviour where the full clearance between the wing and the ground (and the near wake) is now subject to turbulent fluctuations.

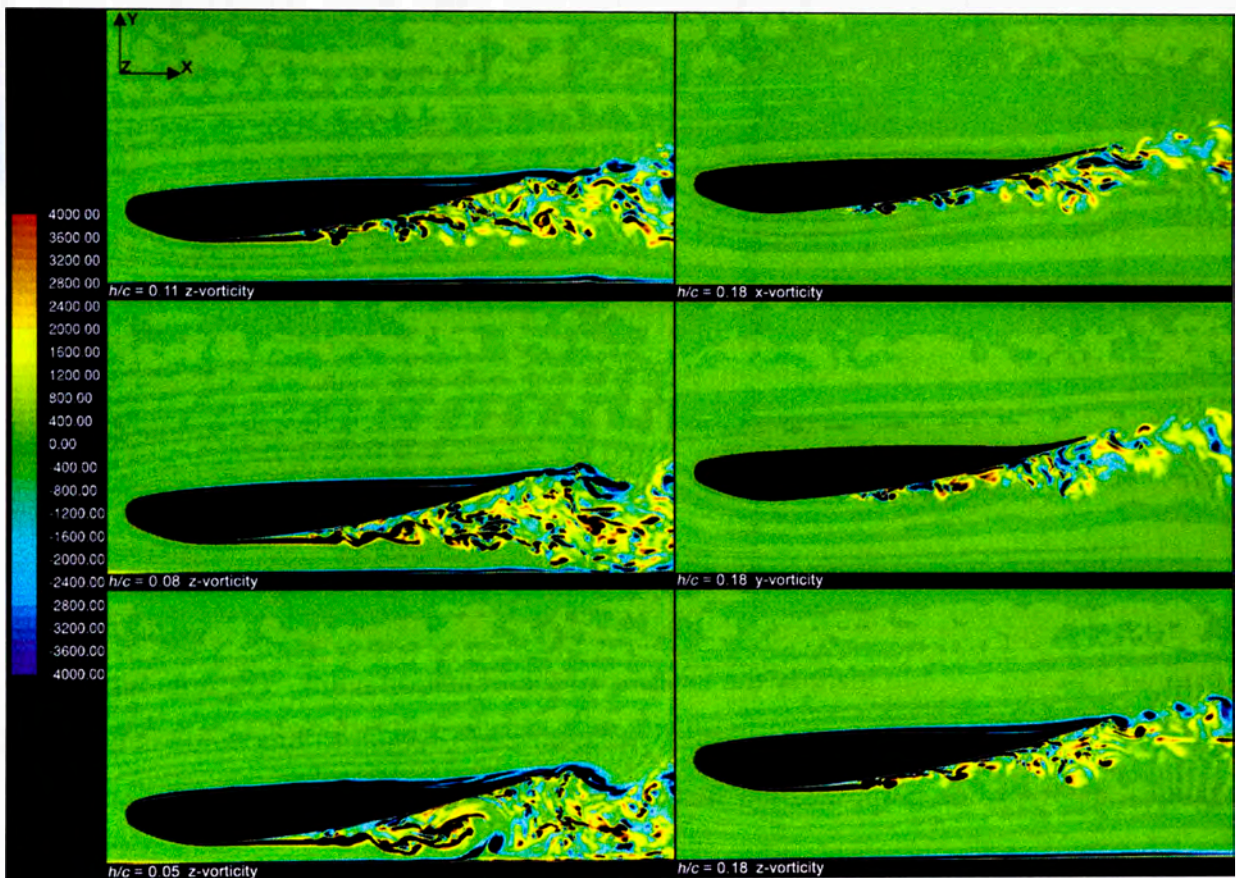


Figure 7.18: Contours of x-, y- and z-vorticity at selected ground clearances

### 7.2.7 Development of Flow Separation

From the observations made in the previous sections, it is clear that one of the primary contributions to the wing's eventual full separation is the inability of energised flow to reach the near wall region when close to the ground. This problem is further elucidated in Figure 7.19 which shows the time-average y-velocity contours at the wing's midplane. These plots only show the positive regions of y-velocity, that is, the regions where the flow is moving vertically upward. Also included in these plots is the zero-x-velocity line which is a cut of the iso-surface show in Figure 7.13.

It can be seen at the higher clearances that as soon as the separated shear layer collapses to turbulence, the flow then moves rapidly up toward the surface of the wing and this upward-moving flow extends to the trailing edge. As the wing's clearance is reduced, this behaviour is initially well preserved until  $h/c = 0.22$ . At this clearance, the blue region adjacent to the wall has become thicker and the extent of the magnitude of the upward moving flow, back toward the trailing edge, has reduced. This trend continues down to  $h/c = 0.11$ , with the blue band near the surface getting thicker (indicating that the flow is not reaching all the way to the wall) and the region of sizable upward flow further receding upstream from the trailing edge, preventing the dissemination of kinetic energy to the rear of the wing's boundary layer. At the lowest two clearances, a dramatic change in behaviour is apparent; the upward movement of the flow after the shear layer collapse completely disappears and the boundary layer region features almost no upward moving flow (indicated by the large black regions in the plots). These bottom two clearance plots show the complete failure of the turbulent mixing to extend up anywhere near the wing's surface.

So far it has been observed that flow separation has been largely influenced by the location of the turbulent energy production in the flow. It has been shown that if this turbulent production is not located sufficiently close to the wall, the near wall will not be fed sufficient energy to prevent flow separation, as so dramatically illustrated at the bottom of Figure 7.19.

What will be examined now is why this turbulent production moves away from the wall at lower clearances. In Figure 7.20 is presented the normalised  $UV$  Reynolds stress criterion that was used in Sec. 7.2.4 to identify the location of the transition point. The contours start at the value  $\tau_{xy}/U_\infty^2 = 0.001$  and the smallest  $x/c$  location that is equal to this value is the transition point. The transition point location was recorded at each clearance and this location, relative to the wing's surface is presented in Figure 7.21 in order to demonstrate the evolution of the transition point with decreasing clearance. Also plotted in the figure is the zero x-velocity line at the clearances of  $h/c = 0.30$  and  $0.05$  (the highest and lowest clearances). This line can be thought of as representing the upper limit of the free shear layer (upstream of the transition point) and so provides a useful insight into the general shape of the shear layer at these clearances.

For most of the clearances, the transition points cluster in one area, albeit moving downstream slowly, until  $h/c = 0.11$  and below, where it starts to move rearward very quickly. To help examine these transition points in more detail, the plot in Figure 7.22 is presented.

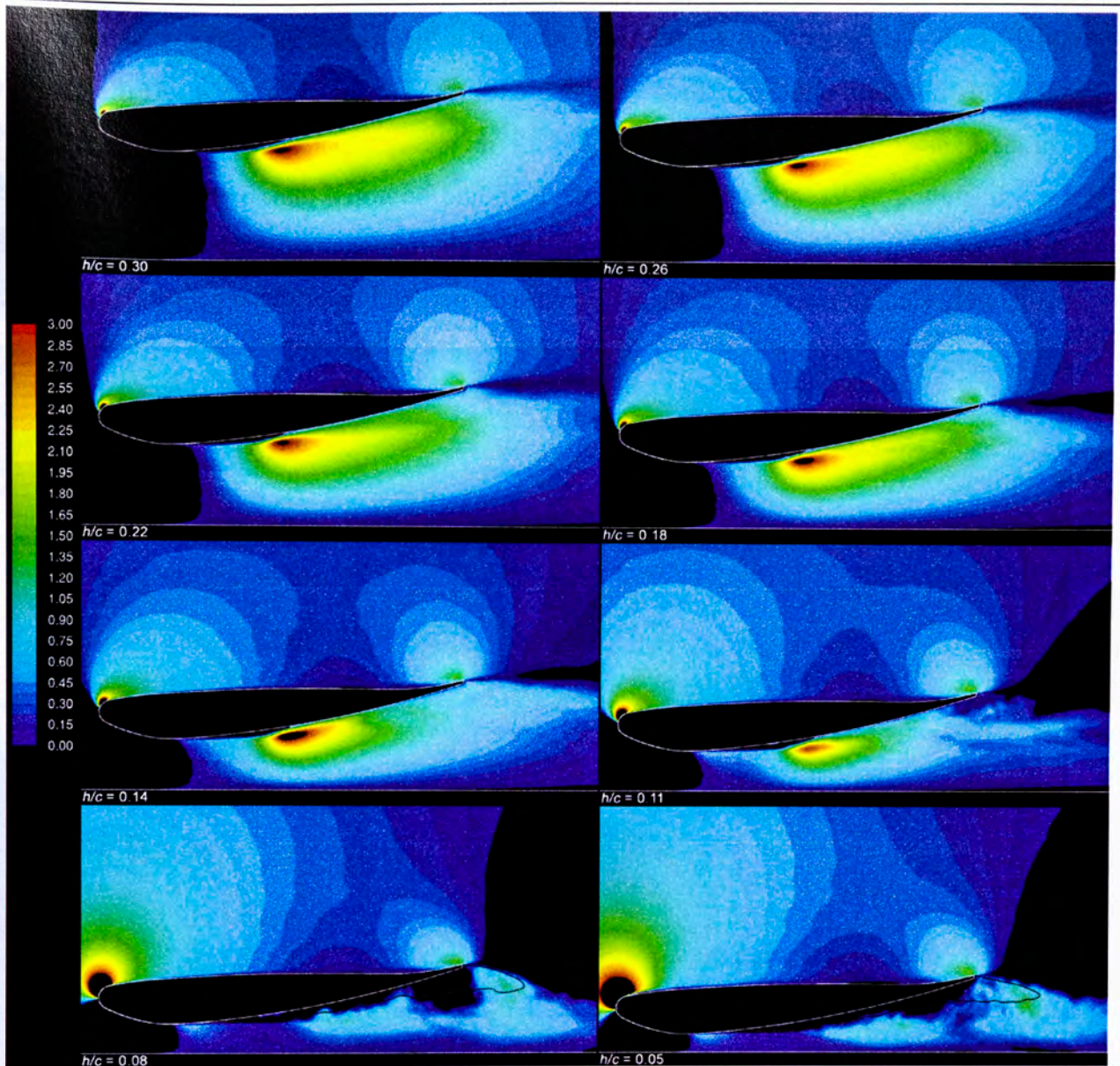


Figure 7.19: Contour plots of time-averaged  $y$ -velocity at the midplane, only plotting the positive values

As well as the large rearward movement of the transition point at the lower clearances (see the black plot in the figure), the separation point moved notably rearward as well, indicated by the red line in the figure; this shows that, even with the rapid movement near the ground, only about a 20 % increase in the distance between the separation and transition points was seen. This observed increase, however, is due to the much lower flow velocities under the wing at these clearances, which therefore takes longer to destabilise the shear layer. The green plot in the figure shows the  $x/c$  location at which the wall shear stress spiked indicating, as mentioned earlier, where the turbulent mixing reaches the wall. The distance between the transition point and it being felt at the wall increased below  $h/c = 0.11$ .

The most important information from Figure 7.22 is the blue plot which indicates the perpendicular distance from the wing surface of the transition point. Between  $h/c = 0.30$  and  $0.11$ , this value moves between two values ( $s/c = 0.0145$  and  $0.0161$ ) which both represent node points on cells in two adjacent rows of cells in the boundary layer mesh of the LES

model. Thus the fluctuation between these two values demonstrates that the distance from the wall to the transition point remained very stable for most of the clearances. At the lowest two clearances, however, the distance to the wall increased very suddenly to  $s/c = 0.0221$  – approximately a 37 % increase in distance. It should be noted that, as this distance increase encompasses only a few mesh cells, its precise magnitude cannot be determined here. It is qualitatively clear, however, that a large increase in perpendicular distance has taken place.

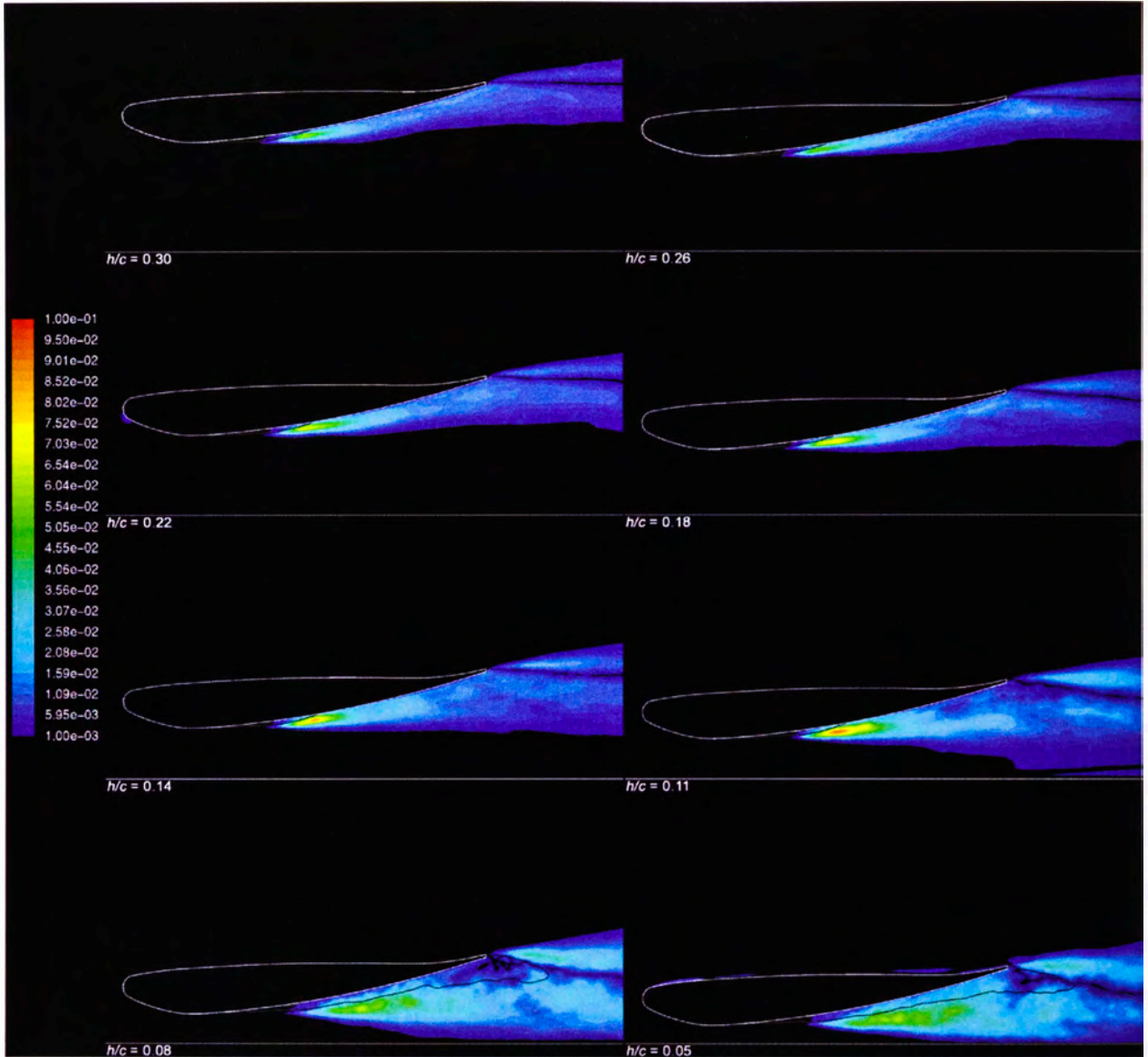


Figure 7.20: Contour plots at midplane of  $UV$  Reynolds stress, normalised by  $U_\infty^2$

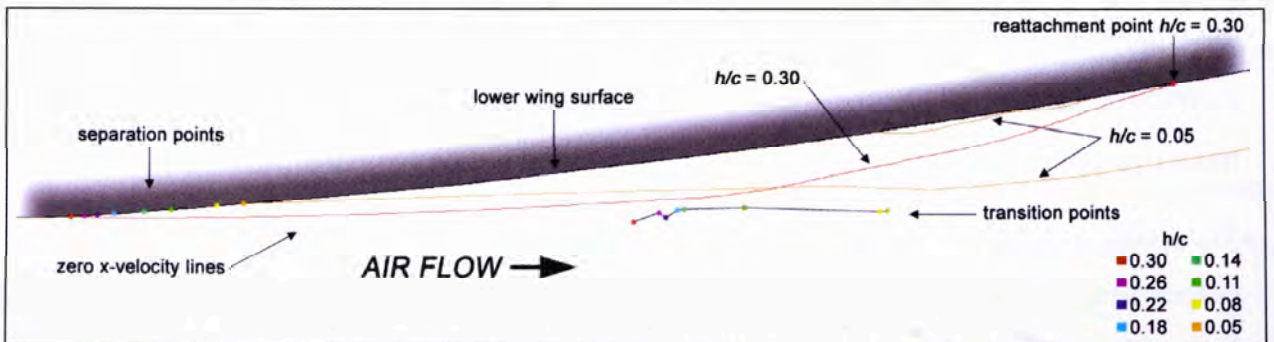


Figure 7.21: Evolution of transition point with ground clearance changes

It is this sudden and significant increase in distance between the wall and the transition point, along with the lower available energy, that prevents any possibility of the energy reaching the wall and flow reattachment taking place. This increase in distance to the wall owes much to the change in shape of the separated shear layer observed earlier in Sec. 7.2.3. Looking again at Figure 7.21, it should be noted that, even with the increase in distance between separation and transition at the lower clearances, if the separated shear layer were to still follow the convex curvature as shown for  $h/c = 0.30$ , then the increase in perpendicular distance from the wall would still only be marginal. Thus, the change in trajectory of the shear layer, induced by the diffuser effect, is quite instrumental in moving the transition point away from the wall and preventing reattachment.

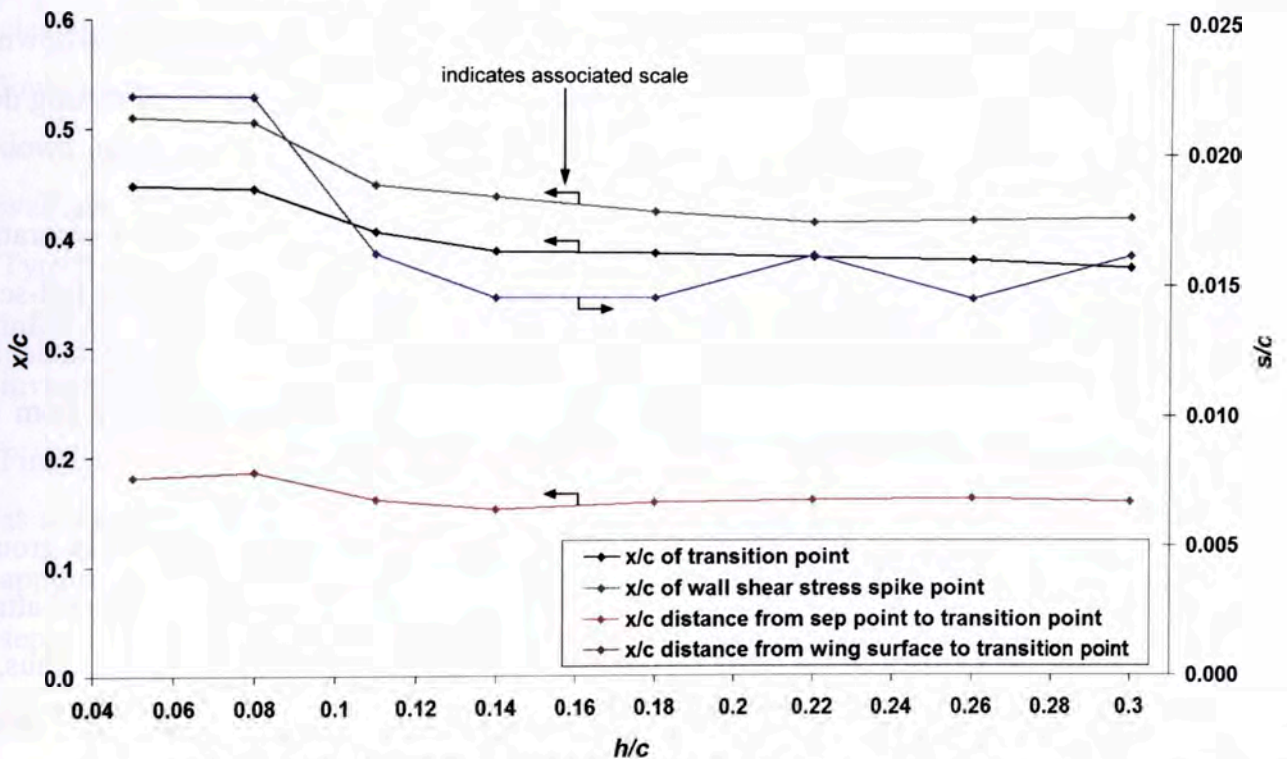


Figure 7.22: Location of transition point with changing ground clearance

As a result of the work in this chapter, the development of quasi-two-dimensional flow separation about the inverted Tyrrell wing in extreme ground effect was found to develop as follows. As the wing is moved toward the ground, the outlet-to-inlet ratio of the diffuser increases exponentially. The larger this ratio, the more challenging it is for the high speed flow through the throat (inlet of the diffuser) to fill the volume under the wing. The high speed flow through the throat continues through the diffuser as a high speed jet, albeit imparting some kinetic energy into the boundary layer through turbulent mixing, as it does so. As the outlet-to-inlet ratio increases, the amount of kinetic energy required to be bled off this high speed jet to avoid flow separation increases, but the mixing achieved is insufficient. This lack of kinetic energy creates an increasingly thick and unstable boundary layer which

initiates flow separation at the trailing edge. This trailing edge separation progresses upstream with increasing outlet-to-inlet ratio (decreasing ground clearance).

The form of flow separation described above is predicated on the free shear layer reattaching as a result of the turbulent mixing reenergising the boundary layer. For most of the clearance range, this process is easily achieved until  $h/c = 0.11$ , where the distance from separation to reattachment increases notably. This is due to the, now, reducing normalised volume flow rate (or the, fairly analogous, reducing average flow velocity) through the throat which reduces the amount of energy available to reenergise the boundary layer. The task of reenergising the boundary layer is even more difficult at  $h/c = 0.08$ , where the normalised volume flow rate through the throat is significantly lower again and, due to the flatter shear layer, the now much less energetic turbulent production at the shear layer breakdown is occurring much further away from the wall. Consequently, most of the turbulent mixing does not even reach the wall and so the wing stands no chance of achieving reattachment.

Two processes of flow separation have been observed in this study; a progressive separation caused by a strengthening diffuser effect and a sudden and much more dangerous full-scale separation which is caused by both the flow diversion over the wing (reducing energy under the wing) and the diffuser effect moving the turbulent production point further away from the wing's surface.

The first form of separation is unavoidable as it is a direct result of the presence of the ground (which obviously cannot be avoided in ground effect applications). A lower angle-of-attack wing will still suffer this form of flow separation, but at a lower ground clearance. Thus, to mitigate this form of separation at extremely low ground clearances, a lower angle of attack must be adopted, sacrificing performance. However, this form of separation may indeed not pose a problem until extremely low clearances as, despite the extent of this separation advancement with decreasing clearance, the  $C_N$  values obtained continued to rise. Clearly the benefit of the diffuser effect outweighs the progressive separation for much of the clearance range.

One could adopt several approaches to avoiding or mitigating the second, sudden form of separation. It may be avoided completely if the flow is tripped near the leading edge in order to induce flow transition straight away. This would avoid a separated shear layer and thus negate the possibility of sudden separation. However, the performance deficit involved with this approach is prohibitive with Zerihan and Zhang (2000) observing an approximate 33 % reduction in peak downforce performance for the Tyrrell wing at a  $3.45^\circ$  angle of attack.

Alternatively, the aerofoil could be redesigned to feature a very large radius bottom surface curvature in the area where the shear layer would normally separate, in order to prevent an adverse pressure gradient sufficient to cause a laminar separated shear layer. However, this curvature would need to continue until transition to turbulence was safely achieved and this would severely affect the overall performance of the aerofoil as a sharp curvature after the throat region was shown earlier in Sec. 5.3.2.2.1 (summarised in point 10, in Sec. 5.4) to be very important to achieving good ground effect performance.

Because employing a large radius lower curvature is too detrimental to performance, a different wing surface that preserves the separated shear layer, but deals with it more effectively, is postulated. The flattening of the shear layer cannot be avoided at low clearances and so the lower surface of the proposed wing would be brought down toward the low-clearance transition point ( $h/c = 0.05$  transition point). Thus, when the shear layer breaks down at very low clearances, the generated turbulence will still be in close proximity to the wall and should therefore be able to achieve reattachment at lower clearances than does the Tyrrell wing. This performance-oriented design modification is suggested here as a logical inference based on the observations of this study. However, a thorough and detailed investigation is needed to validate this concept and this is beyond the scope of this work

Finally, it should be noted that although the phenomena observed in this study were achieved at a Reynolds number of 53,000, these same phenomena would be apparent in higher Re applications if the wing was designed to sufficiently stress the laminar flow to induce separation. This could be done to maximise the diffuser performance of the wing.

### 7.3 Conclusions

A series of LES simulations were conducted to model the quasi-two-dimensional flow separation that occurs on an inverted Tyrrell wing in extreme ground effect. The following conclusions were drawn:

- (1) The Tyrrell wing featured a laminar separated shear layer on the lower surface which for most clearances transitioned to turbulence and reattached.
- (2) Two types of flow separation were observed on the Tyrrell wing: a progressive form which advanced upstream from the trailing edge with decreased ground clearance and a sudden full-scale form which resulted from the laminar separated shear layer's inability to re-establish attached flow after transition to turbulence.
- (3) The progressive form of flow separation, worsening down to the clearance of  $h/c = 0.14$ , coincided with an increase in  $C_N$ , indicating that the suction borne of the diffuser effect

outweighed this separation. At  $h/c = 0.11$ , however,  $C_N$  starts to drop significantly, and this is due to a large diversion of flow (and therefore kinetic energy) over the wing.

- (4) The progressive form of flow separation was found to be caused by the strengthening diffuser effect and not due to an excessive adverse pressure gradient. With decreasing clearance, the outlet-to-inlet ratio of the diffuser increased and made it increasingly difficult for the fast jet flow passing under the wing to impart sufficient flow velocity to the rest of the volume under the wing; this caused the boundary layer to be greatly thickened and stressed, bringing about the progressive separation.
- (5) The sudden full-scale form of flow separation was caused by two primary factors. Firstly, the energy available to energise the boundary layer upon transition to turbulence was severely reduced at  $h/c = 0.08$  as the flow speed under the wing reduced dramatically (thanks to the flow diversion over the wing). Secondly, the source of the turbulent production, from which the boundary layer relies for energy, moved significantly away from the surface of the wing such that the, now, much lower turbulent mixing did not even reach the near wall region, thus preventing reattachment. This movement away from the wall was found to be due to flow constriction at low clearances which changes the trajectory of the shear layer.

# Chapter 8: Conclusions

## 8.1 Conclusions of Research

Flow separation is a phenomenon which negatively affects the performance of an inverted wing in ground effect. The onset of flow separation reduces the beneficial downforce that can be generated and can do so very abruptly and dangerously. It is therefore necessary to have a good understanding of the circumstances in which flow separation is induced and also to gain an understanding of precisely how flow separation transpires under these conditions.

It has been shown in the literature that flow separation tends to be induced earlier (at a lower angle of incidence), the closer a wing is to the ground. However, a thorough understanding of why this is so and how it develops is still unexplained. The literature also notes many behavioural characteristics of wings and aerofoils in ground effect (both inverted downforce-generating and upright lift-generating), however, little attempt has been made to explain the actual ground effect phenomena that is causing this behaviour.

This research programme was undertaken with the purpose of better understanding these ground effect phenomena. Of particular interest in this work were the overall mechanisms of ground effect at play, irrespective of the geometry near the ground, a thorough elucidation of the precise ground effect mechanisms apparent about inverted aerofoils and the processes that leads to flow separation on the underside of inverted wings in ground effect.

To investigate these phenomena, several studies were undertaken utilising Laser Doppler Anemometry and smoke visualisation experimentation, two-dimensional Reynolds-Averaged Navier-Stokes CFD modelling and quasi-two-dimensional Large Eddy Simulation CFD modelling.

### ***8.1.1 Ground Effect Phenomena about 2D Aerofoils***

A numerical investigation was undertaken using a Reynolds-Averaged Navier-Stokes solver to examine the workings of ground effect phenomena in the two-dimensional flow regime. The investigation was conducted in two parts. In the first part, ground effect behaviour was observed about both upright and inverted aerofoils and sought to clearly explain how ground effect works in both cases. In the second part, a closer investigation of the inverted aerofoil case was conducted which examined the influence on ground effect of changes to the

geometric properties of the aerofoil and, through so doing, sought to determine how ground effect may be better exploited.

In the literature, investigations into ground effect phenomena about aerofoils have typically been conducted on either an upright or an inverted configuration, in isolation. By considering one or the other in isolation, a holistic understanding of how ground effect influences aerofoils in general, has not been developed. With a view to addressing this, the first two-dimensional CFD investigation considered the highly cambered Tyrrell aerofoil in both its upright and inverted configurations.

The numerical study was conducted at a representative Reynolds number of 458,800. The investigation was restricted to the two-dimensional case in order to simplify the physics associated with this ground effect problem.

The lift produced by the upright aerofoil slowly diminished down to a ground clearance of  $h/c = 1.00$ . This decrease was due to an identified general ground effect flow mechanism which induced a reduction in the effective angle of attack for both aerofoil configurations, with decreasing clearance. The decrease in the effective angle of attack was due to a reduction, with decreasing ground clearance, in the deflection of the upstream streamlines. As the aerofoil (upright or inverted) came into close ground proximity, the streamlines become progressively more horizontal. This reduction in angle of attack caused a consequent reduction in lift on the upright aerofoil. The reduction in angle of attack was seen for the inverted aerofoil as well; however, the beneficial suction from the diffuser effect, formed between the aerofoil and the ground, more than cancelled this negative effect.

As the aerofoils moved into close ground proximity, the stagnation point at the leading edge was found to move significantly down toward the ground (relative to the aerofoil), revealing another general ground effect flow mechanism. This downward movement occurred on both aerofoils, so this behaviour is not related to the specific aerofoil geometry. The stagnation point movement was due to an overall reduction in flow rate under the aerofoil – diverting more flow over the top of the aerofoil – which caused changes to the local flow field in the vicinity of the stagnation point.

Ground effect phenomena, and the resulting aerodynamic behaviour of ground effect bodies, are influenced by changes to the combined geometry of the body and ground combination. Although work has been conducted in the literature that examines the effect of changing the ground clearance and angle of attack of an inverted aerofoil, little attention has been paid to understanding the influence on ground effect phenomena of more subtle changes in the geometry of an aerofoil. Understanding those influences and determining the underlying

physical mechanisms that causes them was the purpose of the second part of the two-dimensional CFD investigation.

The inverted Tyrrell aerofoil (used in the previous study) and the inverted NACA4412 aerofoil, were first analysed where the ground effect behaviour of both aerofoils were observed and compared over a range of different ground clearances. The aerofoils were quite different. Tyrrell aerofoil was the cross-section of the main-plane of the 1998 Tyrrell Formula 1 racing car and was specifically designed to operate in a ground effect environment, while the NACA4412, a common aerofoil used in aerodynamic research, was not designed for use in a ground effect environment.

Additionally, as it is difficult to determine the reasons behind the observed differences in behaviour of the two aerofoils, it was desirable to be able to change only one key performance variable at a time in order to ascertain the causes of the change in performance. Therefore, at a constant and low ground clearance, three additional aerofoils were initially studied to investigate more precisely the influence on ground effect phenomena of three geometric features representing the key differences between the Tyrrell and NACA4412 aerofoils. These three new aerofoils were based on the Tyrrell aerofoil and were designed to replace one feature of the Tyrrell with the corresponding feature of the NACA4412. The three features tested on the modified Tyrrell aerofoils were the leading edge shape, the camber on the top surface (pressure surface) and the camber on the bottom (suction) surface. Latterly, as a result of this comparison work, two more aerofoils were created to more precisely elucidate the phenomena in play.

The comparison of the performance of the inverted Tyrrell and NACA4412 aerofoils showed that The Tyrrell made greater use of ground effect at low clearances than the NACA4412, producing more downforce and associated drag. The character – or general shape – of the Tyrrell  $C_p$  plots remained consistent with decreasing clearance, whereas the character of the NACA4412  $C_p$  plots changed with decreasing clearance. This behavioural variation on the NACA4412 indicated that a significant change in the encountered aerodynamic phenomena was occurring, as the aerofoil moved into the ground effect regime. This suggests that the NACA4412 aerofoil was ill-equipped to exploit the ground effect phenomena and so, this behavioural change may be considered a qualitative indicator of poor ground effect utilisation.

The investigation into the effect of specific geometric changes to the aerofoil showed that the presence of camber on the top surface of an inverted aerofoil significantly increases suction on the bottom surface and slightly increases pressure on the top surface. This top surface camber proved increases circulation and enhances the diffuser effect. A more-forward

placement of the lowest point on an inverted aerofoil was shown to be advantageous in the generation of peak suction under the aerofoil. The forward limitation on this beneficial design change, however, was not investigated in the present study. Employing a smooth upward curve for the lower aerofoil surface, downstream of the lowest point (as apposed to the sharper upward curve of the Tyrrell aerofoil), tended to stifle the diffuser effect, resulting in reduced suction under the aerofoil.

All of the conclusions in the preceding paragraph were tested through a proof-of-concept aerofoil design, dubbed the ‘Vogt’ aerofoil, which utilised the observations above by modifying the Tyrrell aerofoil by an arbitrary amount (no optimisation process was employed); the top surface camber was increased, the lowest point of the aerofoil was moved upstream while maintaining a sharp upturn on the bottom surface after the lowest point. This aerofoil performed very well, achieving a 7 % improvement of the Tyrrell aerofoil with only a 0.4 % reduction in lift-to-drag ratio.

### ***8.1.2 Performing Numerical Simulations of Unsteady Quasi-2D Flow about Inverted Wings in Ground Effect***

In order to understand flow separation occurring in the highly unsteady turbulent flow about an inverted wing in strong ground effect, a project to develop a CFD model, capable of accurately simulating this flow environment, was undertaken. Given time and resource limitations on the project, it was also necessary to ensure that the model was as efficient as possible in its operations.

Two separate numerical models were developed for the purpose of determining which was the most adept at simulating the quasi-two-dimensional flow about the Tyrrell wing installed in the School’s low speed moving ground wind tunnel. The two models developed were a Large Eddy Simulation model and a Pseudo-Direct Numerical Simulation model which is similar to an LES model, however, it does not employ a sub-grid turbulence model but rather uses a second-order upwinding scheme to generate numerical diffusion which, it is thought, would account for the sub-grid turbulence.

Through the development of the models it became clear that modelling the entire test-section of the wind tunnel (which was used to validate the models) was not feasible as that would severely limit mesh refinement. As a result, a ‘sliver’ model was developed which employed only a small spanwise sliver cut of the wind-tunnel test section (0.133 chord lengths wide) and used periodic boundaries on the two spanwise boundaries. This solution has never been employed for a ground effect configuration before and thus required much verification work to ensure its adequacy.

Both the LES and the P-DNS models utilised the sliver model solution and were then validated against experimental LDA data. The LES model was assessed using three sub-grid turbulence models; the basic and dynamic variants of the Smagorinsky model and Turbulent Kinetic Energy model. In addition, an LES model using the basic Smagorinsky model, but with a doubled spanwise grid resolution was also run and assessed against the LDA data in order to determine the importance of spanwise resolution in such simulations.

The various LES and sub-grid turbulence model combinations and the P-DNS model were all compared against the experimental data and to facilitate this process in the most objective way possible a weighted scoring system was developed which was designed to highlight the best overall performing model.

The Dynamic-Smagorinsky LES model was found to be the clearly superior model with an overall performance score comfortably higher than any other model. This model was selected for the definitive set of simulations which followed this analysis.

The double-spanwise-resolution Smagorinsky LES model was found to be inferior to the Dynamic-Smagorinsky model but superior to the standard (normal resolution) Smagorinsky LES model. This indicates that doubling the spanwise resolution would not offer a sufficiently attractive improvement to the model's predictive power as merely incorporating the dynamic modelling approach to the basic Smagorinsky model produced better results at very little additional computational expense.

A frequency analysis was conducted to compare the chosen model's performance against the experimental results in terms of predicting the turbulent energy cascade. The experiment and the LES model both clearly identified the expected turbulent decay behaviour and how it varied across different  $y/c$  positions. The consistency (between the LES and the experiment) in how the decay behaviour varied in space is of particular importance in demonstrating the predictive capability of the Dynamic-Smagorinsky LES model.

### ***8.1.3 Unsteady Quasi-2D Flow Separation about an Inverted Aerofoil in Ground Effect***

Definitive simulations were conducted about the inverted Tyrrell wing using the Dynamic-Smagorinsky LES model developed for the purpose. A series of different configurations of the wing were modelled in order to examine the onset of flow separation. It was intended to consider, through this study, the process by which ground effect flow separation develops.

As the model was validated against experimental data from the low speed wind tunnel, this set of LES simulations were conducted at the same Reynolds number of 53,000 and assumed a

quasi-two-dimensional flow field. The Tyrrell aerofoil was set at a constant angle of attack of  $5^\circ$ , which is greater than a typical ground effect application but was done so in order to accentuate the ground effect phenomena at play. The aerofoil was simulated at various ground clearances in the extreme ground effect and force-reduction height ranges so as to capture the complete transition to flow separation.

The simulations revealed that the Tyrrell wing featured a laminar separated shear layer on the lower surface which, for most clearances, transitioned to turbulence and then reattached to the lower surface of the wing. Two types of flow separation were seen to develop throughout the clearance range: a progressive form which advanced upstream from the trailing edge with decreased ground clearance and a sudden full-scale form which resulted from the laminar separated shear layer's inability to re-establish attached flow after it had transitioned to turbulence.

The progressive form of flow separation, worsening down to the clearance of  $h/c = 0.14$ , coincided with an increase in  $C_N$ , indicating that the suction borne of the diffuser effect outweighed the negative effects of this separation. At  $h/c = 0.11$ , however,  $C_N$  starts to drop significantly, and this is due to a large diversion of flow (and therefore a source of kinetic energy) over the top of the wing.

The progressive form of flow separation was found to be caused by the strengthening diffuser effect and not due to an excessive adverse pressure gradient (which is often postulated). With decreasing clearance, the outlet-to-inlet ratio of the diffuser increased and made it increasingly difficult for the fast jet flow passing under the wing to impart sufficient flow velocity to the rest of the volume under the wing; this caused the boundary layer to be greatly thickened and stressed, bring about the progressive separation.

The sudden full-scale form of flow separation was caused by two primary factors. Firstly, the energy available to energise the boundary layer upon transition to turbulence was severely reduced at  $h/c = 0.08$  as the flow speed under the wing reduced dramatically (thanks to the flow diversion over the wing). Secondly, the source of the turbulent production, from which the boundary layer relies for energy, moved significantly away from the surface of the wing such that the, now, much lower turbulent mixing did not even reach the near wall region, thus preventing reattachment. This movement away from the wall was found to be due to flow constriction at low clearances which changes the trajectory of the shear layer.

## 8.2 Recommendations for Future Work

The generic ground effect phenomena identified about both the upright and inverted aerofoils provided an insight into the overall workings of ground effect. It would be of fundamental interest to extend this investigation to study the same phenomena and how they behave about different geometries, including bluff bodies.

Three geometric factors were found to influence the ground effect performance of inverted wings in ground effect; the top surface camber near the trailing edge, the streamwise position of the lowest point of the wing and the curvature of the underside of the wing downstream of the lowest point. The extent of the influence of changing these parameters was not investigated in this thesis and it would be useful to understand, for example, just how far forward the lowest point should be located and why. Understanding where these influences are strong, where they are not, and where they may even reverse (if you have far too much top surface camber, for example) and why this happens will further aid in building an understanding of the details of how ground effect manifests about inverted wings.

The LES investigation into flow separation about an inverted Tyrrell wing utilised the sliver model where the spanwise boundaries of the numerical domain were modelled as periodic boundaries. It was noted in Chapter 4 that these periodic boundaries were not sufficiently far apart to ensure no errors were being introduced (though this was thought not to be significant). It would be valuable to perform a full periodic boundary separation independence study to ascertain just how much error was being introduced and to also definitively determine how far apart periodic boundaries should be placed about wings in ground effect.

The LES investigation was necessarily conducted at a relatively low Reynolds number as the validation experiment was conducted in a low-speed wind tunnel. It would be useful to examine the effect of increasing the Reynolds number about the same wing configuration. This would require further validation work. Additionally, as suggested in Chapter 7, a similar separation bubble could be generated at a higher Reynolds number if the wing were designed to induce such behaviour. It is the author's opinion that inducing a separation bubble at a higher Reynolds number and then designing the wing to mitigate the sudden full-scale separation could be very beneficial. It would be very interesting to confirm whether this is the case by first altering the wing to produce the separation bubble at a higher Reynolds number and confirming whether or not similar separation behaviour is apparent.

Based on the conclusions of Chapter 7, a modified wing is suggested here for a future investigation to determine how effectively the sudden form of separation might be mitigated

or even prevented. As the flattening of the shear layer cannot be avoided at low clearances, the lower surface of a modified wing could be brought down toward the (low ground clearance) transition point. Thus, when the shear layer breaks down at very low clearances, the generated turbulence will be in close proximity to the wall and should, therefore, be able to promote reattachment at lower clearances than the Tyrrell wing. The modified lower surface would depart from the original contour of the Tyrrell wing comfortably downstream of the most aft separation point and thus should not greatly influence the separation point behaviour. The new lower surface's intrusion into the original recirculating flow region may change the shape of the shear layer slightly, but the chance of that is not thought to be significant. The increased slope of the lower surface back to the trailing edge will probably increase the adverse pressure gradient slightly but, as this was found not to be the principal contributor to the progressive separation, this should not be a problem. However, the increased slope may exacerbate the diffuser induced progressive separation and if this is so, an increase in chord is probably warranted to lessen this slope. This wing is presented here as a potential design response to the flow phenomena observed and requires extensive investigation.

# Chapter 9: References

- Ahmed, N.A. and Goonarate, J., "Lift Augmentation of a Low-Aspect-Ratio Thick Wing in Ground Effect", *Journal of Aircraft*, Vol. 39, No. 2, March-April 2002, pp. 381-384.
- Barber, T.J., Leonardi, E. and Archer, R.D., "A Technical Note on the Appropriate CFD Boundary Conditions for the Prediction of Ground Effect Aerodynamics", *The Aeronautical Journal*, Vol. 103, No. 1029, November 1999, pp 545-547.
- Barber, T.J., Leonardi, E. and Archer, R.D., "Causes for discrepancies in ground effect analyses", *The Aeronautical Journal*, Vol. 106, No. 1066, December 2002, pp. 653-667.
- Barber, T.J., course-notes for Computational Fluid Dynamics module of AERO4610: Advanced Aerodynamics and Propulsion, School of Mechanical and Manufacturing Engineering, University of New South Wales, Sydney, Australia, 2005.
- Benedict, L.H. and Gould, R.D., "Toward Better Uncertainty Estimates for Turbulence Statistics", *Experiments in Fluids*, Vol. 22, No. 2, December 1996, pp. 129-136.
- Beves, C., Barber, T.J. and Leonardi, E., "Near-Wake Properties of the Tyrrell-026 Aerofoil in Inverted Ground Effect", Proceedings of 5<sup>th</sup> Pacific Symposium on Fluid Flow Visualisation and Image Processing, Australia, 27-29 September 2005.
- Brady, P.D.M., Gaston, M. and Reizes, J., "An Application of a Second Order Upwinding Scheme for an Implicit LES CFD Solver", Transactions of the 16<sup>th</sup> Australasian Fluid Mechanics Conference, Gold Coast Australia, 2-7 December, 2007.
- "BSA Flow Software: Version 4.10, Installation & User's Guide", 10<sup>th</sup> Edition, publication no. 9040U5734, Dantec Dynamics A/S, Skovlunde, Denmark, 2006.
- Burattini, P., Kinet, M., Carati, D. and Knaepen, B., "Correcting Cold Wire Measurements in Isotropic Turbulence with a DNS Database", Transactions of the 16<sup>th</sup> Australasian Fluid Mechanics Conference, Gold Coast Australia, 2-7 December, 2007.
- Burattini, P., Lavoie, P. and Antonia, R.A., "Velocity Derivative Skewness in Isotropic Turbulence and its Measurement with Hot Wires", Transactions of the 16<sup>th</sup> Australasian Fluid Mechanics Conference, Gold Coast Australia, 2-7 December, 2007.
- Coray, P.S., "Establishing a Particle Image Velocimetry (PIV) System for Studying Heat Transfer Enhancements Using Dimpled Surfaces", M.E. Thesis, The University of New South Wales, School of Mechanical and Manufacturing Engineering, Sydney, Australia, February 2005.
- Coulliette, C. and Plotkin, A., "Aerofoil Ground Effect Revisited", *The Aeronautical Journal*, Vol. 100, No. 992, February 1996, pp. 65-74.
- Diasinos, S., Barber, T.J. Leonardi, E. and Hall, S.D., "Validation of a 2D CFD Model for the Implementation of a Moving Ground in the UNSW 3×4 Ft Wind Tunnel", Proceedings of 5<sup>th</sup> Pacific Symposium on Fluid Flow Visualisation and Image Processing, Australia, 27-29 September, 2005.
- Diasinos, S., "The Aerodynamic Interaction of a Rotating Wheel and a Downforce Producing Wing in Ground Effect", Ph.D. Thesis, University of New South Wales, School of Mechanical and Manufacturing Engineering, March 2009.
- Dominy, R.G., "Aerodynamics of Grand Prix Cars", *Proceedings of the Institution of Mechanical Engineers, Part D: Journal of Automobile Engineering*, Vol. 206, No. 4, 1992, pp. 267-274.
- Eisenbach, S. and Friedrich, R., "Large-Eddy Simulation of Flow Separation on an Airfoil at a High Angle of Attack and  $Re = 10^5$  Using Cartesian Grids", *Theoretical and Computational Fluid Dynamics*, Vol. 22, 2008, pp. 213-225.
- Geurts, B.J., *Elements of Direct and Large-Eddy Simulation*, published by R.T. Edwards, Inc., Philadelphia, USA, 2004.
- Guide for the Verification and Validation of Computational Fluid Dynamics Simulations*, American Institute of Aeronautics & Astronautics, USA, 1999.

- Hawkes, E.R., Sankaran, R. and Chen, J.H., "Reignition Dynamics in Massively Parallel Direct Numerical Simulations of CO/H<sub>2</sub> Jet Flames", Transactions of the 16<sup>th</sup> Australasian Fluid Mechanics Conference, Gold Coast Australia, 2-7 December, 2007.
- Hinze, J.O., *Turbulence*, McGraw-Hill, 1959.
- Hsiun, C. and Chen, C., "Aerodynamic Characteristics of a Two-Dimensional Airfoil with Ground Effect", *Journal of Aircraft*, Vol. 33, No. 2, March-April 1996, pp. 386-392.
- Hutchins, N., Nickels, T.B., Marusic, I. and Chong, M.S., "Comparison of High Spatial Resolution Stereo-PIV Measurements in a Turbulent Boundary Layer with Available DNS Dataset", Transactions of the 16<sup>th</sup> Australasian Fluid Mechanics Conference, Gold Coast Australia, 2-7 December, 2007.
- Katz, J., "Considerations Pertinent to Race-Car Wing Design", RAeS Conference on Vehicle Aerodynamics, Royal Aeronautical Society, London, 1994, pp. 23.1-23.7.
- Kim, S.-E., "Large Eddy Simulation Using an Unstructured Mesh Based Finite-Volume Solver", 34<sup>th</sup> AIAA Fluid Dynamics Conference, Portland, Oregon, 28 June - 1 July, 2004.
- Kitsios, V., Ooi, A. and Soria, J., "Spatio-Temporal Stability Analysis of the Separated Flow Past a NACA 0015 Airfoil with ZNMF Jet Control", 16<sup>th</sup> Australasian Fluid Mechanics Conference, Gold Coast Australia, 2-7 December, 2007.
- Kuhmstedt, T. and Milbradt, G., "Aerodynamic Design of Wing in Ground Effect Craft", 3<sup>rd</sup> International Conference on Fast Sea Transportation (FAST95), Lubeck-Travemunde, Germany, pp. 597-608, 23-27 September, 1995.
- Launder, B.E., "Second-Moment Closure: Present... and Future?", *International Journal of Heat and Fluid Flow*, Vol. 10, No. 4, pp. 282-300, December, 1989.
- Mahon, S. and Zhang, X., "Computational Analysis of Pressure and Wake Characteristics of an Aerofoil in Ground Effect", *Journal of Fluids Engineering*, Vol. 127, No. 2, March 2005, pp. 290-298.
- Mahon, S. and Zhang, X., "Computational Analysis of a Inverted Double-Element Airfoil in Ground Effect", *Journal of Fluids Engineering*, Vol. 128, No. 6, November 2006, pp. 1172-1180.
- Mathey, F., Cokljat, D., Bertoglio, J.P. and Sergent, E., "Assessment of the Vortex Method for Large Eddy Simulation Inlet Conditions", *Progress in Computational Fluid Dynamics, An International Journal*, Vol. 6, No. 1/2/3, pp. 58-67, 2006.
- Mattner, T.W., "Large-Eddy Simulations of a Turbulent Mixing Layer using the Stretched-Vortex Subgrid Model", Transactions of the 16<sup>th</sup> Australasian Fluid Mechanics Conference, Gold Coast Australia, 2-7 December, 2007.
- Meneveau, C. and Katz, J., "Scale-Invariance and Turbulence Models for Large-Eddy Simulations", *Annual Review of Fluid Mechanics*, Vol. 32, January 2000, pp. 1-32.
- Mokhtar, W.A., "A Numerical Study of High-Lift Single Element Airfoils with Ground Effect for Racing Cars", Vehicle Aerodynamics 2005, Detroit, Michigan, April 11-14, 2005.
- Murayama, M. and Yamamoto, K., "Validation of Computations Around High-Lift Configurations by Structured- and Unstructured-Mesh", *Journal of Aircraft*, Vol. 43, No. 2, March-April 2006, pp. 395-406.
- Ol, M.V., McAuliffe, B., Hanff, E.S., Scholz, U. and Kähler, C., "Comparison of Laminar Separation Bubble Measurements on a Low Reynolds Number Airfoil in Three Facilities", 35<sup>th</sup> AIAA Fluid Dynamics Conference and Exhibit, Toronto, Canada, AIAA Paper No. 2005-5149, 6-9 June, 2005.
- Ranzenbach, R., "Cambered Airfoil in Ground Effect – Wind Tunnel and Road Conditions", 13<sup>th</sup> AIAA Applied Aerodynamics Conference, San Diego, CA, USA, 19-22 June 1995, Technical Papers. Pt. 2, pp. 1208-1215.
- Ranzenbach, R., Barlow, J.B. and Diaz, R.H., "Multi-Element Airfoil in Ground Effect – An Experimental and Computational Study", 15<sup>th</sup> AIAA Applied Aerodynamics Conference, Atlanta, GA, USA, 23-25 June 1997.
- Reizes, J., personal communication, 2008.
- Roache, P.J., *Verification and Validation in Computational Science and Engineering*, Hermosa Publishers, New Mexico, USA, 1998.
- Robinson, S.K., "Coherent Motions in the Turbulent Boundary Layer", *Annual Review of Fluid Mechanics*, Vol. 23, 1991, pp. 601-639.
- Rodi, W., Ferziger, J.H., Breuer, M. and Pourquié, M., "Status of Large Eddy Simulation: Results of a Workshop", *Journal of Fluids Engineering*, Vol. 119, No. 6, June, 1997, pp. 248-262.

- Shao, H., Jiang, L. and Liu, C., "Direct Numerical Simulation of Flow Separation around a NACA 0012 Airfoil", *Computers and Fluids*, Vol. 34, No. 9, November 2005, pp. 1096-1114.
- Slater, John W., [www.grc.nasa.gov/www/wind/valid/tutorial/tutorial.html](http://www.grc.nasa.gov/www/wind/valid/tutorial/tutorial.html), NASA, last updated 17 July 2008, accessed 9 July 2008.
- Song, S., DeGraaff, D.B. and Eaton, J.K., "Experimental Study of a Separating, Reattaching, and Redeveloping Flow Over a Smoothly Contoured Ramp", *International Journal of Heat and Fluid Flow*, Vol. 25, No. 5, October 2000, pp. 512-519.
- Soso, M. and Wilson, P., "Investigating Changes to the Downforce Curve of a Double Element Airfoil in Ground Effect", Proceedings of the 2004 SAE Motorsports Engineering Conference and Exhibition, Dearborn, Michigan, November 30-December 3, 2004.
- Soso, M.D. and Wilson, P.A., "Aerodynamics of a Wing in Ground Effect in Generic Racing Car Wake Flows", *Journal of Automobile Engineering*, Vol. 220, No. 1, 2006, pp. 1-12.
- Versteeg, H.K. and Malalasekera, W., *An Introduction to Computational Fluid Dynamics: The Finite Volume Method*, Pearson Education, Limited, Essex, England, 1995.
- Wilcox, D.C., *Turbulence Modeling for CFD*, Third Edition, DCW Industries, Inc., La Canada, California, USA, November 2006.
- Williamson, M.J., Kirkpatrick, M.P., Armfield, S.A. and Behnia, M., "Sub-Filter Scale Models for Scalar Transport in Large Eddy Simulations", Transactions of the 16<sup>th</sup> Australasian Fluid Mechanics Conference, Gold Coast Australia, 2-7 December, 2007.
- Young, M.E. and Ooi, A., "Comparative Assessment of LES and URANS for Flow Over a Cylinder at a Reynolds Number of 3900", Transactions of the 16<sup>th</sup> Australasian Fluid Mechanics Conference, Gold Coast Australia, 2-7 December, 2007.
- Zerihan, J. and Zhang, X., "Aerodynamics of a Single Element Wing in Ground Effect", *Journal of Aircraft*, Vol. 37, No. 6, November-December 2000, pp. 1058-1064.
- Zerihan, J., "An Investigation into the Aerodynamics of Wings in Ground Effect", Ph.D. Thesis, University of Southampton, School of Engineering Sciences, April 2001.
- Zerihan, J. and Zhang, X., "Aerodynamics of Gurney Flaps on a Wing in Ground Effect", *AIAA Journal*, Vol. 39, No. 5, May 2001, pp. 772-780.
- Zhang, X. and Zerihan, J., "Aerodynamics of a Double Element Wing in Ground Effect", *AIAA Journal*, Vol. 41, No. 6, June 2003, pp. 1007-1016.
- Zhang, X. and Zerihan, J., "Off-Surface Aerodynamic Measurements of a Wing in Ground Effect", *Journal of Aircraft*, Vol. 40, No. 4, July-August 2003, pp. 716-725.
- Zhang, X., Toet, W. and Zerihan, J., "Ground Effect Aerodynamics of Race Cars", *Applied Mechanics Reviews*, Vol. 59, No. 1, January 2006, pp. 33-49.

# Appendix A: Computational Fluid Dynamics Theory

## A.1 Conservation of Momentum Equations

The conservation of momentum follows a rearrangement of Newton's Second Law ( $F = ma$ ) which can be stated as *'the rate of change of momentum of the fluid element equals the sum of all forces acting on the fluid element.'* Firstly, the rate of change of momentum in the  $x$ -direction, for a fluid element, can be expressed as

$$\rho \frac{Du}{Dt} \quad (44)$$

Eqn. 44 features a substantive derivative. By way of explanation, the substantive derivative for an arbitrary fluid property  $\phi$  is defined as

$$\frac{D\phi}{Dt} = \frac{\partial\phi}{\partial t} + u \frac{\partial\phi}{\partial x} + v \frac{\partial\phi}{\partial y} + w \frac{\partial\phi}{\partial z} = \frac{\partial\phi}{\partial t} + \bar{u} \cdot \text{grad } \phi \quad (45)$$

Eqn. 45, however, is defined in terms of the time rate of change of  $\phi$ , per unit mass, for a moving particle, rather than per unit volume for a stationary fluid element. The relationship between the two is

$$\rho \frac{D\phi}{Dt} = \rho \left[ \frac{\partial\phi}{\partial t} + \bar{u} \cdot \text{grad } \phi \right] + \phi \left[ \frac{\partial\rho}{\partial t} + \text{div}(\rho\bar{u}) \right] = \frac{\partial(\rho\phi)}{\partial t} + \text{div}(\rho\phi\bar{u}) \quad (46)$$

The RHS of Eqn. 46 is essentially Eqn. 1, generalised to express the conservation of the arbitrary quantity  $\phi$  (about a fluid element). Also, since Eqn. 1 equals zero, the third term above is equal to zero. This leaves the following definition of the time rate of change of  $\phi$  for a fluid element:

$$\boxed{\rho \frac{D\phi}{Dt} = \frac{\partial(\rho\phi)}{\partial t} + \text{div}(\rho\phi\bar{u})} \quad (47)$$

Therefore, the time rate of change of momentum in the  $x$ -direction, for a fluid element is

$$\rho \frac{Du}{Dt} = \frac{\partial(\rho u)}{\partial t} + \text{div}(\rho u \bar{u}) = \frac{\partial(\rho u)}{\partial t} + \frac{\partial(\rho u u)}{\partial x} + \frac{\partial(\rho u v)}{\partial y} + \frac{\partial(\rho u w)}{\partial z} \quad (48)$$

Secondly, the sum of all forces over the fluid element in the  $x$ -direction can be expressed as

$$-\frac{\partial p}{\partial x} + \frac{\partial \tau_{xx}}{\partial x} + \frac{\partial \tau_{yx}}{\partial y} + \frac{\partial \tau_{zx}}{\partial z} + S_{Mx} \quad (49)$$

where  $p$  is the normal pressure on the element in the  $x$ -direction, the  $\tau_{ij}$  quantities are viscous shear stresses acting in the direction  $j$  on a surface normal to direction  $i$ , and  $S_{Mx}$  is a source term for any body forces (per unit time, per unit volume) that may be acting in this direction.

The conservation of momentum in the  $x$ -direction is found by simply equating Eqns. 48 and 73. A similar process yields the equivalent equations for the  $y$  and  $z$ -directions.

$$\begin{aligned} \rho \frac{Du}{Dt} &= -\frac{\partial p}{\partial t} + \frac{\partial \tau_{xx}}{\partial x} + \frac{\partial \tau_{yx}}{\partial y} + \frac{\partial \tau_{zx}}{\partial z} + S_{Mx} \\ \rho \frac{Dv}{Dt} &= -\frac{\partial p}{\partial t} + \frac{\partial \tau_{xy}}{\partial x} + \frac{\partial \tau_{yy}}{\partial y} + \frac{\partial \tau_{zy}}{\partial z} + S_{My} \\ \rho \frac{Dw}{Dt} &= -\frac{\partial p}{\partial t} + \frac{\partial \tau_{xz}}{\partial x} + \frac{\partial \tau_{yz}}{\partial y} + \frac{\partial \tau_{zz}}{\partial z} + S_{Mz} \end{aligned} \quad (50)$$

## A.2 Conservation of Energy Equation

The conservation of energy equation is based on the First Law of Thermodynamics. Stated in words; *'the rate of change of energy in a fluid element equals the net rate of heat added to the element plus the net rate of work done on the element.'* Similarly to the conservation of momentum equations, the conservation of energy makes use of the substantive derivative, such that the time rate of change of the energy of the fluid element is

$$\rho \frac{DE}{Dt} = \frac{\partial(\rho E)}{\partial t} + \text{div}(\rho E \bar{u}) = \frac{\partial(\rho E)}{\partial t} + \frac{\partial(\rho E u)}{\partial x} + \frac{\partial(\rho E v)}{\partial y} + \frac{\partial(\rho E w)}{\partial z} \quad (51)$$

The above expression in Eqn. 51 equals the sum of the rate of net heat added and net work done on the fluid element. It can be shown for the heat flux components  $q_x$ ,  $q_y$  and  $q_z$ , that the expression for the rate of change of heat added to the element is

$$-\frac{\partial q_x}{\partial x} - \frac{\partial q_y}{\partial y} - \frac{\partial q_z}{\partial z} = -\text{div} \bar{q} \quad (52)$$

Employing Fourier's Law to express heat flux in terms of temperature

$$q_x = -k \frac{\partial T}{\partial x} \quad q_y = -k \frac{\partial T}{\partial y} \quad q_z = -k \frac{\partial T}{\partial z} \quad (53)$$

where  $T$  is temperature and  $k$  is a constant. Thus the heat flux vector can be expressed

$$\bar{q} = -k \text{ grad } T \quad (54)$$

Thus, the final expression for rate of change of heat added to the element is

$$\text{div}(k \text{ grad } T) \quad (55)$$

The expression for the rate of net work done on the element is very similar to the calculation of the net force on the element from the RHS of the Eqns. 50. These terms are multiplied by their respective velocity components (rate of work equals force multiplied by the velocity component in the direction of the force) and then all summed. The resulting rate of net work done on the element is

$$\begin{aligned}
 & -\text{div}(p\bar{u}) + \frac{\partial(u\tau_{xx})}{\partial x} + \frac{\partial(u\tau_{yx})}{\partial y} + \frac{\partial(u\tau_{zx})}{\partial z} + \frac{\partial(v\tau_{xy})}{\partial x} \\
 & + \frac{\partial(v\tau_{yy})}{\partial y} + \frac{\partial(v\tau_{zy})}{\partial z} + \frac{\partial(w\tau_{xz})}{\partial x} + \frac{\partial(w\tau_{yz})}{\partial y} + \frac{\partial(w\tau_{zz})}{\partial z}
 \end{aligned} \tag{56}$$

Thus, the final conservation of energy equation is

$$\begin{aligned}
 \rho \frac{DE}{Dt} = & \text{div}(k \text{ grad } T) - \text{div}(p\bar{u}) + \frac{\partial(u\tau_{xx})}{\partial x} + \frac{\partial(u\tau_{yx})}{\partial y} + \frac{\partial(u\tau_{zx})}{\partial z} \\
 & + \frac{\partial(v\tau_{xy})}{\partial x} + \frac{\partial(v\tau_{yy})}{\partial y} + \frac{\partial(v\tau_{zy})}{\partial z} + \frac{\partial(w\tau_{xz})}{\partial x} + \frac{\partial(w\tau_{yz})}{\partial y} + \frac{\partial(w\tau_{zz})}{\partial z} + S_E
 \end{aligned} \tag{57}$$

where  $S_E$  is again any body forces or other source terms such as gravity and energy itself  $E$  is defined as

$$E = i + \frac{1}{2}(u^2 + v^2 + w^2) \tag{58}$$

where  $i$  is the internal energy and the second term is the kinetic energy – the potential energy has been accounted for in the body force term.

### A.3 The Navier-Stokes and Transport Equations for the Finite-Volume Method

This section will derive both the Navier-Stokes (N-S) equations and the general transport equation. The N-S equations are a slight development upon the fundamental governing equations discussed in Sec. 2.2.1. The transport equation for the finite-volume method is a very convenient general equation into which all five of the N-S equations may be rearranged. This section will first establish the N-S equation by making some rearrangements to the form of the governing equations and will then present the transport equation.

Assuming the fluid under consideration is a Newtonian fluid enables some mathematical approximations for the viscous stresses. A Newtonian fluid is assumed isotropic and that the viscous stresses on a fluid element are proportional to the rate of deformation of the element. This is true of most gases in most conditions and is thus a robust assumption – particularly for the narrow application area of this research programme. The nine viscous stress components found in the governing equations of Sec. 2.1.1 can now be expressed as

$$\begin{aligned}
\tau_{xx} &= 2\mu \frac{\partial u}{\partial x} + \lambda \operatorname{div} \bar{u} & \tau_{yy} &= 2\mu \frac{\partial v}{\partial y} + \lambda \operatorname{div} \bar{u} & \tau_{zz} &= 2\mu \frac{\partial w}{\partial z} + \lambda \operatorname{div} \bar{u} \\
\tau_{xy} = \tau_{yx} &= \mu \left( \frac{\partial u}{\partial y} + \frac{\partial v}{\partial x} \right) & \tau_{xz} = \tau_{zx} &= \mu \left( \frac{\partial u}{\partial z} + \frac{\partial w}{\partial x} \right) \\
\tau_{yz} = \tau_{zy} &= \mu \left( \frac{\partial v}{\partial z} + \frac{\partial w}{\partial y} \right)
\end{aligned} \tag{59}$$

where  $\mu$  is the dynamic viscosity and  $\lambda$  is the viscosity which is assumed to be

$$\lambda = -\frac{2}{3}\mu \tag{60}$$

Additionally, if the energy equation is recast with the internal energy  $i$  as the subject of the substantial derivative (and also assuming a Newtonian fluid), the N-S equations may be expressed in the following form for a compressible fluid.

Mass	$\frac{\partial \rho}{\partial t} + \operatorname{div}(\rho \bar{u}) = 0$	
x-momentum	$\frac{\partial(\rho u)}{\partial t} + \operatorname{div}(\rho u \bar{u}) = -\frac{\partial p}{\partial x} + \operatorname{div}(\mu \operatorname{grad} u) + S_{Mx}$	
y-momentum	$\frac{\partial(\rho v)}{\partial t} + \operatorname{div}(\rho v \bar{u}) = -\frac{\partial p}{\partial y} + \operatorname{div}(\mu \operatorname{grad} v) + S_{My}$	(61)
z-momentum	$\frac{\partial(\rho w)}{\partial t} + \operatorname{div}(\rho w \bar{u}) = -\frac{\partial p}{\partial z} + \operatorname{div}(\mu \operatorname{grad} w) + S_{Mz}$	
Internal energy	$\frac{\partial(\rho i)}{\partial t} + \operatorname{div}(\rho i \bar{u}) = -p \operatorname{div} \bar{u} + \operatorname{div}(k \operatorname{grad} T) + \Phi + S_i$	

It can be shown that, for the internal energy equation

$$\Phi = \mu \left\{ \begin{aligned} &2 \left[ \left( \frac{\partial u}{\partial x} \right)^2 + \left( \frac{\partial v}{\partial y} \right)^2 + \left( \frac{\partial w}{\partial z} \right)^2 \right] + \left( \frac{\partial u}{\partial y} + \frac{\partial v}{\partial x} \right)^2 \\ &+ \left( \frac{\partial u}{\partial z} + \frac{\partial w}{\partial x} \right)^2 + \left( \frac{\partial v}{\partial z} + \frac{\partial w}{\partial y} \right)^2 \end{aligned} \right\} + \lambda (\operatorname{div} \bar{u})^2 \tag{62}$$

And finally, the equations of state for a perfect gas:

$$\begin{aligned}
p &= \rho R T \\
i &= C_v T
\end{aligned} \tag{63}$$

The general transport equation may be determined by observing the similarity between the N-S equations (Eqns. 61). The following general form, for an arbitrary quantity  $\phi$ , includes all the important elements of the N-S equations with any non-conforming terms recast as part of the source term  $S_\phi$

$$\frac{\partial(\rho \phi)}{\partial t} + \operatorname{div}(\rho \phi \bar{u}) = \operatorname{div}(\Gamma \operatorname{grad} \phi) + S_\phi \tag{64}$$

## A.4 Discretisation of Flow Properties

This section will cover the flow discretisation process. For simplicity we will consider a steady-state, one-dimensional convection-diffusion flow.

The key step in the finite-volume method is to present the transport equation in integral form – integrated over the control volume of the finite element. Thus, Eqn. 64 can be re-presented

$$\int_{CV} \frac{\partial(\rho\phi)}{\partial t} dV + \int_{CV} \text{div}(\rho\phi\bar{u}) dV = \int_{CV} \text{div}(\Gamma \text{grad } \phi) dV + \int_{CV} S_\phi dV \quad (65)$$

The convective and diffusive terms (second on the LHS and first on the RHS, respectively) may be rewritten using Gauss' divergence theorem in order to express them in terms of an integral of the bounding surface of the control volume rather than an integration of the volume itself. This yields the following:

$$\frac{\partial}{\partial t} \left( \int_{CV} \rho\phi dV \right) + \int_A \tilde{n}(\rho\phi\bar{u}) dA = \int_A \tilde{n}(\Gamma \text{grad } \phi) dA + \int_{CV} S_\phi dV \quad (66)$$

where the vector  $\tilde{n}$  acts normally to each bounding surface of the integration.

For the steady-state, one-dimensional convection-diffusion problem of interest here, Eqn. 66 can be simplified by eliminating the transient term on the left:

$$\int_A \tilde{n}(\rho\phi\bar{u}) dA = \int_A \tilde{n}(\Gamma \text{grad } \phi) dA + \int_{CV} S_\phi dV \quad (67)$$

Now, let us take one step back and consider the differential form of the steady-state, one-dimensional, convection-diffusion problem. It is expressed as

$$\frac{d}{dx}(\rho\bar{u}\phi) = \frac{d}{dx} \left( \Gamma \frac{d\phi}{dx} \right) \quad (68)$$

Additionally, the following conservation equation must also be satisfied.

$$\frac{d(\rho\bar{u})}{dx} = 0 \quad (69)$$

Before attempting to apply the control volume integration to these equations, let us first establish the convention system as shown in Figure A.1. This convention applies for the case of solving for the quantity  $\phi$  at the east and west faces of the cell with node labelled  $P$ ,  $\phi_e$  and  $\phi_w$ , respectively.

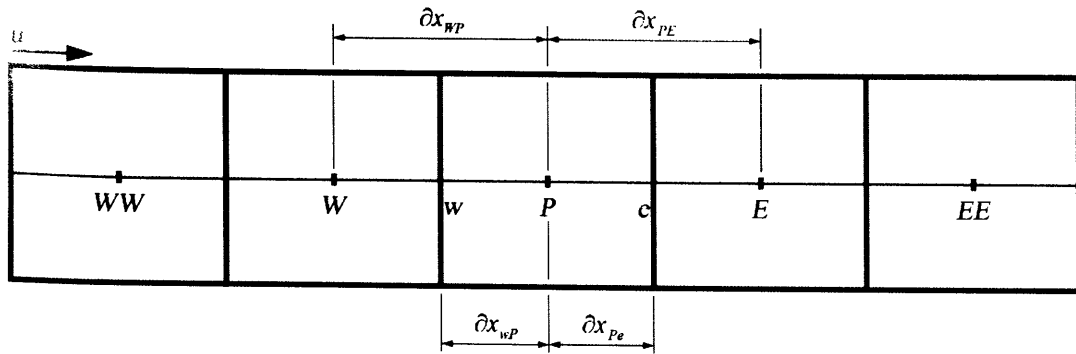


Figure A.1: A discretised domain with node and face naming convention

Using the integrations from Eqn. 67, and noting that this one-dimensional flow (from left the right) will result in no flux across the upper and lower control volume boundaries of the cell of interest P ( $\vec{n} \cdot \vec{u} = 0$  at these points), the following integral form is obtained:

$$(\rho \bar{u} A \phi)_e - (\rho \bar{u} A \phi)_w = \left( \Gamma A \frac{\partial \phi}{\partial x} \right)_e - \left( \Gamma A \frac{\partial \phi}{\partial x} \right)_w \quad (70)$$

The continuity equation (Eqn. 69), like the above, is integrated using Gauss' divergence theorem to obtain the following:

$$(\rho \bar{u} A)_e - (\rho \bar{u} A)_w = 0 \quad (71)$$

To solve these equations, we must approximate the various terms. The established convention with the finite-volume method is to solve directly for the node values of each finite element (W, P, E etc) and to approximate the face values ( $w$ ,  $e$ ). For the diffusive terms this is achieved by using a linear interpolation, or central differencing, to approximate the face values. Thus the diffusion coefficients are found:

$$\Gamma_w = \frac{\Gamma_W + \Gamma_P}{2} \quad \text{and} \quad \Gamma_e = \frac{\Gamma_P + \Gamma_E}{2} \quad (72)$$

and the diffusive flux at the surface is linearly interpolated between the node values as follows:

$$\begin{aligned} \left( \Gamma A \frac{d\phi}{dx} \right)_e &= \Gamma_e A_e \left( \frac{\phi_E - \phi_P}{\Delta x_{PE}} \right) \\ \left( \Gamma A \frac{d\phi}{dx} \right)_w &= \Gamma_w A_w \left( \frac{\phi_P - \phi_W}{\Delta x_{WP}} \right) \end{aligned} \quad (73)$$

This treatment of diffusion provides a good approximation and is used throughout. In order to approximate the terms in Eqns. 70 and 71, we will define some simplifying variable as follows:

$$\begin{aligned} F_w &= (\rho \bar{u})_w & F_e &= (\rho \bar{u})_e \\ D_w &= \frac{\Gamma_w}{\Delta x_{WP}} & D_e &= \frac{\Gamma_e}{\Delta x_{PE}} \end{aligned} \quad (74)$$

Applying these variables and the linear approximation of diffusion just discussed to Eqns. 70 and 71 yields

$$F_e \phi_e - F_w \phi_w = D_e (\phi_E - \phi_P) - D_w (\phi_P - \phi_W) \quad (75)$$

and for continuity:

$$F_e - F_w = 0 \quad (76)$$

For this simple example, we will assume the velocity field is already known which means the only quantity we need to solve for in the above equations is the transported quantity  $\phi$ .

It is at this point that a discretisation scheme must be applied in order to approximate the value of  $\phi$  at each cell face in the flow domain ( $\phi_e$  and  $\phi_w$  in Eqn. 75) as these values are not solved for as part of the solution process (only node values are solved for explicitly). Various discretisation schemes are available and some common examples are graphically demonstrated in Figure A.2 for the approximation of the face value  $\phi_w$ .

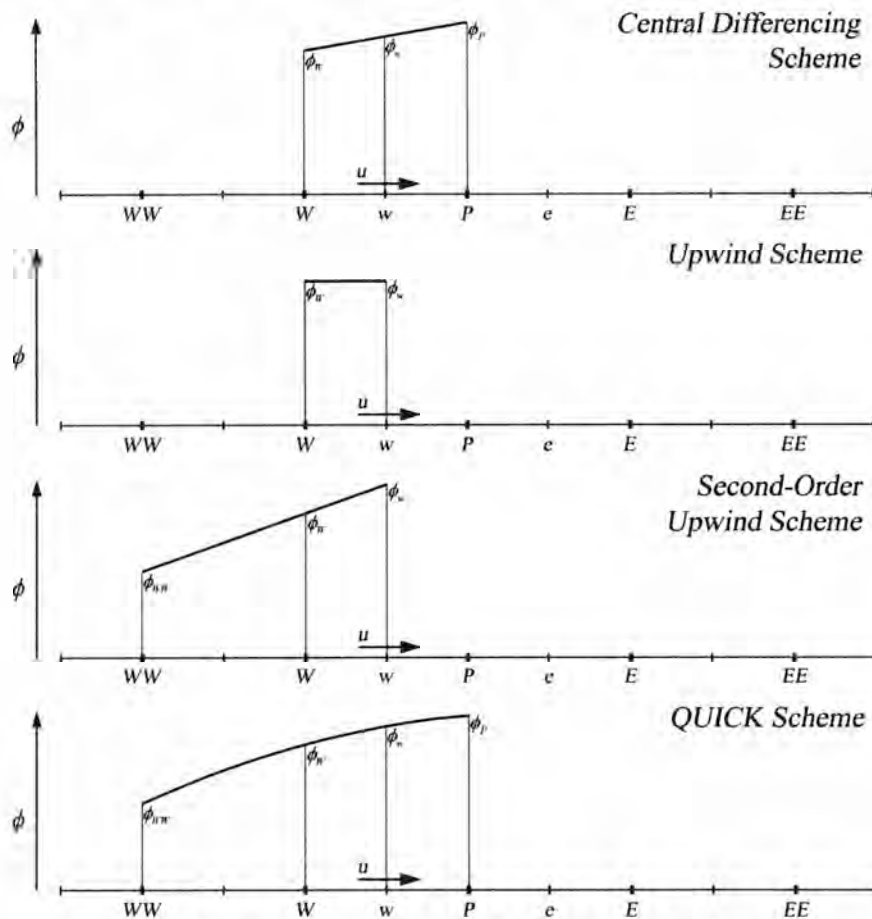


Figure A.2: Various discretisation scheme approximations for  $\phi_w$

The Central Differencing Scheme is a second-order accurate scheme that is reasonably accurate for slow moving flows but, as can be seen from Figure A.2, the face value,  $\phi_w$ , is influenced equally strongly from both of its neighbouring cells,  $\phi_W$  and  $\phi_P$ . For a high velocity, this face value would obviously be predominately influenced by the upwind cell node (or nodes) and much less by the downstream cell nodes. The central differencing

scheme is therefore said to lack ‘transportiveness’ as it does not account for flow direction. This produces severe numerical stability problems for flows of even moderate velocities and is therefore only appropriate for the approximation of the effect of diffusion (which disperses in all directions) and also for flows calculated on very fine grids which is discussed more in the Large Eddy Simulation (LES) section (Sec. 2.6).

The Upwind Scheme is only first-order accurate as it sets the face value to be equal to the immediate upwind cell’s node value. However, as it takes account of flow direction, it is very numerically stable, if inaccurate.

The Second-Order Upwind Scheme draws influence from the two nearest upwind cell nodes,  $\phi_{WW}$  and  $\phi_W$ , and linearly extrapolates from these node values to the face value of interest. This is, as the name suggests, a second-order accurate scheme that also takes account of transportiveness and is thus an improvement upon the Upwind Scheme.

The QUICK (Quadratic Upstream Interpolation for Convective Kinetics) Scheme is used extensively throughout this research programme as it is generally quite stable and also accurate. It is a third-order accurate scheme that draws influence from the two nearest upwind nodes and the first downwind node,  $\phi_P$ . The scheme interpolates between these nodes using a quadratic function that (due to the selection of nodes) is upstream-weighted and, therefore, transportive. This scheme will be demonstrated below.

For simplicity we assume that the grid, shown in Figure 2.1, is evenly spaced ( $\delta x_{WP} = \delta x_{PE}$  etc). This characteristic allows us to simplify the expression for the values  $\phi_w$  and  $\phi_e$ , as shown below (with the flow moving from left to right):

$$\begin{aligned}\phi_w &= \frac{6}{8}\phi_W + \frac{3}{8}\phi_P - \frac{1}{8}\phi_{WW} \\ \phi_e &= \frac{6}{8}\phi_P + \frac{3}{8}\phi_E - \frac{1}{8}\phi_W\end{aligned}\tag{77}$$

Substituting these approximations into Eqn. 75 yields the following algebraic approximation:

$$\begin{aligned}F_e\left(\frac{6}{8}\phi_P + \frac{3}{8}\phi_E - \frac{1}{8}\phi_W\right) - F_w\left(\frac{6}{8}\phi_W + \frac{3}{8}\phi_P - \frac{1}{8}\phi_{WW}\right) \\ = D_e(\phi_E - \phi_P) - D_w(\phi_P - \phi_W)\end{aligned}\tag{78}$$

Rearranging coefficients about the various  $\phi$  variables gives:

$$\begin{aligned}\left[D_w - \frac{3}{8}F_w + D_e + \frac{6}{8}F_e\right]\phi_P = \left[D_w + \frac{6}{8}F_w + \frac{1}{8}F_e\right]\phi_W \\ + \left[D_e - \frac{3}{8}F_e\right]\phi_E - \frac{1}{8}F_w\phi_{WW}\end{aligned}\tag{79}$$

Eqn. 79 has four unknown variables and is solved as part of a set of matrix equations, with each equation centred about a different node.

For convenience, this will be recast in the standard form for expressing discretised equations as follows:

$$a_P \phi_P = a_W \phi_W + a_E \phi_E + a_{WW} \phi_{WW} \quad (80)$$

where

$$\begin{aligned} a_W &= D_w + \frac{6}{8} F_w + \frac{1}{8} F_e \\ a_E &= D_e - \frac{3}{8} F_e \\ a_{WW} &= -\frac{1}{8} F_w \\ a_P &= a_W + a_E + a_{WW} + (F_e - F_w) \end{aligned} \quad (81)$$

The QUICK scheme is used for the approximation of flow properties for all the two-dimensional Reynolds-Averaged Navier-Stokes simulations (see Sec. 2.4) conducted in this research programme. For simulations conducted throughout this research using LES (Sec. 2.5), a central differencing scheme was employed as the fineness of the grids used renders this linear interpolation scheme accurate for convecting flows, in addition to its usual numerical stability.

## A.5 The SIMPLE Algorithm

The SIMPLE algorithm involves five steps for each iteration.

Firstly, the flow is initialised with a set of ‘guessed’ values for each quantity –  $u^*$ ,  $v^*$ ,  $p^*$  and  $\phi^*$ . There, of course, could be more than one scalar flow quantity  $\phi$ . The initial values for  $u^*$ ,  $v^*$  and  $p^*$  are substituted into the following discretised momentum equations to yield new intermediate values of  $u$  and  $v$ -velocity components,  $u^*$  and  $v^*$ .

$$\begin{aligned} a_{i,j} u^*_{i,j} &= \sum a_{nb} u^*_{nb} + (p^*_{I-1,j} - p^*_{I,j}) A_{i,j} + b_{i,j} \\ a_{i,j} v^*_{i,j} &= \sum a_{nb} v^*_{nb} + (p^*_{i,j-1} - p^*_{i,j}) A_{i,j} + b_{i,j} \end{aligned} \quad (82)$$

The second step determines an appropriate pressure-correction that is required due to the imbalance found in the continuity equation as a result of the incorrect velocity and pressure fields. The correct pressure and velocity quantities are defined below as the sum of the intermediate quantities and a corrector value.

$$\begin{aligned}
p &= p^* + p' \\
u &= u^* + u' \\
v &= v^* + v'
\end{aligned}
\tag{83}$$

To apply Eqns. 83, Eqns. 82 (expressions for the *intermediate* value) are subtracted from Eqns. 10 (expressions for the *correct* value) to yield an expression for the corrector. Eqns. 83 are then substituted into the resulting equations and yield the following expressions for the corrector velocities.

$$\begin{aligned}
a_{i,j}u'_{i,j} &= \sum a_{nb}u'_{nb} + (p'_{l-1,j} - p'_{l,j})A_{i,j} \\
a_{l,j}v'_{l,j} &= \sum a_{nb}v'_{nb} + (p'_{l,j-1} - p'_{l,j})A_{l,j}
\end{aligned}
\tag{84}$$

The summation terms are dropped at this point as their influence is considered negligible (especially as convergence is approached as they tend to zero there anyway). Thus, Eqns. 84 are simplified as follows:

$$\begin{aligned}
u'_{i,j} &= d_{i,j} (p'_{l-1,j} - p'_{l,j}) \\
v'_{l,j} &= d_{l,j} (p'_{l,j-1} - p'_{l,j})
\end{aligned}
\tag{85}$$

where

$$d_{i,j} = \frac{A_{i,j}}{a_{i,j}} \quad \text{and} \quad d_{l,j} = \frac{A_{l,j}}{a_{l,j}}
\tag{86}$$

When substituted back into the equations for the correct velocities in Eqns. 83, we obtain

$$\boxed{
\begin{aligned}
u_{i,j} &= u^*_{i,j} + d_{i,j} (p'_{l-1,j} - p'_{l,j}) \\
v_{l,j} &= v^*_{l,j} + d_{l,j} (p'_{l,j-1} - p'_{l,j})
\end{aligned}
}
\tag{87}$$

We now have equations for determining the correct velocity components but they are dependant on the corrector for pressure  $p'$  which we will determine now through consideration of the discretised continuity equation

$$\left[ (\rho u A)_{i+1,j} - (\rho u A)_{i,j} \right] + \left[ (\rho v A)_{l,j+1} - (\rho v A)_{l,j} \right] = 0
\tag{88}$$

If Eqns. 87, and the similarly determined equations for  $u_{i+1,j}$  and  $v_{l,j+1}$  (not shown here), are substituted into Eqn. 88, the following expression for the pressure corrector  $p'$  may be found.

$$\begin{aligned}
a_{l,j}p'_{l,j} &= a_{l+1,j}p'_{l+1,j} + a_{l-1,j}p'_{l-1,j} \\
&+ a_{l,j+1}p'_{l,j+1} + a_{l,j-1}p'_{l,j-1} + b'_{l,j}
\end{aligned}
\tag{89}$$

where

$$\begin{aligned}
a_{I,J} &= a_{I+1,J} + a_{I-1,J} + a_{I,J+1} + a_{I,J-1} \\
a_{I+1,J} &= (\rho dA)_{i+1,J} \\
a_{I-1,J} &= (\rho dA)_{i,J} \\
a_{I,J+1} &= (\rho dA)_{I,j+1} \\
a_{I,J-1} &= (\rho dA)_{I,j} \\
b'_{I,J} &= (\rho u^* A)_{i,J} + (\rho u^* A)_{i+1,J} + (\rho v^* A)_{I,j} + (\rho v^* A)_{I,j+1}
\end{aligned} \tag{90}$$

The third step in the SIMPLE algorithm is to apply the pressure corrector  $p'$ , just determined, to Eqns. 87 to obtain the new velocity components and to the first of Eqns. 83 to obtain the new pressure value.

It should be noted that this pressure corrector is usually applied with a fairly significant under-relaxation coefficient which if, for example, is set equal to 0.3, will only apply (add) 30 % of the calculated  $p'$  to the initial  $p^*$  value. This does not affect the end solution but markedly slows the convergence speed of the solution for the purpose of ensuring numerical stability.

The fourth and final step is to use the newly obtained  $u$ ,  $v$  and  $p$  values to determine a new value for any other scalar quantities of the flow  $\phi$ , as was demonstrated in the previous section.

At this point, a convergence check is applied – whereby if the change in the flow variables, between the initial and final values for the iteration, are sufficiently small, the flow is considered ‘converged’. If not, however, another iteration is performed with the variables for the next  $i+1^{\text{th}}$  iteration set equal to those from the  $i^{\text{th}}$  iteration as shown.

$$\begin{aligned}
p^{*i+1} &= p^i, & u^{*i+1} &= u^i \\
v^{*i+1} &= v^i, & \phi^{*i+1} &= \phi^i
\end{aligned} \tag{91}$$

A flowchart of the SIMPLE algorithm is shown in Figure A.3.

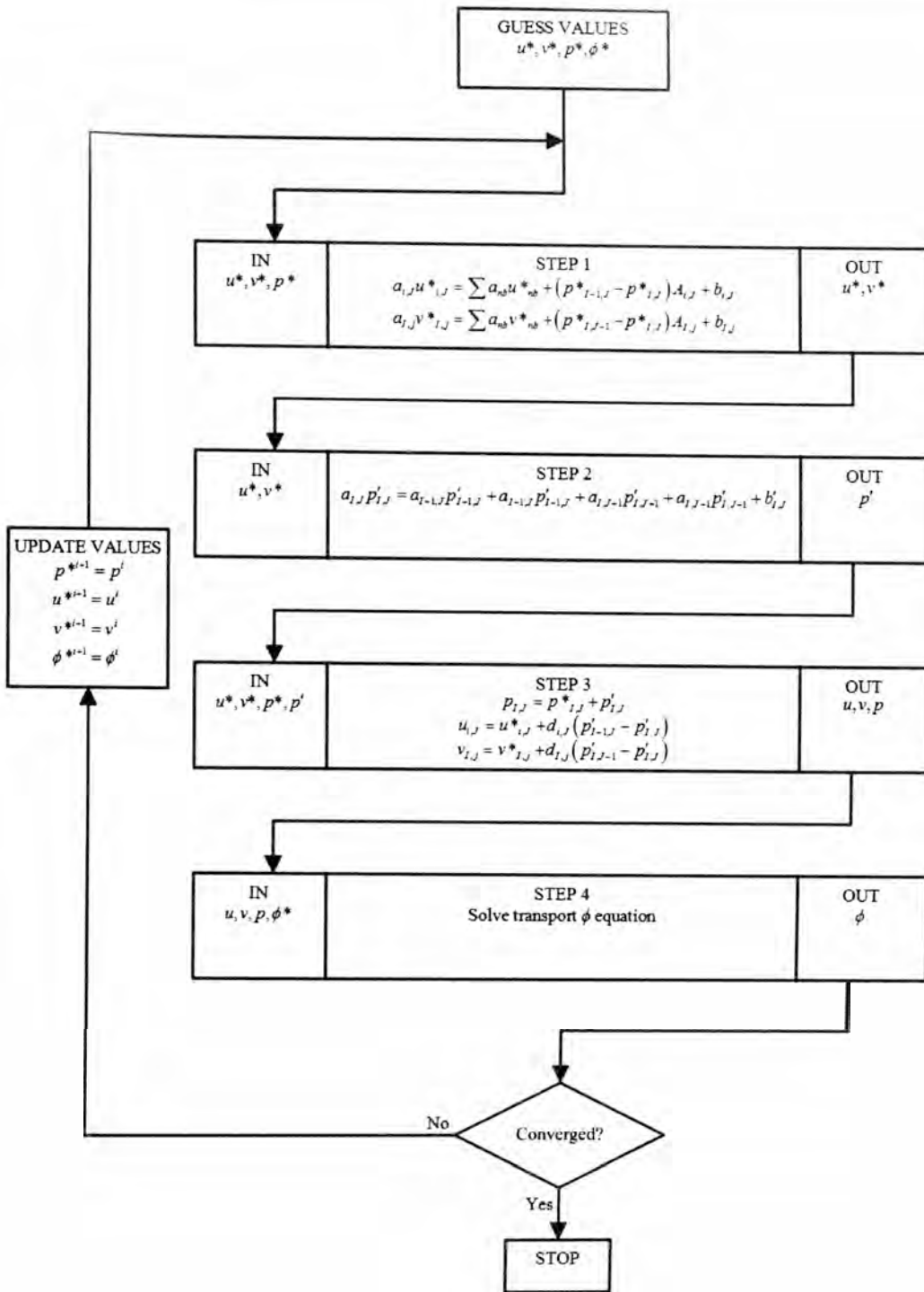


Figure A.3: The SIMPLE algorithm.

Applying the SIMPLE algorithm to unsteady or time-dependant CFD solutions requires only a small additional term be added to the pressure corrector, Eqn. 89. This is brought about because of the additional term in the conservation equation which is now of the form

$$\frac{\partial \rho}{\partial t} + \frac{\partial (\rho u)}{\partial x} + \frac{\partial (\rho v)}{\partial y} = 0 \quad (92)$$

and, when discretised, takes the form

$$\frac{(\rho_p - \rho_p^0)}{\Delta t} \Delta V + [(\rho u A)_{i+1,j} - (\rho u A)_{i,j}] + [(\rho v A)_{i,j+1} - (\rho v A)_{i,j}] = 0 \quad (93)$$

This yields the same pressure corrector equation as in Eqn. 89 but with an additional source term such that

$$b'_{i,j} = (\rho u^* A)_{i,j} + (\rho u^* A)_{i+1,j} + (\rho v^* A)_{i,j} + (\rho v^* A)_{i,j+1} + \frac{(\rho_P^0 - \rho_P) \Delta V}{\Delta t} \quad (94)$$

With an unsteady solution process, the iterative SIMPLE algorithm is run till acceptable convergence within each timestep and then the time-step is updated and the SIMPLE iterative process is repeated. This is shown in the flowchart of Figure A.4.

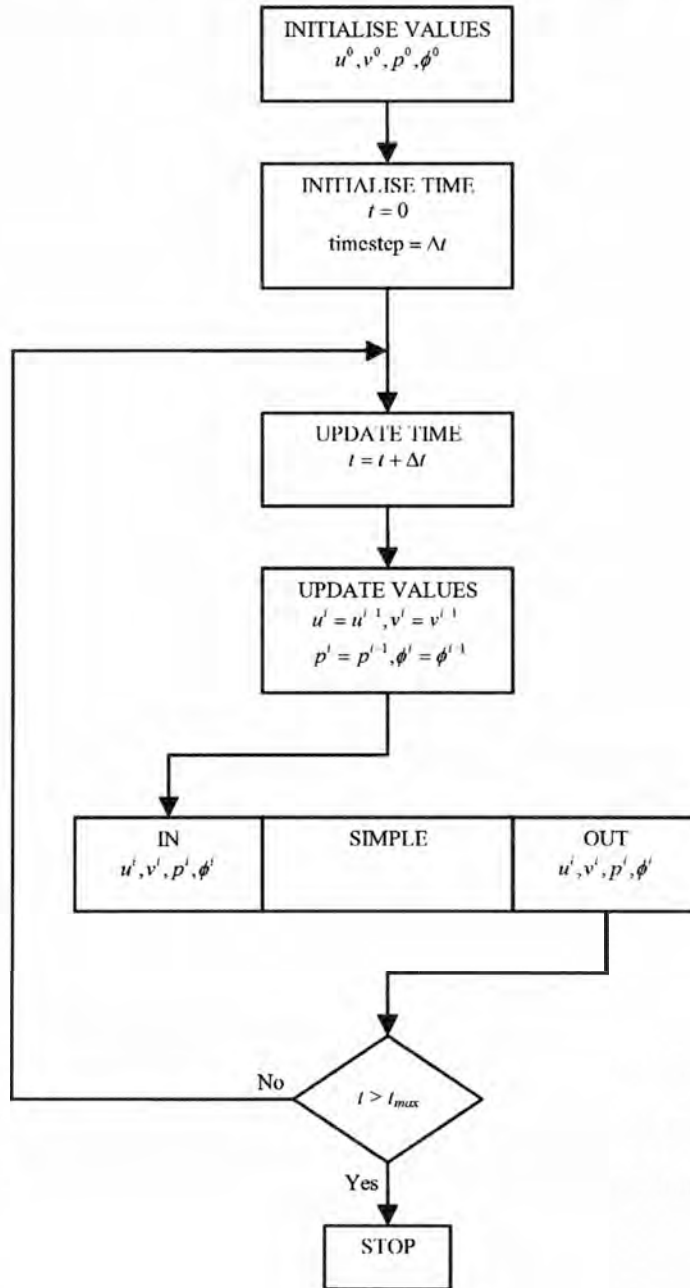


Figure A.4: Unsteady SIMPLE algorithm.

This research programme employs the SIMPLEC algorithm which is almost identical to the SIMPLE process described above, however, makes a small alteration to the simplification

process used on Eqns. 84. The result of which is a slight increase in numerical stability (which can be translated to a quicker convergence time by increasing the under-relaxation coefficient).

## A.6 Verification and Validation Process

Verification and validation are processes that, when performed thoroughly, ensure a solution is sufficiently accurate for the user's requirements. Implicit in this process is the control and minimisation of several kinds of error that may be generated in a CFD code. A thorough summary of the different types of error are discussed below in Appendix A.7.

Both verification and validation processes are well summarised in Figure A.5, which is adapted from a similar figure in an undergraduate course on CFD by Barber (2005). CFD attempts to simulate the reality (the top box in Figure A.5) and achieves this by first creating a conceptual model of reality. This conceptual model is then implemented in a computer model and the resulting computer simulation is finally checked against reality to ensure its validity.

The first step in the process (analysis to achieve the conceptual model) is the stage where the applicable governing equations are determined, the simplifying assumptions are made (e.g. no buoyancy effects or simplifying complex geometry) and the boundary conditions specified. All these choices must be justified through a qualification process.

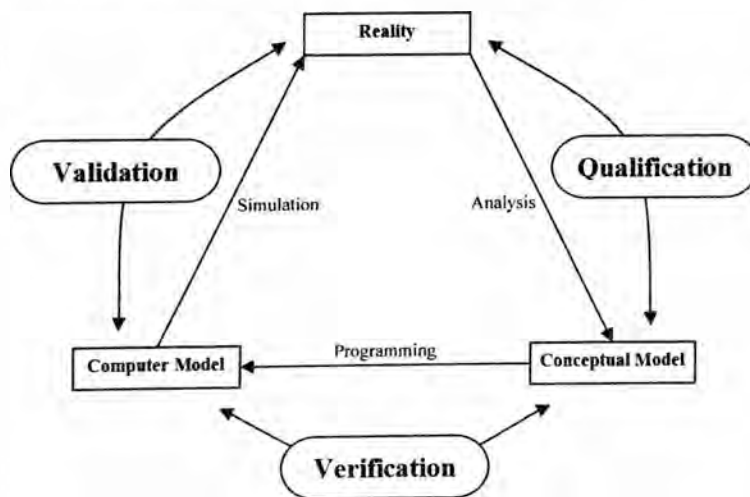


Figure A.5: Schematic of CFD approach (adapted from Barber, 2005)

One of the most obvious verification tasks is a grid independence study whereby the model's sensitivity to grid resolution is determined by running the simulation at several different grid intensities. If the change in the flow field and other important flow parameters between grid 'p' and finer grid 'q' are deemed negligible, then the model with grid 'p' can be deemed 'grid-independent', that is, any errors caused by the grid itself have been minimised. Grid 'p' will then be adopted thereafter as using a finer grid will bring about no appreciable reduction in error.

A similar study can be performed for temporal resolution (for time-dependant problems), whereby a simulation is run with several different time-steps. The time-step below which the behaviour of the important parameters stop varying with ever smaller time-steps, is deemed an adequately small time-step to achieve temporal independence.

The grid domain needs to have external boundaries at which the simulation is truncated. These boundaries are placed as close as possible to the geometry of interest in order to maximise the economy of the simulation. However, just like employing the largest grid size and largest time-step that are acceptable to maintain accuracy, how far these boundaries must be located in order not to compromise the solution must also be determined. Boundary independence studies maintain the same grid density but systematically adjust the displacement of the external boundaries (which, of course, requires additional cells to fill the space left by a boundary that has been moved further away). Like the studies above, when the change in flow parameters between boundary location changes become negligible, the model is considered boundary independent.

This discussion of verification techniques is not exhaustive but does provide an overview of the general process. Details of the verification process employed in this research programme are discussed in Chapter 4.

Whereas verification is described as ‘solving the equations right’, validation is often described as ‘solving the right equations’ – this is, it aims to ensure the computer simulation that has been developed is capable of predicting reality. Are we solving the right equations in order to simulate reality? This process is achieved by comparing the simulation against a benchmark study of some kind or a reliable set of experimental values which one can confidently describe, in this context, as ‘reality’. The final step, therefore, before one can claim that a CFD model is fit for use as a flow prediction tool is to ‘prove’ it works by comparing it against reality.

Most obviously, the validation process compares the important flow features and parameters (ideally both qualitative and quantitative) of the simulation and the experimental data and a judgement is made as to whether the correlation between the data-sets is adequate.

Validation is also used to help develop the computer model. If a comparison between the simulation and the experimental data shows a discrepancy in the boundary conditions, for example, then they may be altered and the model improved.

A similar process is often employed when evaluating turbulence models (see Sec. 2.5.2) or sub-grid turbulence models (see Sec. 2.6.2) where mathematical models, rather than

governing physical equations, are used to characterise the turbulent behaviour of the flow. Turbulence models tend only to work in certain application areas and, as such, are often compared against each other to determine which one best replicates the general flow behaviour that the model is attempting to simulate. Thus, the results from several turbulence models may be compared against the benchmark experimental case and the best conforming results adopted as part of the definitive model.

Once the verification and validation process has been completed – and, thus, the model has proved itself capable of faithfully replicating a real world flow problem, it may then confidently be used to predict other flow situations for which experimental data does not exist (for if it did, why would one use CFD?). The user must be careful not to apply the model to application areas too far beyond those in which it was verified and validated, but, as long as this is not abused, the model can be used with confidence.

## A.7 Error Sources in CFD

The NASA National Project for Applications-oriented Research in CFD (NPARC) Alliance provides a very useful summary of the key contributors to error within a CFD code and model (Slater, 2008). This list is presented in Table A.1 with the error sources divided into categories of ‘acknowledged’ and ‘unacknowledged’ errors – the former being identifiable, known sources of error and the latter being unquantifiable, potential sources of error. It is important to note that the error sources in the first category are usually quantifiable and thus a determination can be made as to the severity (and acceptability) of generating such errors.

**Table A.1: Sources of Error (Slater, 2008)**

<b>Acknowledged errors:</b>	<b>Unacknowledged errors:</b>
1. Physical approximation error Physical modelling error Geometry modelling error	1. Computer programming error 2. Usage error
2. Computer round-off error	
3. Iterative convergence error	
4. Discretisation error Spatial discretisation error Temporal discretisation error	

**Physical Approximation Error:** These are sources of error associated with the process of attempting to represent a real physical problem or situation within an, often simplified, computational conceptual model. Physical modelling errors are introduced where the computational model does not faithfully represent the physical reality. This can occur through a poor understanding of the physical reality (possibly due to a lack of information – thus requiring an educated guess or approximation), or a deliberate simplification of the physical model in order to minimise the solution time – such as making an assumption that

buoyancy effects are negligible and thus, not modelling them. Geometry modelling errors occur when the actual geometry of the model is incorrectly translated to the computational model – usually by simplification of the geometry in order to speed up the solution time.

**Computer Round-off Error:** Computer round-off errors occur at every calculation that the CFD solver makes due to the limited precision with which the computer can store the resulting number in memory. Round-off errors are typically small when compared to other types of error, however, due to the iterative nature of CFD solvers, the overall or total extent of the round-off error tends to grow with each iteration. Computer round-off errors can be significantly minimised by storing the numbers with double precision accuracy. The Fluent commercial CFD software package stores double precision floating point numbers using 64 bits of memory instead of the 32 bits used for single precision numbers. Double precision numbers allocate 53 bits of memory to the significand which equates to approximately 16 decimal digits of precision. Single precision allocates 24 bits to the significand, equating to about 7 decimal digits. The downside of this approach is that the memory demands (RAM) of the CFD solver will typically double under such circumstances – which can be problematic when simulating very large jobs. Double precision numbers were used in all cases throughout this research programme.

**Iterative Convergence Error:** Iterative convergence error is somewhat related to round-off error. A converging iterative process requires that the variation between the solution of iterations  $n+2$  and  $n+1$  be smaller than the variation between iterations  $n+1$  and  $n$ . As the solution progresses this variation should, in theory, tend to zero – at which point the solution has ‘converged’ and the iterative process is stopped. However, due to round-off error, the variation between iterations does not tend to zero but to some finite number. In practise, once this finite number is reached the simulation is considered converged. This finite number is termed the iterative convergence error.

**Discretisation Error:** Discretisation errors are those that are introduced to the problem due to the process of discretising the governing equations, both spatially and temporally. Firstly, with regard to spatial discretisation errors, the construction of the grid itself has a large impact on the errors generated. If a grid’s resolution is increased (more node points, smaller finite-volumes or cells), the errors obtained as a result of the discretisation process will be smaller such that, if the resolution tended to infinity (spatial distance between nodes tending to zero), the errors obtained would tend to zero. This is one of the primary sources of error within CFD solutions and much attention is given to determining the extent of the error incurred by the grid resolution through grid convergence studies.

The quality of the grid also contributes to the discretisation errors generated in a solution. A poorly constructed grid can generate significant errors that render a solution useless and so, much care is taken in the grid construction process to monitor grid density (and minimising its spatial rate-of-change), the aspect-ratio of cells (and, again, minimising its spatial rate-of-change) and minimising cell skewness (the departure from 90° corners for quadrilateral cells or departure from equilateral for triangular cells), among others.

Finally, temporal discretisation is analogous to the situation just discussed for spatial discretisation: if the time-step tends to zero, the temporal discretisation error will also tend to zero. Consequently, like grid convergence studies, it is also important to consider the error induced through the choice of time-step size.

**Computer Programming Error:** The first of the unacknowledged errors are programming errors which are simply bugs in the programming code which can introduce errors into a solution process. This kind of error should be eliminated through validation studies of the code before it is used and is the responsibility of the software vendor for commercial packages. This research programme makes use of the long-standing Fluent commercial CFD package and, as such, the potential for such errors are considered minimal.

**Usage Error:** Usage errors are the result of mistakes made by the operator of the CFD solver, rather than any flaw in the software itself. These errors are usually the result of lack of understanding or training on the part of the operator and are manifested in the form of conceptual errors in the process of creating the CFD model or simply operator errors when performing the simulation (such as inputting improper parameters into the solver settings).

## A.8 Reynolds-Averaged Navier-Stokes Equations

We will define  $\Phi$  as the time-average of the arbitrary quantity  $\phi$  as follows

$$\Phi = \bar{\phi} = \frac{1}{\Delta t} \int_0^{\Delta t} \phi dt \quad (95)$$

where  $\Delta t$  is the time interval over which the time-average is taken and, for a steady flow, anything in excess of the slowest eddy time-scales (from the largest eddies) is quite adequate.

We will also define the quantity  $\phi$  (at any instant in time) as the summation of the time-averaged quantity (which is constant) and an instantaneous fluctuation about the mean quantity as shown below

$$\phi = \Phi + \phi' \quad (96)$$

where  $\phi'$  is the fluctuating component – and it should be noted that its time average, by definition, equals zero.

Reynolds-averaging is then applied by replacing all the quantities in the governing equations with the summation of the average and fluctuating components, as in Eqn. 96, and then applying the time-averaging to all the equations, as in Eqn. 95. This is demonstrated below with the Navier-Stokes equations for an incompressible flow. Firstly, the instantaneous N-S equations are pre-presented below from Eqns. 6, simplified for an incompressible flow:

$$\begin{aligned}
 \text{Mass} \quad \text{div } \bar{u} &= 0 \\
 \text{x-momentum} \quad \frac{\partial u}{\partial t} + \text{div}(u\bar{u}) &= -\frac{1}{\rho} \frac{\partial p}{\partial x} + \nu \text{div grad } u \\
 \text{y-momentum} \quad \frac{\partial v}{\partial t} + \text{div}(v\bar{u}) &= -\frac{1}{\rho} \frac{\partial p}{\partial y} + \nu \text{div grad } v \\
 \text{z-momentum} \quad \frac{\partial w}{\partial t} + \text{div}(w\bar{u}) &= -\frac{1}{\rho} \frac{\partial p}{\partial z} + \nu \text{div grad } w
 \end{aligned} \tag{97}$$

where  $\nu$  is the dynamic viscosity, which is assumed to be constant.

The following quantities are substituted into Eqns. 97:

$$\begin{aligned}
 \bar{u} &= U + \bar{u}', \quad u = U + u', \quad v = V + v' \\
 v &= V + v', \quad w = W + w', \quad p = P + p'
 \end{aligned} \tag{98}$$

The resulting equations are then time-averaged using the following rules for the time-averaging of the combination of a vector  $\bar{a} = A + \bar{a}'$  and a scalar  $\phi = \Phi + \phi'$ .

$$\begin{aligned}
 \overline{\text{div } \bar{a}} &= \text{div } A \\
 \overline{\text{div}(\phi\bar{a})} &= \overline{\text{div}(\phi\bar{a})} = \text{div}(\Phi A) + \overline{\text{div}(\phi'\bar{a}')} \\
 \overline{\text{div grad } \phi} &= \text{div grad } \Phi
 \end{aligned} \tag{99}$$

The resulting time-averaged N-S equations are as follows:

$$\begin{aligned}
 \text{Mass} \quad \text{div } U &= 0 \\
 \text{x-momentum} \quad \frac{\partial U}{\partial t} + \text{div}(UU) + \overline{\text{div}(u'u')} &= -\frac{1}{\rho} \frac{\partial P}{\partial x} + \nu \text{div grad } U \\
 \text{y-momentum} \quad \frac{\partial V}{\partial t} + \text{div}(VU) + \overline{\text{div}(v'u')} &= -\frac{1}{\rho} \frac{\partial P}{\partial y} + \nu \text{div grad } V \\
 \text{z-momentum} \quad \frac{\partial W}{\partial t} + \text{div}(WU) + \overline{\text{div}(w'u')} &= -\frac{1}{\rho} \frac{\partial P}{\partial z} + \nu \text{div grad } W
 \end{aligned} \tag{100}$$

The time-averaging process has resulted in additional terms in the governing equations. The momentum equations from Eqns. 100 are repeated below with the third term, in each, moved to the RHS and written in longhand to identify the resulting extra quantities obtained through the time-averaging process.

$$\begin{aligned}
\frac{\partial U}{\partial t} + \text{div}(UU) &= -\frac{1}{\rho} \frac{\partial P}{\partial x} + \nu \text{div grad } U + \left[ -\frac{\partial \overline{u'^2}}{\partial x} - \frac{\partial \overline{u'v'}}{\partial y} - \frac{\partial \overline{u'w'}}{\partial z} \right] \\
\frac{\partial V}{\partial t} + \text{div}(VU) &= -\frac{1}{\rho} \frac{\partial P}{\partial y} + \nu \text{div grad } V + \left[ -\frac{\partial \overline{u'v'}}{\partial x} - \frac{\partial \overline{v'^2}}{\partial y} - \frac{\partial \overline{v'w'}}{\partial z} \right] \\
\frac{\partial W}{\partial t} + \text{div}(WU) &= -\frac{1}{\rho} \frac{\partial P}{\partial z} + \nu \text{div grad } W + \left[ -\frac{\partial \overline{u'w'}}{\partial x} - \frac{\partial \overline{v'w'}}{\partial y} - \frac{\partial \overline{w'^2}}{\partial z} \right]
\end{aligned} \tag{101}$$

As can be seen from Eqns. 101, there are six additional quantities as a result of time-averaging – three normal stresses and three shear stresses. These are termed the Reynolds stresses:

$$\begin{aligned}
\tau_{xx} &= -\rho \overline{u'^2}, & \tau_{yy} &= -\rho \overline{v'^2}, & \tau_{zz} &= -\rho \overline{w'^2} \\
\tau_{xy} &= -\rho \overline{u'v'}, & \tau_{xz} &= -\rho \overline{u'w'}, & \tau_{yz} &= -\rho \overline{v'w'}
\end{aligned} \tag{102}$$

## Appendix B: Dividing Streamline Movement

This section is intended to present a thorough theoretical treatment of the flow condition under an inverted aerofoil in order to explain why the dividing streamline moves downward (relative to the leading edge position) with decreasing ground clearance.

First, it is instructive to consider an energy balance of the flow over the aerofoil. If  $E_A$  is the energy level before the air reaches the aerofoil and  $E_B$  is the energy level after the air has passed the aerofoil, then the following energy balance applies.

$$E_A + E_{added} - E_{losses} = E_B \quad (103)$$

There is no energy added to the system between points  $A$  and  $B$ , however, there are losses in the system (e.g. drag). The energy level at  $B$  is therefore lower than at  $A$  and the reduced momentum in the wake is the result.

A fundamental characteristic of fluid mechanics is that the flow field facing an obstacle (like an aerofoil) will always establish itself such that it incurs the lowest possible loss of energy. This tendency is evident in the well-known Kutta Condition. To further underscore this point, a fluid flow, if allowed, will alter an obstruction to offer the least resistance (so the flow suffers the least energy loss) – as is the case with the position of a wind-direction indicator whose tail offers the least obstruction to the air flow when parallel with the flow direction.

Returning to the current aerofoil configuration; when the aerofoil is brought further down toward the ground, the flow field will adjust itself into the lowest energy-loss situation. If we assume that the dividing streamline has not moved during this process, then this new flow regime will suffer greater flow constriction than the prior case as schematically demonstrated in Figure B.6. This is because the aerofoil effectively impinges upon the flow heading under the aerofoil to a greater degree by virtue of blocking a greater proportion of the volume through which the flow must pass. This will *only increase* the energy loss suffered by the flow going under the aerofoil. The flow over the aerofoil would see little, if any, change in flow field or increase in energy loss.

Therefore, as there is an increased energy loss overall at this new ground clearance, and no new energy being added to the system, there is nothing to maintain the dividing streamline in its prior position. The flow will, therefore, adjust to a lower energy state – one where the dividing streamline is positioned lower, delivering a lower volume flow rate under the aerofoil (and decreasing the aerofoil's constriction of the under-aerofoil flow) so as to minimise the energy that is lost in this new configuration.

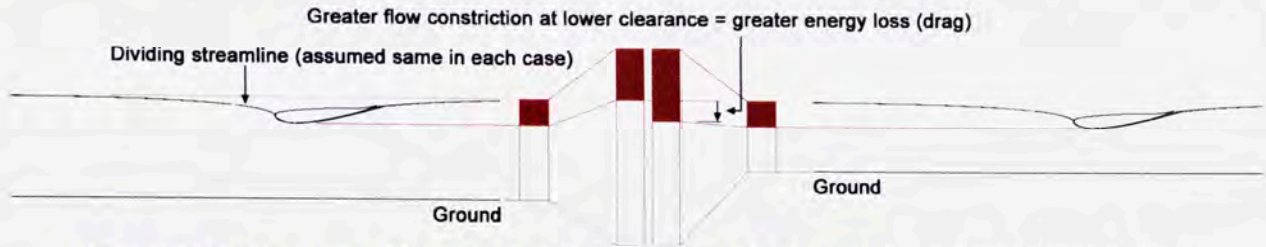


Figure B.6: Schematic of flow constriction on flow under inverted aerofoil in ground effect

Figure B.7 expands on the proportional blocks in Figure B.6 and shows the flow proportions of the constricted flow volume and the blocked-off volume for all clearances of the Tyrrell aerofoil. Added to this figure is a plot of what would be the flow proportions if the dividing streamline from  $h/c = 3.0$  were maintained in this position (relative to the aerofoil) all the way down to the lowest clearance. In such a circumstance (where the flow would not have been allowed to self-adjust at new ground clearances), the flow would have been much more heavily constricted at the lower clearances.

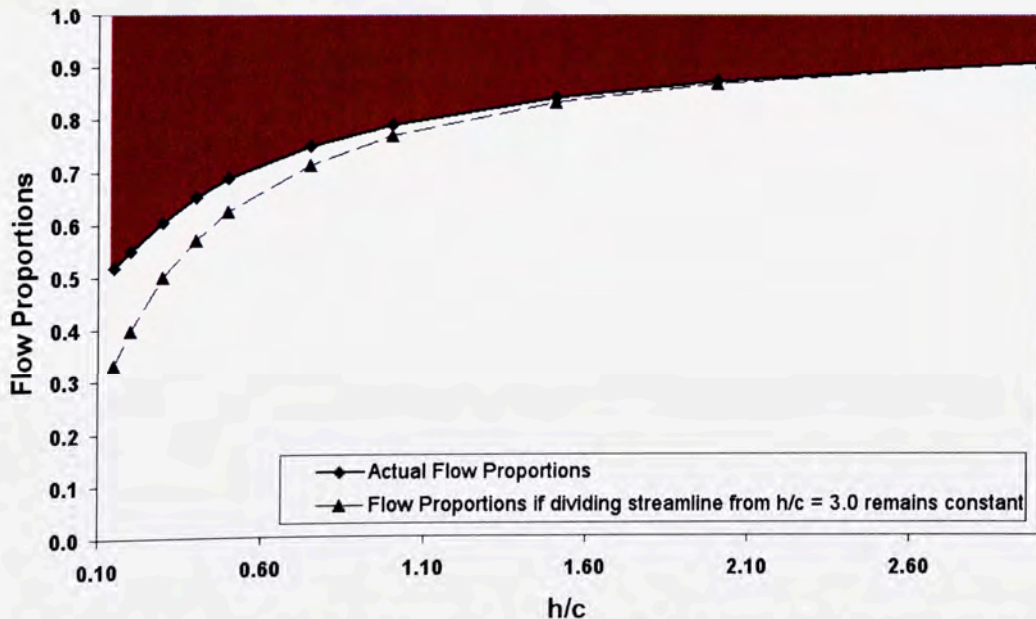


Figure B.7: Volume proportions under inverted Tyrrell aerofoil vs. ground clearance; (dark) aerofoil-blocked volume proportion, (white) unblocked volume proportion under aerofoil

At  $h/c = 0.15$ , the flow heading under the aerofoil must fit through a volume only 52 % of its original freestream allowance and this results in a significant velocity increase to facilitate this, as well as a significant increase in drag and energy-loss. However, if the flow were not allowed to naturally adjust, the flow under the wing would be occupying only 33 % of the

space it enjoys in freestream, which would increase the drag and energy-loss significantly. In practise, the flow field naturally diverts flow over the top of the aerofoil as clearance is reduced (lowering the dividing streamline) and, in so doing, offsets some of the energy losses it would otherwise incur.

In summary, maintaining the dividing streamline height (relative to the leading edge) while moving the aerofoil toward the ground can not be achieved – much less would the dividing streamline actually move upwards – because the presence of the ground increases the flow constriction under the aerofoil which increases the energy losses. The flow, self-adjusting to a low-energy condition, dictates the downward movement of the dividing streamline. This could be changed if energy was added to the system (like a suction fan in the diffuser) but that is beyond the scope of this work.

## Appendix C: Derivation of LDA Transformation Matrix

This appendix is intended to explain the development of the transformation matrix used to obtain orthogonal  $x$ -,  $y$ - and  $z$ -components of velocity ( $u$ ,  $v$  and  $w$ ) from the LDA optical measurement system, as discussed in Sec. 3.3.2.

The  $u$  component is measured directly and so only the  $v$  and  $w$  components need to be obtained through a transformation. The velocity vector  $\mathbf{U}$ , projected onto the  $y$ - $z$  plane, is shown in Figure C.8 in aid of the following derivation.

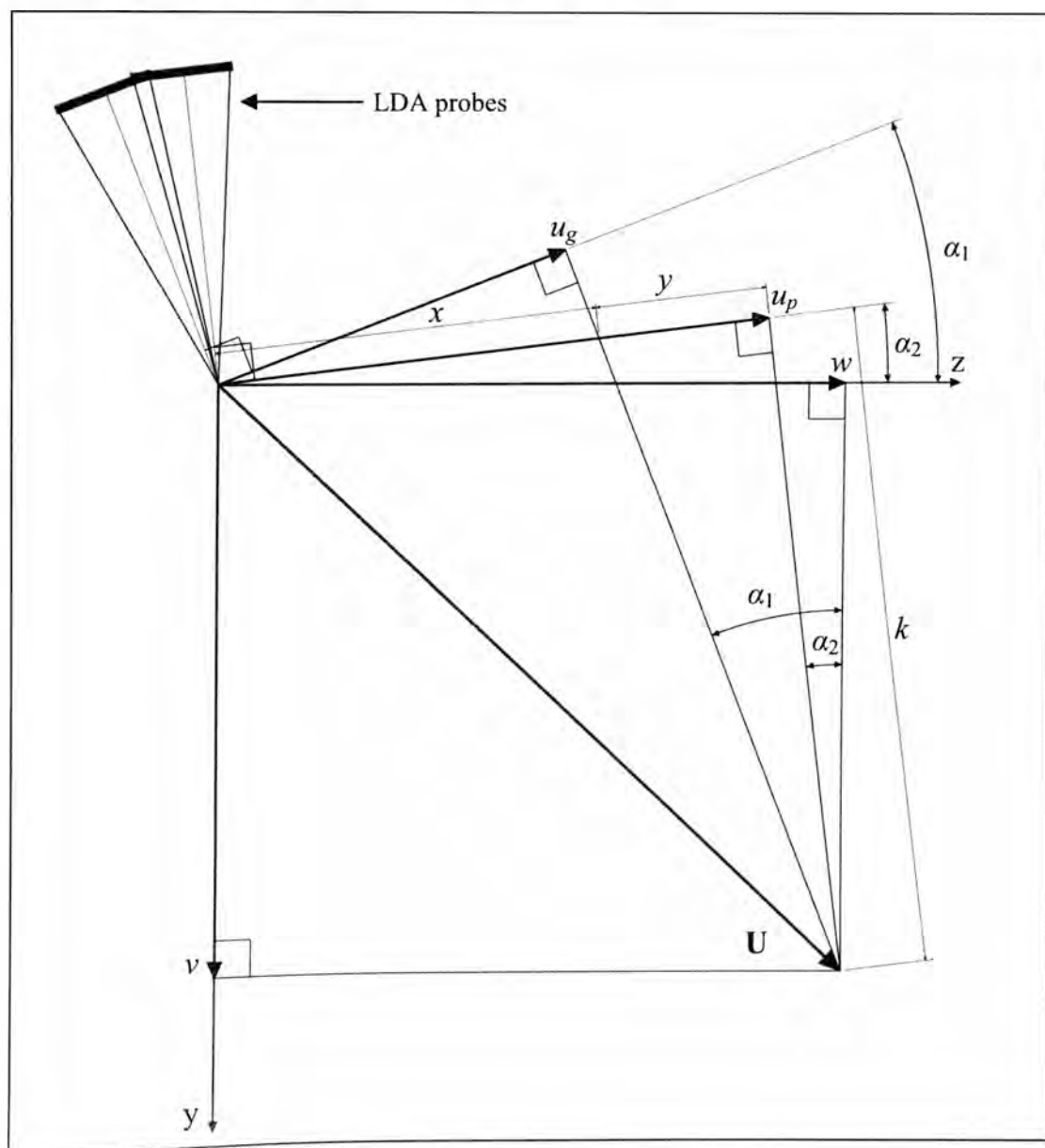


Figure C.8: Derivation of transformation matrix

$$\begin{aligned} v &= k \cos \alpha_2 - u_p \sin \alpha_2 \\ w &= k \sin \alpha_2 + u_p \cos \alpha_2 \end{aligned} \quad (104)$$

$$x = \frac{u_g}{\cos(\alpha_1 - \alpha_2)}$$

$$y = u_p - x = u_p - \frac{u_g}{\cos(\alpha_1 - \alpha_2)} \quad (105)$$

$$k = \frac{y}{\tan(\alpha_1 - \alpha_2)} = \frac{\cos(\alpha_1 - \alpha_2) y}{\sin(\alpha_1 - \alpha_2)} = \frac{u_p \cos(\alpha_1 - \alpha_2) - u_g}{\sin(\alpha_1 - \alpha_2)}$$

Substituting the expression for  $k$  obtained in Eqns. 105, the following definitions for  $v$  and  $w$  are obtained.

$$v = \frac{\cos \alpha_2 (u_p \cos(\alpha_1 - \alpha_2) - u_g)}{\sin(\alpha_1 - \alpha_2)} - u_p \sin \alpha_2 \quad (106)$$

$$v = u_g \left[ \frac{-\cos \alpha_2}{\sin(\alpha_1 - \alpha_2)} \right] + u_p \left[ \frac{\cos \alpha_2}{\tan(\alpha_1 - \alpha_2)} - \sin \alpha_2 \right]$$

$$w = \frac{\sin \alpha_2 (u_p \cos(\alpha_1 - \alpha_2) - u_g)}{\sin(\alpha_1 - \alpha_2)} + u_p \cos \alpha_2 \quad (107)$$

$$w = u_g \left[ \frac{-\sin \alpha_2}{\sin(\alpha_1 - \alpha_2)} \right] + u_p \left[ \frac{\sin \alpha_2}{\tan(\alpha_1 - \alpha_2)} + \cos \alpha_2 \right]$$

These expressions for  $v$  and  $w$ , and given that  $u$  is measured directly, lead to the following transformation matrix equation as previously mentioned in Sec. 3.3.2.

$$\begin{Bmatrix} u \\ v \\ w \end{Bmatrix} = \begin{bmatrix} 0 & 1 & 0 \\ \frac{-\cos \alpha_2}{\sin(\alpha_1 - \alpha_2)} & 0 & \frac{\cos \alpha_2}{\tan(\alpha_1 - \alpha_2)} - \sin \alpha_2 \\ \frac{-\sin \alpha_2}{\sin(\alpha_1 - \alpha_2)} & 0 & \frac{\sin \alpha_2}{\tan(\alpha_1 - \alpha_2)} + \cos \alpha_2 \end{bmatrix} \cdot \begin{Bmatrix} u_2 \\ u_1 \\ u_3 \end{Bmatrix} \begin{matrix} u_{green} \\ \leftarrow u_{blue} \\ u_{purple} \end{matrix} \quad (108)$$

# Appendix D: Experimental and Numerical Velocity Profile Comparisons

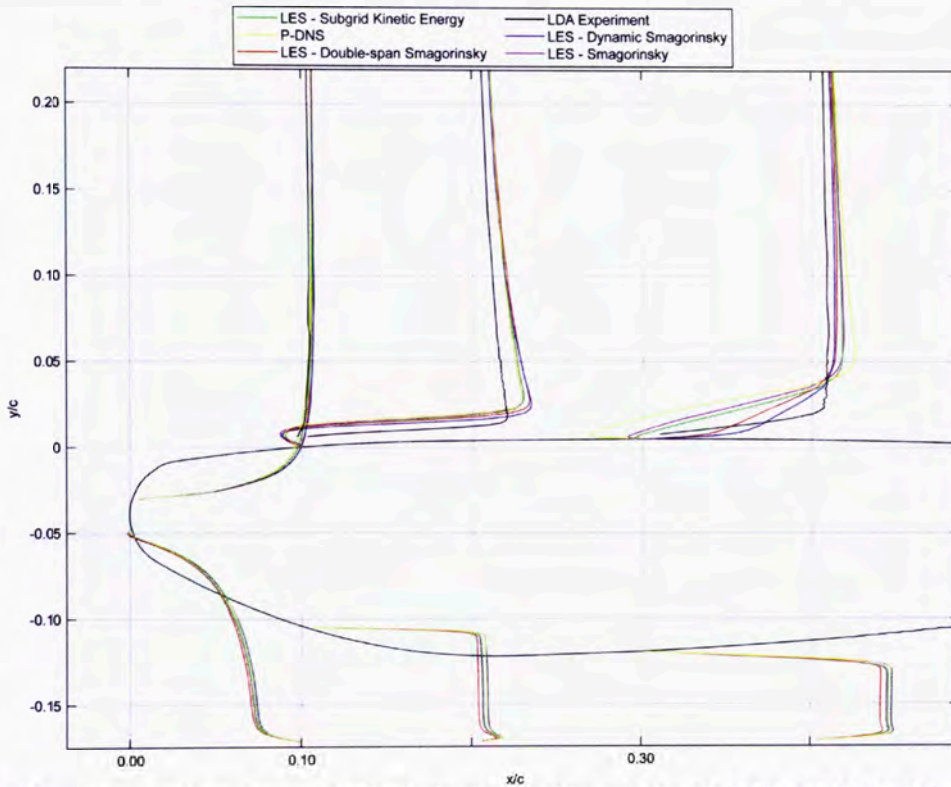


Figure D.9: Experimental and numerical x-velocity profiles at  $x/c = 0, 0.10$  and  $0.30$ ;  $0.1 x/c = 10$  m/s

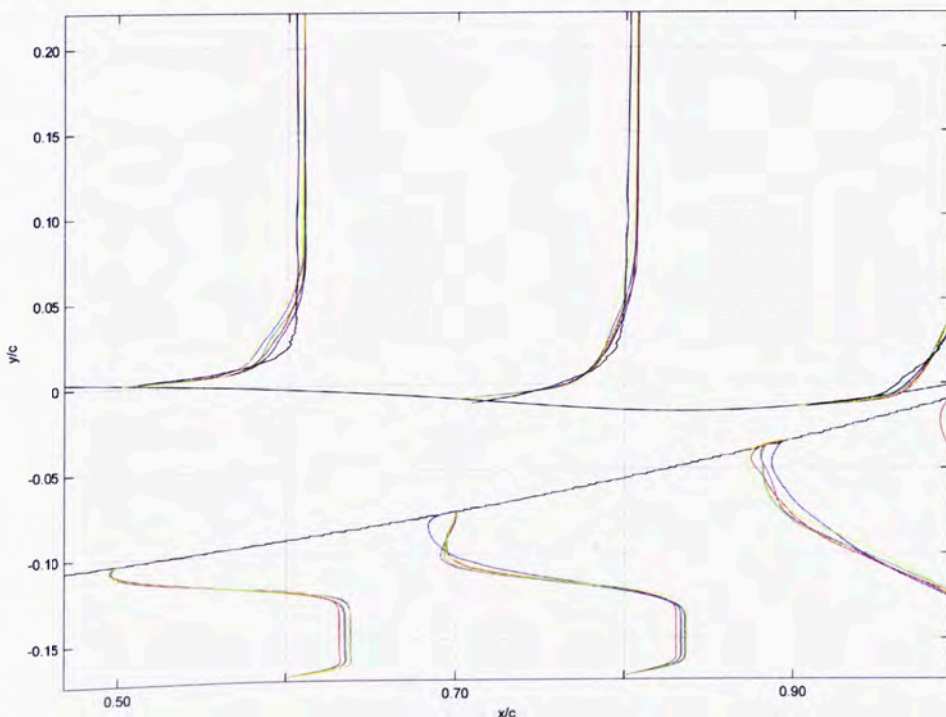


Figure D.10: Experimental and numerical x-velocity profiles at  $x/c = 0.5$  and  $0.70$ ;  $0.1 x/c = 10$  m/s

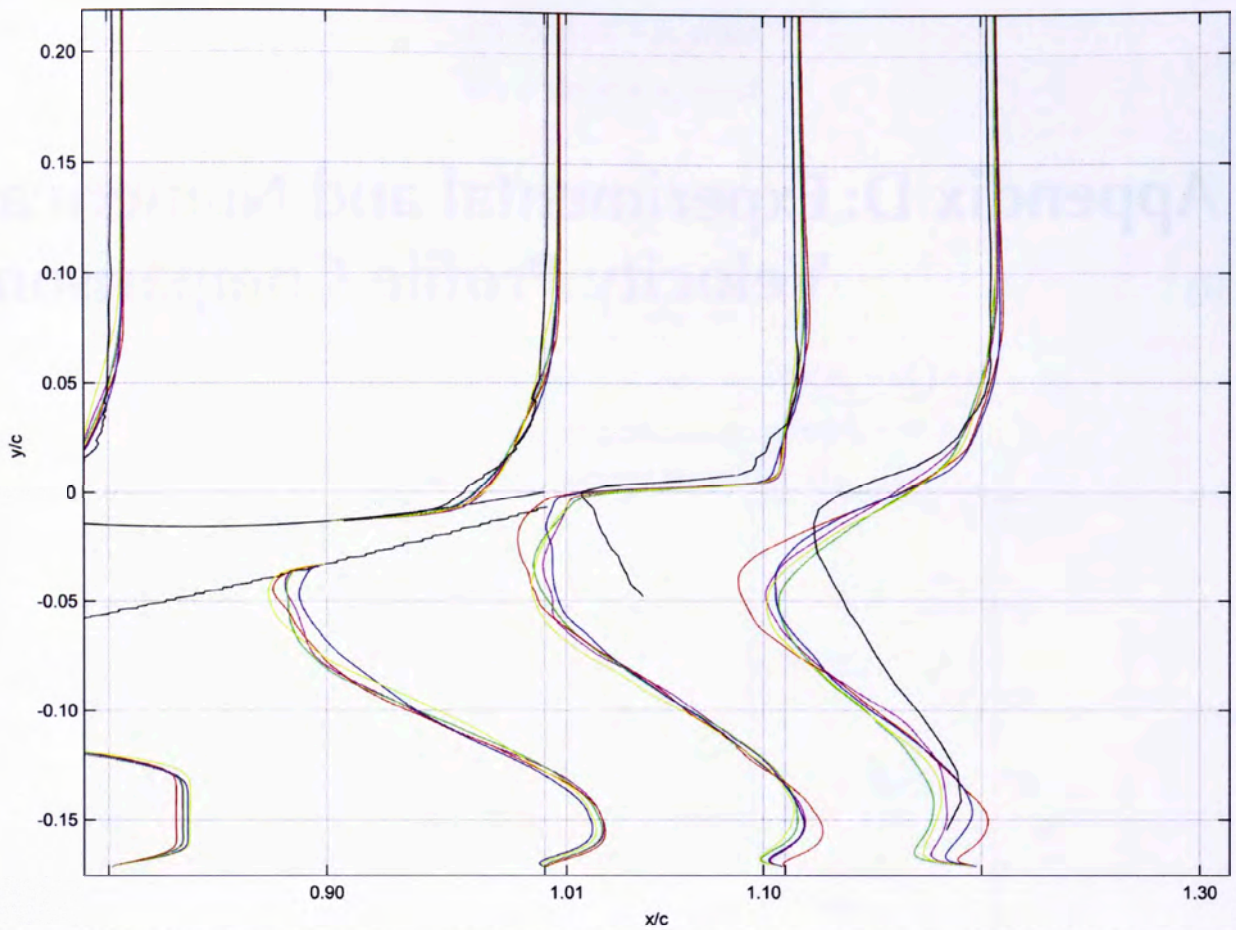


Figure D.11: Experimental and numerical x-velocity profiles at  $x/c = 0.9, 1.01$  and  $1.10$ ;  $0.1 x/c = 10$  m/s

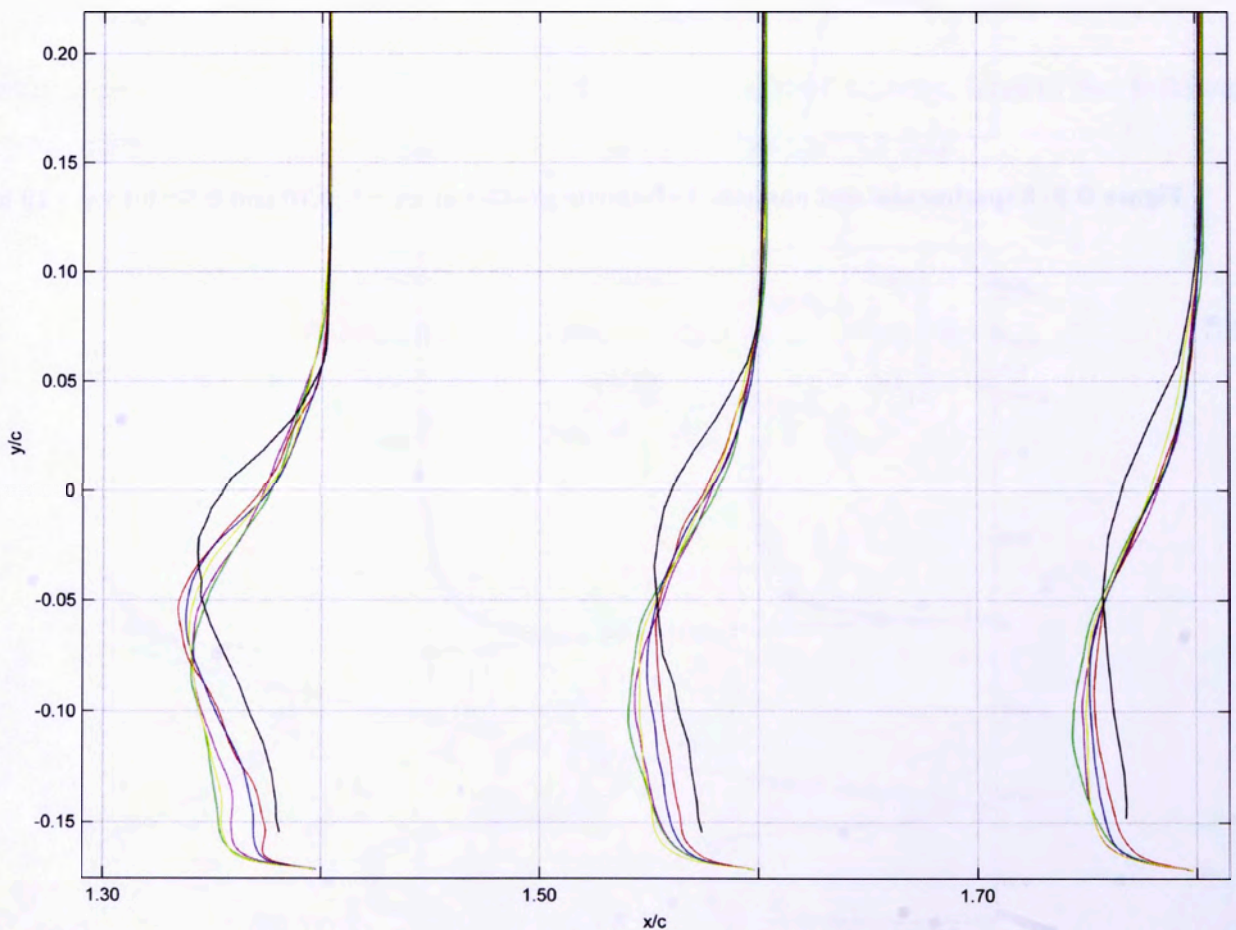
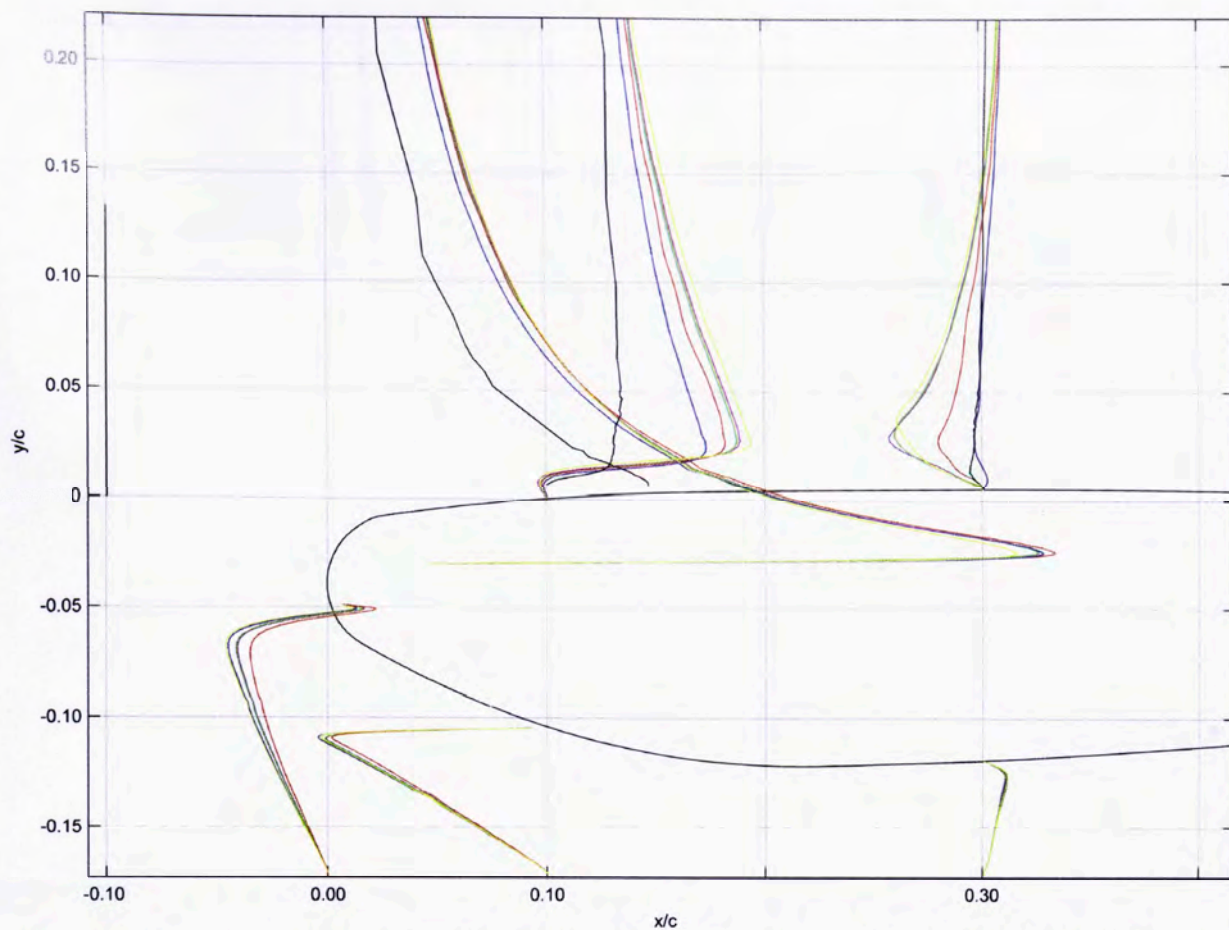
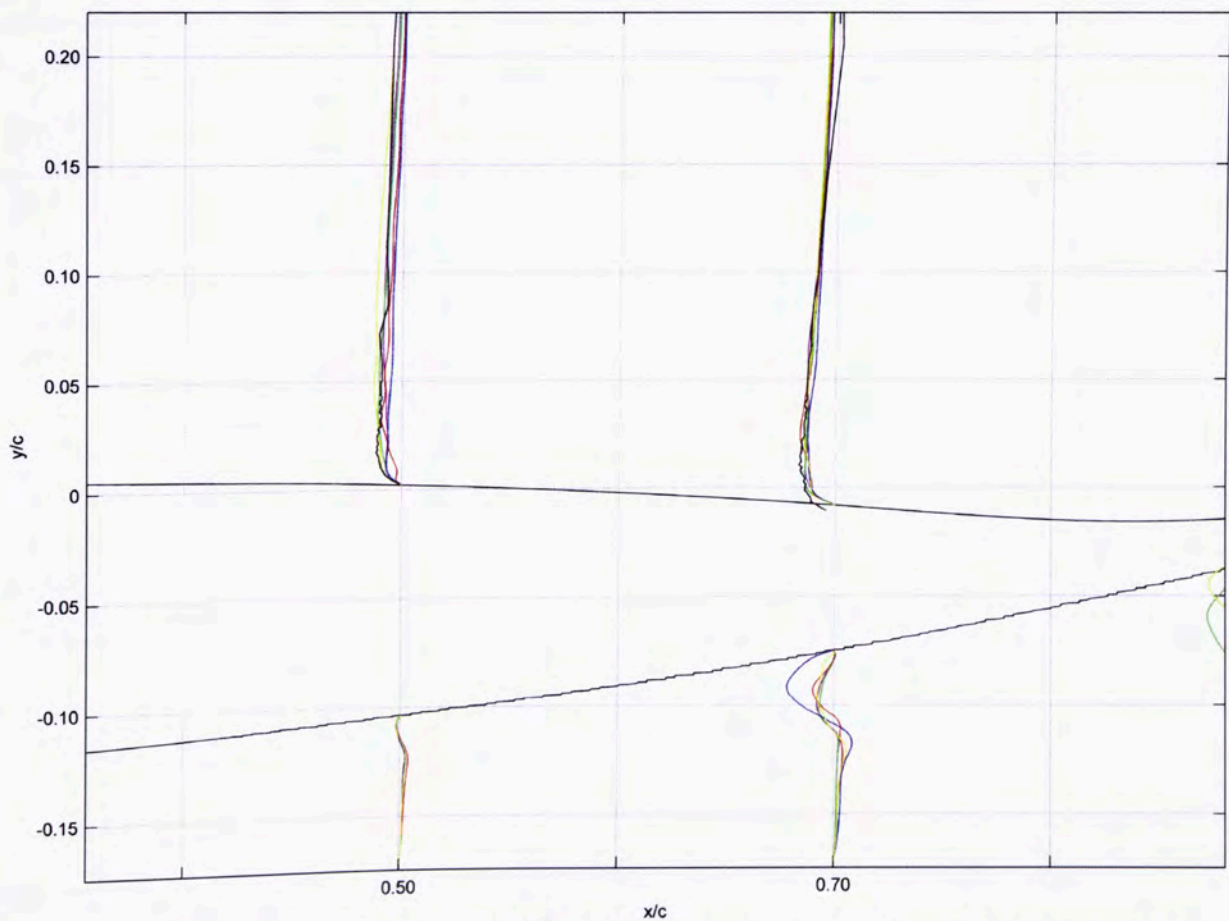


Figure D.12: Experimental and numerical x-velocity profiles at  $x/c = 1.30, 1.50$  and  $1.70$ ;  $0.1 x/c = 10$  m/s



**Figure D.13: Experimental and numerical y-velocity profiles at  $x/c = 0, 0.10$  and  $0.30$ ;  $0.1 x/c = 3$  m/s**



**Figure D.14: Experimental and numerical y-velocity profiles at  $x/c = 0.5$  and  $0.70$ ;  $0.1 x/c = 3$  m/s**

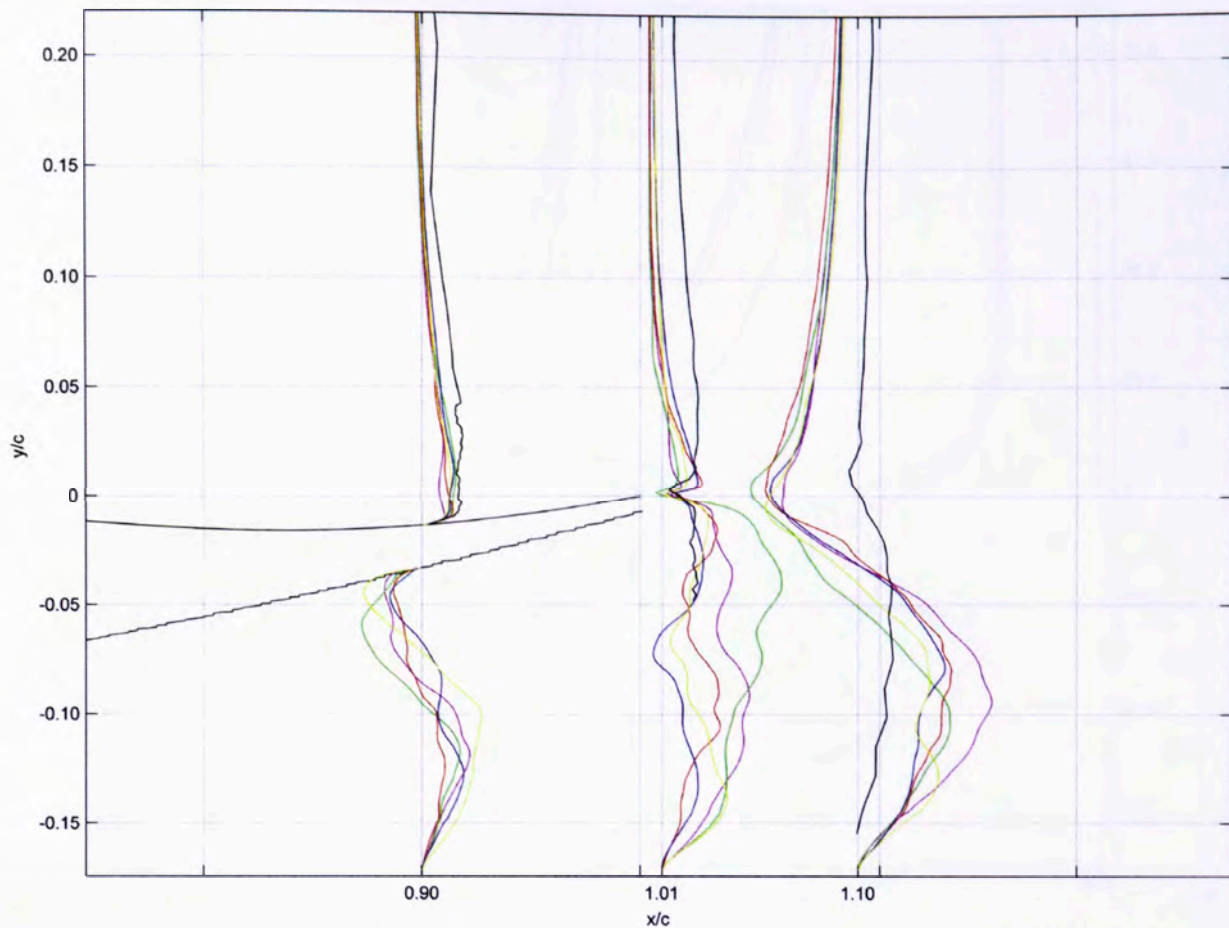


Figure D.15: Experimental and numerical y-velocity profiles at  $x/c = 0.9, 1.01$  and  $1.10; 0.1 x/c = 3$  m/s

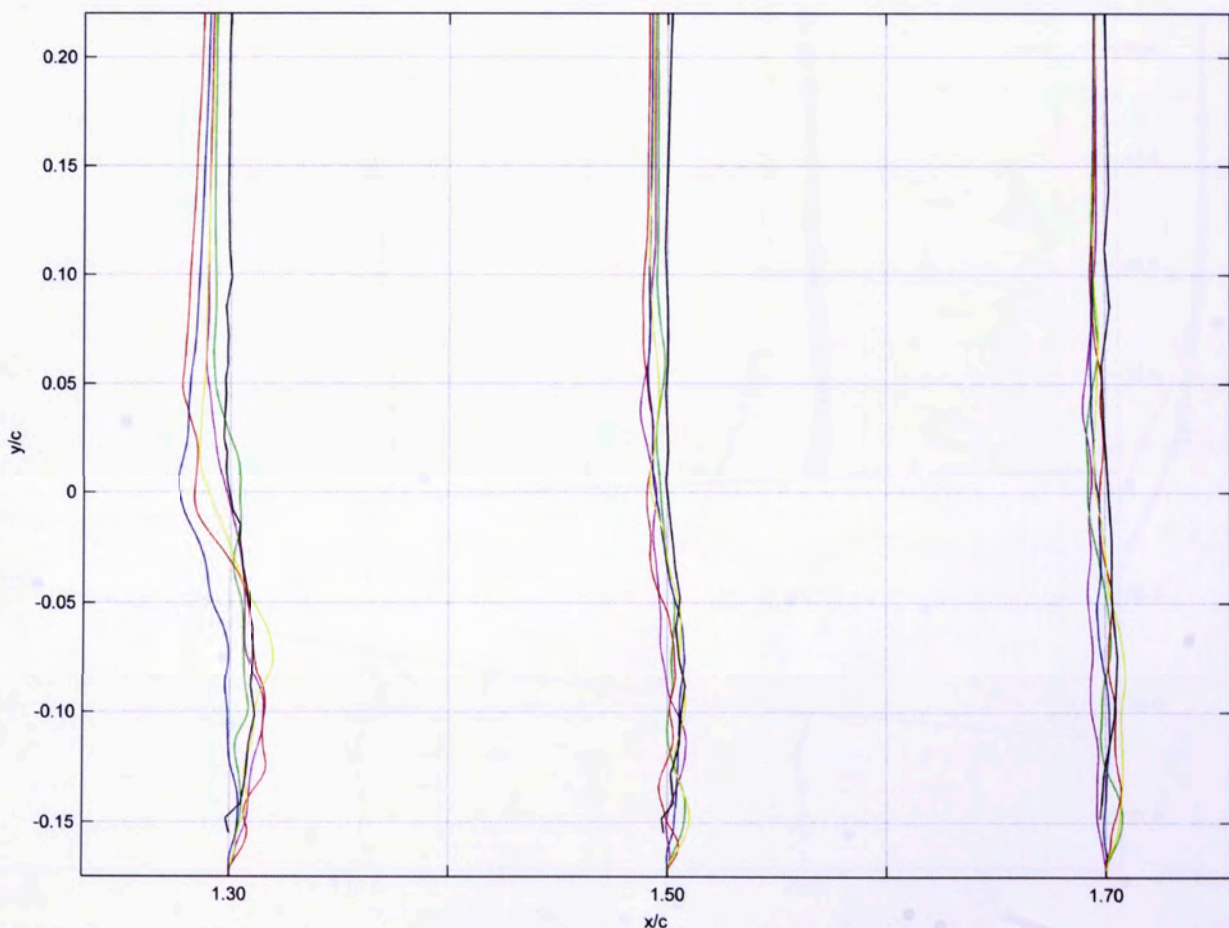


Figure D.16: Experimental and numerical y-velocity profiles at  $x/c = 1.30, 1.50$  and  $1.70; 0.1 x/c = 3$  m/s

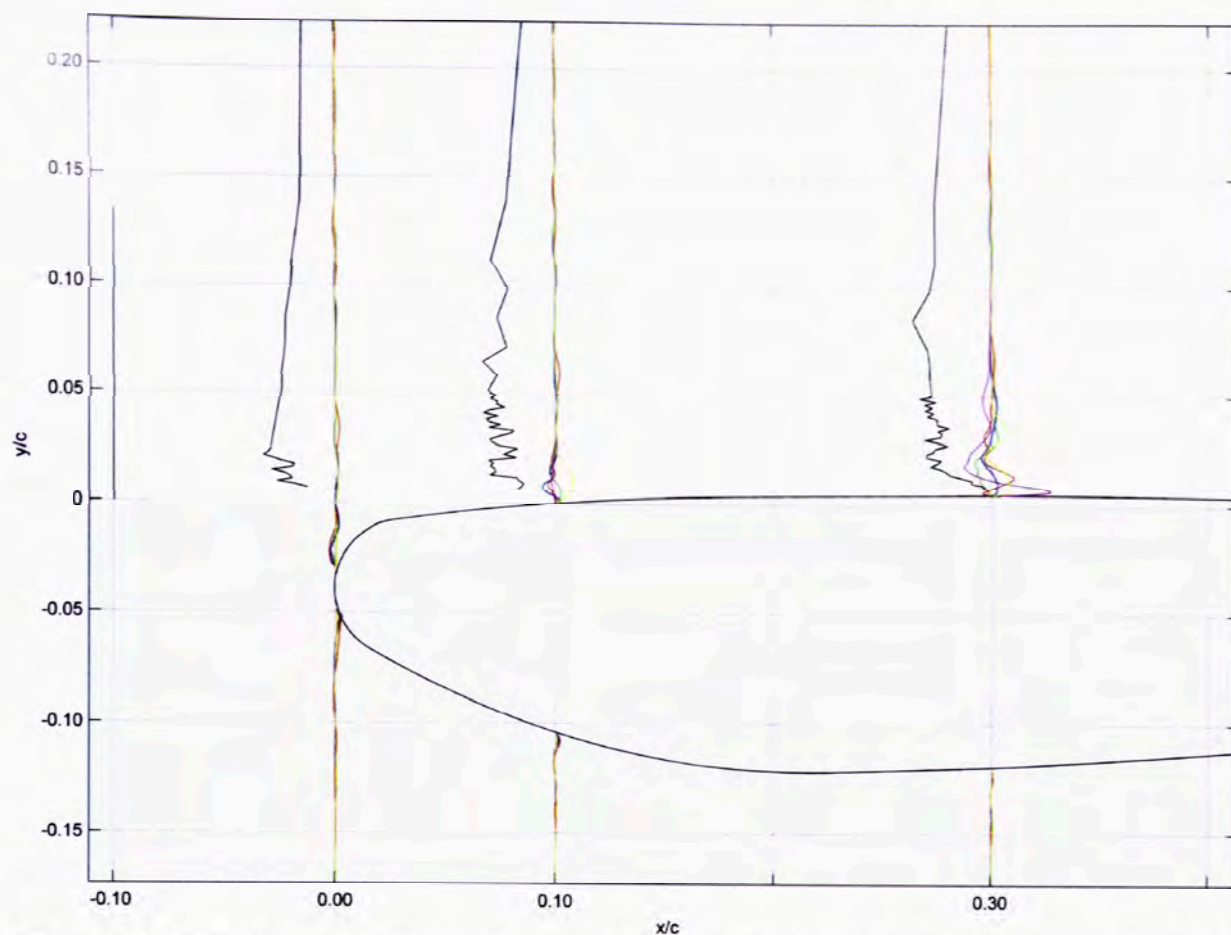


Figure D.17: Experimental and numerical  $z$ -velocity profiles at  $x/c = 0, 0.10$  and  $0.30$ ;  $0.1 x/c = 2$  m/s

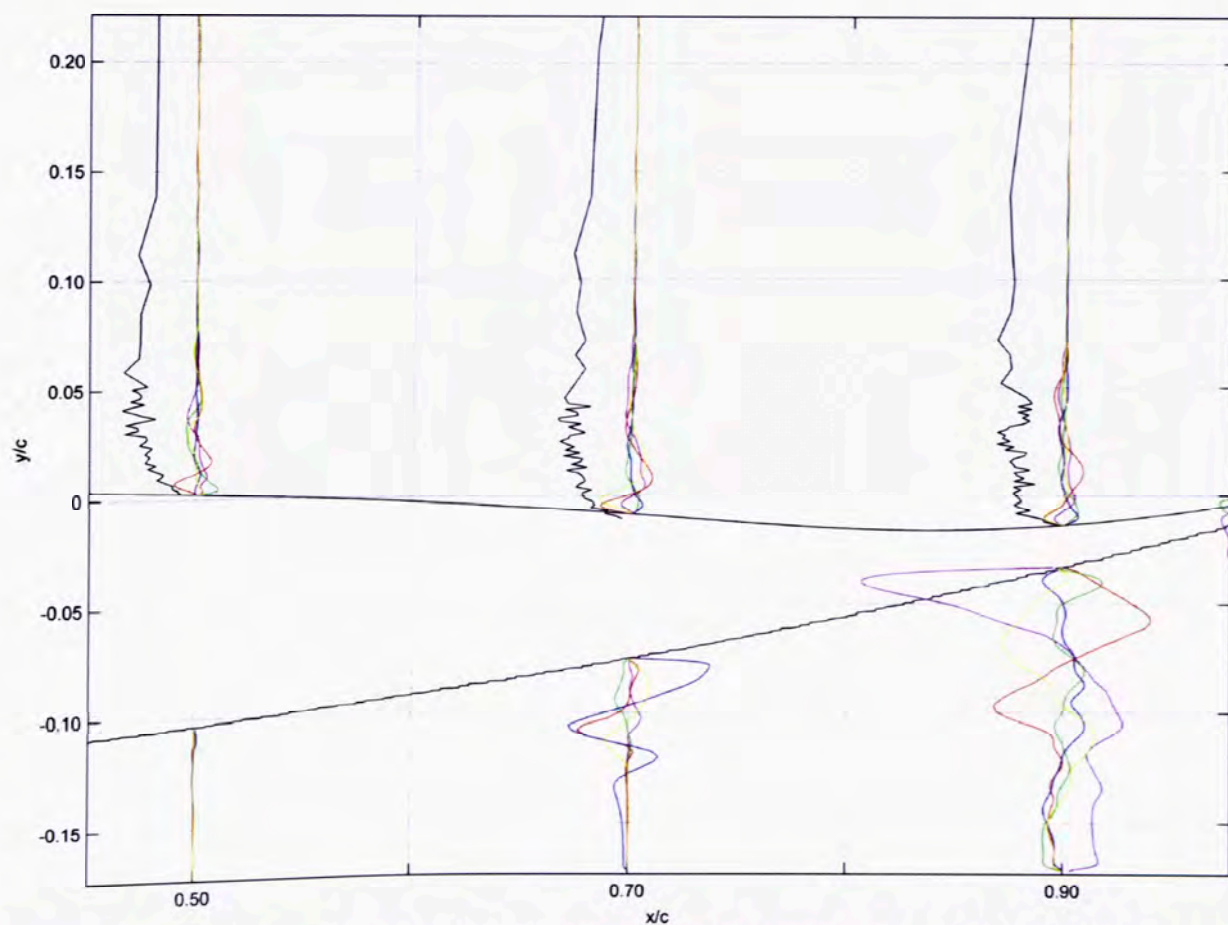
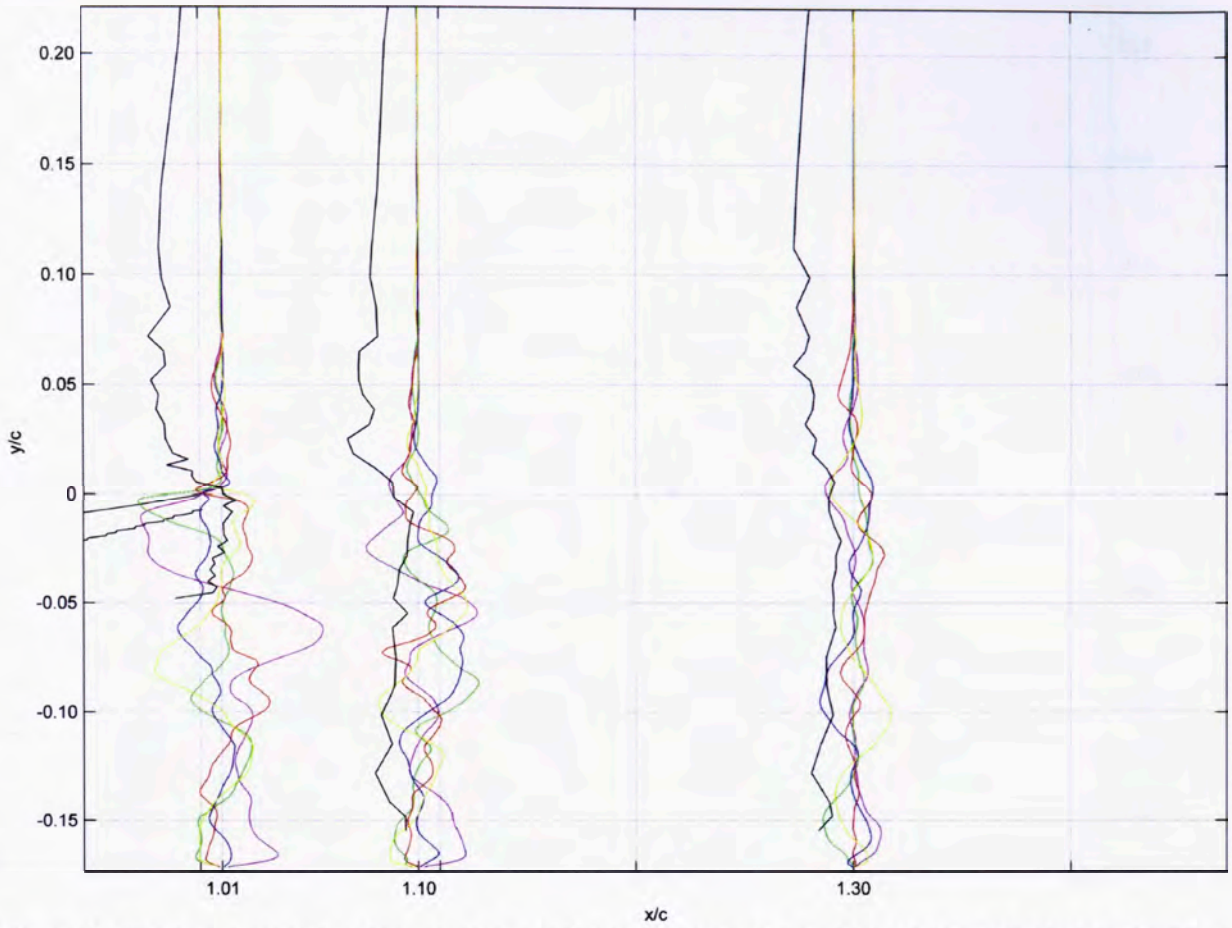
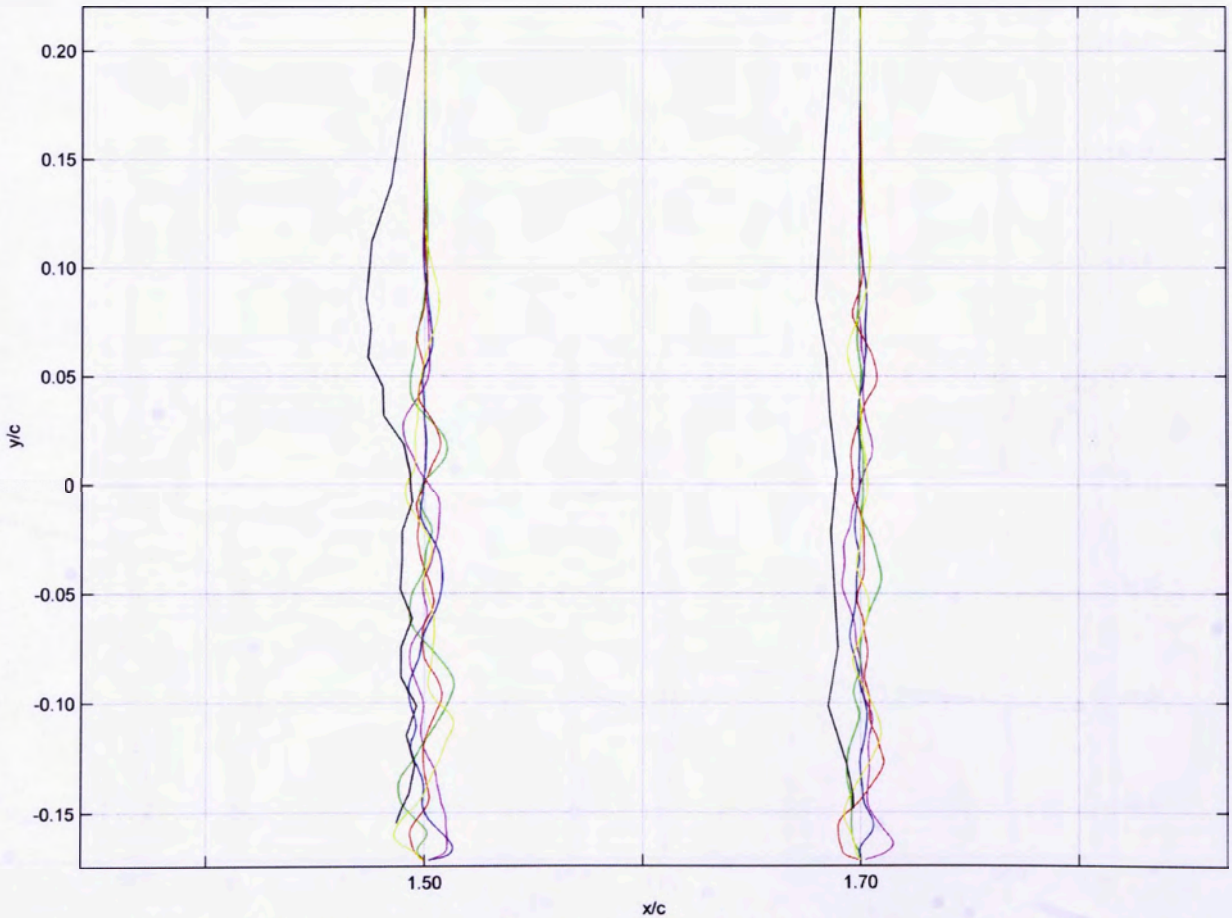


Figure D.18: Experimental and numerical  $z$ -velocity profiles at  $x/c = 0.5, 0.70$  and  $0.9$ ;  $0.1 x/c = 2$  m/s



**Figure D.19: Experimental and numerical z-velocity profiles at  $x/c = 1.01, 1.10$  and  $1.30$ ;  $0.1 x/c = 2$  m/s**



**Figure D.20: Experimental and numerical z-velocity profiles at  $x/c = 1.50$  and  $1.70$ ;  $0.1 x/c = 2$  m/s**

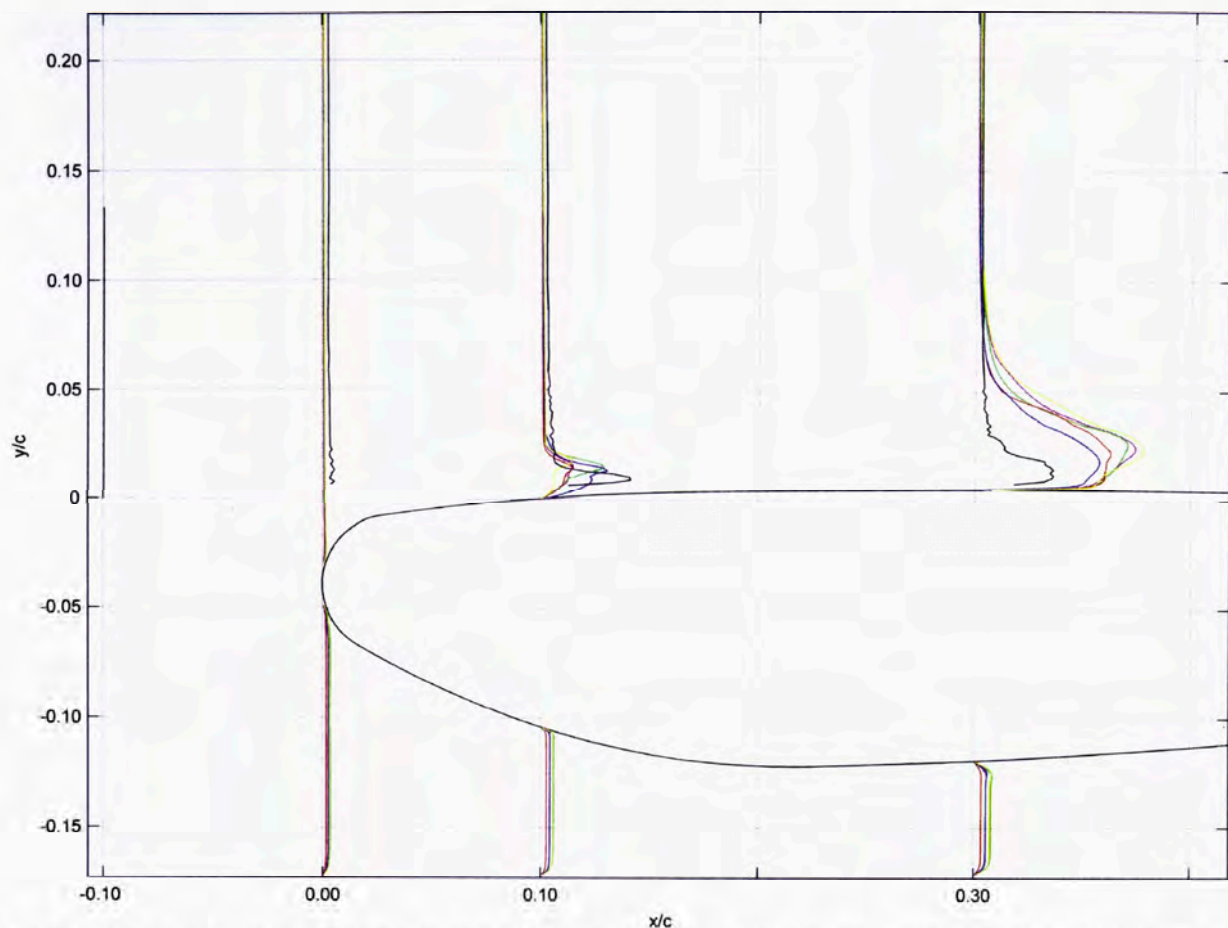


Figure D.21: Experimental and numerical RMS-x-velocity profiles at  $x/c = 0, 0.10$  and  $0.30$ ;  $0.1 x/c = 4$  m/s

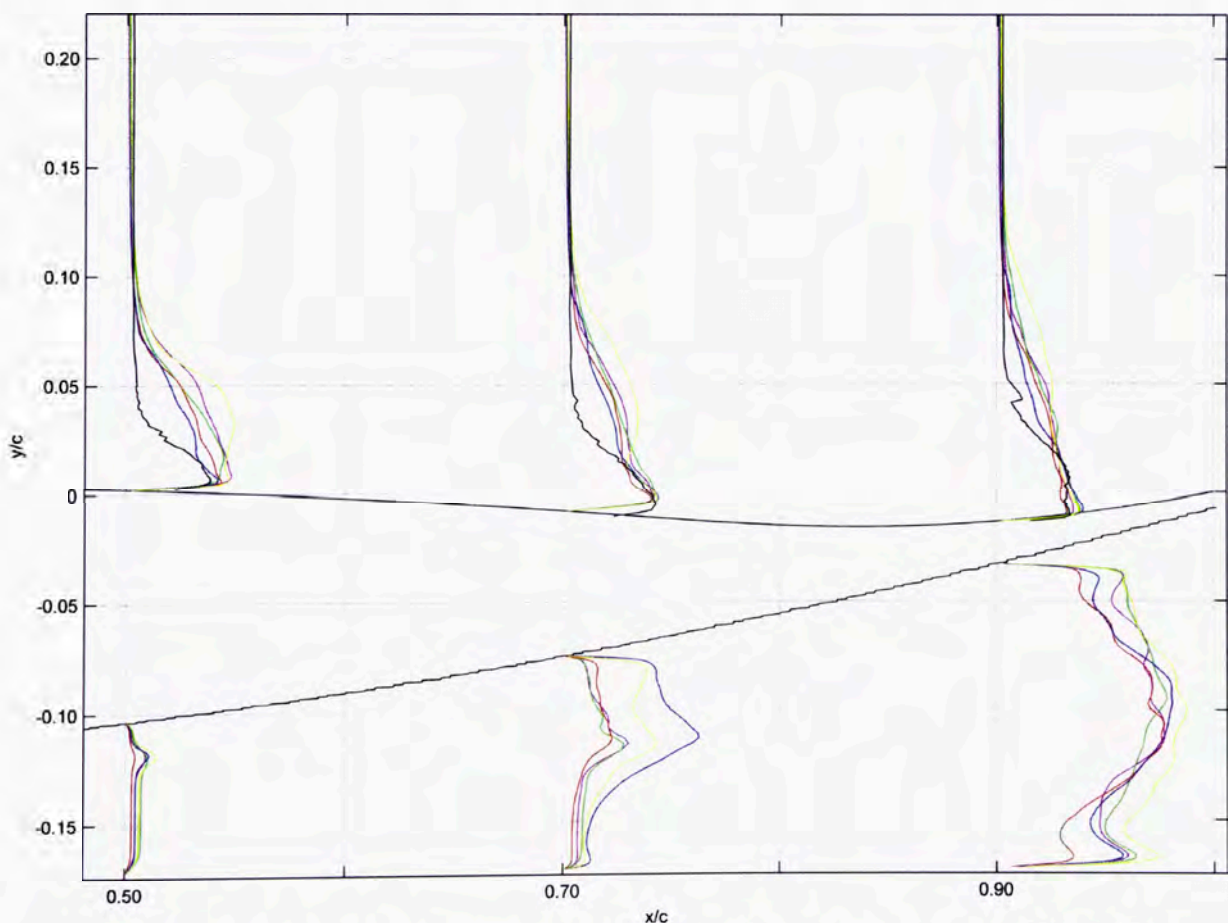
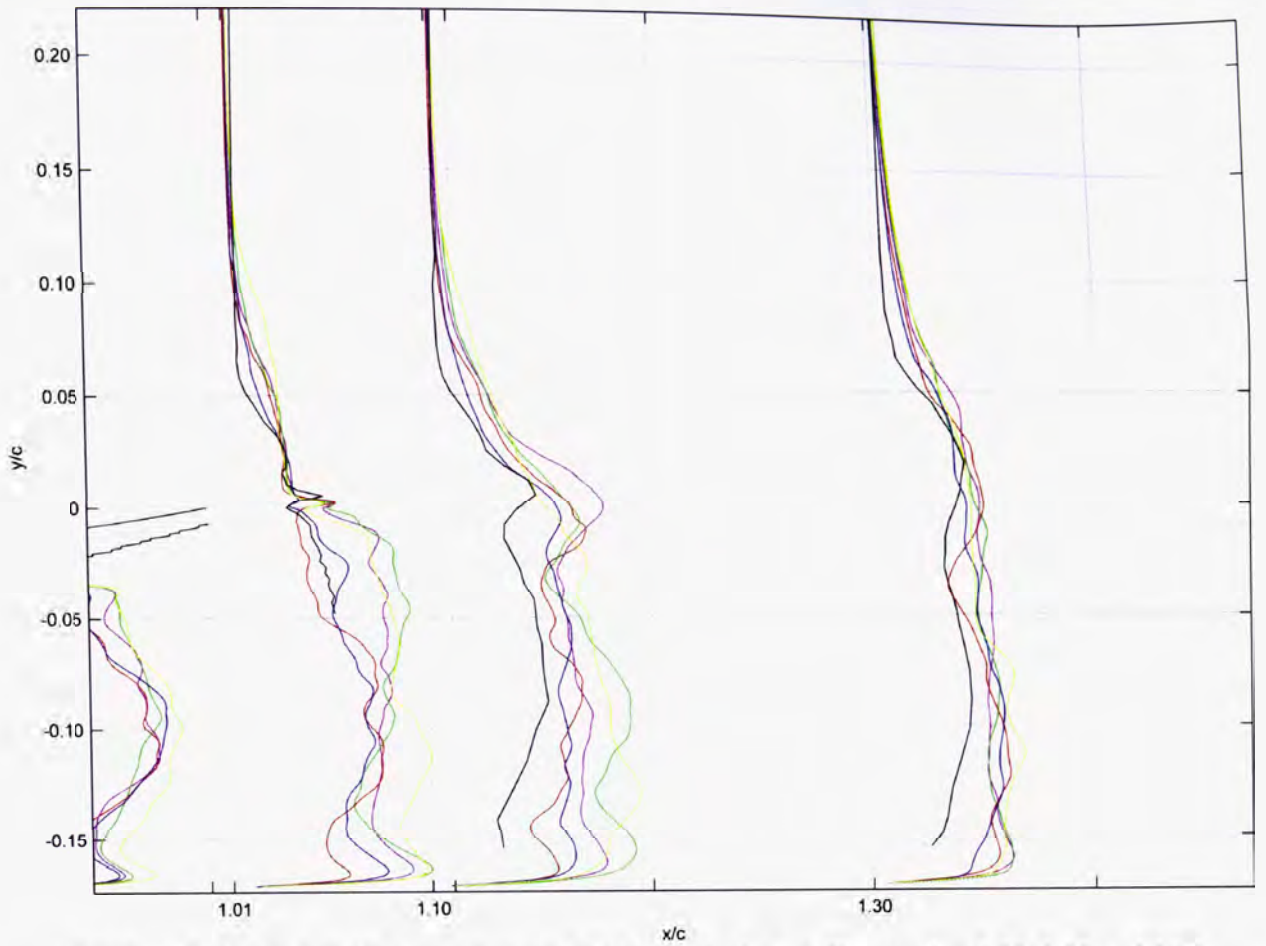
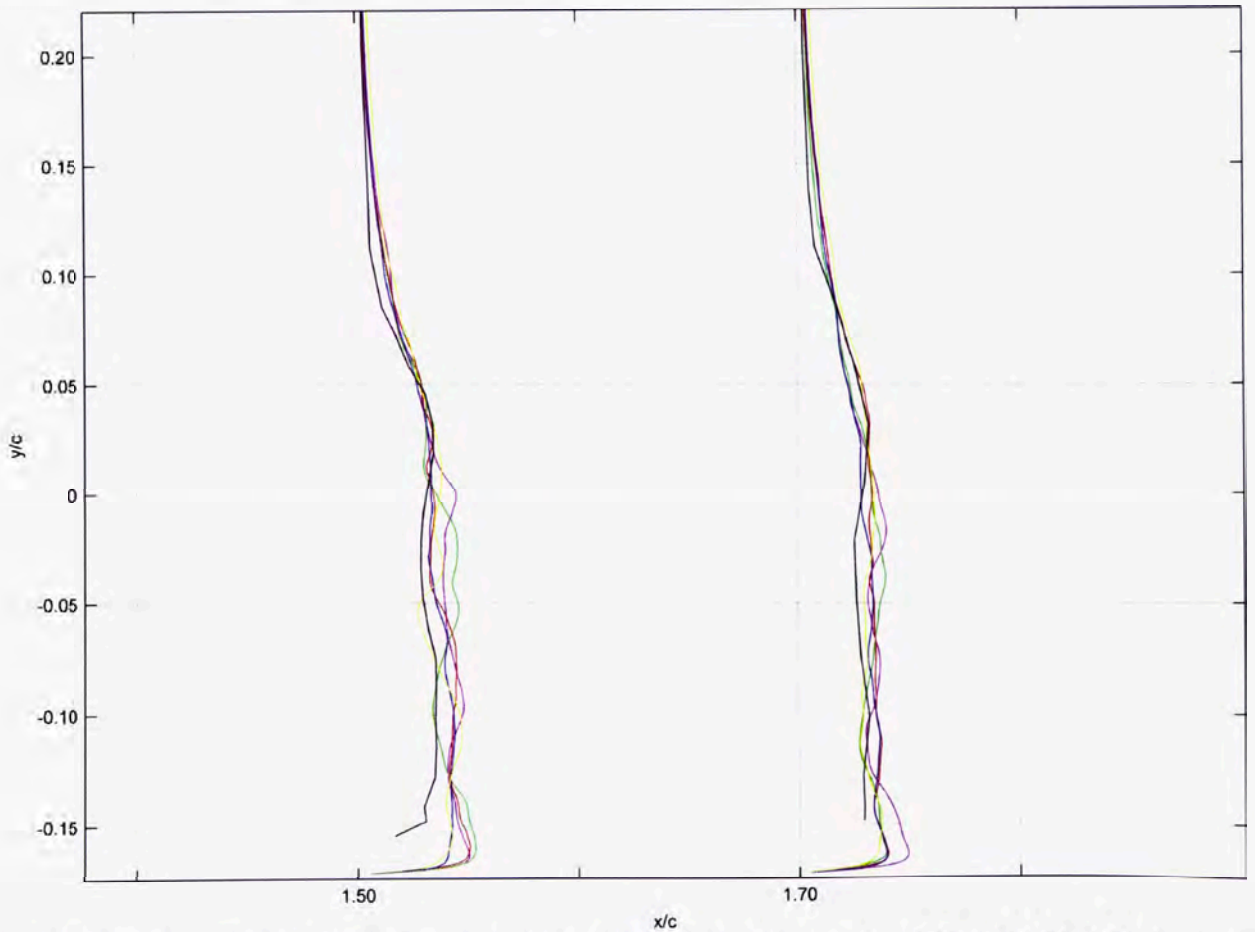


Figure D.22: Experimental and numerical RMS-x-velocity profiles at  $x/c = 0.5, 0.70$  and  $0.9$ ;  $0.1 x/c = 4$  m/s



**Figure D.23: Experimental and numerical RMS-x-velocity profiles at  $x/c = 1.01, 1.10$  and  $1.30$ ;  $0.1 x/c = 4$  m/s**



**Figure D.24: Experimental and numerical RMS-x-velocity profiles at  $x/c = 1.50$  and  $1.70$ ;  $0.1 x/c = 4$  m/s**

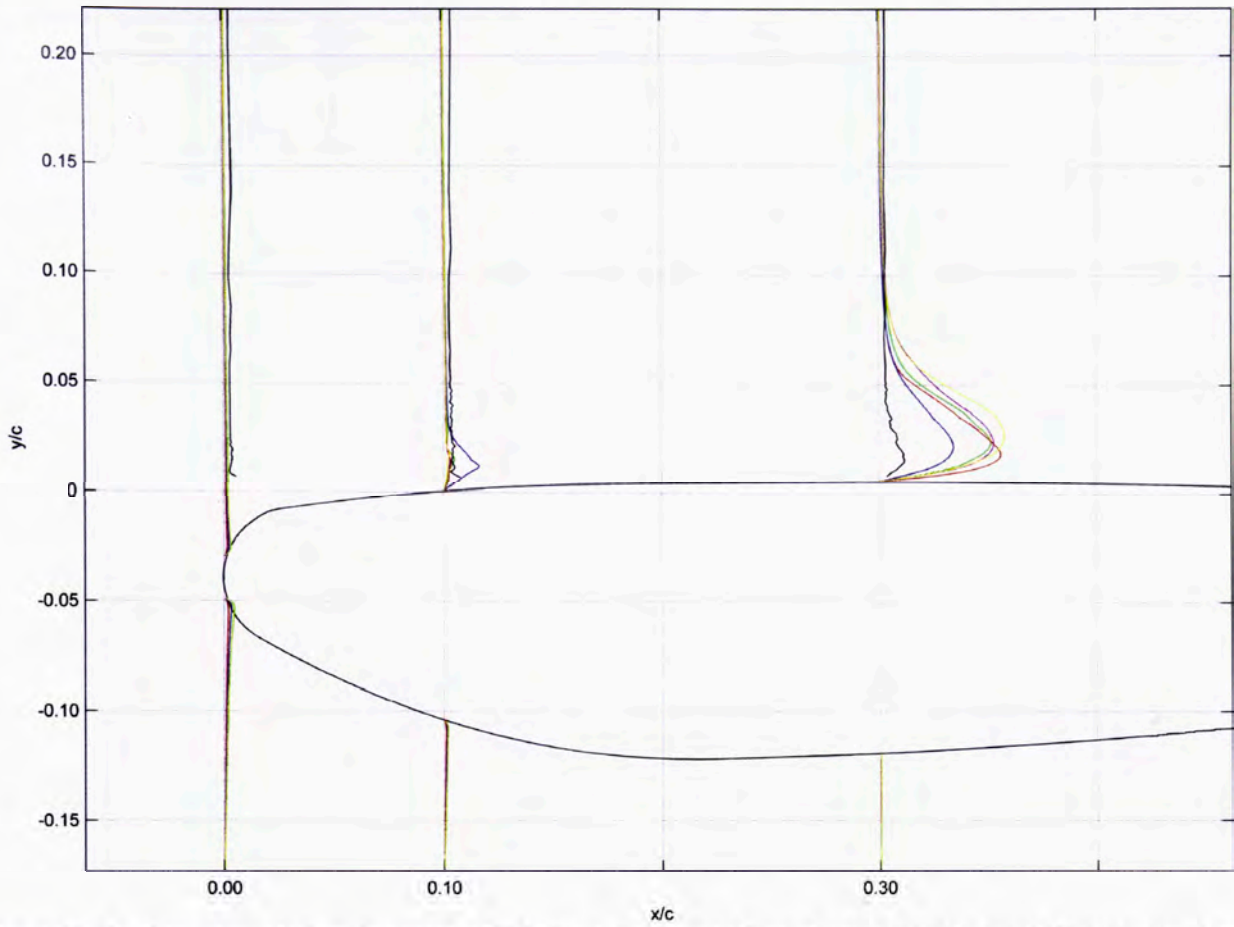


Figure D.25: Experimental and numerical RMS-y-velocity profiles at  $x/c = 0, 0.10$  and  $0.30$ ;  $0.1 x/c = 4$  m/s

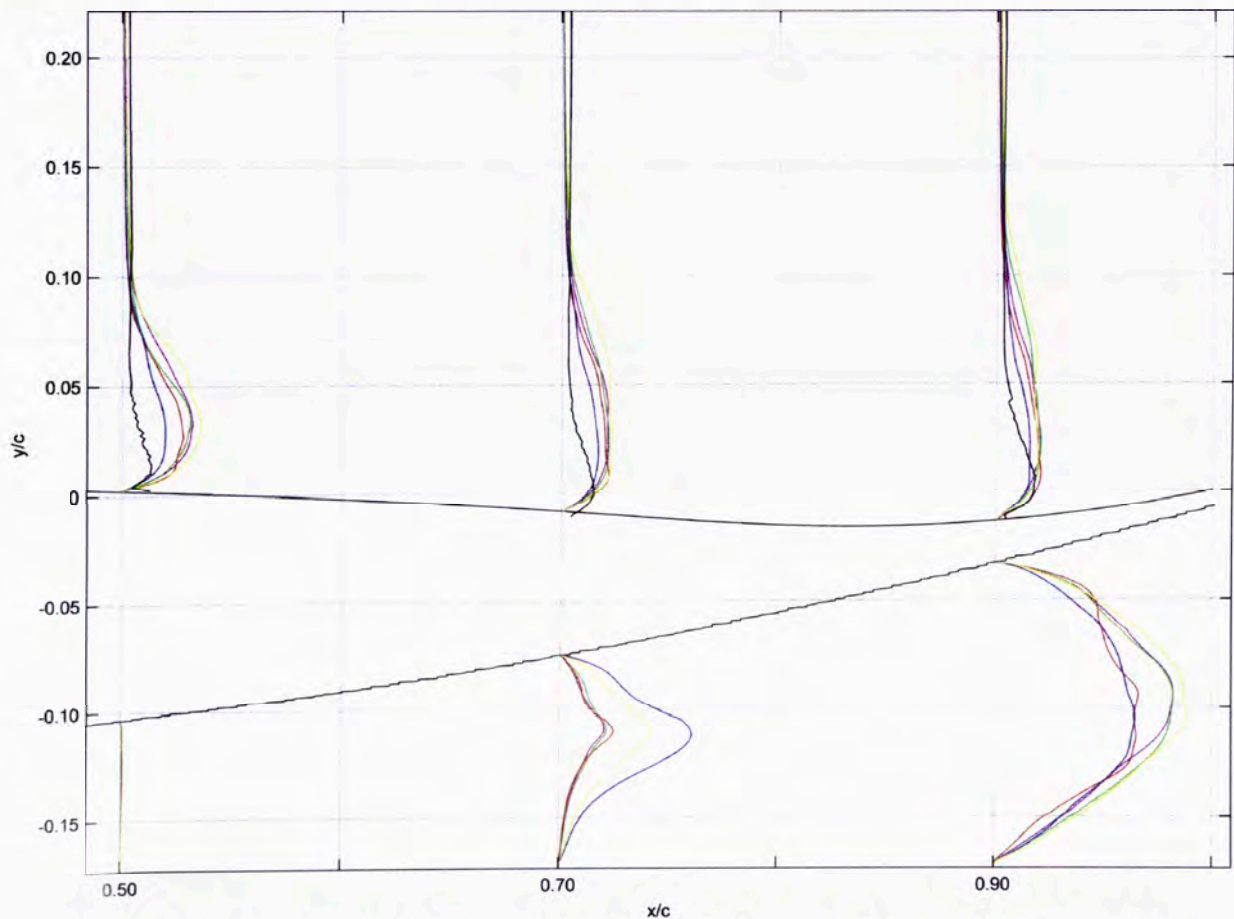
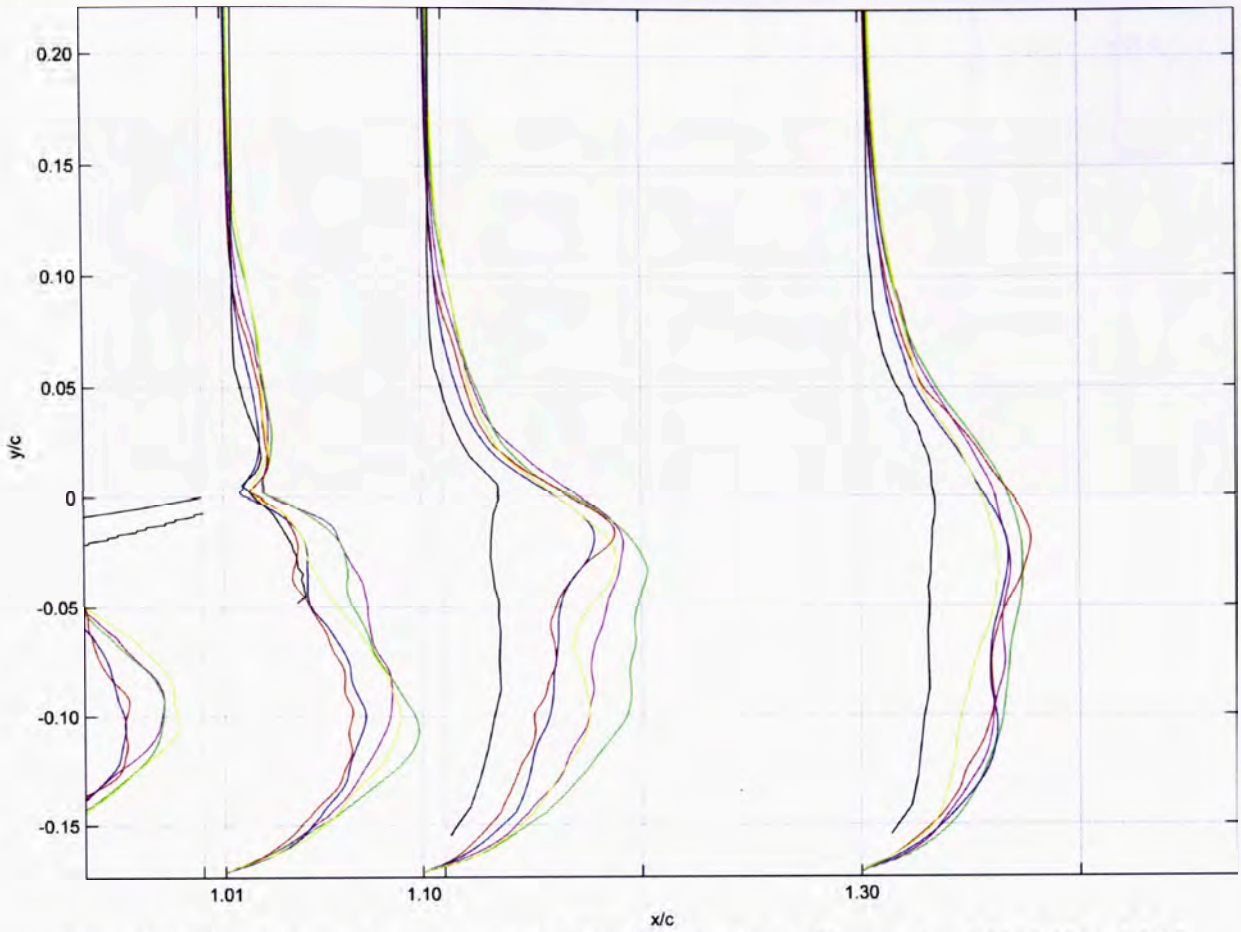
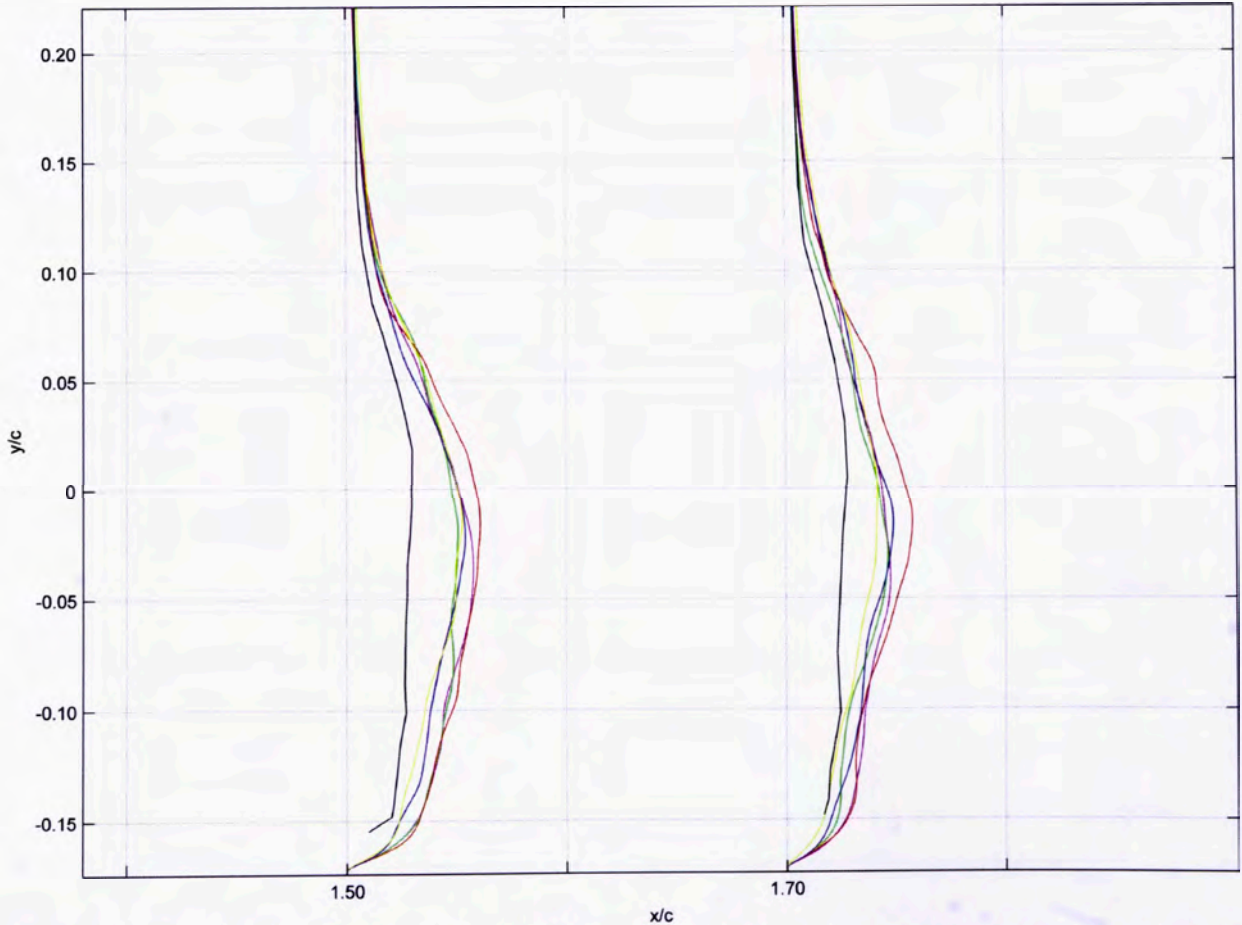


Figure D.26: Experimental and numerical RMS-y-velocity profiles at  $x/c = 0.5, 0.70$  and  $0.9$ ;  $0.1 x/c = 4$  m/s



**Figure D.27: Experimental and numerical RMS-y-velocity profiles at  $x/c = 1.01$ ,  $1.10$  and  $1.30$ ;  $0.1 x/c = 4$  m/s**



**Figure D.28: Experimental and numerical RMS-y-velocity profiles at  $x/c = 1.50$  and  $1.70$ ;  $0.1 x/c = 4$  m/s**

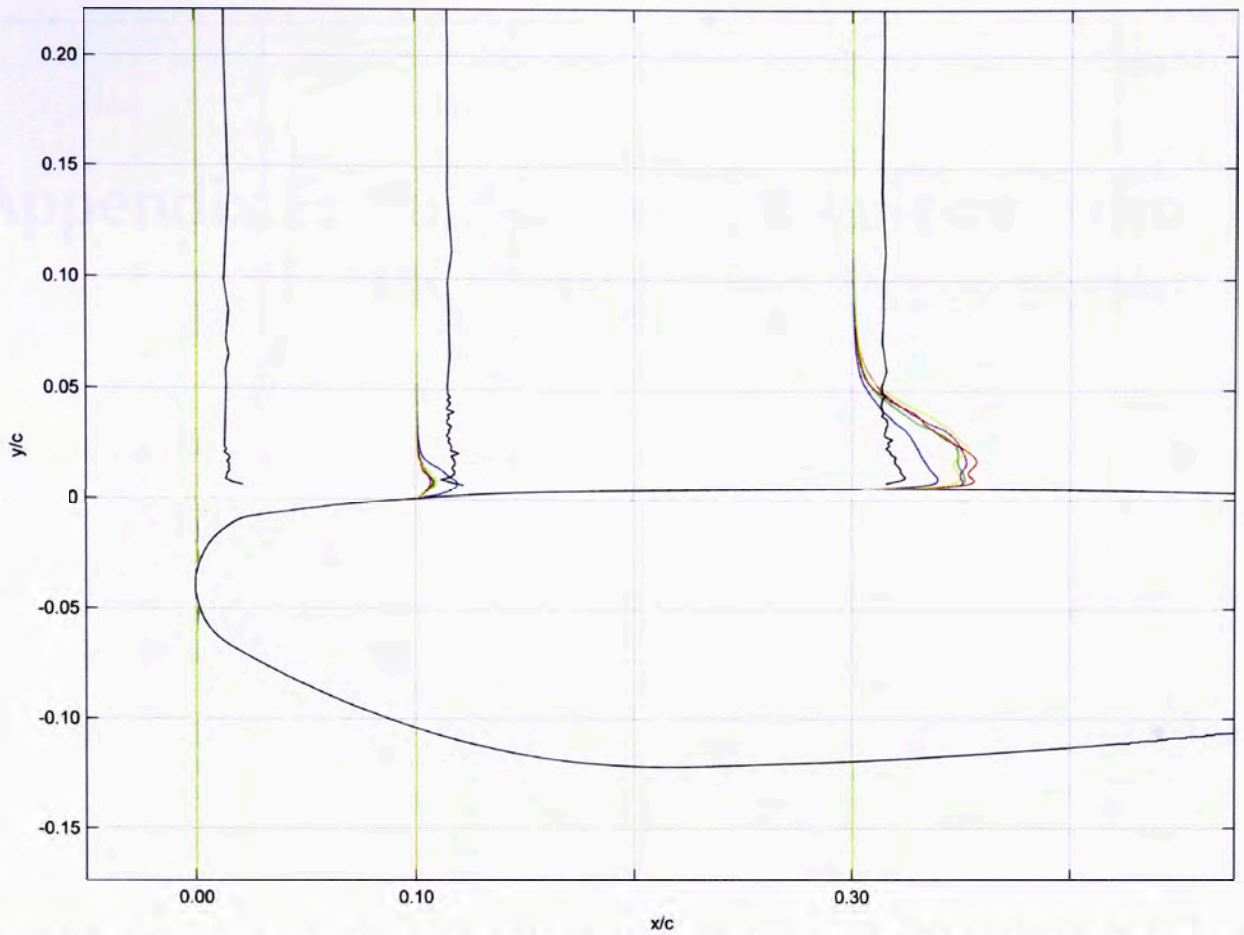


**Figure D.29: Experimental and numerical RMS-z-velocity profiles at  $x/c = 0, 0.10$  and  $0.30$ ;  $0.1 x/c = 4$  m/s**

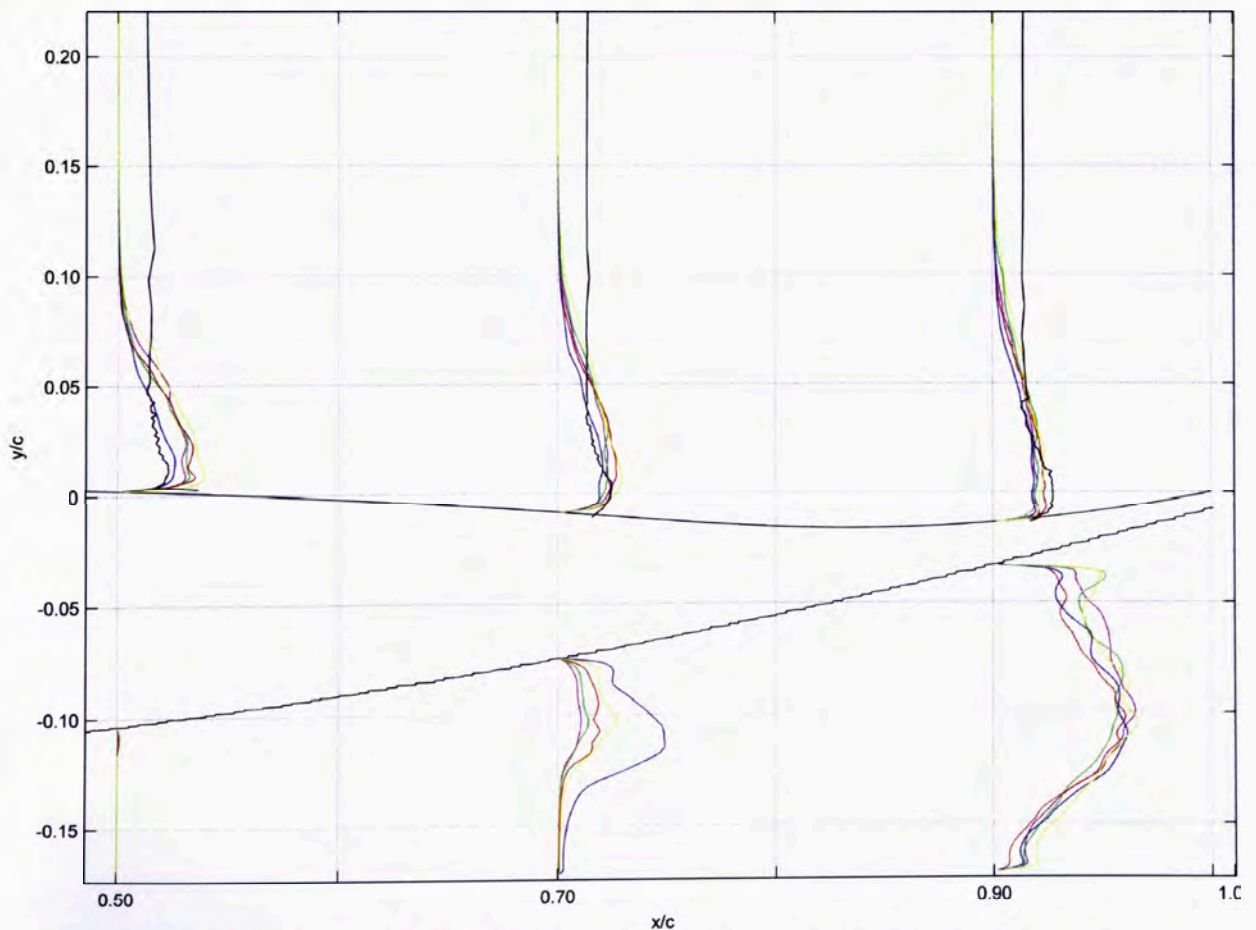


**Figure D.30: Experimental and numerical RMS-z-velocity profiles at  $x/c = 0.5, 0.70$  and  $0.9$ ;  
 $0.1 x/c = 4$  m/s**

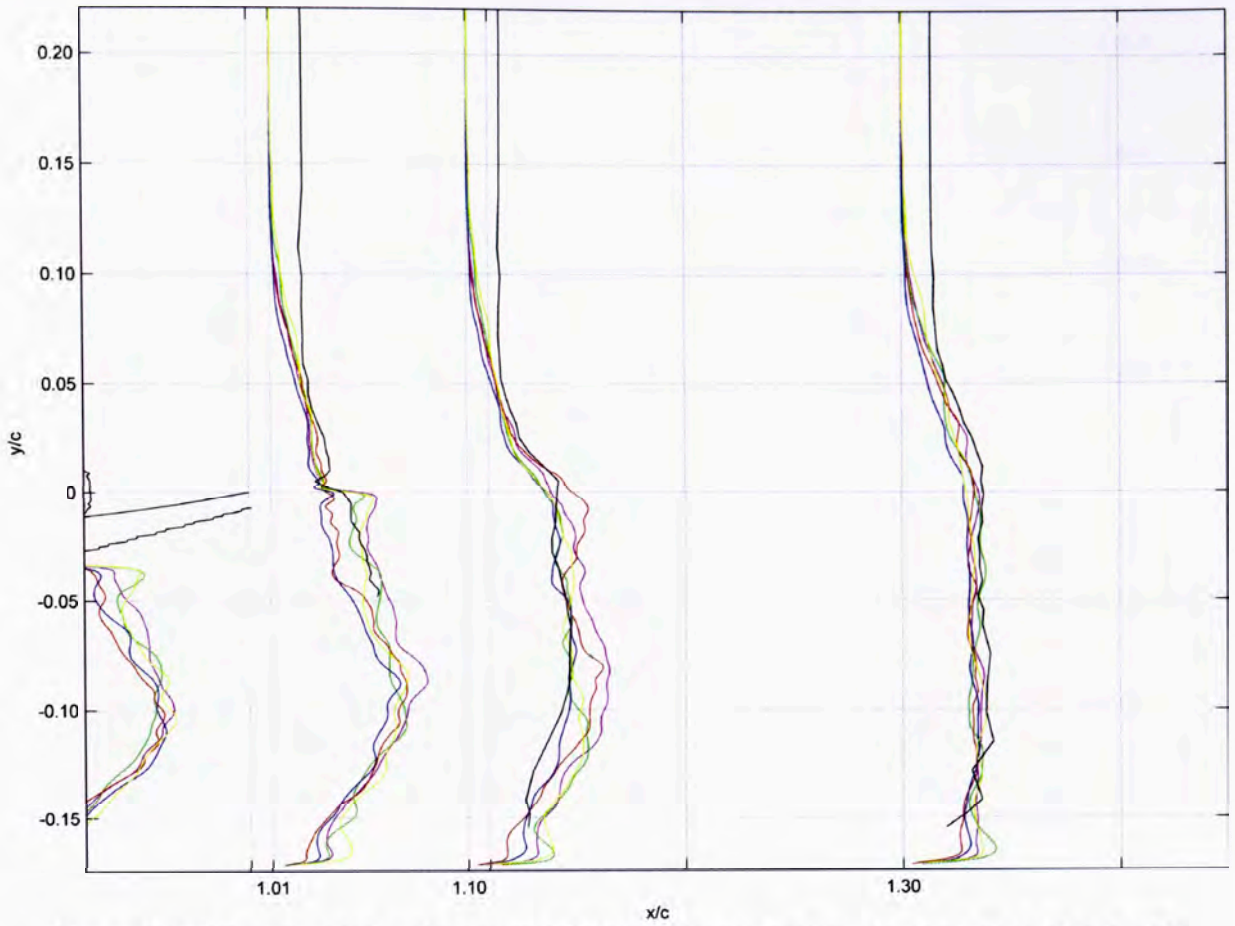


**Figure D.31: Experimental and numerical RMS-z-velocity profiles at  $x/c = 1.01, 1.10$  and  $1.30$ ;  $0.1 x/c = 4$  m/s**

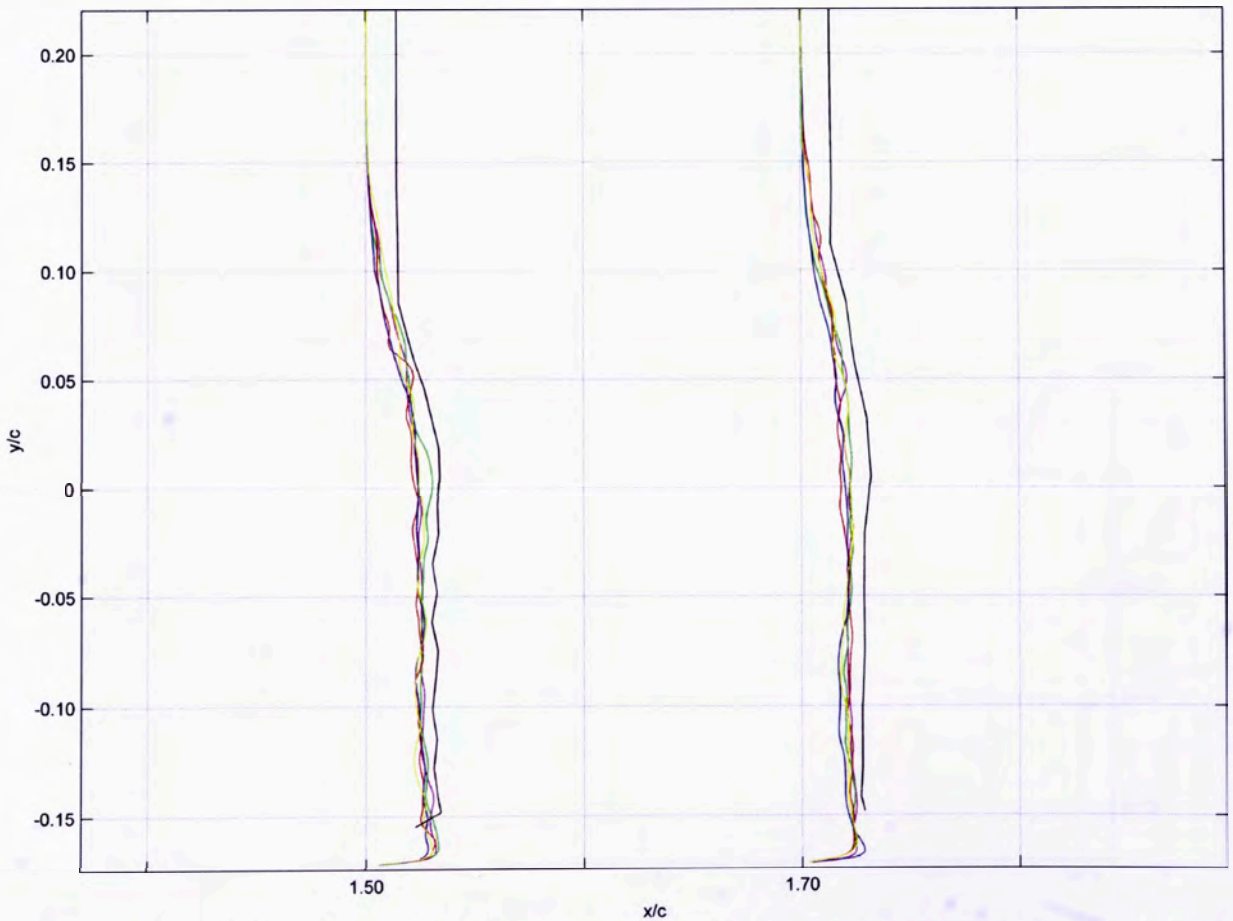


**Figure D.32: Experimental and numerical RMS-z-velocity profiles at  $x/c = 1.50$  and  $1.70$ ;  $0.1 x/c = 4$  m/s**

# Appendix E: Publications Resulting from Ph.D. Research Programme

The following is a list of all publications that have resulted from this research programme. All publications, be it journal or conference, underwent a peer-review process before publication was approved.

## E.1 Peer-Reviewed Journal Papers

- [1] Vogt, J.W., Barber, T.J. and Leonardi, E., “Flow Field Phenomena about Lift and Downforce Generating Cambered Aerofoils in Ground Effect”, *WSEAS Transactions on Fluid Mechanics*, Vol. 3, No. 3, pp. 234-243, July 2008.
- [2] Vogt, J.W. and Barber, T.J., “Variation of Ground Effect Phenomena about Downforce Generating Tyrrell and NACA4412 Aerofoils”, *International Journal of Aerodynamics*, Vol. 1, No. 1, pp. 82-96, 2010.

## E.2 Peer-Reviewed Conference Papers

- [1] Vogt, J.W., Barber, T.J. and Leonardi, E., “Flow Field Phenomena about Lift and Downforce Generating Cambered Aerofoils in Ground Effect”, Proceedings of 16<sup>th</sup> Australian Fluid Mechanics Conference, Gold Coast, Australia, 2-7 December, 2007.
- [2] Vogt, J.W., Barber, T.J. and Leonardi, E., “Effect of Inverted Aerofoil Geometry on Aerodynamic Performance in Ground Effect”, Proceedings of XXII International Congress on Theoretical and Applied Mechanics, Adelaide, 25-29 August, 2008.



